Lecture Notes in Intelligent Transportation and Infrastructure
Series Editor: Janusz Kacprzyk

Ajit Kumar Parwani
PL. Ramkumar *Editors*

Recent Advances in Mechanical Infrastructure

Proceedings of ICRAM 2019

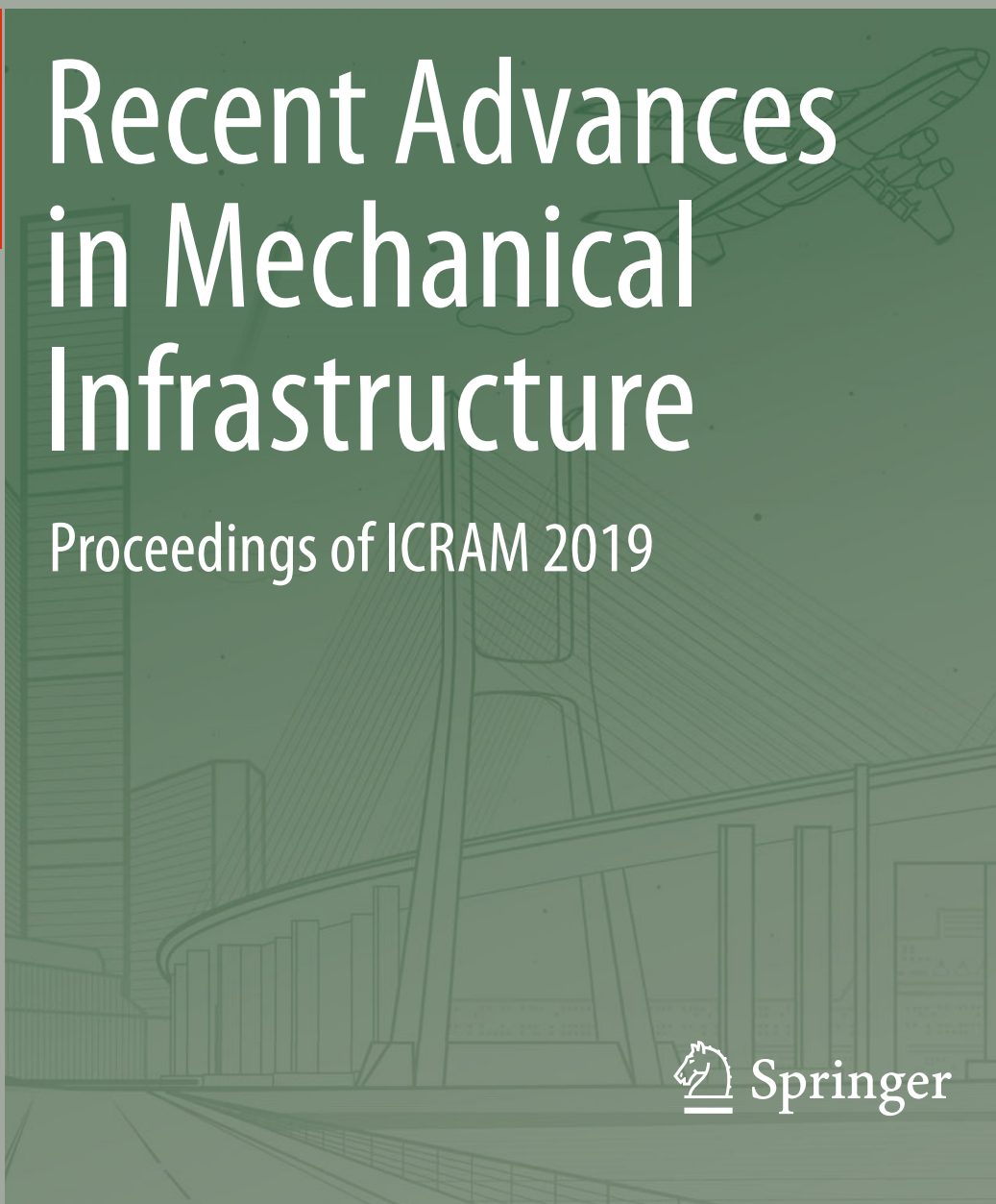

Springer

Lecture Notes in Intelligent Transportation and Infrastructure

Series Editor

Janusz Kacprzyk, Systems Research Institute, Polish Academy of Sciences, Warszawa, Poland

The series "Lecture Notes in Intelligent Transportation and Infrastructure" (LNITI) publishes new developments and advances in the various areas of intelligent transportation and infrastructure. The intent is to cover the theory, applications, and perspectives on the state-of-the-art and future developments relevant to topics such as intelligent transportation systems, smart mobility, urban logistics, smart grids, critical infrastructure, smart architecture, smart citizens, intelligent governance, smart architecture and construction design, as well as green and sustainable urban structures. The series contains monographs, conference proceedings, edited volumes, lecture notes and textbooks. Of particular value to both the contributors and the readership are the short publication timeframe and the world-wide distribution, which enable wide and rapid dissemination of high-quality research output.

More information about this series at http://www.springer.com/series/15991

Ajit Kumar Parwani · PL. Ramkumar
Editors

Recent Advances in Mechanical Infrastructure

Proceedings of ICRAM 2019

Springer

Editors
Ajit Kumar Parwani
Department of Mechanical Engineering,
Faculty of Mechanical Engineering
Institute of Infrastructure Technology
Research and Management
Ahmedabad, Gujarat, India

PL. Ramkumar
Department of Mechanical Engineering,
Faculty of Mechanical Engineering
Institute of Infrastructure Technology
Research and Management
Ahmedabad, Gujarat, India

ISSN 2523-3440 ISSN 2523-3459 (electronic)
Lecture Notes in Intelligent Transportation and Infrastructure
ISBN 978-981-32-9970-2 ISBN 978-981-32-9971-9 (eBook)
https://doi.org/10.1007/978-981-32-9971-9

This Springer imprint is published by the registered company Springer Nature Singapore Pte Ltd.
The registered company address is: 152 Beach Road, #21-01/04 Gateway East, Singapore 189721, Singapore

Preface

This book is brought out to mark the occasion of International Conference on Recent Advances in Mechanical Infrastructure (ICRAM-2019) during 20–21 April 2019 organised by Department of Mechanical Engineering, IITRAM, Ahmedabad. The purpose of this conference is to provide a platform for academicians, researchers and industrial professionals to exchange their views, ideas and experiences and collaborate for expediting progress in the fields of thermal, manufacturing, planning and design infrastructure.

The level of interest in the subject matter of the conference was maintained by submitting 109 suitable papers at the conference. Every submitted paper went through a peer review process. Each paper received at least two reviews. Finally, 33 papers were selected for presentation in three different tracks like thermal, manufacturing and design Infrastructure.

The conference conveners would like to thank the delegates who have contributed to the conference proceedings as book chapters. We would also like to thank our outstanding keynote speakers—Dr. S. S. Mahapatra, Professor, NIT Rourkela, Dr. Vivek Vitankar, Director, FluiDimensions and Dr. Udayraj, Assistant Professor, IIT Bhilai—for sharing their deep insights into future challenges and trends.

We would like to thank all the reviewers for their great effort in reviewing the papers submitted to ICRAM-2019. We extend our sincere appreciation to our sponsors—SERB-DST Government of India, GUJCOST Government of Gujarat and KC Engineers Limited—without whom our work would not be possible.

We are grateful to the Management of IITRAM for their help and support in organising this mega-event.

We hope that this book will motivate many academicians and industrial professionals to specialise in the fields of thermal, manufacturing, planning and design Infrastructure.

Ahmedabad, India

Ajit Kumar Parwani
PL. Ramkumar

Contents

About the Editors

Dr. Ajit Kumar Parwani is working as Assistant Professor in the Department of Mechanical Engineering at Institute of Infrastructure Technology Research and Management (IITRAM), Ahmedabad, India. He has completed his Ph.D. from Indian Institute of Technology (IIT), Delhi, India in 2013. He has over 15 years of teaching and research experience. His research interests include Heat transfer, Inverse heat transfer, Computational heat transfer, Renewable energy and IC Engines. He has published several papers in international journals. He has filed an Indian patent title "Simultaneous reduction of NOx and CO_2 using exhaust gas recirculation and carbon capture". He has conducted several workshops, short term training programs and seminars. He has two ongoing research projects funded by SERB-DST, Government of India and Institute of Plasma Research, Government of India.

Dr. PL. Ramkumar is an Assistant professor in Mechanical Engineering department at IITRAM, Ahmadabad. He served as a lecturer in the Mechanical Engineering department at the Birla Institute of Technology and Science, Pilani, KK Birla Goa campus, Goa, India for 8 years. He has over 12 years of teaching and research experience. He has been teaching core mechanical courses like Computer aided design, Mechanics of solids, Computer aided analysis and design, Product design etc. He completed his graduation in Mechanical Engineering from Madurai Kamaraj University in 2003. He obtained M. E degree in Computer Aided Design from Anna University, Tamilnadu, India in 2008 securing **University rank** with **Gold medal**. He received his PhD from BITS PILANI in the year 2016. His area of research includes experimental analysis of manufacturing processes, process modeling, computer aided analysis and optimization. He has organized various workshops and conferences. He has published good number of research papers in the international journal / conferences of repute. He is life a member of various prestigious societies which includes Institute of Engineers (MIE), Indian Institute of Metals (IIM) and Hong Kong Society of Mechanical Engineers (HKMSE).

Recent Advances in Manufacturing Infrastructure

Experimental Performance Evaluation of Mist Cooling Using Biodegradable Coconut Oil in Turning of EN24 Steel in Minimization of Tool Wear, Surface Roughness, and Chip Thickness

Miriyala VeeraBhadraRao, Bhushan T. Patil, Vasim A. Shaikh and D. S. S. Sudhakar

Abstract Cooling and lubrication are essential factors for any machining process for reducing cutting tool tip temperatures, cutting tool forces, and increasing cutting tool life as well as work surface quality. Also, to reduce the machining coolants with better cooling and lubricity, minimum quantity lubrication is employed. Coconut oil being biodegradable is recommended in most machining processes as coolant. Comparative evaluations were drawn from data collected during turning experiments in dry, water flooding, and coconut oil mist using MQL method in view of tool wear and surface roughness of machined workpieces under study. It was found that the performance of edible biodegradable vegetable cutting fluids using coconut oil is better than dry and flood cooling. Mist method of cooling uses less quantity fluids and is comparatively safer and cleaner in applications. Through the design of experiments (DOE) and analysis of variance (ANOVA), tool wear, surface roughness, and chip thickness had a comparable reduction in values and are beneficial in machining.

Keywords Turning · EN24 steel · Coconut oil · Mist cooling · MQL

1 Introduction

Machining is an ancient manufacturing process involving removal of material from the workpiece by a hard cutting tool with or without the use of coolants and lubricants. In today's trend, there are large combination and variations in work material and cutting tools based on the application. For example, in space application, we tend to use high strength to weight ratio materials like aluminum composites, Inconel which are hard to machine. Machining poses difficulties like early tool failures, large energy consumptions, and inaccuracies. High temperatures and forces, lower tool life, energy inefficiencies have led to large-scale developments and research

M. VeeraBhadraRao (✉) · B. T. Patil · V. A. Shaikh · D. S. S. Sudhakar
Fr. Conceicao Rodrigues College of Engineering, Fr. Agnel Ashram, Bandstand, Bandra (W), Mumbai, India
e-mail: mdnvbr@gmail.com

A. K. Parwani and PL. Ramkumar (eds.), *Recent Advances in Mechanical Infrastructure*, Lecture Notes in Intelligent Transportation and Infrastructure,
https://doi.org/10.1007/978-981-32-9971-9_1

in machining sector. Operator's safety issues and environmental hazards led to the usage of eco-friendly cooling in machining using biodegradable fluids like coconut oil and are fast replacing mineral oil-based cutting fluids. There is a wide scope of research on conservation of useful material, effective methods for reduction of energy, time, etc. Minimum quantity lubrication (MQL) employs running pressurized mist fluid quantities of ten to fifty times lesser than flooded cooling technique. MQL unit requires an air compressor at operative pressure ranges from 5 to 10 bars, quantity flow rate of 50 ml/hr to 130 ml/hr, and a contracted nozzle through which coolant flows onto the work–tool interface [1–4, 10].

2 Literature Reviews

For the present experimentation of performance evaluations of coconut oil using mist lubrication, some few literature reviews were studied as shown below in Table 1.

3 Experimentation

3.1 Setup

The work material is EN24 alloy steel (Dia. 60 mm × 250 mm long) which is medium carbon steel. Initial truing and centering are done prior to actual experimental working. Length of cut for experimentation was 200 mm. The material was tested for its chemical composition at test laboratories. The chemical composition of the work material is as shown in Table 2 as per ASTM standards.

Kirloskar engine lathe was used for experimentation. Surface speed ranged from 90 to 110 m/min, RPM of spindle was 560–1000, and depth of cut was kept constant at 0.5 mm. The cutting tool used in this experiment was uncoated carbide inserts of *P* grade CNMG120408. MQL setup employs solenoid operative switching to on/off the supply of coolant. Compressor is used to pressurize air which flows at air inlet. Pressure is maintained at 8 bars in all conditions of machining. Level of coolant oil was maintained minimum 50% in the tank for uninterrupted flow of mist coolant [12]. Virgin coconut oils were used in MQL cooling systems in turning experimentation. The surface roughness readings were measured through Mitutoyo make surface roughness tester. The flank tool wear was measured by using Trinocular inverted metallurgical microscope (100X–1000X magnification) along with desktop computer and Drexel software to take the images from microscope. Chip thickness measurement at different combination experimental runs was done by digital vernier caliper having least count of 0.01 mm. Three readings are randomly taken for every chip, and average values are noted for analysis work. Experiments were conducted initially to compare the flank wear and surface roughness values in dry, wet, and mist

Table 1 Summary of literature reviews

Authors	Conditions	Results/conclusions/tools used
Chinchanikar et al. [5]	**Workpiece**: AISI 52,100 steel (60–62 HRc) diameter 60 mm, 600 length. **Tool**: TiSiN-TiAlN carbide inserts **Coolant**: Dry cooling and vegetable oils, mineral oils **Machine variables**: Feed, speed, depth of cut	i. Coconut oil-based cutting fluids produced lower surface roughness values with higher values of cutting parameters ii. Used ANOVA, regression, and response surface method (RSM) for analysis
Dhar et al. [6]	**Workpiece**: AISI 1040 steel Diameter 110 mm, 620 length **Tool**: SNMG carbide inserts **Coolant**: Dry, wet, and MQL **Machine variables**: Feed, speed, depth of cut	i. MQL machining is better in reducing cutting temperatures, maintaining sharpness of cutting tool ii. Color of the chips in MQL machining is lighter due to reduction of cutting temperature iii. Used simple spreadsheets and graphs for analysis
Gunjal and Patil [7]	**Workpiece**: AISI 4340 steel, diameter 250 mm, 300 lengths. **Tool**: PVD—CNMG120408 **Coolant**: Soybean, coconut, and canola oil. **Cutting speed**: Variable (three levels)	i. Canola oil provides good tool life than soybean oil and coconut oils ii. Speeds higher than 240 m/min show sudden failure of tools in all MQL cooling environments iii. There is no considerable variation in surface roughness under varying machining conditions iv. Used simple spreadsheets and graphs for analysis
Lohar [8]	**Work piece**: AISI 4340 steel Diameter 60 mm, 90 lengths **Tool**: TNMA 160,404 **Variables**: Feed rate, cutting speed, depth of cut, and cooling conditions	i. Cutting forces and temperatures in MQL is 40 and 36% lesser compared to dry and wet turning ii. 30% improvements in surface finish are observed in MQL conditions iii. Environment is having significant contribution w. r. t. machining factors iv. Used ANOVA for analysis

(continued)

Table 1 (continued)

Authors	Conditions	Results/conclusions/tools used
Rahim et al. [9]	**Work piece**: AISI 1045 steel, diameter 150 mm **Tool**: Uncoated carbide **Variables**: Dry, MQL Temperature measurement by IR camera	i. 10–30% reduction in cutting temperatures and 5–28% reduction in cutting forces for MQL condition are observed ii. Used simple spreadsheets and graphs
Venkata Ramana and Krishna Mohan Rao [11]	**Variables**: Machining environment, speed, feed, depth of cut, tool **Material** (three levels each)	i. MQL outperforms dry and wet environments. ii. Chip thickness is less in MQL. The back surface of chips is bright and smooth indicating less friction and heat. Low slip angles are observed which leads to less tool wear and high surface finish iii. Used: spreadsheet and graphs for analysis

Table 2 Percentage of chemical composition of EN24 steel

Carbon	0.35–0.45%	Phosphorus	0.05% max.
Nickel	1.30–1.80%	Manganese	0.45–0.70%
Sulfur	0.05% max.	Molybdenum	0.20–0.35%
Chromium	0.90–1.40%	Silicon	0.10–0.35%

lubrication conditions and are discussed. Next set of experimentations employed full factorial designs using ANOVA to predict the factor effects.

3.2 Design of Experiments (DOE) and ANOVA

For the experiments, 2 factors with 3 levels each as shown in Table 3 were selected. The values of feed rates were carefully selected after pilot experimentations and test runs earlier. Feed rates higher than 0.355 mm/rev. exhibited larger flank wear and high surface roughness, so limited maximum to 0.355 mm/rev. Machining time of 100 s was taken for all experimental runs.

Referring Table 3 values of flank wear, surface roughness and chip thickness, main effects plot (data means) for flank wear (mm) and for surface roughness (Ra values) are constructed using Minitab 14 as shown in Fig. 1a and b, respectively.

Table 3 L_9 full orthogonal array for turning experiment

Treatment no.	(A) Cooling method	(B) Feed rate	Flank wear (mm)	Surface roughness Ra(microns)	Chip thickness (mm)
1	1 (Dry)	1 (0.2)	0.083	2.61	0.54
2	1 (Dry)	2 (0.25)	0.094	1.19	0.68
3	1 (Dry)	3 (0.355)	0.146	2.09	0.72
4	2 (Wet)	1 (0.2)	0.035	1.07	0.56
5	2(Wet)	2 (0.25)	0.045	2.55	0.68
6	2 (Wet)	3 (0.355)	0.049	2.88	0.71
7	3 (Mist)	1 (0.2)	0.038	2.49	0.65
8	3 (Mist)	2 (0.25)	0.034	2.21	0.81
9	3 (Mist)	3 (0.355)	0.038	2.32	0.56

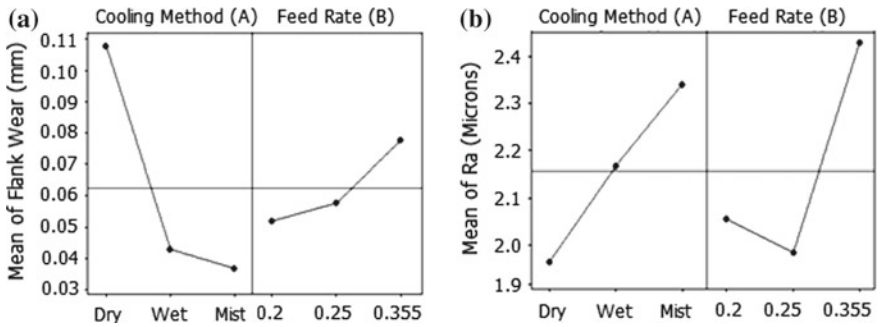

Fig. 1 Main effect plot for **a** flank wear and **b** surface roughness (Ra)

It is clearly evident in Fig. 1a that mist cooling lubrication method is better as flank wear is lowest. Flank wear is least at lower feed rates of 0.2 mm/rev. Figure 1b explains that surface roughness is higher in mist lubrication and lowest for dry. In fact, the values of surface finish are better with lower roughness values as we adopt mist lubrication. Surface finish is found to be better at lower feed rates of 0.2 and 0.25 mm/rev, and it is not feasible to go for higher feed rates else it will affect surface finish of work material. Analysis of variance (ANOVA) for tool wear and surface roughness is computed using Minitab 14 and Microsoft Excel spreadsheets taking confidence interval of 95%. Cooling rate is found to be significant factor in flank wear as found in Table 4, and F factor is greater than F-critical values. Both the factors, viz. cooling rate and feed rate, are found to be insignificant in surface roughness as indicated in Table 5.

Table 4 ANOVA table for flank wear

Source	DF	SS	MS	*F* factor	*P*	*F* critical at α = 0.05%	Result
Cooling rate	2	0.0092	0.0045	14.38	0.015	6.94	Significant
Feed rate (mm/rev.)	2	0.0011	0.0005	1.69	0.293	6.94	Insignificant
Error	4	0.0013	0.0003				
Total	8	0.0012					

$S = 0.01795$ R-Sq = 88.93% R-Sq (Adj.) = 77.87%

Table 5 ANOVA table for surface roughness

Source	DF	SS	MS	*F* factor	*P*	*F* critical at α = 0.05%	Result
Cooling rate	2	0.2132	0.1066	0.16	0.853	6.94	Insignificant
Feed rate (mm/rev.)	2	0.3442	0.1721	0.27	0.779	6.94	Insignificant
Error	4	2.5864	0.6465				
Total	8	3.1438					

$S = 0.8041$ R-Sq = 17.73% R-Sq (Adj.) = 0.00%

3.3 Chip Studies

Chip studies were conducted to understand the chip thickness values in different cutting conditions under different feed rates with constant speed of 1000 RPM values and depth of cut of 0.5 mm, respectively.

Referring to Fig. 2 and Table 6, chip thickness is lesser for low feed rates as shown by the blue bars. Less chip thickness ensures less contact of tool with the

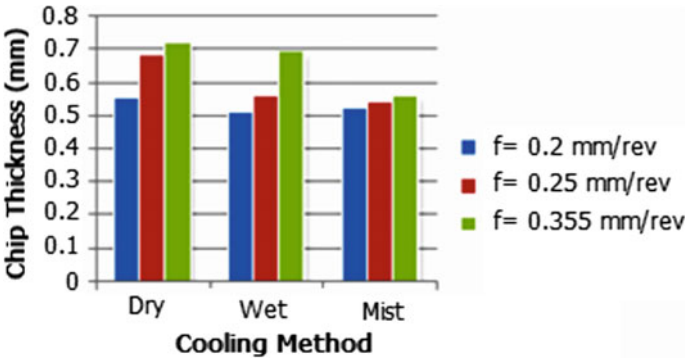

Fig. 2 Graph of chip thickness versus cooling method and feed rates

Table 6 Chip thickness and nature of chip for different feed rates and cutting conditions

Feed -> Cooling condition	Chip thickness (mm)			Nature of chip
	0.2 mm/rev	0.25 mm/rev	0.355 mm/rev	
Dry	0.55	0.68	0.72	Chip longer, BUE, **darker** chips, sharp
Wet cooling	0.51	0.56	0.69	**Medium**-sized chips, sharp, hard
Mist flow	0.52	0.54	0.56	**Longer** continuous chips, smooth flow, flexible

workpiece, hence low cutting action on the tool which will ensure longer tool life. It is recommended for less chip thickness in machining. For all conditions of feed rates, mist lubrication is found to be providing lesser chip thickness values which prove that it lowers the friction between tool and work. Higher values of chip thickness are seen in dry cutting, which means very lesser lubrication hence loss of tool material during cutting due to erosion. Cooling by fluid is essential, and proper application by use of mist under pressure ensures lower chip thickness values [11].

Referring to Table 6, under dry cutting, the chips formed are longer since the material used is ductile material, but the chips are very hot and burn out losing its metal shine and exhibit dark blue colors. It also shows signs of bad surface finish due to the fact that chips carry away tool material during cutting process which is built-up edge (BUE) formation which lessens the life of the tool and hence early tool failure. Chips are sharp and prove harmful to the workers. The underside of the chips is sharper. Under wet lubrication, chips are found to be hard due to sudden quenching effect of the chips due to water sprinkling over it. They break away easily, and hence, they are long at initial cuts, but break easily as they move along. The same hardness effect is possible over the work surface, and surface topology of work is affected due to the hardness. Chips are sharp.

Under mist flow (coconut oil) lubrication, chips are longer continuous and smooth flow is seen. They are not easy to break away into small pieces, showing high ductility even after machining. The surface quality of work material is found to be smooth and neat in operation.

3.4 Comparative Evaluations of Dry, Wet, and Mist Lubrication

Turning experiments were conducted at 1000 RPM constant cutting speed, 0.5 mm depth of cut, to evaluate the machining performances between dry, wet, and mist cooling for different feed rates of 0.2, 0.25, and 0.355 mm/rev, respectively, and based on the readings collected till machining time of 600 s, the graph is plotted as

shown in Fig. 3. ISO flank wear criteria VB of 0.4 mm max. are standard for tool life analysis; however for the sake of comparison, only up to 600 s, the graphs are plotted and compared to know the performances of machining. Also, Fig. 3 shows the image photograph taken from inverted microscope at 100X magnification.

It is evident that at higher feed rate of 0.355 mm/rev at dry cutting, tool failure was early as 100 s machining time was reached. Feeds of 0.25 mm/rev at dry condition lasted till 300 s. Lower feeds ensured longer working times more than 600 s. Lower flank wear is observed for mist cooling as compared to dry and wet lubrication at all feed rates; lowest wear noted was at feed rates of 0.2 mm/rev under mist lubrication. This shows that mist cooling has better lubricity and cooling between tool and chip interfaces due to which the wear is very less than others.

Along with flank wear measurements, surface roughness values in terms of Ra were measured from time to time. Three sets of readings were taken on the machined surface for every 200 mm length of cut, and average values are taken for plotting the graph as depicted in Fig. 4.

At initial conditions, wet lubrication gave good surface finish, later showed higher Ra values (bad surface finish) as it reached 600 s. At higher machining times, the water molecules during flooded lubrication fail to lubricate the surface, lose its contact, and evaporate due to higher heat generation. This can be overcome by mist cooling where

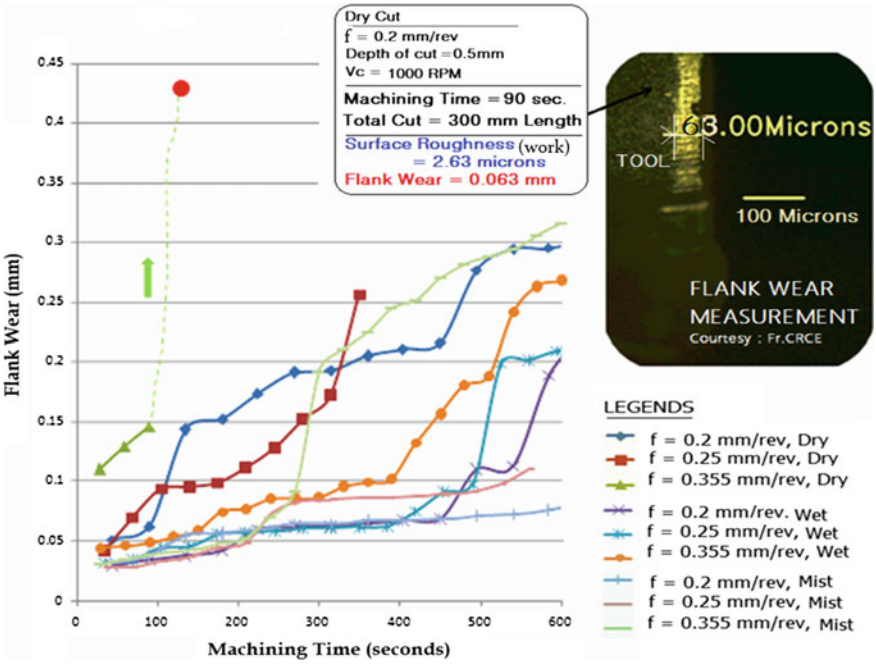

Fig. 3 Flank wear (mm) versus machining time (s) for different feed rates and cooling conditions, ISO flank wear criteria (VB = 0.4 mm max.)

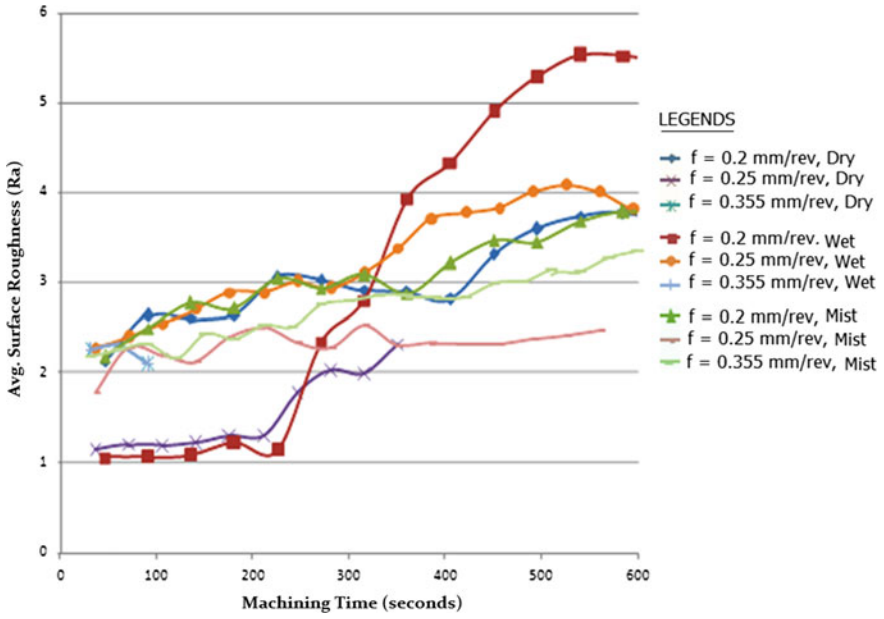

Fig. 4 Average surface roughness (Ra values) versus machining time (s) for different feed rates and cooling conditions

oil has constant contact for long-time machining; surface roughness values seen in mist lubrication are found to be stable and constant throughout the experimentation.

4 Conclusions

i. Lower flank wear at all feed ranges is found during mist machining as compared to dry and wet machining. In dry machining, early tool failures below 300 s are observed above feed rates of 0.25 mm/rev.
ii. Higher surface roughness values are observed in wet (flood) machining for all feed ranges due to more friction between tool and work, as a result of lower lubricating capabilities of water.
iii. Main effect plots indicate average values of levels of factors for flank wear are lowest for mist machining. However, surface roughness values are seen higher from dry to wet, followed by mist machining. As feed rates increase, surface roughness values are found to increase.
iv. ANOVA for flank wear shows cooling method as the significant factor since F calculated is much greater than F critical at 95% level of confidence.

v. Chip thickness is relatively lesser in mist machining at all feed rates. Chips are long and have smooth flow and bright color in mist machining due to its better lubrication. Edges of chips are blunt and are safe to handle.

References

1. Boubekri N, Shaikh V, Foster P (2012) A technology enabler for green machining: minimum quantity lubrication (MQL). J Manuf Technol Manag 21(5):556–566. https://doi.org/10.1108/17410381011046968
2. Boubekri N, Shaikh Vasim (2012) Machining using minimum quantity lubrication: a technology for sustainability. Int J Appl Sci Technol 2(1):111–115
3. Boubekri N, Shaikh V (2014) Minimum quantity lubrication (MQL) in machining: benefits and drawbacks. J Ind Intell Inf 3(3):205–209. https://doi.org/10.12720/jiii.3.3.205-209
4. Childs T, Katsuhiro Maekawa Toshiyuki O, Yasuo Y (1999) Metal machining—theory and applications, Arnold publications. Wiley
5. Chinchanikar Satish AV, Salve PN (2014) Comparative Evaluations of surface roughness during hard turning under dry and with water-based and vegetable oil-based cutting fluids. Procedia, Mater Sci 2(5):1966–1975. https://doi.org/10.1016/j.mspro.2014.07.529
6. Dhar NR, Islam MW, Islam S, Mithu MAH (2006) The influence of minimum quantity of lubrication (MQL) on cutting temperature, chip and dimensional accuracy in turning AISI-1040 steel, 171:93–99. https://doi.org/10.1016/j.jmatprotec.2005.06.047
7. Gunjal SU, Patil NG (2018) Experimental investigations into turning of hardened AISI 4340 steel using vegetable based cutting fluids under minimum quantity lubrication. Procedia Manuf 20:18–23. https://doi.org/10.1016/j.promfg.2018.02.003
8. Lohar DV (2013) Performance evaluation of minimum quantity lubrication (MQL) using CBN tool during hard turning of AISI 4340 and its comparison with dry and wet turning. Bonfring Int J Ind Eng Manag Sci 3(3):102–106. https://doi.org/10.9756/BIJIEMS.4392
9. Rahim EA, Ibrahim MR, Rahim AA, Aziz S, Mohid Z (2015) Experimental investigation of minimum quantity lubrication (MQL) as a sustainable cooling technique. Procedia CIRP 26:351–354. https://doi.org/10.1016/j.procir.2014.07.029
10. Shaikh Vasim A, Boubekri N (2010) Effects of minimum quantity lubrication in drilling 1018 steel. Int J Manuf Technol Res 2(2):1–14
11. Venkata Ramana M, Krishna Mohan Rao G, Hanumantha Rao D (2014) Chip morphology in turning of Ti-6Al-4 V alloy under different machining conditions. J Prod Eng 17(1):27–32
12. Walker Tim (2013) The MQL handbook—a guide to machining with minimum quantity lubrication, unist Inc.

Multi-response Optimization of Ni55.8Ti Shape Memory Alloy Using Taguchi–Grey Relational Analysis Approach

Piyush Rathi, Rutvik Ghiya, Hem Shah, Pratyush Srivastava, Shalin Patel, Rakesh Chaudhari and Jay Vora

Abstract Wire electrical discharge machining process is largely applicable to any conductive material regardless of its hardness. The present study aims to investigate the influence of input process parameters such as pulse on time, pulse off time and current on output responses of MRR and SR for $Ni_{55.8}Ti$ shape memory alloy. Taguchi's L_9 orthogonal array design has been utilized to conduct the experiments. ANOVA is used to study significance and non-significance of the response variables. All the process parameters are found to be significant for both the output responses. Grey relational analysis have been used to obtain an optimal combination of WEDM parameters to maximize the cutting rate while minimizing surface roughness for shape memory alloys, which is the most preferred material for aerospace and biomedical application because of its high resistance to corrosion and a non-toxic nature. Predicted values obtained at an optimal condition using GRA have been validated by experimental trail and show a very close relation.

Keywords WEDM · Anova · Shape memory alloys · Nitinol · Grey relational analysis

1 Introduction

A shape memory alloy (SMA) is new generation alloy that "remembers" its original shape after heating. It was first discovered by Ölander [1], and the term "shape memory" was discovered by Vernon [2]. These shape memory alloys were not used for any practical purpose till shape memory effect was observed in nickel-titanium alloy. Shape memory alloys exhibit in several compositions, out of which nickel-titanium (NiTi) alloys became relatively popular for its biomedical applications due to high corrosion and wear resistance, pseudo-elasticity and biocompatibility. Nitinol also found its applications in various fields like automotive, aerospace, actuators,

P. Rathi · R. Ghiya · H. Shah · P. Srivastava · S. Patel · R. Chaudhari (✉) · J. Vora
Department of Mechanical Engineering, Pandit Deendayal Petroleum University, Gandhinagar, India
e-mail: chaudharirakesh5@gmail.com

A. K. Parwani and PL. Ramkumar (eds.), *Recent Advances in Mechanical Infrastructure*, Lecture Notes in Intelligent Transportation and Infrastructure,
https://doi.org/10.1007/978-981-32-9971-9_2

sensors and, especially, biomedical. SMAs have been found to have super-elasticity, also known as pseudo-elasticity, which is the ability of material to return to their initial shape when the applied stress is removed. It is used in eyeglass frames, hip replacements, orthopaedic braces, etc [3]. Most of the applications of SMA require complex geometries, high accuracy and surface finish. However, these qualities are achieved at the cost of high machining cost, low material removal rate or less tool life. Weinert and Petzoldt [4] concluded that the machining of NiTi-based alloys is complex using conventional techniques like turning, drilling and deep hole drilling. Poor chip breaking, tool wear rate and formation burr have been observed while machining shape memory alloys using conventional machining techniques [4]. High viscosity, toughness, severe strain hardening, poor surface finish are some of the difficulties observed by the researchers for SMAs using conventional machining technique [4, 5]. Thus, machining of shape memory alloys is best suited for non-conventional machining techniques.

WEDM is a non-conventional machining technique which is widely used nowadays to manufacture products having very complicated geometric structure and possessing properties which makes it difficult to machine using conventional machining processes [6]. In WEDM process, a potential difference is created between the wire and the electrically conductive workpiece using electrical energy which gives rise to a high-temperature thermal spark and the removal of material takes place as the metal melts due to this high temperature. The process is carried out in the presence of appropriate dielectric fluid. The workpiece is mounted on an automatic guided $X-Y$ motor mechanism, and the wire is continuously fed through the workpiece using a spool along the fixed path so as to avoid the wear of the wire. Generally, deionized water is used as a dielectric fluid which is flushed at the point of machining continuously for creating a spark. WEDM process is widely used to produce complex-shaped geometries with close tolerances. However, WEDM process involves large number input parameters, and precise controlling of these parameters is required to obtain required geometry with subsequent mechanical properties. Thus, some of the past studies are pivoted to the optimization of WEDM parameters with the help of suitable technique. Sharma et al. [7] conducted an experiment on machining of NiTi material for WEDM process. Pulse on time (Ton), pulse off time (Toff), servo voltage (SV) and peak current (IP) are selected as input parameters to know the influence on output parameter such as material removal rate (MRR), surface roughness (SR) and dimensional shift. They have achieved the optimized result at parameter setting of Ton = 124 μs, Toff = 25 μs, SV = 30 V, IP = 110 μ by using desirability approach for multi-objective optimization. Manjaiah et al. [8] found that discharge energy and spark intensity are major reason behind higher MRR and also with increase in pulse on time, whereas SR decreases with pulse off time. Himadri Majumder et al. [9] have conducted an experiment on nitinol using WEDM for optimization of SR and microhardness. They concluded that the discharge current is the most important input factor to govern optimized results. They found noticeable debris, microcracks and recast layers. Thus, selection of levels of input process parameters plays an important role in the process.

Taguchi method has been used to quit successfully in several industrial applications by reducing the number of experiments. Sadeghi et al. [10] with the help of Taguchi's method found out effect of process parameters on MRR and SR during WEDM process. Gowd et al. [11] used taguchi orthogonal array for WEDM of SS304, the most influencing parameters of pulse off time and pulse on time were reported for the output responses of MRR and SR. Bharti et al. [12] reported that the process parameters like MRR, SR and tool wear rate (TWR) are mainly influenced by pulse on time and discharge current with the less influential parameters of duty cycle and tool lift time.

The Taguchi methods are generally used to find the optimal set of input process parameters required to enhance single quality characteristics. Taguchi's technique can optimize only one objective at a time with no consideration of its effect of on another output parameter which may result in either lower production or pitiable quality. To satisfy such conflicting objectives at the same time, an optimum parameters' setting is required. Such situations can be tackled conveniently by making use of optimization techniques for the parameters' optimization. The grey relational analysis (GRA) is an optimization technique which is used for solving the complex interrelationships between the multiple output responses [13]. Lin et al. [14] concluded that GRA is more simple and easy as compared to the fuzzy-based Taguchi technique for simultaneous optimization of EDM process. Rajyalakshmi et al. [6] applied the grey–Taguchi method, shows an increased value of the MRR and reduced value of SR. Tosun [15] applied GRA technique and minimized the SR and burr height by obtaining an optimal drilling parameter setting. Material removal rate (MRR) and surface roughness (SR) define the productivity and quality of the products. Thus, for the current study, MRR and SR are selected as output responses.

To obtain highly corrosion resistance and a biological surface, EDM process is used for machining of nitinol shape memory alloys [16]. MRR and SR define the productivity and quality of the product [17]. Thus, for the current study, MRR and SR are considered as output responses.

From the available literature, it has been observed that a little amount of work has been carried out to investigate the machining shape memory alloys using WEDM process. In present work, pulse on time, pulse off time and current are considered as three input variables and MRR and SR as two most output responses. Taguchi's L9 orthogonal array has been used for experimentation along with GRA technique for simultaneous optimization of output responses. ANOVA was used to investigate the effect and contribution of individual process parameter on the individual output response variable. Further, confirmation test was carried out to validate the result obtained from grey relational analysis.

2 Experimental Set-up and Experimentation

In the present study, a cylindrical bar of nitinol shape memory alloy (SMA) having a diameter of 6 mm with density equal to 6.5 g/cm3 was utilized to machine the

Table 1 Chemical composition (wt%) of nitinol

Element	Ti	Ni	Co	Cu	Cr	N
Wt (%)	Balance	55.78	0.005	0.005	0.005	0.001
	Fe	Nb	C	H	O	
	0.012	0.005	0.039	0.001	0.0344	

specimens of 1.5 mm thickness using A Concord wire-cut EDM machine DK7732 with EDM oil as the dielectric. A 0.18-mm-diameter molybdenum wire was used as the tool electrode (cathode). Three important machining parameters, pulse on time, pulse off time and discharge current, are selected on the machining responses such as material removal rate and surface roughness on nitinol shape memory alloy. Table 1 shows the chemical composition (wt%) of nitinol. The design of experiment was based on a Taguchi orthogonal design L9 with three control factors with three levels each which are listed in Table 2.

MRR was calculated by using difference in weight of the sample before and after machining divided by the time taken for the machining. MRR is calculated as shown in Eq. (1).

$$\text{MRR} = \frac{\Delta W * 1000}{\rho * t} \tag{1}$$

where

ΔW weight loss from the work piece,
t duration of the machining process,
ρ 6.5 g/cm^3 the density of the workpiece.

Mitutoyo makes Surftest SJ410 model was used to measure the SR of machined surface. For measuring SR, the cut-off length was kept as 2.5 mm and optional length was kept as 5 mm with a stylus speed of 0.2 mm/s. In this study, average surface roughness (Ra) value is considered which represents the average departure of the surface from perfection over a prescribed sampling length. This value is frequently used in industries and academics. Table 3 shows the experimentally measured values of MRR and SR for selected nine experimental trials.

Table 2 Control parameters and their levels

Factors	Process parameters	Level 1	Level 2	Level 3
A	Pulse on time (T_{on})	90	100	110
B	Pulse off time (T_{off})	20	25	30
C	Discharge current (*A*)	2	4	6

Table 3 Experimental values for MRR, SR and microhardness

Run	*A* (μs)	*B* (μs)	*C* (Ampere)	MRR (mm^3/sec)	SR (μm)
1	1	1	1	0.34533	7.189
2	1	2	2	0.48724	9.73
3	1	3	3	0.52307	11.021
4	2	1	2	0.61326	9.32
5	2	2	3	0.62402	11.26
6	2	3	1	0.24873	7.594
7	3	1	3	0.72590	11.86
8	3	2	1	0.32044	9.208
9	3	3	2	0.47425	10.936

3 Results and Discussion

3.1 Effect of Input Process Parameter on MRR

Experimentally measured values of MRR for selected nine experimental trials are shown in Table 3. For higher productivity, higher value of MRR is desirable outcome. Thus, MRR is in the category of higher-the-better performance characteristics. Statistical software Minitab 14 was used for the experimental data analysis. Analysis of variance (ANOVA) was performed at 95% confidence level to determine the effect of process parameters on each output response variable and is shown in Table 4 for MRR. As seen in Table 4, factor *C* found to be the most significant effect on MRR with 81.10% contribution followed by factor *B* and factor *A* with 16.32% contribution and 2.55%, respectively. The value of *P* must be lower than 0.05 to keep the particular input parameter significant for the 95% confidence level. All the selected input process parameters are found to be significant for MRR. An extreme close relation was observed between the *R*-squared values which mean that the model is best fit for selected responses. Figure 1 shows the main effect plot for MRR considering the variation of all input parameters. The main aspect for MRR is discharge energy and spark

Table 4 Analysis of variance for MRR

Source	DF	SS	MS	*F*	*P*	Contribution (%)
A	2	0.005044	0.002522	85.06	0.012	2.55
B	2	0.032287	0.016143	544.50	0.002	16.32
C	2	0.160398	0.080199	2705.03	0.000	81.10
Error	2	0.000059	0.000030			0.03
Total	8	0.197789				100

R-sq = 99.97%, *R*-sq (adj) = 99.88%, *R*-sq (pred) = 99.39%

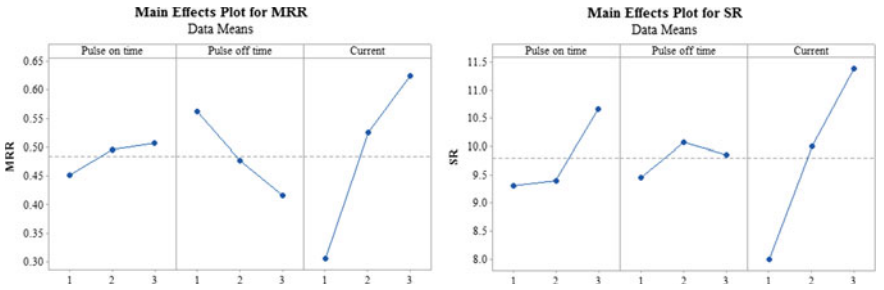

Fig. 1 Main effect plot for MRR and SR

intensity. With the increase in discharge energy, MRR also increases as discharge energy convert into thermal energy which in turn melt and vaporize the material [17]. From Fig. 1, with the increase in the value of pulse on time and current, value of MRR has found to be increased. The discharge energy and spark intensity increase with increase in pulse on time, which will remove more material and gives higher MRR. Whereas, for current, discharge energy is function of current and is directly proportional, so with increase in current, MRR also increases. Increase in pulse off time has negative effect on MRR. As spark intensity reduces with the increase in pulse off time, which decreases discharge energy and hence decreases MRR.

3.2 Effect of Input Process Parameter on SR

Table 3 shows experimentally measured values of the surface roughness of the machined workpiece. In the Taguchi method, the SR is in the category of lower-the-better performance characteristics. ANOVA for surface roughness is shown in Table 5. As seen in Table 5, factor *C* has a most significant effect on the SR with 81.02% contribution followed by factors *A* and *B* with 16.20 and 2.68% contribution, respectively. All the factors are found to be significant for SR. Further, *R*-squared values for SR model were observed with an extreme close relation means that the model is well suited for SR prediction within the range. Main effect plot for SR

Table 5 Analysis of variance for SR

Source	DF	SS	MS	*F*	*P*	Contribution (%)
A	2	3.47110	1.735540	155.79	0.006	16.20
B	2	0.57340	0.286720	25.74	0.037	2.68
C	2	17.3585	8.679250	779.10	0.001	81.02
Error	2	0.02230	0.000030			0.1
Total	8	21.4253				100

R-sq = 99.90%, *R*-sq (adj) = 99.58%, *R*-sq (pred) = 97.89%

considering the variation of all input parameters is shown in Fig. 1. With changes in pulse on time, current and pulse off time values, the thermal energy in the circuit changes, and this majorly contributes to crater size and thereby SR values. Figure 1 shows that the increase in SR is observed with an increase in pulse on time. As the pulse on time increases, the discharge energy increases, and this in turn increases the melting of material [16]. This leads to increased crater size and gives higher SR. Increase in the SR has been observed with an increase in pulse off time (in the range 20–25 μs), and beyond 25 μs value of pulse off time, SR was found be decreased. The SR seems to increase with increase in current. At higher currents, the ionization of deionized water takes place, which leads to high discharge and thermal energy, creating larger and deeper craters, and increasing SR.

The optimal combination of input parameters for MRR is obtained as $A_3B_1C_3$. From the experiments in L9 orthogonal array, run 7 with the same combination $A_3B_1C_3$ produced the best MRR of 0.7259 mm^3/s. Further, the optimal combination of input parameters for SR is obtained as $A_1B_1C_1$. Run 1 with the same combination $A_1B_1C_1$ produced the best SR of 7.189 μm. A conflict has been observed for the two quality characteristics for optimal factor levels. This arises a need for optimization of two quality objectives for optimal solution.

3.3 Multi-objective Optimization Using Taguchi Grey Method

In the present study, MRR and SR are the two performance measure. In such situation, the objective function is transformed to single-objective function problem using GRA technique. Smaller-the-better type, nominal-the-best type, and larger-the-better type are three types of single quality characteristic (QCH). In the current study, MRR belonged to larger-the-better type and SR belonged to smaller-the-better type QCH. For the optimization of two QCHs for nitinol WEDM process, the following steps are outlined:

Step 1 S/N ratio

For each performance measure, firstly calculation signal-to-noise ratio is first step in GRA. MRR is a higher-the-better QCH and can be expressed as:

$$\frac{S}{N}\text{ratio} = -10\lg(1/\text{n})\sum_{n=1}^{n}\left(\frac{1}{y_{ij}^2}\right) \tag{2}$$

where

$i = 1, 2,\ldots, n$; j=1, 2,…, k; n = number of replications; and
ij = output value of response.

The function for SR can be expressed as:

$$\frac{S}{N}\text{ratio} = -10\lg(1/\text{n})\sum_{n=1}^{n}\left(\text{y}_{ij}^{2}\right) \tag{3}$$

Step 2 Normalization of S/N ratio
Before using grey relational analysis, the *S/N* ratios need to be normalized. Values of η_{1i} and η_{2i} represent *S/N* ratios for MRR and SR, respectively. Higher the value of *S/N* ratio, better will be the grey relational coefficient (GRC). Thus, higher-is-better characteristics are considered for GRC. The normalized *S/N* ratios for MRR and SR are denoted by η_{1i}^{*} and η_{2i}^{*}, respectively, and obtained by Eqs. (4) and (5), respectively, as follows:

$$\eta_{1i}^{*} = \frac{\eta_{1i}^{*} - \min\eta_{1i}}{\max\eta_{1i} - \min\eta_{1i}}, i = 1, 2, \ldots, 9 \tag{4}$$

$$\eta_{2i}^{*} = \frac{\max\eta_{2i} - \eta_{2i}}{\max\eta_{2i} - \min\eta_{2i}}, i = 1, 2, \ldots, 9 \tag{5}$$

Smallest and the largest values of η_{1i} are represented by min η_{1i} and max η_{1i}, respectively, for MRR. Similarly, min η_{2i} and max η_{2i} are the smallest and the largest value of η_{2i} for the surface roughness.
Step 3. Calculation of Grey Relational Coefficient (GRC)
The grey relational coefficient (GRC) of a sequence $\gamma_{1i}\left(\eta_{1i}, \eta_{1i}^{*}\right)$ $(i = 1, 2, \ldots, 9)$ can be obtained by using Eq. (6) as follows [18]:

$$\gamma_{1i}\left(\eta_{1i}, \eta_{1i}^{*}\right) = \frac{\Delta\min + \xi\,\Delta\max}{\Delta_{01}i + \xi\,\Delta\max} \tag{6}$$

Similarly, the grey relational coefficient of a sequence $\gamma_{2i}\left(\eta_{2i}, \eta_{2i}^{*}\right)$ $(i = 1, 2, \ldots, 9)$ obtained by using Eq. (7) is as follows:

$$\gamma_{1i}\left(\eta_{2i}, \eta_{2i}^{*}\right) = \frac{\Delta\min + \xi\,\Delta\,\max}{\Delta_{02}i + \xi\,\Delta\,\max} \tag{7}$$

where ξ is the distinguishing coefficient and range between 0 and 1 can be defined for the value of ξ; commonly, it is set as 0.5 [19]. The $\Delta_{01}i$ and $\Delta_{02}i$ are the absolute deviations of η_{1i}^{*} and η_{2i}^{*} from the reference sequences, η_{01} and η_{02}, of the MRR and SR, respectively, are as shown in Eqs. (8) and (9):

$$\Delta_{01}(i) = \left|\eta_{01} - \eta_{1i}^{*}\right|, i = 1, 2, \ldots., 9 \tag{8}$$

$$\Delta_{02}(i) = \left|\eta_{02} - \eta_{2i}^{*}\right|, \text{i} = 1, 2, \ldots., 9 \tag{9}$$

where Δ_{min} and Δ_{max} represent smallest and largest value in the overall sequence for all the experiments from both MRR and SR.

Step 4 Calculation of Grey relational grades (GRG)

Average of GRC represents the grey relational grade which is calculated as below:

$$\bar{\gamma}_i = \frac{1}{2}\sum_{j=1}^{2}\gamma_{ji} \tag{10}$$

Step 5 Obtain the ordinal value of $\bar{\gamma}_i$. Lowest $\bar{\gamma}_i$ receives a higher rank, and highest γ_i receives rank 1 as the ordinal value is to rank the $\bar{\gamma}_i$ values in a descending order. For GRG, larger-the-better characteristic was used, since a larger value gives the better performance of the method.

By using the above grey relational method, GRC for MRR and SR is obtained along with GRG as shown in Table 6.

By using GRG values, factor response tables have been constructed as shown in Table 7. Greater level value means more significance and presents the optimal parameter setting to achieve multiple objectives. Higher value of individual input parameters for GRG has been indicated by bold in Table 7. Thus, GRA technique shows that for the dual objectives of material removal rate and surface roughness, the optimal parameter setting of WEDM process is $A_2B_1C_3$.

Table 6 Grey relational coefficients for MRR, SR and GRG

Run	MRR grey relational coefficients	SR grey relational coefficients	Grey relational grade	Rank
1	0.355	1.000	0.677	1
2	0.506	0.453	0.479	6
3	0.555	0.369	0.462	7
4	0.708	0.491	0.599	3
5	0.730	0.358	0.544	5
6	0.276	0.820	0.548	4
7	1.000	0.333	0.667	2
8	0.333	0.503	0.418	9
9	0.490	0.374	0.432	8

Table 7 Factor response table from grey relational analysis

Process parameter	Level 1	Level 2	Level 3
Pulse on time	0.53975	**0.563935**	0.505515
Pulse off time	**0.647866**	0.480533	0.480801
Discharge current	0.547961	0.503582	**0.557656**

Table 8 Comparison between experimental and predicted values for MRR and SR

	Optimal machining parameters	
	Predicted	Experimental
Levels	$A_2B_1C_3$	$A_2B_1C_3$
MRR (mm^3/sec)	0.7117	0.7193
SR (μm)	10.645	10.553

4 Confirmation Test

Conformation test has been conducted to validate the predicted results obtained from the GRA. The predicted MRR ($\bar{y}_{\text{predict}}$), at the optimal parameters, is calculated by following equation:

$$\bar{y}_{1(\text{predict})} = \bar{y}_{1(A_2)} + \bar{y}_{1(B_1)} + \bar{y}_{1(C_3)} - 2\bar{y}_{1(\text{avg})} \tag{10}$$

where $\bar{y}_{1(A_2)}$, $\bar{y}_{1(B_1)}$, $\bar{y}_{1(C_3)}$ are the MRR averages obtained for the factor levels A_2, B_1, C_3, respectively. $\bar{y}_{1(\text{avg})}$ is the average value of MRR. Equation 10 gives the value of $\bar{y}_{1(predict)}$ for MRR as 0.7117 mm^3/sec. Similarly, predicted value of SR was calculated and found to be 10.645 μm.

Confirmation experiment was conducted at optimal combination of A_2, B_1, C_3, and values of MRR and SR are determined. Predicted and experimental values are shown in Table 8, and good agreement can be observed between these values which show the suitability of experimental investigation.

5 Conclusions

Ni55.8Ti shape memory alloy is used for WEDM process to investigate the effect of pulse on time, pulse off time and current on output responses of MRR and SR. Following conclusions are drawn based on the results of the present study:

(a) All the input variables such as pulse on time, pulse off time and current are found to be significant for both the output responses.
(b) Through ANOVA, current was found to be the most significant factor for MRR with 81.10% contribution followed by pulse off time with 16.32% contribution and pulse on time with 2.55% contribution. Further, for SR, current was most significant factor with 81.02% contribution followed by pulse on time with 16.20% contribution and pulse on time with 2.68% contribution.
(c) An extreme close relation was observed between the *R*-squared values for both the output responses which show that the model is best fit for selected responses.
(d) The optimized process parameter settings using GRA to maximize MRR and to minimize SR were found to be pulse on time 100 μs, pulse off time at 20 μs and discharge current at 6A (A_2, B_1, C_3).

(e) Validation experiment has been conducted at final optimal parameter setting. Good agreement between predicted and experimental values is observed which show the suitability of experimental investigation. Output responses of MRR as 0.7193 mm^3/sec and SR as 10.553 are obtained at optimal parameter setting of $(A_2B_1C_3)$.

References

1. Ölander A (1932) An electrochemical investigation of solid cadmium-gold alloys. J Am Chem Soc 54(10):3819–3833
2. Vernon LB, Vernon HM (1941) Process of manufacturing articles of thermoplastic synthetic resins. Google Patents
3. Jani JM et al (2014) A review of shape memory alloy research, applications and opportunities. Materials & Design (1980–2015) 56:1078–1113
4. Weinert K, Petzoldt V (2004) Machining of NiTi based shape memory alloys. Mater Sci Eng, A 378(1–2):180–184
5. Lin H, Lin K, Chen Y (2000) A study on the machining characteristics of TiNi shape memory alloys. J Mater Process Technol 105(3):327–332
6. Rajyalakshmi G, Ramaiah PV (2013) Multiple process parameter optimization of wire electrical discharge machining on Inconel 825 using Taguchi grey relational analysis. Int J Adv Manuf Technol 69(5–8):1249–1262
7. Sharma N, Raj T, Jangra KK (2017) Parameter optimization and experimental study on wire electrical discharge machining of porous Ni40Ti60 alloy. Proc Inst Mech Eng, Part B: J Eng Manuf 231(6):956–970
8. Manjaiah M et al (2015) Effect of electrode material in wire electro discharge machining characteristics of Ti50Ni50—xCux shape memory alloy. Precis Eng 41:68–77
9. Majumder H, Maity K (2018) Application of GRNN and multivariate hybrid approach to predict and optimize WEDM responses for Ni-Ti shape memory alloy. Appl Soft Comput 70:665–679
10. Sadeghi M et al (2011) Optimization of cutting conditions in WEDM process using regression modelling and Tabu-search algorithm. Proc Inst Mech Eng, Part B: J Eng Manuf 225(10):1825–1834
11. Gowd GH et al (2014) Multi objective optimization of process parameters in WEDM during machining of SS304. Procedia Mater Sci 5:1408–1416
12. Bharti PS, Maheshwari S, Sharma C (2010) Experimental investigation of Inconel 718 during die-sinking electric discharge machining. Int J Eng Sci Technol 2(11):6464–6473
13. Julong D (1989) Introduction to grey system theory. J Grey Syst 1(1):1–24
14. Lin C, Lin J, Ko T (2002) Optimisation of the EDM process based on the orthogonal array with fuzzy logic and grey relational analysis method. Int J Adv Manuf Technol 19(4):271–277
15. Tosun N (2006) Determination of optimum parameters for multi-performance characteristics in drilling by using grey relational analysis. Int J Adv Manuf Technol 28(5–6):450–455
16. Magabe R, et al (2019) Modeling and optimization of Wire-EDM parameters for machining of Ni 55.8 Ti shape memory alloy using hybrid approach of Taguchi and NSGA-II. Int J Adv Manuf Technol 1–15
17. Tonday H, Tigga A (2016) Analysis of effects of cutting parameters of wire electrical discharge machining on material removal rate and surface integrity. In: IOP conference series: materials science and engineering. IOP Publishing
18. Wen K et al (2003) Grey relational model method and application. Gau-Lih Book Co., Taipei
19. Ng DK (1994) Grey system and grey relational model. ACM SIGICE Bulletin 20(2):2–9

Evaluation of Surface Roughness by Machine Vision Using Neural Networks Approach

Ketaki Joshi and Bhushan Patil

Abstract Surface quality of industrial components is critical from operational, ergonomics and esthetics point-of-view. Surface roughness measurement using traditional contact-type instruments may not be feasible in the industries insisting on 100% inspection and monitoring. Machine vision-based machine learning has a potential of facilitating automated inspection of manufactured components for their surface quality. The paper presents a machine vision-based machine learning approach that works on the principle of surface texture characterization by vision-based texture analysis techniques followed by supervised machine learning using multilayer feed-forward artificial neural network with backpropagation for fitting the response (surface roughness) with the inputs (vision-based texture parameters). Performance of various texture analysis techniques based on the histogram, gray level co-occurrence matrix, Fourier and wavelet transform used for generating the training data and training algorithms used for training the networks are compared. The approach can be potentially used to estimate surface roughness of industrial components.

Keywords Surface roughness · Machine vision · Texture analysis · Artificial neural networks

1 Introduction

Evaluation of surface roughness (Ra) using machine vision-based machine learning approach is based on the principle of surface texture characterization of machined surface images using texture analysis techniques and machine learning to establish

K. Joshi (✉) · B. Patil
Fr. Conceicao Rodrigues College of Engineering, Affiliated to University of Mumbai, Bandra, India
e-mail: ketaki.joshi@fragnel.edu.in

B. Patil
e-mail: bhushan.patil@fragnel.edu.in

A. K. Parwani and PL. Ramkumar (eds.), *Recent Advances in Mechanical Infrastructure*, Lecture Notes in Intelligent Transportation and Infrastructure,
https://doi.org/10.1007/978-981-32-9971-9_3

the relationship of these parameters with Ra value. Vision-based surface texture characterization is based on the concept that an image is represented as a two-dimensional image intensity function characterized by the illumination and the reflectance [1]. Machine learning then models the relationship between vision-based texture parameters and surface roughness and develops the mechanism of surface roughness evaluation for components with unknown roughness values.

Surface textures from images are commonly characterized using statistical or filter-based texture analysis techniques [2]. Various researchers have used statistical methods such as histogram properties, gray level characteristics, gray level co-occurrence and co-occurrence matrices. Histogram-based features such as mean, variance, skewness, range, median, kurtosis, energy and entropy are used for surface texture characterization by various researchers [3–7]. Various researchers have used gray level co-occurrence matrix (GLCM) [8, 9] and features such as energy (angular second moment), entropy, correlation, contrast, inverse difference, absolute value, maximum probability based on GLCM for surface texture characterization [10–13]. Discrete Fourier transform (DFT) and various features based on DFT such as major peak frequency, average power spectrum, principal component magnitude squared, ratio of major to minor axis, central power spectrum percentage based on DFT are also used by researchers for surface texture characterization or roughness estimation [14–18]. Wavelet transforms can be applied on signals [19–23] as well as images. Many researchers have used energy features extracted from discrete wavelet transform (DWT) applied on the images for surface texture characterization [24–27].

For evaluation of surface roughness, the neural network needs to be trained using vision-based texture parameters as the set of inputs and roughness values obtained using a stylus-based instrument as the desired output. Multilayer feedforward networks with backpropagation can be effectively used to model the relationship and their performance can be further improved with various measures such as momentum, variable learning rate and conjugate gradient [28]. Researchers have used image-based texture parameters values to classify surface textures or evaluate surface roughness using artificial neural networks (ANN) trained with image-based texture data.

2 Problem Definition

The objective of this paper is to demonstrate the approach of evaluation of surface roughness using an artificial neural network trained with various vision-based texture parameters. In order to enhance the performance of the machine vision-based machine learning tool, performance of various texture analysis techniques for surface characterization and training algorithms for multilayer feedforward network with backpropagation is evaluated and compared.

3 Methodology

Initially, images of 120 specimens machined using different machining processes such as honing, surface grinding and lapping resulting in different surface textures were captured using image acquisition device (camera). The surface roughness values of the 120 specimens under study were measured using traditional stylus-based surface roughness tester. The surface textures with the ranges of surface roughness (R_a) values obtained for three types of surfaces under study are given in Fig. 1.

The images were then acquired in MATLAB, preprocessed for enhancing the features and processed to extract texture parameters as mentioned in Table 1.

The vision-based texture parameter values were used as the input data, and surface roughness (R_a) values were used as the target data for training a two-layer feedforward artificial neural network with backpropagation using 'trainlm' training algorithm as shown in Fig. 2. 70% of the input data samples were used for training, 15% for validating and 15% for testing the network. Performance of various texture analysis techniques was evaluated by using different texture parameter sets based on the histogram, GLCM, DFT and DWT to trains ANNs and compared in terms of correlation coefficient of the linear regression between network inputs and targets.

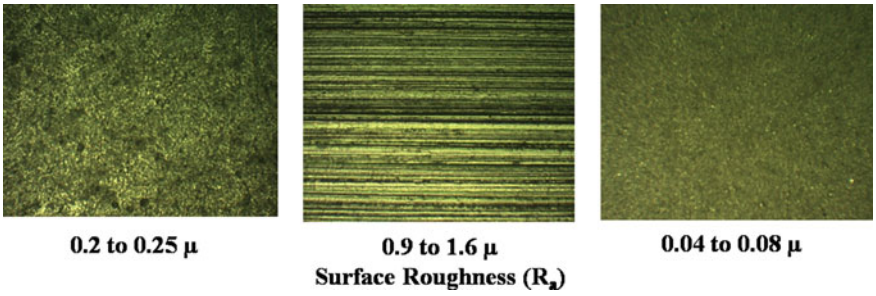

Fig. 1 Sample images of machined surfaces belonging to different surface texture classes

Table 1 Texture parameters used for surface roughness estimation

Texture analysis approach	Texture parameters
Histogram	Average height departure, root mean square, max peak to valley, skewness, kurtosis evaluated over surface and sampling lengths
GLCM	Contrast, correlation, energy and homogeneity extracted by considering correlation along different directions along 0°, 45°, 90° and 135° using offset [0, 1], [−1, 1], [−1, 0] and [−1, −1]
DFT	Major peak frequency, average power spectrum, principal component magnitude squared, ratio of major to minor axis, central power spectrum percentage
DWT	Max, min, average, standard deviation of approximation coefficient at level-1 and level-2 in horizontal, vertical and diagonal directions

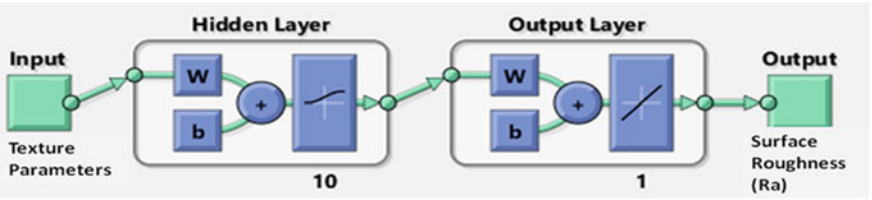

Fig. 2 Two-layer feedforward artificial neural network with backpropagation used for evaluation of surface roughness based on machine vision-based texture parameters

Furthermore, the performance of different training algorithms was also evaluated by training the networks with different algorithms and compared based on correlation coefficient and mean squared error.

4 Results and Discussion

The results of training of ANNs with different texture parameters are in Table 2.

It can be observed that HST parameters and DFT parameters are having low R values for training neural networks in the current case. GLCM and DWT are showing better results in training neural networks for evaluation of surface roughness of components used in the current study.

The results of the comparison of different training algorithms are as shown in Table 3.

Among gradient descent algorithms, traingd and traingdm were unable to converge with descent performance even in 1000 epoch showing their limitations toward function approximation in the current case. Among traingda, traingdx and trainrp, the function trainrp showed faster convergence with better performance.

Among conjugate gradient algorithms, traincgf and trainscg were performing better than other functions, however, trainscg converged in less iteration than others.

Among quasi-Newton algorithms, trainlm and trainbfg showed better performance over others in terms of efficiency as well as convergence. The network being small, trainbfg also proved to be effective in the current case.

Table 2 Performance of ANNs with texture parameter sets for estimation of R_a

Neural network input	R (Training)	R (Validation)	R (Testing)	R (All)
Histogram parameters	0.86662	0.85993	0.88595	0.84543
GLCM parameters	0.90388	0.83729	0.76294	0.87052
DFT parameters	0.81586	0.88511	0.64181	0.77674
DWT parameters	0.90463	0.84487	0.71209	0.88945

Table 3 Performance of various learning rules in ANNs for estimation of R_a

Feedforward backpropagation training algorithms	Training function	R (Training)	R (Validation)	R (All)	Best validation MSE	Epoch
Gradient descent	Traingd	−0.40629	−0.56229	−0.42245	0.005057	1000
	Traingdm	−0.34194	−0.70242	−0.4238	0.007393	1000
	Traingda	0.56521	0.65669	0.52286	0.001854	92
	Traingdx	0.69961	0.54436	0.66037	0.001909	245
	Trainrp	0.73615	0.7875	0.71598	0.001178	37
Conjugate gradient	Traincgb	0.6905	0.54383	0.64508	0.0012107	16
	Traincgf	0.73073	0.83412	0.70771	0.0012019	29
	Traincgp	0.47585	0.7076	0.49242	0.0012276	11
	Trainscg	0.71837	0.7866	0.70634	0.001199	17
Quasi-Newton	Trainlm	0.90388	0.79315	0.77601	0.001161	10
	Trainbfg	0.67345	0.82171	0.69355	0.001727	27
	Trainbr	0.65612	–	0.64024	0.00129	162
	Trainoss	0.6046	0.60369	0.58836	0.001656	20
Random order	Trainr	0.51669	0.46707	0.51014	0.001674	1000

The results support theory and previous research findings by researchers for various problems including classification, forecasting, detection [27, 29–32].

To conclude, training functions, trainlm, trainrp, trainscg and traincgf showed better performance than other training functions in terms of convergence speed, correlation coefficient as well as MSE. 'Trainlm' needed least number of epochs to converge and provided the highest performance in terms of correlation coefficient and MSE.

5 Conclusion

Multilayer feedforward networks with backpropagation trained using machine vision-based surface texture characteristics can be effectively used to evaluate surface roughness of machined components. Statistical texture analysis techniques and filter-based texture analysis techniques effectively characterize machined surfaces and facilitate prediction of surface roughness using a machine learning approach. Various techniques based on histogram, GLCM, DFT and DWT when tested, it was found that GLCM and DWT-based two-layer feedforward network with backpropagation showed better performance in terms of correlation coefficient for the components in the current study. Various training functions when compared, it was found

that quasi-Newton and conjugate gradient algorithms performed better than gradient descent. Among all different algorithms, trainlm, trainrp, trainscg and traincgf showed much better performance over others in the current scenario. Trainlm training function outperformed in terms of correlation coefficient, mean squared error and convergence speed.

References

1. Palani S, Natarajan U (2011) Prediction of surface roughness in CNC end milling by machine vision system using artificial neural network based on 2D Fourier transform. Int J Adv Manuf Technol 54(9–12):1033–1042
2. Materka A, Strzelecki M (1998) Texture analysis methods–a review. Technical university of lodz, institute of electronics, COST B11 report, Brussels, pp 9–11
3. Xie X (2008) A review of recent advances in surface defect detection using texture analysis techniques. ELCVIA Electron Lett Comput Vis Image Anal 7(3)
4. Kumar R, Kulashekar P, Dhanasekar B, Ramamoorthy B (2005) Application of digital image magnification for surface roughness evaluation using machine vision. Int J Mach Tools Manuf 45(2):228–234
5. Al-Kindi GA, Shirinzadeh B (2007) An evaluation of surface roughness parameters measurement using vision-based data. Int J Mach Tools Manuf 47(3):697–708
6. Natarajan U, Palani S, Anandampillai B, Chellamalai M (2012) Prediction and comparison of surface roughness in CNC-turning process by machine vision system using ANN-BP and ANFIS and ANN-DEA models. Int J Mach Mach Mater 12(1–2):154–177
7. Dhanapalan N, Thanigaiyarasu G, Vani K (2014) Prediction of surface roughness of 6061 aluminium alloy end milling: a machine vision approach. Int J Mach Mach Mater 16(3–4):285–302
8. Haralick R (1979) Statistical and structural approaches to texture. In: Proceedings of the IEEE 67(5):786–804
9. Tuceryan M, Jain AK (1993) Texture analysis. Handbook of pattern recognition and computer vision 2:235–276
10. Tian GY, Lu RS (2006) Hybrid vision system for online measurement of surface roughness. JOSA A 23(12):3072–3079
11. Wang X, Georganas ND (2009) GLCM texture based fractal method for evaluating fabric surface roughness. In: Electrical and computer engineering, 2009. CCECE'09. Canadian conference, IEEE, pp 104–107
12. Gadelmawla ES (2011) Estimation of surface roughness for turning operations using image texture features. Proc Inst Mech Eng, Part B: J Eng Manuf 225(8):1281–1292
13. Nathan D, Thanigaiyarasu G, Vani K (2014) Study on the relationship between surface roughness of AA6061 alloy end milling and image texture features of milled surface. Procedia Eng 97:150–157
14. Kumanan S, Jesuthanam CP, Ashok Kumar R (2008) Application of multiple regression and adaptive neuro fuzzy inference system for the prediction of surface roughness. Int J Adv Manuf Technol 35(7):778–788
15. Fadare DA, Oni AO (2009) Development and application of a machine vision system for measurement of tool wear. ARPN J Eng Appl Sci 4(4):42–49
16. Natarajan U, Palani S, Anandampilai B (2012) Prediction of surface roughness in milling by machine vision using ANFIS. Comput-Aided Des Appl 9(3):269–288
17. Saric T, Simunovic G, Simunovic K (2013) Use of neural networks in prediction and simulation of steel surface roughness. Int J Simul Model 12(4):225–236
18. Palani S, Kesavanarayana Y (2014) Prediction of surface roughness in end milling process by machine vision using neuro fuzzy network. In: 2014 International conference IEEE science engineering and management research (ICSEMR), pp 1–5

19. Sharma M, Acharya UR (2018) Analysis of knee-joint vibroarthographic signals using bandwidth-duration localized three-channel filter bank. Comput Electr Eng 72:191–202
20. Sharma M, San Tan R, Acharya UR (2018) A novel automated diagnostic system for classification of myocardial infarction ECG signals using an optimal biorthogonal filter bank. Comput Biol Med 102:341–356
21. Sharma M, Bhurane AA, Acharya UR (2018) MMSFL-OWFB: a novel class of orthogonal wavelet filters for epileptic seizure detection. Knowl-Based Syst 160:265–277
22. Sharma M, Agarwal S, Acharya UR (2018) Application of an optimal class of antisymmetric wavelet filter banks for obstructive sleep apnea diagnosis using ECG signals. Comput Biol Med
23. Sharma M, Achuth PV, Deb D, Puthankattil SD, Acharya UR (2018) An automated diagnosis of depression using three-channel bandwidth-duration localized wavelet filter bank with EEG signals. Cogn Syst Res 52:508–520
24. Chang SI, Ravathur JS (2005) Computer vision based non-contact surface roughness assessment using wavelet transform and response surface methodology. Qual Eng 17(3):435–451
25. Morala-Argüello P, Barreiro J, Alegre E (2012) A evaluation of surface roughness classes by computer vision using wavelet transform in the frequency domain. Int J Adv Manuf Technol 59(1–4):213–220
26. Srivatsa T, Srinivas H. K, Kumbar R, Madhusudhan T (2016) Surface roughness evaluation of turned surfaces using wavelet packet transform. ImpAl J Interdiscip Res 2(6)
27. Nathan D, Thanigaiyarasu G, Vani K (2016) Comparison of artificial neural network approach and data mining technique for the prediction of surface roughness in end milled components with texture images. Int J Adv Engg Tech/Vol. Vii/Issue I/Jan.-March, 587, 592
28. Demuth H, Beale M (2009) Matlab neural network toolbox user's guide version 6. The MathWorks Inc.
29. Baptista FD, Rodrigues S, Morgado-Dias F (2013) Performance comparison of ANN training algorithms for classification. In: 2013 IEEE 8th International symposium IEEE intelligent signal processing (WISP), pp 115–120
30. Dao VN, Vemuri VR (2002) A performance comparison of different back propagation neural networks methods in computer network intrusion detection. Differ EquS Dyn Syst 10(1&2):201–214
31. Aggarwal R, Kumar R (2015) Effect of training functions of artificial neural networks (ANN) on time series forecasting. Int J Comput Appl 109(3)
32. Sharma B, Venugopalan K (2014) Comparison of neural network training functions for hematoma classification in brain CT images. IOSR J Comput Eng 16(1):35

Challenges of Sustainable Manufacturing for Indian Organization: A Study

Lakhan, Ravinder Kumar, Pratyaksh Tyagi, Lincon Nagar and Devdutt Gaur

Abstract Sustainable manufacturing had gained prominent importance in modern time all over the globe. Modern manufacturing is shifting from use of tradition practices and natural resources to sustainable practices and alternate green energy sources. Use of traditional practices and natural resources generate lot of wastes and pollution in environment. However, the implementation and adaption of sustainable manufacturing practices is a challenging task for Indian organizations. Most of Indian manufacturing organizations are not able to overcome challenges of sustainable manufacturing and adopt its practices. In this paper, authors have reviewed different research papers and identified challenges of sustainable manufacturing. By strategic planning, challenges can be overcome and implementation of sustainable manufacturing in Indian manufacturing organizations can be feasible. To analyses the practical challenges and feasibility of sustainable manufacturing adoption at ground level authors have done a case study in Indian organization manufacturing electric goods.

Keywords Sustainable manufacturing · Challenges · Practices · Manufacturing · Indian

1 Introduction

Due to unsuitable practices, Indian manufacturing industries since long has been one of the main contributors to waste and pollution. In this paper, authors have identified the challenges in the path of sustainable manufacturing. Green manufacturing means ability to sustain, less wastage or carbon-less manufacturing. Production processes and products need to be green and sustainable so that they can be recycled, remanufactured and reused when it reaches the end of their lifespan. Closed-loop

Lakhan (✉) · R. Kumar · P. Tyagi · L. Nagar · D. Gaur
Department of Mechanical Engineering, Amity University, Noida, UP 201303, India
e-mail: Lsharma.edu@gmail.com

R. Kumar
e-mail: Rkumar19@amity.edu

A. K. Parwani and PL. Ramkumar (eds.), *Recent Advances in Mechanical Infrastructure*, Lecture Notes in Intelligent Transportation and Infrastructure,
https://doi.org/10.1007/978-981-32-9971-9_4

production model and manufacturing technologies are also used for eliminating the use of energy and wastewater and recycling physical waste.

In current globalized trend, the association between academic and industry professionals will be very important when it comes to identifying the solutions to green issues. In this paper, the challenges of sustainable manufacturing are identified by intense review of different research papers.

2 Literature Review

The most fundamental type of collaboration in a sustainable way for the industry to enhance product life cycle and improve manufacturing uses the cyber-physical system which is associated with Industry 4.0 [1]. [2] described and investigated the challenges faced in the adaptation of flexible and green concept so as to solve the current issues faced by industries in manufacturing sector. [3] discussed statistical technique for featuring the differences of the most essential enablers and challenges so as to strategically implement green manufacturing. [4] discussed the social, economic and environmental performance to describe green issues and sustainability in manufacturing. [5] investigated and analysed the challenges in the implementation of green manufacturing in order to assist the organizations in achieving highly competitive levels. [6] proposed a hierarchical framework for implementation of sustainable manufacturing which includes measures of performance improvement. [7] investigated the meaning of green manufacturing as stated by various researchers by carefully studying various definitions and identifying current trend in green manufacturing. [9] studied and investigated existing challenges faced in implementation of different sorts of sustainability and green approaches. [10] studied from economic, social and environmental perspectives, and the challenges towards implementation of green manufacturing (Tables 1, 2 and 3).

[16] described various business goals and strategic capabilities to enable the creation of values using sustainable manufacturing and also present a future vision towards green processes and systems. The main factors which drive the process of globalization are economy, innovation, social, environment and legislation. The authors emphasized on the fact that the fundamental enablers of globalization are competitive green manufacturing [17]. [18] studied the excessive consumption of natural resources by emerging industries, emission of greenhouse gases and other factors related to environmental, social and economic perspectives. [19] studied about the relationship between financial development of a company and corporate social sustainably cultural.

Table 1 Environmental challenges

S. No.	Challenges	Description	References
1	Less sustainable awareness	There is limited access to sustainability concept and literature	[1–4, 7–9]
2	End-to-end engineering	Less framework in organization	[1, 6]
3	Less service orientation manufacturing	Less organization support	[1, 8]
4	Lack of standards value or benchmarks	Shortage of practicable guidelines and parameters	[3, 4, 6, 7, 9]
5	Less support from higher management	Total neglected from concerned higher management in an organization	[3–6, 9, 10, 12]
6	Negative attitudes towards sustainability	Total neglected by concerned top position holder in an organization	[3, 6, 7, 11, 14]
7	Implementation and operating problems and challenges	Difficulties for the sustainable technology's implementation and operations	[4, 12, 13]
8	Weak legislation	Absence of environmental laws	[5, 10]
9	Low enforcement	Complexity of law	[5, 9, 10]
10	Uncertain future legislation	Ineffective legislation	[5, 10]
11	Green technology adaption	Less awareness towards green technology and cost-effectiveness	[2–4, 7, 8]
12	Technological risk	Risk of implementing new technology	[5, 9, 10]

3 Challenges

The challenges are the hindrances or the problems faced by the industries in the implementation of policies or an action plan on sustainability. In this paper, we have compiled a list of challenges (identified from literature review and expert discussion) categorized based on environmental, economic and social perspectives (as shown in Tables 1, 2 and 3) which are faced by the industries practising sustainable manufacturing techniques.

4 Case Study

The case study has been done in "ABC India Ltd." located at Sahibabad, which is a leading manufacturer of electrical goods in India. The company is manufacturing four segments of products: lighting and fixtures, cables, switchgears and electrical

Table 2 Economical challenges

S. No.	Challenges	Description	References
1.	Less funds to green projects	Less government interest, neglected methodology to green funds distribution	[2–4, 9, 12, 15, 16]
2.	Too high cost	Initial expenses are high to sustainable technologies' implementation	[3, 4, 6 9, 12, 17]
3.	Uncertain benefits	Uncertain or insignificant economic advantage	[5], [8, 10, 17]
4.	Trade-offs	Slow return on investment	[5, 10, 13]
5.	Lack of organizational resources	Concerns related to environment do not have much enough importance in current market, which results no financial sources or capital	[5, 6, 10, 13, 18]
6.	Neglected approach for judicious funds	The allocation of capital and funds from banking system at low interest rates also, financial institutes are not present	[2, 5, 6, 11, 18]

Table 3 Social challenges

S. No.	Challenges	Description	References
1.	Less awareness to local customers in green product	Less environmental oriented	[2, 3, 5, 6, 10, 12, 14, 16]
2.	Shortage to locally conducted awareness programmes	Absence of practicable guidelines and parameters	[3, 6, 9, 12, 17, 18]
3.	Employee resistance	Negative reactions towards new concepts on sustainability	[4, 6, 9, 20, 21]
4.	Low public pressure.	There is no such public pressure imparted from local communities, NGOs and media.	[5, 6, 9, 10, 20, 23]

consumer durables. The company has 12 manufacturing units and 43 branch offices in India. Company network consists of 4000 professionals and over 7575 dealers. In last financial year, the organization has a turnover of 8260.27 crores. The organization follows the philosophy of green, efficient, satisfactory and sustainable production. Products are developed with the vision to reduce carbon emissions, improve environmental protection and quality of life, and offer profitable solutions to market issues. ABC India Ltd. is an efficient plant which is specialized in the production of MCM switches and modular switches for households, commercial purposes and various

infrastructures across the country. During our visit to the company, we observed that the case organization has adopted various sustainable practices of manufacturing such as recycling, reusing and reducing waste.

4.1 Case Study Using SWOT Analysis

This is a foundational evaluation concept or model which measures the organization capabilities what they can and cannot do, and its potential opportunities also cross-ponding threats to implementation or working on the opportunities (refer Table 4).

Table 4 SWOT analysis

Strengths	Weaknesses
• Strong network of 40 countries, 7575 dealers and 4000 professionals • 12 high service orientation manufacturing plant • Process according to standardized value or performance benchmarks • Supportive higher management • Good legislation in organization • Green project funds' share is high • Low-carbon emissions' machinery	• Training programme for workers and professionals in such big network is difficult • Uncertain future legislation and benefits • Technological risk • Small market share • Instant fall in real estate • Less awareness of local
Opportunities	**Threats**
• Emerging markets worldwide • Green energy and green packing evolves the new businesses under one domain • Carbon management leads to innovative and new technologies • Reverse logistics helps in increasing resources • Acquiring Chinese firms for low-cost manufacturing • Supplier–environmental collaboration creates and expands the network and trust • Green projects as per consumer and environmentally friendly • Green governments' project	• Unorganized sector and market • High cost of implementation technologies • Highly regulated sector • Trade wars • High competition globally in this sector • High public pressure • New government environmental rules • Network disintegration • Cost of product fluctuation • Dollars and INR variation

5 Conclusion

In this paper, authors identified the challenges coming in the path of implementation of the sustainable manufacturing system. In total, authors identified 22 challenges of sustainable manufacturing by literature review and industrial expert opinion. For practically verification and checking at ground level authors conducted a case study of electrical component manufacturing organization by using SWOT analysis technique. Green manufacturing techniques, technologies and equipment are the biggest strength of case industry, but small market share and high competition lead to threats and weakness; but this manufacturing sector is emerging worldwide which creates the opportunity, and it will be fulfilling the company motto is green and sustainable manufacturing products. All the challenges discussed in this paper will help the decision-makers of different industries to implement the sustainable manufacturing for quality product at low cost. The green manufacturing and sustainability practices are need of time. If organizations work on challenges of sustainability, they can adopt new and modern practices economically.

References

1. Carvalho N, Chaim O, Cazarini E, Gerolamo M (2018) Manufacturing in the fourth industrial revolution: a positive prospect in sustainable manufacturing. Proc Manuf 21:671–678
2. Kulatunga A, Jayawickrama M, Jayatilaka PR (2013) Drivers and barriers to implement sustainable manufacturing concepts in sri lankan manufacturing sector. In: Proceedings of the 11th global conference on sustainable manufacturing—innovative solution, pp 172–77
3. Bhanot N, Rao V, Deshmukh SG (2015) Enablers and barriers of sustainable manufacturing: results from a survey of researchers and industry professionals. Proc CIRP 29:562–567
4. Mutingi M, Musiyarira H, Mbohwa C, Kommula VP (2017) An analysis of enablers and barriers of sustainable manufacturing in southern Africa. In: WCECS, vol II
5. Mitta VK, Egede P, Herrmann C, Sangwan KS (2013) Comparison of drivers and barriers to green manufacturing: a case of India and Germany. In: Procedia CIRP, pp 723–728
6. Bhakar V, Digalwar AK, Sangwan KS (2018) Sustainability assessment framework for manufacturing sector—a conceptual model. Proc CIRP 69:248–253
7. Moldavska A, Welo T (2017) The concept of sustainable manufacturing and its definitions: a content-analysis based literature review. J Clean Prod 166:744–755
8. Thomas-Seale LEJ, Kirkman-Brown JC, Attallah MM, Espino DM, Shepherd DET (2018) The barriers to the progression of additive manufacture: perspectives from UK industry. Int J Prod Econ 198:104–118
9. Stewart R, Bey N, Boks C (2016) Exploration of the barriers to implementing different types of sustainability approaches. Proc CIRP 48:22–27
10. Mittal VK, Sangwan KS (2014) Prioritizing barriers to green manufacturing: environmental, social and economic perspective. Proc CIRP 17:559–564
11. Amrina E, Yusof SM (2012) Drivers and barriers to sustainable manufacturing initiatives in Malaysian automotive companies. In: Proceedings of the Asia Pacific industrial engineering & management systems conference, pp 629–634
12. Luthra S, Kumar V, Kumar S, Haleem A (2011) Barriers to implement green supply chain management in auto industries using interpretive structural modeling technique—an Indian perspective. JIEM 4(2):231–257

13. Ariffin R, Ghazilla R (2015) Drivers analysis and barriers in green manufacturing practices in Malaysian SMEs: a preliminary findings. Proc CIRP 26:658–663
14. Koho M, Torvinen S, Romiguer AT (2011) Objectives, enablers and challenges of sustainable development and sustainable manufacturing: views and opinions of Spanish companies. In: ISAM IEEE, pp 1–6
15. NMCC (2006) The national strategy for manufacturing (India)
16. Badurdeen F, Jawahir IS (2017) Strategies for value creation through sustainable manufacturing. Proc Manuf 8:20–27
17. Jovane F, Seliger G, Stock T (2017) Competitive sustainable globalization general considerations and perspectives. Proc Manuf 8:1–19
18. Mittal VK, Sangwan KS (2014) Prioritizing drivers for green manufacturing: environmental, social and economic perspectives. Proc CIRP 15:135–140
19. Schönborn G, Cecilia BC, Pinzone M, Hanisch C, Georgoulias K, Lanz M (2019) Why social sustainability counts: the impact of corporate social sustainability culture on financial success. Sustain Prod Consumption 17:1–10
20. Sutherland JW, Richter JS, Hutchins MJ, Dornfeld D, Dzombak R, Mangold J, Robinson S, Hauschild MZ, Bonou A, Schonsleben P, Friemann F (2016) CIRP Ann Manuf Technol 65:689–712
21. Kulkarni S, Rao P, Patil Y (2014) Proc Soc Behav Sci 133:364–371
22. Kumar N, Agrahari RP, Roy D (2015) Review of green supply chain processes. IFAC-PapersOnLine 48(3):374–381
23. Govindan K, Khodaverdi R, Vafadarnikjoo A (2015) Intuitionistic fuzzy based DEMATEL method for developing green practices and performances in a green supply chain. Expert Syst Appl 42:7207–7220
24. Mani V, Agrawal R, Sharma V (2015) Proc Soc Behav Sci 189:234–251

Investigation on the Effect of Input Parameters on Surface Quality During Rotary Tool Near-Dry EDM

Vineet Kumar Yadav, Ramver, Pradeep Kumar and Akshay Dvivedi

Abstract This paper presents an experimental study on rotary tool near-dry EDM (RT-ND-EDM) of high-speed steel using a two-phase mixture of water and air as a dielectric medium. The RT-ND-EDM is an environmentally friendly process variant of EDM. Parametric investigation was performed to understand the effect of various input parameters on the quality of machined surface. The experimental results revealed that surface roughness (SR) increased with an increase in peak current and pulse on time. An increase in gas pressure first decreased and then increased the SR, and finally SR decreased with increased in liquid flow rate. In addition, analysis of RT-ND-EDMed surface using FE-SEM technique revealed that the machined surface had irregularities such as micro-cracks, debris deposition, micro-holes, micropores.

Keywords EDM · RT-ND-EDM · Surface roughness · Surface integrity

1 Introduction

Electrical discharge machining (EDM), which is also called as spark erosion machining, falls under a broader category of non-traditional machining processes. The major area of application of EDM process is in tool and die manufacturing industries, credited to its ability to machine complex shapes irrespective of hardness and toughness of the work material. It removes allowances through successive discrete electrical discharge, known as spark discharge, by ablation and melting in the presence of dielectric medium. Hydrocarbon-based dielectric mediums are generally used in EDM process. However, the use of hydrocarbon-based dielectric mediums (e.g., EDM oil, kerosene, etc.) in EDM process causes environmental hazards: toxic fumes, aerosols, odors, etc., generated during the decomposition of hydrocarbon substances. Furthermore,

V. K. Yadav · Ramver (✉) · P. Kumar · A. Dvivedi
Mechanical and Industrial Engineering Department, Indian Institute of Technology (IIT), Roorkee 247667, India
e-mail: ramver.pme@gmail.com

V. K. Yadav
e-mail: vineet437@gmail.com

A. K. Parwani and PL. Ramkumar (eds.), *Recent Advances in Mechanical Infrastructure*, Lecture Notes in Intelligent Transportation and Infrastructure,
https://doi.org/10.1007/978-981-32-9971-9_5

hydrocarbon-based dielectric mediums have shortcomings from health and safety point of views, and it may cause skin irritation, cancer, and fire hazards. Therefore, the recent research in EDM focuses on the exploitation of gases or two-phase (mixture of liquid and gas) fluids as alternate clean and safe dielectric mediums.

In this context, EDM in gaseous dielectric medium was successfully demonstrated by Ramani and Cassidenti 1985 [1]. They used inert gases instead of customary liquid as dielectric mediums to drill holes. In 1997, Kunieda et al. performed a comparative investigation on EDM using air, oxygen, and EDM oil dielectric mediums [2]. To match the material removal capability of dry EDM (EDM in gaseous medium) process with that of conventional EDM (EDM in liquid medium) process, a mixture of oxygen and inert gases was suggested. However, the problems of debris deposition on tool and frequent short-circuits were encountered in dry EDM process.

To overcome the limitations of dry EDM process, a novel modification to dry EDM was proposed by Tanimura et al. 1989 [3]. To tailored the advantages of liquid as well as gaseous dielectric mediums, mist (two-phase mixture of liquid in gases) was used in near-dry EDM process. Cao et al. 2007 evaluated the relative performance of EDM process in liquid, dry, and near-dry conditions [4]. It was reported that near-dry EDM process outperformed wet and dry EDM process in terms of material removal rate (MRR), form accuracy and machined surface integrity [4–7]. Various dielectric mediums were explored to increase the productivity of near-dry EDM process, especially, a drastic improvement in MRR was reported, when glycerin as liquid phase in mist was used as a dielectric medium [8, 9]. In addition, Yadav et al. 2017 reported three times higher MRR with tool rotation in near-dry EDM process using glycerin–air dielectric medium [10].

In this paper, the RT-ND-EDM of high-speed steel (HSS) using a two-phase mixture of water and air was performed on the indigenous developed facility. Parametric investigation was performed using various input parameters on the machined surface quality. Moreover, the machined surface morphology was analyzed using FE-SEM micrographs.

2 Materials and Methods

The present experimental study was performed on an EDM machine. An indigenously customized attachment was used for the generation of two-phase dielectric medium [10]. Figure 1 illustrates the schematic of the developed experimental facility, which consists of rotary and mixing unit as addition attachments to the basic die-sinking EDM machine.

In this experimental investigation, HSS and commercially pure copper were selected as work and tool material, respectively. Tubular shape tool was used with the outer and inner diameters of 6 and 3 mm, respectively. HSS is a high-performance cutting tool material, and it has been used widely in tool and die manufacturing industries. The experiments for the current investigation were performed using one-factor at time method. The various input parameters can be referred from Table 1. Mitutoyo

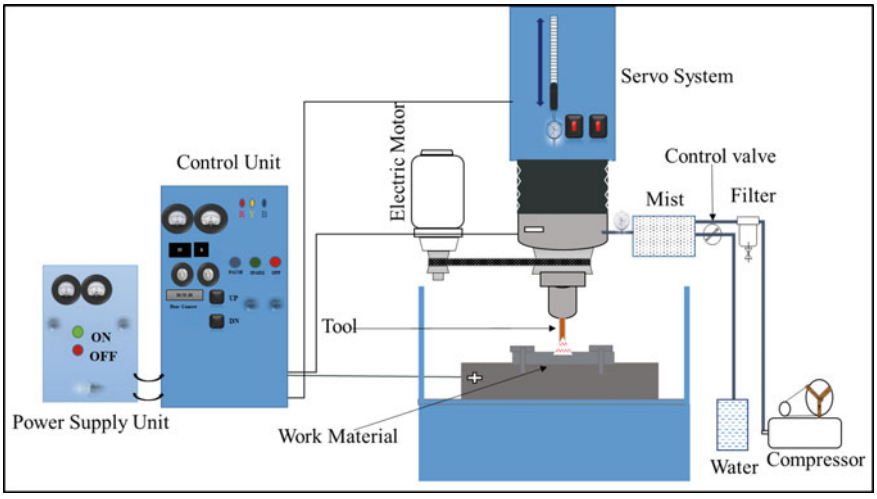

Fig. 1 Schematic of the developed facility for experimentation

Table 1 Machining conditions used in the experimental study

Input parameters	Descriptions
Peak current (A)	3–15
Pulse on time (μs)	190–390
Liquid flow rate (ml/min)	3.2–9.6
Gas pressure (psi)	10–50
Tool rotation speed (rpm)	1000
Polarity	Straight (work, +)
Dielectric medium	Two-phase (distilled water in air)
Lift setting	4

SJ400 surface roughness tester was used to measure the SR of the machined surface. Morphology of the RT-ND-EDMed surface was studied using FE-SEM, Carl Zeiss.

3 Results and Discussions

The experimental results of SR and FE-SEM analysis of RT-ND-EDMed surface in water–air dielectric medium are presented and discussed, subsequently. The trend of SR results against the selected process parameters of RT-ND-EDM is depicted in Figs. 2 and 3.

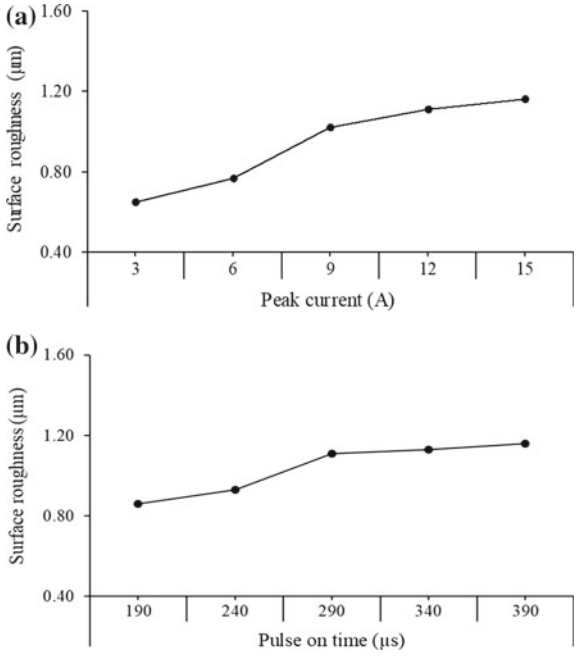

Fig. 2 Influence of input parameters on SR of RT-ND-EDMed surface; **a** peak current; **b** pulse on time

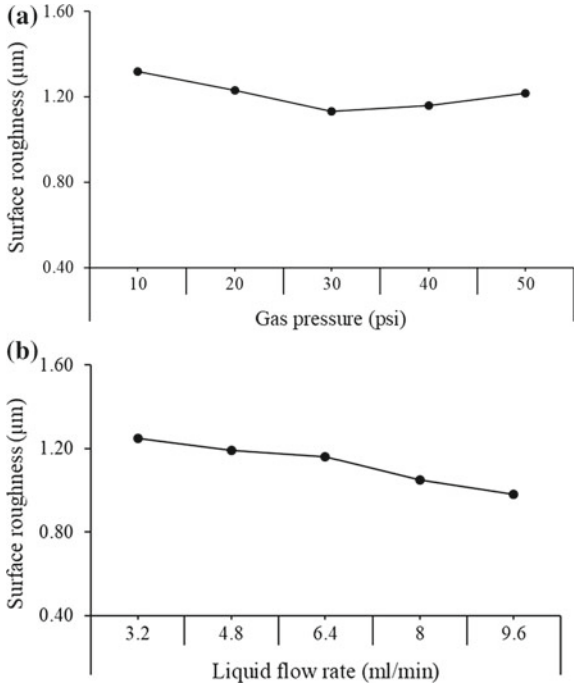

Fig. 3 Influence of input parameters on SR of RT-ND-EDMed surface; **a** gas pressure; **b** liquid flow rate

3.1 The Effect of Selected Process Parameters on SR

The Effect of Peak Current on SR
It can be observed from Fig. 2a that the trend of average SR (R_a-value) against peak current is of increasing in nature. This kind of trend in SR can be explained by the fact that the available thermal energy of individual sparks to the material removal phenomenon increases with increase in current value. The increased thermal energy of individual spark discharges consequences intense material extraction, i.e., deeper micro-craters are formed and subsequently resulted in higher values of SR.

The Effect of Pulse on Time on SR
As can be seen from Fig. 2b, the trend of average SR (R_a-value) against pulse on time is similar to that with peak current. The increase in pulse on time resulted in longer duration of spark discharges, which eventually cause increased thermal energy of individual spark discharges. Thereby, SR increased by increasing the pulse on time.

The Effect of Gas Pressure on SR
The effect of gas pressure on SR is shown in Fig. 3a. From Fig. 3a, it can be observed that the SR initially decreased as the gas pressure increased up to 30 psi and then increased marginally with further increased in gas pressure. Initially, as the gas pressure increased, the velocity of dielectric stream flowing through the inter-electrode gap (IEG) also increased. As the dielectric stream flowed faster, it can suspend and flush debris particles effectively from the machining zone, and therefore, promoted the stable and uniform sparking in the IEG, thus resulted in decreased SR value. However, higher gas pressure (beyond 30 psi) resulted in unstable sparking in the IEG attributed to the turbulence caused by high-velocity dielectric stream, subsequently, SR was increased.

The Effect of Liquid Flow Rate on SR
Figure 3b shows that as the amount of liquid (water) phase in dielectric medium (mist) increased, the SR decreased monotonously. In RT-ND-EDM process, the amount of liquid phase in the dielectric medium stimulates the cooling/solidification rate of the molten pool or the formation rate of debris particles. Therefore, the increased amount of liquid phase promotes rapid formation of debris from the molten pool, and these debris particles can be flushed out by high-velocity dielectric stream [11]. Hence, this causes reduction in SR value of the RT-ND-EDMed surface.

3.2 Analysis of RT-ND-EDMed Surface Morphology

Due to higher discharge energy in the machining zone, high temperature was generated which caused melting and vaporization of material. To analyze the morphology of machined surface, micrographs were taken using FE-SEM. A typical FE-SEM

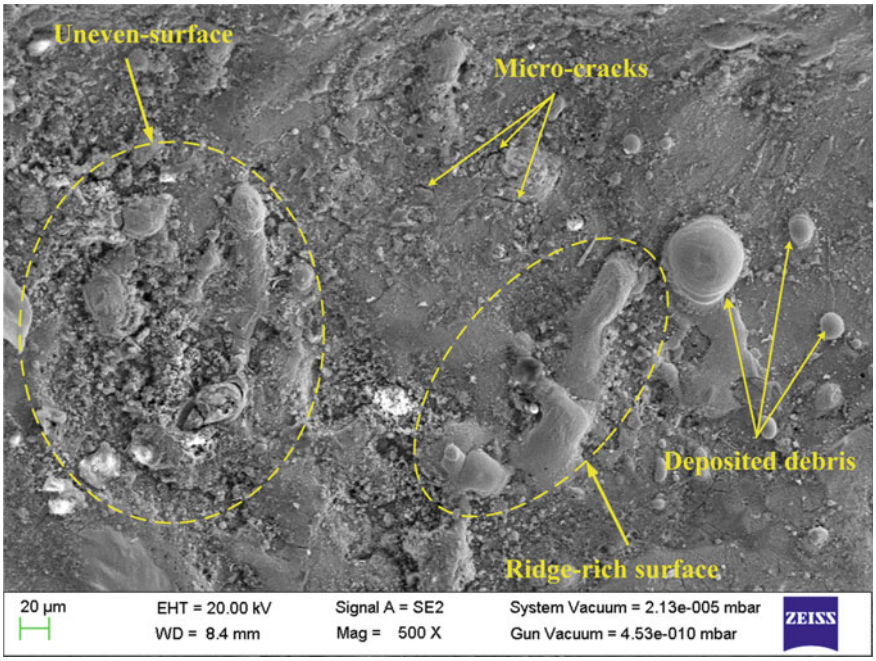

Fig. 4 Surface morphology of machined surface @500× magnification

micrograph is shown in Fig. 4. It was observed from the figure that the RT-ND-EDMed surface consist of micro-cracks, ridge-rich surface, globules, micro-holes, pores etc. The inconsistency on the machined surface is due to re-solidification of the molten metal on the machined surface [12].

4 Conclusions

In this research, process performance of RT-ND-EDM has been investigated for SR using two phase-dielectric (mixture of water and air). Furthermore, the morphology of the machined surface was analyzed. The SR increased on increasing the peak current, pulse on time, and decreased on increasing the liquid flow rate. On increasing the gas pressure the SR first decreased and then increased. The analysis of the machined surface revealed that the RT-ND-EDMed surface had irregularities such as micro-cracks, globules, micro-holes, micropores.

References

1. Ramani V, Cassidenti ML (1985) Inert-gas electrical discharge machining. NASA Tech Br No NPO-15660
2. Kunieda M, Yoshida M, Taniguchi N (1997) Electrical discharge machining in gas. CIRP Ann Manuf Technol 46(1):143–146
3. Tanimura T, Isuzugawa K, Fujita I, Iwamoto A, Kamitani T (1989) Development of EDM in the mist. In: Proceedings of ninth international symposium of electro machining (ISEM IX) Nagoya, Japan, pp 313–316
4. Kao CC, Tao J, Shih AJ (2007) Near dry electrical discharge machining. Int J Mach Tools Manuf 47(15):2273–2281
5. Dhakar K, Dvivedi A (2017) Dry and near-dry electric discharge machining processes. Springer, Cham
6. Yadav VK, Kumar P, Dvivedi A (2017) Parametric investigations on rotary tool near-dry electric discharge machining. In: 10th international conference on precision, meso, micro nano engineering (COPEN 10), IIT Madras, Chennai, 06–09 Dec, pp 575–578
7. Tao J, Shih AJ, Ni J (2008) Experimental study of the dry and near-dry electrical discharge milling processes. J Manuf Sci Eng 130(1):011002
8. Dhakar K, Dvivedi A, Dhiman A (2016) Experimental investigation on effects of dielectric mediums in near-dry electric discharge machining. J Mech Sci Technol 30(5):2179–2185
9. Dhakar K, Dvivedi A (2016) Parametric evaluation on near-dry electric discharge machining. Mater Manuf Process 31(4):413–421
10. Yadav VK, Kumar P, Dvivedi A (2017) Investigations on rotary tool near-dry electric discharge machining. In: Applications of process engineering principles in materials processing, energy and environmental technologies. Springer, Cham, pp 327–334. https://doi.org/10.1007/978-3-319-51091-0_31
11. Yadav VK, Kumar P, Dvivedi A (2019) Effect of tool rotation in near-dry EDM process on machining characteristics of HSS. Mater Manuf Process 34(7):779–790. https://doi.org/10.1080/10426914.2019.1605171
12. Ramver, Dvivedi A, Kumar P (2019) On improvement in surface integrity of μ-EDMed Ti–6Al–4V alloy by μ-ECM process. In: 148th annual meeting & exhibition supplemental proceedings. The minerals, metals & materials series. Springer, Cham. https://doi.org/10.1007/978-3-030-05861-6_73

Application of Utility Function Approach Aggregated with Imperialist Competitive Algorithm for Optimization of Turning Parameters of AISI D2 Steel

Soni Kumari, Din Bandhu, Anshuman Kumar, Rajiv Kumar Yadav and K. Vivekananda

Abstract In the fast-growing infrastructure, machining plays a vital role in industrial evolution. However, obtaining optimal machining parameters is still a challenging assignment for manufacturers because an inappropriate selection of machining parameters specifically spindle speed (N), feed rate (f), and depth of cut (d) adversely affects the overall machining performance. Therefore, this work attempts to provide optimal parameters setting for machining AISI D2 steel in dry condition with PVD-coated carbide tool. The evaluation of the optimal parameters setting has also been done by means of utility function approach aggregated with the imperialist competitive algorithm.

Keywords AISI D2 · Imperialist Competitive Algorithm (ICA) · Turning · Optimization

1 Introduction

The time consumed in machining operation directly affects the rate of productivity and further the economics of the industry. To fulfill the demand for quality products with a higher rate of productivity, reduction in machining time is essential, especially amid the machining of hard and tough materials. Besides other factors like machine

S. Kumari (✉)
Department of Mechanical Engineering, GLA University, Mathura, India
e-mail: soni.1802@gmail.com

D. Bandhu
Department of Mechanical Engineering, IITRAM, Ahmedabad, India

A. Kumar
Department of Mechanical Engineering, KL University, Guntur, India

R. K. Yadav
Department of Mechanical Engineering, AITM, Varanasi, India

K. Vivekananda
Department of Mechanical Engineering, FST, IFHE University, Hyderabad, India

A. K. Parwani and PL. Ramkumar (eds.), *Recent Advances in Mechanical Infrastructure*, Lecture Notes in Intelligent Transportation and Infrastructure,
https://doi.org/10.1007/978-981-32-9971-9_6

quality and set-up, selection of work materials and cutting tools, operator's skill, the condition of machining environment, etc., the selection of an appropriate machining parameter also helps in minimization of the machining time [1, 2].

The materials which demonstrate the characteristics namely exaggerated tool wear, inferior surface finish, complexities in chip formation, and elevated cutting forces amid their machining are known as difficult to cut materials and one such material is AISI D2 steel [3]. It is an air-hardening, heat treatable tool steel with high carbon and chromium contents. It offers excellent properties namely strength, wear resistant, and abrasion resistant with a high melting temperature of 1421 °C. Generally, it is supplied in the annealed condition and tenders hardness between 57 and 62 HRC [2, 3]. Such materials are mainly utilized for prolonged tooling applications like forming dies and rolls, threading dies and rolls, cutting and stamping tools, etc. They are also used to make utensils namely knives, shear blades, slitters, tire shredders, etc. [2–4]. To empathize the machining characteristics of AISI D2 steel, some formulations of the hypothesis have been done as follows.

Rajbongshi et al. [5] performed dry turning operation on AISI D2 steel with the aid of textured and non-textured cutting tools. Eight attempts have been carried out by taking three factors (feed rate, cutting speed, and depth of cut) into account with all of them having two levels. Scrutinizing has been done to know the importance of tribological adaptations at the chip-tool interface. The coated carbide tool has linear microgrooves created over its flank face and the surface texturing process was employed to examine its impact on that. Little flank wear and better surface finish have been seen with the textured tool as against the non-textured tools. Thus, the machinability of the material has been improved with the tool having a textured flank face. Abdul Rahim et al. [6] studied the present altered trend of AISI D2 materials and found that the existence of alloy carbides have a prodigious result on the machinability of these materials. Optimization of machining parameters with less surface roughness has been accomplished at an optimum MRR. Khan et al. [7] examined and collated the wear action of cutting tool relating to the workpiece. The flank wear of two different alumina-based and ceramic tools consisting of SiC and Ti[C, N] has been evaluated by keeping the feed rate and depth of cut constant but cutting speed variable. It has been perceived that the machining with Ti[C, N] particles-based cutting tool yields better result as compared to SiC whisker-based tool. López-Luiz et al. [8] performed dry turning operation on AISI D2 steel and optimized the surface roughness (R_a) and flank wear of PVD-TiAlN-coated WC insert cutting tool using Taguchi-based approach and RSM technique. The main affecting parameters, viz. depth of cut on the surface roughness and feed rate on the flank wear have been identified using variance analysis. Panda et al. [9] endeavored dry turning operation using TiN/TiCN/Al_2O_3-coated carbide inserts on AISI 52100 steel and examined machinability of the material by evaluating flank wear, surface roughness, and chip morphology. ANOVA, quadratic regression, and artificial neural network methods have been utilized to determine and model the effect of machining variables [cutting speed (N), depth of cut (d), and feed rate (f)], respectively. Taguchi-based GLA method has been applied for optimizing multi-parameter of cutting conditions. Patel et al. [2] proposed an integrated optimization module and optimized correlated

multi-response features using FIS, nonlinear regression, and JAYA algorithms for machining of AISI D2 steel. Cutting speed, torch height, and gas pressure have been selected as machining parameters to determine the MRR and R_a amid plasma arc cutting of the material. GA and TLBO have been employed for testing the application potential. It has also been perceived that the JAYA algorithm has less convergence time than these both. Khan et al. [10] conducted surface grinding operation on AISI D2 steel on the basis of three conditions, i.e., dry, flood cooling and minimum quantity lubrication and calculated responses, viz. surface temperature, surface quality, and normal force. A comparison was drawn among them. ANOVA approach has been adopted to determine the main influencing factor on aforesaid responses. RSM and Grey-Taguchi technique has been employed for mathematical formulation and multi-objective optimization, respectively. Kumari et al. [11] executed dry turning operation on AISI D2 steel using carbide tool coated with PVD and investigated the influence of input parameters, viz. d, N, and f on R_a and MRR. Formulation of experimentation was based on the L_9 orthogonal array. Multiple responses have been altered into an equivalent single response using grey relation analysis technique. Optimal machining condition has been appraised with the help of harmony search algorithm and validated using the genetic algorithm. Liew et al. [12] integrated Taguchi approach and response surface methodology to reveal the optimal parameters in multi-response turning operation of AISI D2 steel with the aid of coated carbide tool. It has been perceived that the feed (f) and cutting speed (N) are the exceptionally prominent factors for R_a and tool wear, respectively. Kumar et al. [13] investigated the surface roughness, flank wear, and the temperature at the chip-tool interface amid turning process of AISI D2 steel. Formulation of responses has been determined using artificial neural networks and response surface methodology, and relative evaluation was done for forecasted and real results. For flank wear, satisfactory outcomes have been achieved by ANN, whereas for tool-chip interface temperature and surface roughness, RSM results were precise.

2 Imperialist Competitive Algorithm (ICA)

The imperialist competitive algorithm (ICA), designed by Atashpaz-Gargari, Hashemzadeh, and Lucas in 2008 [14], is one of the meta-heuristic methods to determine the optimum solution of nonlinear integer programming problems. Socio-political behavior is the foundation and inspiration behind its formulation [14, 15]. Initially, it has been especially used in solving continuous optimization problems, but now it finds its applications in numerous multifaceted desecrate combinational optimization problems, viz. assembly line balancing problems, facility layout problems, shop scheduling problems, traveling salesman problem, etc. In general, it has been implemented for all optimization problems related to management, engineering, and industry sectors [15–17].

Just like GA, it is also a population-based algorithm. It commences with an uncertain initial population where each of them characterizes a country. These

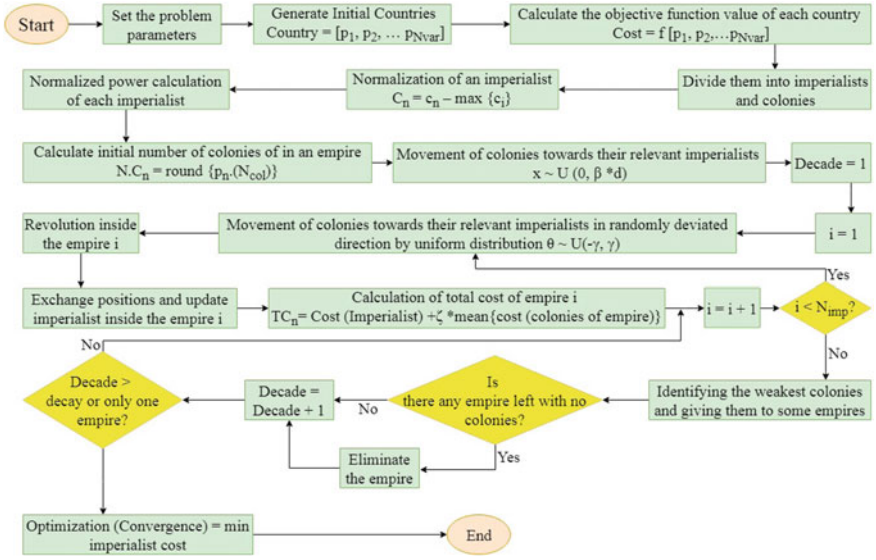

Fig. 1 Imperialist competitive algorithm (ICA)

countries are of two types: one being imperialist and other as colonies. Initially, some best countries have been selected as imperialists, whereas the rest acts as colonies. These colonies are further classified and distributed among the imperialists based on their power. Now, a combination of imperialists and some colonies form empires and compete among themselves. The existence of an empire depends upon its power to grab colonies from other empires. Thus, the power of the strongest empire keeps on increasing, whereas the weaker one gets collapsed. After many iterations, convergence occurs where only one empire has remained with some colonies [14, 16, 17].

ICA involves the following steps [16] as shown in Fig. 1.

3 Experimental Details

In this work, the impact of different machining variables, viz. spindle speed, feed, and depth of cut has been examined amid turning of AISI D2 steel. The values for the aforementioned machining variables, set during the experimentation, have been listed in Table 1.

An appropriate design of experiments (DOE) become crucial for the accomplishment of experimentation and to decide the total experiments to be performed, the concept of Taguchi's L_9 orthogonal array (Table 2) has been implemented. All these experiments have been performed on a lathe for the purpose of acquiring the experimental data as itemized in Table 2. PVD-coated carbide tool has been employed to

Table 1 Machining variables and their levels

S. No.	Process parameters	*L*1	*L*2	*L*3
1	Spindle speed (*N*)	257	386	566
2	Feed rate (*f*)	1.5	2.0	2.5
3	Depth of cut (*d*)	0.5	1.0	1.5

perform the turning operation on the work material. The MRR and R_a have been measured as the machining evaluation characteristics. A surface roughness tester, made up of Talysurf, has been utilized to assess the surface roughness of the material. The experimental results have been depicted in Table 2.

4 Result and Discussion

Initially, the output responses namely MRR and R_a have been converted into individual utility degree (sometimes called as preference number). In order to assess the individual utility index (presented in Table 2) for aforesaid characteristic, the following equations have been used:

For assessing MRR:

$$A = \frac{9}{\log \frac{X_{\text{Higher}}}{X_{\text{Lower}}}} \tag{1}$$

The expression for the preference number on a logarithmic scale can be written like this:

$$\text{UMRR} = A \times \log \frac{X_i}{X_{\text{Lower}}} \tag{2}$$

For assessing surface roughness:

$$A = \frac{9}{\log \frac{X_{\text{Lower}}}{X_{\text{Higher}}}} \tag{3}$$

The expression for the preference number R_a on a logarithmic scale can be written like this:

$$U_{R_a} = A \times \log \frac{X_i}{X_{\text{Higher}}} \tag{4}$$

Table 2 Formulation of DOE using L_9 orthogonal array, experimental data, and utility indices

S. No.	N (rpm)	f (mm/min)	d (mm)	MRR (mm^3/min)	R_a (μm)	U_{MRR}	U_{Ra}	$U_{overall}$
1	257	1.5	0.5	1087.386	3.87	6.968627	1.503444	4.236036
2	257	2	1	803.3234	2.92	3.017295	5.125334	4.071315
3	257	2.5	1.5	637.5	2.46	0	7.329583	3.664792
4	386	1.5	1	1256.97	4.35	8.85999	0	4.429995
5	386	2	1.5	923.789	3.81	4.840781	1.704363	3.272572
6	386	2.5	0.5	708.434	2.16	1.376853	9.001883	5.189368
7	566	1.5	1.5	789.67	3.03	2.793582	4.649837	3.721709
8	566	2	0.5	762.7177	2.66	2.340378	6.324494	4.332436
9	566	2.5	1	1270.528	3.93	9.000001	1.305615	5.152808

The calculation of the overall utility index is done based on the following equation:

$$U = \sum_{i}^{n} W_i U_i \tag{5}$$

After that, a mathematical model for U_{overall} has been formulated with the aid of nonlinear regression and considered as an objective function for the ICA. The optimal machining condition is furnished in Table 3 and also illustrated in Fig. 2.

$$U_{\text{overall}} = 1.821 \times N^{(0.110)} \times f^{(0.243)} \times d^{(-0.186)}$$

Table 3 Optimal parametric combination obtained through ICA

Methods	N	f	d	Overall utility index
ICA	566	2.50	0.50	5.19293413855071

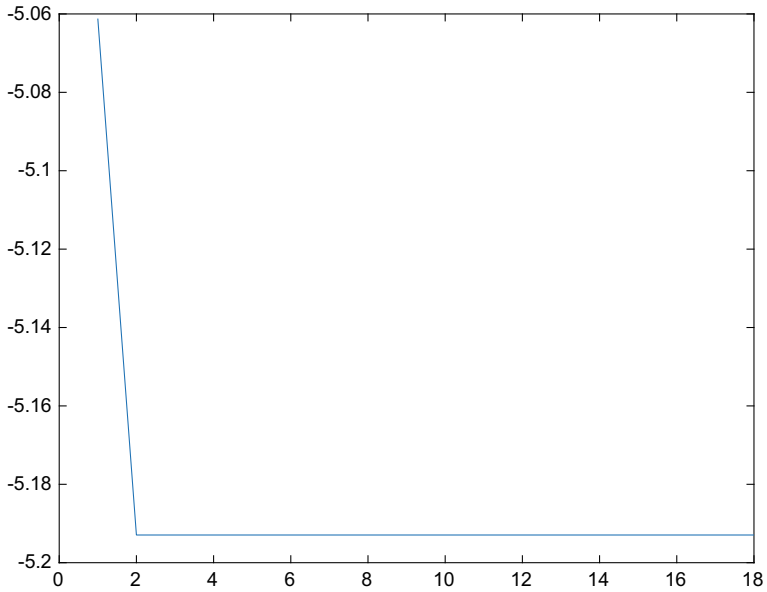

Fig. 2 Illustration of optimal parametric combination obtained through ICA

5 Result and Discussion

The present work deals with the application of utility function approach aggregated with the imperialist competitive algorithm to figure out the optimal machining amid turning of AISI D2 steel. It is clear from the results that the proposed methodology is capable of parametric appraisal and effectively optimizes the simultaneous process output responses for AISI D2 steel turning.

References

1. Qehaja N, Jakupi K, Bunjaku A, Bruçi M, Osmani H (2015) Effect of machining parameters and machining time on surface roughness in dry turning process. Proc Eng 100:135–140
2. Patel P, Nakum B, Abhishek K, Rakesh Kumar V (2018) Machining performance optimization during plasma arc cutting of AISI D2 steel: application of FIS, nonlinear regression and JAYA optimization algorithm. J Braz Soc Mech Sci Eng 40(4)
3. Sharma J, Singh B (2014) Investigation of effects of dry and near dry machining on AISI D2 steel using vegetable oil. J Clean Prod 66:619–623
4. Arsecularatne JA, Zhang LC, Montross C, Mathew P (2006) On machining of hardened AISI D2 steel with PCBN tools 171:244–252
5. Rajbongshi SK, Annebushan Singh M, Kumar Sarma D (2018) A comparative study in machining of AISI D2 steel using textured and non-textured coated carbide tool at the flank face. J Manuf Process 36:360–372
6. bin Abdul Rahim MAS, bin Minhat M, Hussein NISB, bin Salleh MS (2018) A comprehensive review on cold work of AISI D2 tool steel. Metall Res Technol 115(1):104
7. Khan MA, Kumar AS, Kumaran ST, Uthayakumar M, Ko TJ (2018) Effect of tool wear on machining GFRP and AISI D2 steel using alumina based ceramic cutting tools. Silicon 1–6
8. López-Luiz N, Alemán OJ, Hernández FA, Dávila MM, Baltazar-Hernández VH (2018) Experimentation on tool wear and surface roughness in AISI D2 steel turning with WC insert. Mod Mech Eng 08(03):204–220
9. Panda A, Sahoo AK, Panigrahi I, Rout AK (2018) Investigating machinability in hard turning of AISI 52100 bearing steel through performance measurement: QR, ANN and GRA study. Int J Automot Mech Eng 15(1):4935–4961
10. Khan AM et al (2018) Multi-objective optimization for grinding of AISI D2 steel with Al_2O_3 wheel under MQL. Materials (Basel) 11(11)
11. Kumari S, Kumar A, Kumar Yadav R, Vivekananda K (2018) Optimisation of machining parameters using grey relation analysis integrated with harmony search for turning of AISI D2 steel. Mater Today Proc 5(5):12750–12756
12. Liew PJ, Shaaroni A, Razak JA, Kasim MS, Sulaiman MA (2017) Optimization of cutting condition in the turning of AISI D2 steel by using carbon nanofiber nanofluid. Int J Appl Eng Res 12(10):2243–2252
13. Kumar R, Sahoo AK, Das RK, Panda A, Mishra PC (2018) Modelling of flank wear, surface roughness and cutting temperature in sustainable hard turning of AISI D2 steel. Proc Manuf 20:406–413
14. Seidgar H, Kiani M, Abedi M, Fazlollahtabar H (2014) An efficient imperialist competitive algorithm for scheduling in the two-stage assembly flow shop problem. Int J Prod Res 52(4):1240–1256
15. Abhishek K, Datta S, Masanta M, Mahapatra SS (2017) Fuzzy embedded imperialist competitive algorithm (ICA) for multi-response optimization during machining of CFRP (Epoxy) composites. In: Proceedings of the 2017 international conference on advances in mechanical, industrial, automation and management systems AMIAMS 2017, pp 100–103

16. Hosseini S, Al Khaled A (2014) A survey on the imperialist competitive algorithm metaheuristic: implementation in engineering domain and directions for future research. Appl Soft Comput J 24:1078–1094
17. Mikaeil R, Haghshenas SS, Haghshenas SS, Ataei M (2018) Performance prediction of circular saw machine using imperialist competitive algorithm and fuzzy clustering technique. Neural Comput Appl 29(6):283–292

Optimization of Quality Characteristics in Laser Drilling of Ti6Al4V Using VIKOR

Suman Chatterjee, Kumar Abhishek and Siba Sankar Mahapatra

Abstract High precision and accuracy in machining of complicated parts requisite the application of lasers in the machining of advanced and hard to cut materials. Titanium and its alloys have widespread applications in several sectors namely aerospace, micro-electromechanical systems (MEMS), and medical discipline because of their plentiful advantages such as biocompatibility, corrosion resistance, and conductivity. Titanium and its alloys are hard-to-machine materials due to their thermal conductivity, toughness, and strength. To achieve good machinability and quality of machined surfaces, lasers are the best alternatives due to its aforementioned advantages. In the present study, experimental investigation of the quality of holes has been studied using CO_2 laser. The present study was extended to explore the implementation of the VIKOR method, a novel multi-criteria decision-making (MCDM)-based methodology, amalgamated with Taguchi technique for concurrent optimization of several allied drilling variables, viz. laser power, frequency, and gas assistant in laser drilling of titanium alloy (Ti6Al4V) by means of CO_2 laser. The ideal setting of machining variables has been displayed by main effects plot for S/N ratio on the overall quality index (Q_i). The adequacy of schemed methodology has been certified by the acquired result.

Keywords Ti6Al4V · Laser drilling · Taguchi · VIKOR · Optimization

S. Chatterjee · S. S. Mahapatra
Department of Mechanical Engineering, National Institute of Technology, Rourkela, Odisha, India
e-mail: mrsumanmech@gmail.com

K. Abhishek (✉)
Department of Mechanical Engineering, Institute of Infrastructure, Technology, Research and Management, Ahmedabad 380026, India
e-mail: krabhishek1987@gmail.com

A. K. Parwani and PL. Ramkumar (eds.), *Recent Advances in Mechanical Infrastructure*, Lecture Notes in Intelligent Transportation and Infrastructure,
https://doi.org/10.1007/978-981-32-9971-9_7

1 Introduction

Laser beam-based material processing has widespread benefits and applications in various field material processing such as welding, cutting, sintering, forming, additive manufacturing, and drilling processes. The laser can process hard-to-machined materials such as superalloys and composites with stringent design requirements and with high precision [1]. There are various superalloys, viz. titanium alloy, nickel alloy, and stainless steel alloy, which are widely applied materials in the field of aerospace, aviation, shipping industries, chemical industries, and biomedical engineering due to their favorable mechanical properties, viz. strength, toughness, corrosion resistance, and low thermal conductivity [2]. Among aforementioned discussed materials, titanium alloy of grade-V (Ti6Al4V) has widespread application in various fields like medical implants, aerospace, aviation, automobile sectors, and chemical industries by virtue of its properties like biocompatibility, low thermal, high corrosion resistance, and weight-to-strength ratio. Titanium alloys are used in the manufacturing of engines, airframes, allograft parts (in the human body), and production of fins. To attain the desired quality products, the micro-machining process is required.

Shelton and Shin [3] have studied the influence of CO_2 laser on performance characteristics namely workpiece surface finish, microstructure, and edge burrs during laser machining of various superalloy, viz. AISI 316, Ti6Al4V, Inconel 718, and AISI 422. Yan et al. [4] have employed a CO_2 laser and minimized the spatter area and hole taper in the drilling of thick aluminum sheets. Chatterjee et al. [5] have operationalized CO_2 laser drilling on titanium alloy by varying the laser process parameters at three different levels. The study was conducted to comprehend the influence of process parameters on quality characteristics. Because laser machining is an exorbitant process, the design of experiment (DOE) methodology has been employed for systematic experimental layout which reduces the time consumption and experimental cost. The prepared experimental scheme can be accompanied by regression methods to simulate the process numerically [6, 7]. Chatterjee et al. [5] have employed an empirical model to compare and analyzed the circularity, taper, and spatter area in laser percussion drilling on titanium alloys. Ghoreishi et al. [8] have proposed a statistical model to examine and collate the taper hole and circularity amid laser percussion drilling on materials namely stainless steel and mild steel. Sahu et al. [9] have proposed the VIKOR method embedded with the design of experiment approach (DOE) using Taguchi L_9 orthogonal array to transform the multi-response to MPCI for optimization of process responses.

With an increase in demand for miniaturization of the product generates the necessity of micro-machining processes with higher accuracy, precision, and good quality. To achieve the aforementioned aspects of the products leads to an increase in time and price of the required product. In the present paper, a CO_2 laser is used to drill microhole on Ti6Al4V titanium alloy. Design of experiment (DOE) methodology has been applied to design the experimental run and to evaluate the consequence of parameters namely assistant gas pressure, pulse frequency, and laser power upon the attribute of holes from the perspective of taper, circularity, and spatter area. To determine the

best (optimal) parametric conditions for the quality of holes, the VIKOR method has been introduced to commute the multi-responses to single multi-performance characteristics index (MPCI).

2 Experimental Procedure

2.1 VIKOR

VIKOR, developed by Opricovic, is a well-known multi-criteria decision-making (MCDM) technique on the basis of ideal point approach. It runs on a basic principle of finding out the positive and negative ideal solutions in the first place [10]. The positive and negative ideal solutions indicate the best and the worst values of preferences, respectively, in compliance with the measurement standards. Later on, the precedence of the schemes has been set along the foundation of the nearness of the alternative evaluated value to the ideal schemes.

The following equation is a form of LP-metric aggregate function, adopted by VIKOR for compromise ranking of multi-criteria measurement [11].

$$L_{Pi} = \left\{ \sum_{j}^{n} \left[w_j \left(f_j^* - f_{ij} \right) / \left(f_j^* - f_j^- \right) p \right] \right\}^{1/p}, \tag{1}$$

Here, $1 \leq p \leq \infty$; $j = 1, 2, 3, \ldots, n$ the variable i represents the number of alternatives, viz. $B_1, B_2, \ldots, B_m$. For alternative B_i, the assessed value of the jth criterion is designated by f_{ij} and denotes the number of criteria. The distance between the positive ideal solution and the alternative B_i has been represented by a measure L_{pi}. With this programming scheme, the VIKOR algorithm amplifies the group applicability so that the compromise solution can be acknowledged by an administrator. The MCDM problems can be solved under VIKOR as follows:

Step 1. Ascertain the positive and negative ideal solution values f_j^* and f_j^-, respectively, for all criterion ratings.

$$f_j^* = \left[\left(\max_i f_{ij} | j \in C_1 \right), \left(\min_i f_{ij} | j \in C_2 \right) \right], \tag{2}$$

$$f_j^- = \left[\left(\min_i f_{ij} | j \in C_1 \right), \left(\max_i f_{ij} | j \in C_2 \right) \right], \tag{3}$$

where $j = 1, 2, 3, \ldots, n$. C_1 indicates a beneficial criterion whereas C_2 represents a non-beneficial criterion.

Step 2. Ascertainment of S_i and R_i using the relations:

$$S_i = \sum_{j=1}^{n} w_j\left(f_j^* - f_{ij}\right)/\left(f_j^* - f_j^-\right), \tag{4}$$

$$R_i = \max\left[w_j\left(f_j^* - f_{ij}\right)/\left(f_j^* - f_j^-\right)\right]. \tag{5}$$

Where $i = 1, 2, 3, \ldots, m$, and S_i signifies the best favorable solution (optimal) of schemes comprehensive evaluation. R_i signifies the worst lower solution of schemes comprehensive evaluation. w_j denotes the fuzzy weighted average for each criterion which has been determined by the principle of the fuzzy approach discussed in Sect. 4.

Step 3. Determine the value of interest's ratio Q_i using the following formula,

$$Q_i = v\left(S_i - S^*\right)/\left(S^- - S^*\right) + (1 - v)\left(R_i - R^*\right)/\left(R^- - R^*\right) \tag{6}$$

Here, $S^* = \min S_i$, $S^- = \max S_i$, $R^* = \min R_i$, $R^- = \max R_i$ and v expresses a weight for scheme of maximum group applicability. Here, the assigned value, $v = 0.5$, whereas $1 - v$ describes the weight of individual regret.

Step 4. Then, the ranking of the preferences has to be done based on S, R,, and Q values in increasing order.
Step 5. The scheme with the smallest Q value in ranking has been deliberated as an optimal compromise solution only when the ensuing two criteria are fulfilled at the same time.

Criterion 1. The equation for acceptable advantage:

$$Q\left(B^{(2)}\right) - Q\left(B^{(1)}\right) \geq \frac{1}{(J-1)}. \tag{7}$$

Here, $B^{(2)}$ denotes the alternative with the second position of Q in ranking.

Criterion 2. Acceptable stability in the decision-making process: The alternative $B^{(1)}$ must also be the top-ranked by S or/and R with Q ranking in the rank table simultaneously. This compromise solution is stable within a decision-making process. It may fluctuate when v-value differs. When $v > 0.5$, the decision will be made as per the majority criteria. When $v \approx 0.5$, the decision will be made on the basis of overall as well as individual's evaluation. When $v < 0.5$, rejection of the process set is done. Here, v describes the weight for the scheme of majority criteria, i.e., maximum group applicability in the decision-making process.

Let us assume that the criterion 1 is not fulfilled, that means $Q\left(B^{(m)}\right) - Q\left(B^{(1)}\right) \langle \frac{1}{(J-1)}$. Now, preferences $B^{(1)}$,$B^{(2)} \ldots B^{(m)}$ are the same compromise solution. Now, $B^{(1)}$ will not persuade any comparative aids from others. But, the compromise (nearness) solution will be based on the equivalent preference when the maximum value comes into consideration. Now let us consider that criterion 2 has

not been fulfilled then decision making will not be stable and become inferior providing a relative aid to $B^{(1)}$. Hence, the identical compromise solution has been obtained from $B^{(1)}$ and $B^{(2)}$.

Step 6: Choose the best preference by assigning $Q\left(B^{(m)}\right)$ as an optimal solution among the smallest of Q_J.

2.2 Experimentation

Laser drilling on Ti6Al4V has been accomplished on ORION-3015 CO_2 laser cutting machine (LVD Company, Belgium) (Fig. 1) where nitrogen has been implemented as an associate gas to purge the excess material after cutting operation. The process of purging or flushing has been controlled by the Fanuc CNC controller. In order to regulate the setup of laser processing, CADMAN-L 3D software has been used. The workpiece is exposed to focus immobile laser beam through coaxial CO_2 gas jet. With an increase in temperature, the work material starts melting which leads to depression at center. The molten metal is removed by employing nitrogen gas with flushing pressure in the range of 34–40 bars. The laser process parameters and

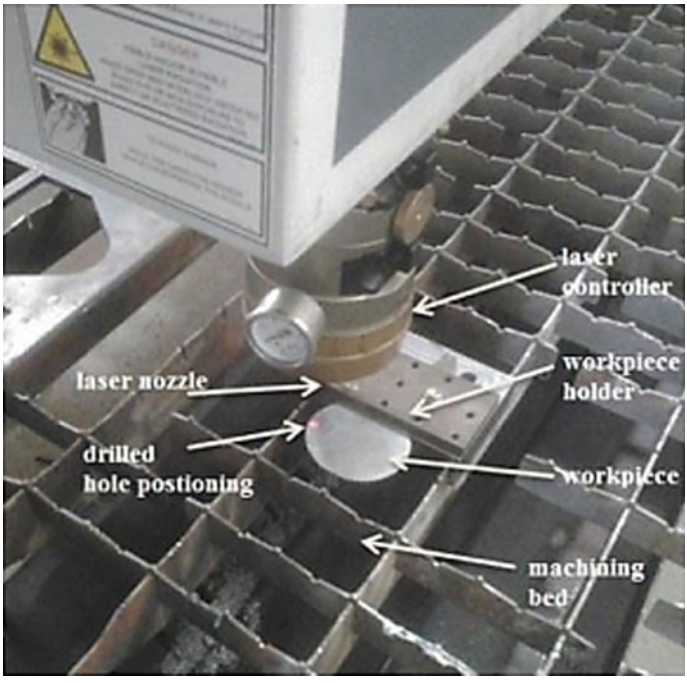

Fig. 1 Schematic setup of workpiece and laser setup

their levels are presented in Table 1. The measure the performance measures laser drilled samples are polished with 200–1400-micron grade sandpaper and etched. The etched samples are taken under optical microscope ranges from 5× to 100× (RADIAL INSTRUMENT with Samsung camera setup) to analyze the spatter area, circularity, and taper through image processing tool ImageJ software. The circularity can be calculated using the ratio of minimum ferret hole diameter (R_1) to maximum ferret hole diameter (R_2) [1, 12]. Ferret's diameter is a stretch among the two parallel tangents drawn at contrary corners of the hole (Fig. 2). The spatter area can be portrayed as an area where the material in the molten state has been placed. The

Table 1 Laser drilling parametric settings and S/N ratio of VIKOR index

S. No.	Process parameters			VIKOR index	S/N ratio
	Flushing pressure (Pa)	Laser power (W)	Pulse frequency (Hz)		
1	34	2000	1600	0.514	5.7807
2	34	2250	1800	0.511	5.8316
3	34	2500	2000	0.559	5.0518
4	37	2000	1800	0.762	2.3609
5	37	2250	2000	0.282	10.9950
6	**37**	**2500**	**1600**	**0.017**	**35.3910**
7	40	2000	2000	0.514	5.7807
8	40	2250	1600	0.999	0.0009
9	40	2500	1800	0.982	0.1578

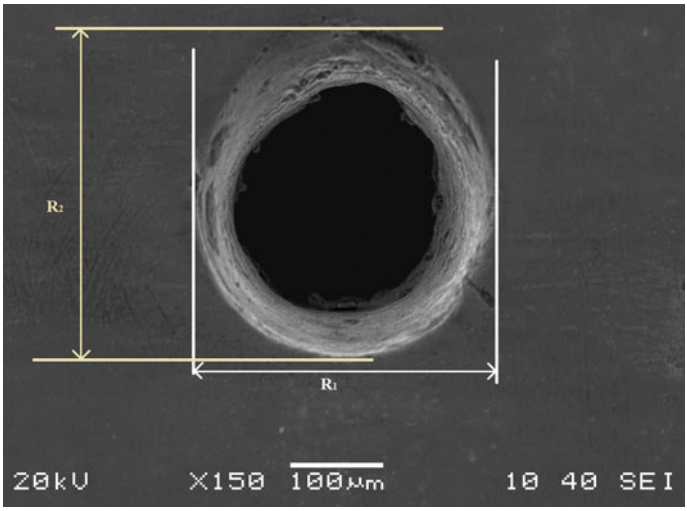

Fig. 2 Ferret diameter of laser holes

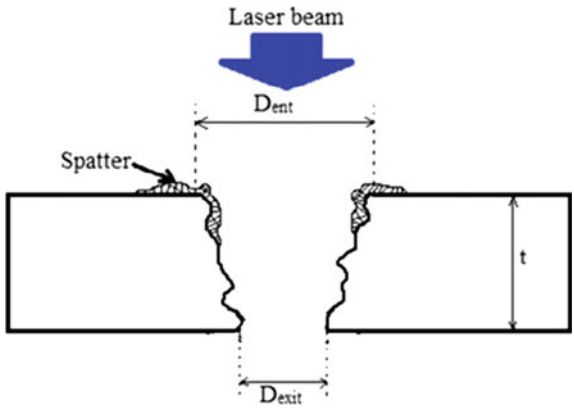

Fig. 3 Schematic representation of spatter and taper formation in laser-drilled samples

taper is calculated using Eq. 7 [1, 5]. Here, as shown in Fig. 3, it has been analyzed that the diameter at entry (D_{ent}) is constantly larger than the diameter at exit (D_{exit}).

$$\text{Taper} = \frac{D_{\text{entry}} - D_{\text{exit}}}{2t} \tag{8}$$

3 Results and Discussion

CO_2 laser drilling on Ti6Al4V has been performed accordingly (Table 1) and performance measures are calculated according to the aforementioned process. The performance measures calculated to define the quality of holes are circularity, taper, and spatter area. As the quality requirement of each performance measures is different, such circularity should be a maximum, and taper and spatter area should be minimum. To obtain optimum parametric settings and the desired requirements, multi-criteria decision-making (MCDM) technique known as VIKOR has been used. The VIKOR calculation has been performed according to Eqs. 1–6, respectively. Finally, the signal-to-noise (S/N) ratio has been performed for VIKOR index (Table 2). The S/N ratio plot obtained from the analysis suggests that optimum parametric setting is obtained for parametric setting $A_2B_3C_1$ (flushing pressure at 37 Pa, laser power at 2500 W and pulse frequency at 1600 Hz). As the obtained parametric settings are within the experimental setup, so there is no requirement of performing a confirmation test. The acquired parametric setting having lowest VIKOR index and S/N ratio values shows the adaptability of the proposed methodology (Fig. 4).

Table 2 ANOVA technique for VIKOR index

Factors	DF	Seq SS	Adj SS	Adj MS	*F*	% contribution
A	2	0.35161	0.35161	0.175805	1.28	44.5
B	2	0.01212	0.01212	0.006059	0.04	1.53
C	2	0.15168	0.15168	0.075842	0.55	19.20
Error	2	0.27471	0.27471	0.137355		
Total	8	0.79012				

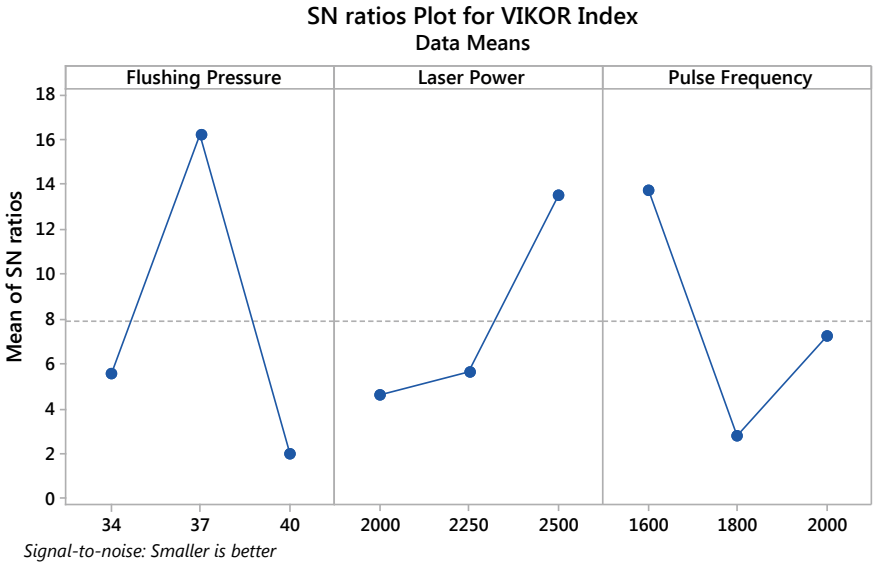

Fig. 4 S/N ratio plot for VIKOR index

4 Conclusion

In the present investigation, laser drilling on titanium alloy using continuous wave CO_2 laser has been used. The present study was performed to identify the optimum setting for the performance measures such as flushing pressure, laser power, and laser pulse frequency using multi-criteria decision-making (MCDM) method known as VIKOR. The multiple performance measures are converted to single MPCI value and converted to the S/N ratio. The obtained optimum parametric settings are available with the existing experimental setup having lowest VIKOR index value and highest S/N ratio values recommend the adaptability and robustness of the suggested methodology.

References

1. Chatterjee S, Mahapatra SS, Abhishek K (2016) Simulation and optimization of machining parameters in drilling of titanium alloys. Simul Model Prac Theo 62:31–48
2. Chatterjee S, Mahapatra SS, Sahu AK, Bhardwaj VK, Choubey A, Upadhyay BN, Bindra KS (2017) Experimental and parametric evaluation of quality characteristics in Nd: YAG laser micro-drilling of Ti6Al4V and AISI 316. In: ASME 2017 Gas Turbine India conference. ASME, pp V002T10A006-V002T10A006
3. Shelton JA, Shin YC (2010) Comparative evaluation of laser-assisted micro-milling for AISI 316, AISI 422, TI-6AL-4V and Inconel 718 in a side-cutting configuration. J Micro- Mech Micro-Eng. https://doi.org/10.1088/0960-1317/20/7/075012
4. Yan Y, Ji L, Bao Y, Jiang Y (2012) An experimental and numerical study on laser percussion drilling of thick-section alumina. J Mater Process Technol 212(6):1257–1270
5. Chatterjee S, Mahapatra SS, Mondal A, Abhishek K (2018) An experimental study on drilling of titanium alloy using CO_2 laser. Sādhanā 43(8):131. https://doi.org/10.1007/s12046-018-0903-1
6. Ghoreishi M (2006) Statistical analysis of repeatability in laser percussion drilling. Int J Adv Manuf Technol 29:70–78
7. Biswas R, Kuar AS, Biswas SK, Mitra S (2010) Characterization of hole circularity in pulsed Nd: YAG laser micro-drilling of TiN-Al_2O_3 composites. Int J Adv Manuf Tech 51(9–12):983–994
8. Ghoreishi M, Low DKY, Li L (2002) Comparative statistical analysis of hole taper and circularity in laser percussion drilling. Int J Mach Tools Manuf 42:985–995
9. Sahu AK, Mahapatra SS, Chatterjee S (2018) Optimization of electro-discharge coating process using harmony search. Mater Today Proc 5(5):12673–12680
10. Wu M, Liu Z (2011) The supplier selection application based on two methods: VIKOR algorithm with entropy method and Fuzzy TOPSIS with vague sets method. Int J Manag Sci Eng Manag 6(2):109–115
11. Datta S, Samantra C, Mahapatra SS, Banerjee S, Bandyopadhyay A (2012) Green supplier evaluation and selection using VIKOR method embedded in fuzzy expert system with interval-valued fuzzy numbers. Int. J. Procurement Manage 5(5):647–678
12. Bharatish A, Murthy HN, Anand B, Madhusoodana CD, Praveena GS, Krishna M (2013) Characterization of hole circularity and heat affected zone in pulsed CO_2 laser drilling of alumina ceramics. Opt Laser Tech 53:22–32

Experimental Investigation on Surface Morphology of Micro-EDMed Ti-6Al-4 V Alloy

Ramver, Vineet Kumar Yadav, Pradeep Kumar and Akshay Dvivedi

Abstract Micro-machining of titanium alloys by conventional machining processes have limitations, for instance, high tool wear, chatter, vibrations, etc. To overcome these limitations of conventional machining processes, micro-EDM is suitable to machine titanium alloys owing to its ability to machine hard materials. In the present work, micro-EDM was used to drill micro-holes in Ti-6Al-4 V alloy using EDM oil as a dielectric medium. The effect of applied voltage on the morphology of machined surface was investigated. Microscopic characterization of machined surface showed that the surface obtained at higher applied voltage embraces relatively higher non-conformities such as micropore, debris deposition, porosity, uneven surface, etc., as compared to those at lower applied voltage.

1 Introduction

In this perpetually evolving world, the demand for miniaturized parts and products has been burgeoning in various industries, like automotive, biomedical, avionics, optics, electronics, etc. These miniaturized components have features with sizes up to a few hundred micrometers. The conventional machining methods like micro-turning, milling, etc., are now applied to produce such features; however, the direct contact between the tool and work surfaces during machining engenders difficulties [1, 2]. To overcome these drawbacks, advanced machining processes especially micro-electrical discharge machining (micro-EDM) has been used to fabricate such features on difficult to machine materials such as Ti-6Al-4 V alloys. Micro-EDM process is possessing the ability to fabricate complex 3D features such as micro-holes, micro-channels, and micro-molds on any electrically conductive work material irre-

Ramver · V. K. Yadav (✉) · P. Kumar · A. Dvivedi
Mechanical and Industrial Engineering Department, Indian Institute of Technology (IIT), Roorkee 247667, India
e-mail: vineet437@gmail.com

Ramver
e-mail: ramver.pme@gmail.com

A. K. Parwani and PL. Ramkumar (eds.), *Recent Advances in Mechanical Infrastructure*, Lecture Notes in Intelligent Transportation and Infrastructure,
https://doi.org/10.1007/978-981-32-9971-9_8

spective of their hardness [3–5]. The distinguished benefit of choosing micro-EDM over the conventional processes is that micro-EDM is a "non-contact type" process. Thus, the inaccuracies caused due to the direct contact such as micro-tool deformation, chatter, residual stresses, and vibration problem are almost negligible [6].

The basic micro-EDM configuration consists of three sub-systems: tool and work electrodes; dielectric medium, such as hydrocarbon oil, deionized water, and mist; and power supply unit [7, 8]. The distinct characteristics of micro-EDM that from EDM are the size of tool electrode (generally less than 1 mm) and the lower spark discharge energy [9]. The tool electrode and work material are immersed in a dielectric medium and are separated by a narrow distance, in the range of a few to tens of micrometers, called as inter-electrode gap (IEG). Both the electrodes are connected to a voltage source, known as power supply unit (PSU). The PSU is used to polarize or ionize the dielectric medium packed in the IEG, which subsequently resulted in electrical breakdown of the dielectric medium in the form of a plasma channel in the IEG. In general, the material removal phenomenon is accomplished by melting and vaporization of work material. In micro-EDM, due to smaller IEG, the accuracy of the machined part is quite high. However, issues related to the surface quality of the micro-EDMed part are still a challenging task that restricts the extensive application of micro-EDM [10]. For the process design and control, understanding the effect of process parameters on the surface quality is an important aspect. In this study, micro-EDM experiments were carried out to machine Ti-6Al-4 V alloy using EDM oil as a dielectric medium. Also, the surface morphology of micro-EDMed surface was analyzed and discussed. This experimental study also contributes in advancing the basic understanding of the mechanisms of the micro-EDM process.

2 Materials and Method

The present experimental study was performed on a micro-EDM machine. The schematic of the experimental facility, which consists of power supply unit, dielectric unit, work table with three-axis positioning system, and z-axis drive, is shown in Fig. 1. In this experimental investigation, Ti-6Al-4 V alloy and copper were selected as work and tool materials, respectively. Ti-6Al-4 V alloy is mostly used in aerospace, biomedical, and petro-chemical industries. EDM oil was used as dielectric medium in this investigation.

The experiments were performed to analyze the effect of voltage. Table 1 summarizes the experimental conditions.

3 Results and Discussions

In micro-EDM process, spark discharge energy has a strong influence over the response parameters such as morphology of machined surface, MRR, and machining

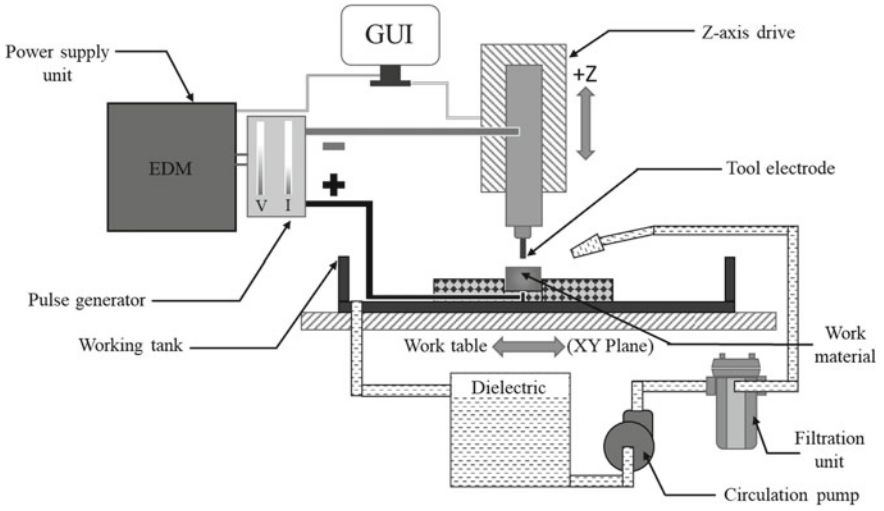

Fig. 1 Schematic representation of experimental facility

Table 1 Parametric settings used in the experiments

Parameters	Descriptions
Tool electrode	Copper, Ø700 μm (hollow)
Polarity	Work, +
Sensitivity	90%
Feed rate	5 μm/s
Circuit type	RC type
Working medium	EDM oil
Voltage	80, 140 V
Capacitance	10,000 pF

accuracy. The individual spark discharge energy can be governed by varying applied voltage across the IEG. Lower applied voltage across the IEG may result in lesser polarization of the dielectric medium, which implied that lesser amount of charge flow through the IEG. Subsequently, it resulted in lean plasma channel having smaller amount of discharge (thermal) energy available for material removal. Thus, lower MRR may be an issue; however, lower discharge energy provided better control over the machining accuracy. On the contrary, higher applied voltage across the IEG may result in greater polarization of the dielectric medium and accordingly higher amount of charge flow through the IEG [11]. As a consequence, it formed an intense plasma channel having a higher amount of discharge energy available for the material removal phenomenon. Thereby, higher MRR can be achieved; however, higher discharge energy may cause higher tool wear rate, ultimately which may relieve the control over machining accuracy. Therefore, the selection of suitable level of applied

voltage in μ-EDM is a crucial choice and which depends upon the intended use of the machined component. For instances, in some applications, the machining accuracy or the quality of machined surface is of prime importance, while in others, the MRR can dictate economy of machining operations.

The effect of discharge energy on the morphology of machined surface at low as well as at high voltage was analyzed in the subsequent subsections.

3.1 Effect of Discharge Energy on the Micro-EDMed Surface at Lower Voltage

The morphology of micro-EDMed Ti-6Al-4 V alloy surfaces was examined using FE-SEM. The FE-SEM micrographs illustrating various features on the micro-EDMed surface at lower voltage using EDM oil as dielectric medium are depicted in Fig. 2a–c. As it is a well-known fact that material removal in micro-EDM process takes place via multitude of small discrete spark discharges. These randomly occurring small spark discharges craft a typical micro-EDMed surface covered with overlapped micro-craters [12]. Micro-EDM at lower voltage generated a relatively smooth machined surface and can be observed from Fig. 2c. This relatively smooth micro-EDMed surface was an outcome of shallower micro-craters. This type of micro-craters was generated, as only a smaller fraction of the work material was removed, because individual sparks were having smaller amount of discharge energy. As discussed in the preceding section, micro-EDM at lower voltage condition resulted in smaller discharge energy. Therefore, relatively smooth and shallow micro-craters were observed, as endorsed by Fig. 2c.

The presence of micropores can be confirmed from Fig. 2c. Micropores belong to the surface defects category related to the expulsion of entrapped gases during solidification of molten pool. The shape of micropores was resembling to that of narrow wells having wider opening toward machined surface.

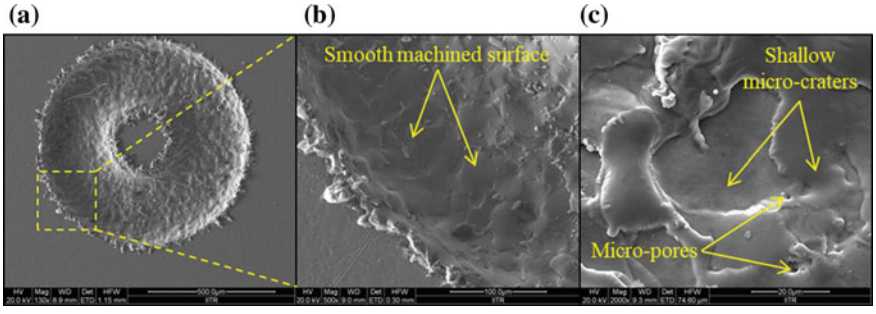

Fig. 2 Morphology of machined surface at lower voltage using EDM oil as dielectric medium

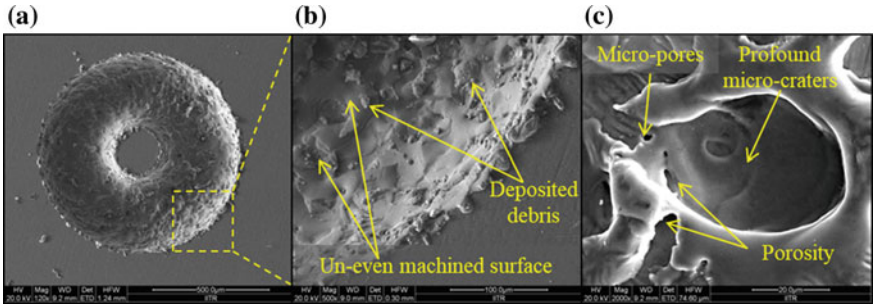

Fig. 3 Morphology of machined surface at higher voltage using EDM oil as dielectric medium

3.2 Effect of Discharge Energy on the Micro-EDMed Surface at Higher Voltage

Figure 3a–c depicts morphology of FE-SEM micrographs of machined surfaces at higher voltage using EDM oil as dielectric medium. It can be inferred from Fig. 3 that at higher applied voltage, irregular machined surface was obtained. It was having relatively large and profound micro-craters, more deposited debris, uneven surface, etc. These characteristics may be attributed to the fact that increased applied voltage resulted in higher discharge energy. As mentioned earlier, higher discharge energy can melt more work material in the molten pool. Consequently, it can form larger and deeper micro-craters in each sparks. Due to excessive availability of molten material, the flushing of machining zone was inadequate. Thereby, the molten material which was not flushed away effectively from the IEG may attach to machined surface in the form of debris [13]. As it can be seen from Fig. 3b that at higher voltage, micro-EDMed surface is having more deposited debris. It is a well-known fact that the discharge energy and the temperature of molten pool follow same trend. Accordingly, higher applied voltage condition produced higher temperature of molten pool. Subsequently, the molten pool was having higher affinity to absorb the dissolved gases from the surrounding dielectric medium. As the spark discharge extinguished, cooling of molten pool propelled the expulsion of absorbed gases from molten pool. Therefore, expulsion of absorbed gases during solidification formed micropores. However, a small fraction of absorbed gases gets entrapped due to sudden cooling and eventually resulted in porosity in the re-solidified material.

4 Conclusions

In order to analyze the surface morphology of micro-EDMed Ti-6Al-4 V alloy, experiments were performed at low and high applied voltages. The machined surface was characterized by using FE-SEM micrographs. From the above investiga-

tion, it can be concluded that the spark discharge energy has a strong influence on the surface morphology of micro-EDMed Ti-6Al-4 V alloy using EDM oil as dielectric material. The experimental results revealed that machining of Ti-6Al-4 V alloy at lower applied voltage produced relatively lesser debris deposition, micropores, porosity, etc., as compared to that of higher applied voltage. The inferences from this investigation contribute to advancing the basic understanding of process mechanism of micro-EDM.

References

1. Singh T, Dvivedi A (2018) On pressurized feeding approach for effective control on working gap in ECDM. Mater Manuf Process. https://doi.org/10.1080/10426914.2017.1339319
2. Singh T, Dvivedi A (2018) On performance evaluation of textured tools during microchanneling with ECDM. J Manuf Process https://doi.org/10.1016/j.jmapro.2018.03.033
3. Van Ossenbruggen C (1969) Micro-spark erosion. Philips Tech Tijdschr 20:200–213
4. Rajurkar KP, Yu ZY (2000) 3D Micro-EDM using CAD/CAM. CIRP Ann Manuf Technol 49(1):127–130. https://doi.org/10.1016/S0007-8506(07)62911-4
5. Masuzawa T (2000) State of the art of micromachining. CIRP Ann Technol 49(1):473–488
6. Tsai YY, Masuzawa T (2004) An index to evaluate the wear resistance of the electrode in micro-EDM. J Mater Process Technol 149(1–3):304–309. https://doi.org/10.1016/j.jmatprotec.2004.02.043
7. Yadav VK, Kumar P, Dvivedi A (2017) Investigations on rotary tool near-dry electric discharge machining. In: Applications of process engineering principles in materials processing, energy and environmental technologies. Springer, Cham, pp 327–334. https://doi.org/10.1007/978-3-319-51091-0_31
8. Yadav VK, Kumar P, Dvivedi A (2017) Parametric investigations on rotary tool near-dry electric discharge machining. 10th International Conference Precision, Meso, Micro Nano Eng. (COPEN 10), IIT Madras, Dec 06–09, Chennai, pp 575–578
9. Uhlmann E, Roehner M (2008) Investigations on reduction of tool electrode wear in micro-EDM using novel electrode materials. CIRP J Manuf Sci Technol 1(2):92–96. https://doi.org/10.1016/j.cirpj.2008.09.011
10. Urso GD, Merla C (2014) Workpiece and electrode influence on micro-EDM drilling performance. Precis Eng 38(4):903–914. https://doi.org/10.1016/j.precisioneng.2014.05.007
11. Liu H, Wang Z, Chi G, Wang Y (2018) Influence of open-circuit voltage on micro electrical discharge machining of Ni-Al2O3 functionally graded materials. Procedia CIRP 68:5–10. https://doi.org/10.1016/j.procir.2017.12.013
12. Ramver, Dvivedi A, Kumar P (2019) On improvement in surface integrity of μ-EDMed Ti–6Al–4 V alloy by μ-ECM process. In: The Minerals, Metals & Materials Series (eds) TMS 2019 148th annual meeting & exhibition supplemental proceedings. The Minerals, Metals & Materials Series. (2019), Springer, Cham. https://doi.org/10.1007/978-3-030-05861-6_73
13. Yadav VK, Kumar P, Dvivedi A (2019) Effect of tool rotation in near-dry EDM process on machining characteristics of HSS. Mater Manuf Process 34(7):779–790. https://doi.org/10.1080/10426914.2019.1605171

Multi-objective Optimization and Experimental Investigation of CNC Oxy-Fuel Gas Cutting Parameters Using Taguchi Coupled Data Envelopment Analysis

Dilip Kumar Bagal, Ajit Kumar Pattanaik, Dulu Patnaik, Abhishek Barua, Siddharth Jeet and Surya Narayan Panda

Abstract An optimized design of the various machining parameters for the CNC oxy-fuel gas cutting process on SAE/AISI–4140 steel has been carried out by using DEA-based Taguchi methodology. SAE/AISI–4140 steel or Chromoly steel has high fatigue strength, impact resistance, durability, and noble ductile properties. The main output responses are bevel angle, dross breadth, and dross height, and the input parameters are nozzle speed, oxy-fuel speed, and torch height. Nine experiments were piloted based on a L9 orthogonal array of Taguchi design. The relative efficiency was determined from data envelopment analysis (DEA) method with Lingo version 14 software package. These scores were significantly affected by the machining parameters of oxy-fuel gas cutting process directly.

Keywords CNC oxy-fuel gas cutting · SAE/AISI–4140 steel · DEA · Taguchi methodology · Relative efficiency

1 Introduction

Cutting of thick plates is the challenging task in industrial practice. CNC profile cutting process has got an advancement up to the highly sophisticated and automatic operation to cut thick plates. That may be either gas, i.e., oxy-fuel cutting or plasma cutting machine. There is the requirement of a variety of shapes or profiles to be cut from varying thickness of plates from 1 to 250 mm in industrial practice from a variety of materials of plates like mild steel, stainless steel, etc. Such cut shaped

D. K. Bagal (✉) · A. K. Pattanaik · D. Patnaik
Government College of Engineering, Kalahandi, Bhawanipatna, Odisha, India
e-mail: dilipbagal90@gmail.com

A. Barua · S. Jeet
Centre for Advanced Post Graduate Studies, BPUT, Rourkela, Odisha, India

S. N. Panda
Birsa Institute of Technology Sindri, Dhanbad, Jharkhand, India

A. K. Parwani and PL. Ramkumar (eds.), *Recent Advances in Mechanical Infrastructure*, Lecture Notes in Intelligent Transportation and Infrastructure,
https://doi.org/10.1007/978-981-32-9971-9_9

profiles are used in manufacturing and fabrication work [1]. In oxy-flame cutting, a preheated flame is engaged to the edge, corner of the extensive portion of the specimen to be cut [2–6]. The molten metal is cleared away by the streaming oxygen and the combusted iron around as indicated by:

$$\text{Fe(hot solid)} + \frac{1}{2}\text{O}_2\text{(gaseous state)} = \text{FeO(liquid state)},\ \Delta H^0_{298} = -63.8\,\text{kcal/mole} \tag{1}$$

In the event that additional stoichiometric amounts of oxygen supply to the iron specimen being cut, there is the probability for FeO to react and coagulate to advanced forms Fe_3O_4 and Fe_2O_3 oxides according to [7–10]:

$$\text{FeO} + \frac{1}{6}\text{O}_2 = \frac{1}{3}\text{Fe}_3\text{O}_4,\ \Delta H^0_{298} = -25.5\,\text{kcal/mole(FeO further oxidized)} \tag{2}$$

$$\text{FeO} + \frac{1}{4}\text{O}_2 = \frac{1}{2}\text{Fe}_3\text{O}_4,\ \Delta H^0_{298} = -34.6\,\text{kcal/mole(FeO further oxidized)} \tag{3}$$

2 Experimental Setup and Methodology

The entire experiment process is investigated by the CNC profile cutting machine titled as LINDE controller profile cutter manufactured by SIEMENS Company. The specimen of AISI-4140 Chromoly steel is taken with thickness of 85 mm and the experimental setup of oxy-fuel gas cutting process procedure is shown in Fig. 1. The standards of input parameters are given in Table 1.

Fig. 1 Experimental setup and workpiece (Sample number 1)

Table 1 Input parameters

Process parameters	Units	Code	L(1)	L(2)	L(3)
Nozzle speed	m/min	A	1	1.5	2
Torch height	mm	B	2.0	2.5	3.0
Oxy-fuel speed	mm/min	C	450	550	650

2.1 Data Envelopment Analysis Model (DEA)

It is a linear programming built technique for assessing the comparative efficiency of a usual of decision-making units (DMUs). As the Taguchi optimization technique has only proficiency to optimize the single-objective problem, thus the data envelopment analysis model is being currently employed for optimization of multi-objective problem. The following are the steps of DEA approach:

Step 1: The output responses are normalized first. The given dross height response is normalized by the following equation:

$$Z_{ij} = \frac{X_{ij}}{\max X_{ij}} \tag{4}$$

for $i = 1, 2\ldots, m$ and $j = 1, 2\ldots, n$.

For the bevel angle and dross breadth parameters, the normalization is done as per the following equation:

$$Z_{ij} = \frac{\min X_{ij}}{X_{ij}} \tag{5}$$

for $i = 1, 2\ldots, m$ and $j = 1, 2\ldots, n$, where X_{ij} is the mean for the ith response in the jth experiment.

Step 2: Relative efficiency for each experiment was calculated by using Lingo 14 software package. The following equation is used for the computation of the relative efficiency:

$$\max E_{kk} = \sum_{y}^{k} O_{ky} V_{ky} \tag{6}$$

Such that,

$$\sum I_{kx} U_{kx} = 1 \tag{7}$$

$E_{ks} \leq 1$ For all the design such that,

$$U_{kx}, V_{ky} > 0 \tag{8}$$

Step 3: Calculation for S/N ratio. Applying Taguchi method to obtain relative efficiency value according to the larger-the-better criterion by the help of Minitab 16 software as per the following formula:

$$\eta = -10 \log_{10}\left(\frac{1}{n}\sum_{i=1}^{n}\frac{1}{y_i^2}\right) \tag{9}$$

3 Result and Discussion

Experimental layout with output data shown in Table 2 has been analyzed by aforementioned procedure. Data have been normalized by means of Eqs. (4) and (5) as per objective criteria. Normalized data of bevel angle and dross breadth have been taken as input factor, while normalized data of dross height have been considered as output factor for determining the relative efficiency (refer Table 3). Finally, Taguchi methodology has been applied to relative efficiency for evaluating optimal parametric setting. Nozzle speed, torch height, and oxy-fuel speed at their 3rd, 1st, and 1st level, respectively, are found as more favorable machining condition (refer Table 4). Each normalized data are fed into the "Lingo 14" software for determining the relative efficiency (refer Fig. 3). Figure 2 gives the percentage contribution chart in 3D pie plot. Table 6 shows the factor ranking in accordance with their degree of significance.

Table 2 Taguchi design of L9 with input and output values

S. No.	Nozzle speed (mm/s)	Torch height (mm)	Oxy-fuel speed (mm/min)	Bevel angle (°)	Dross width (mm)	Dross height (mm)
1	1	2.0	450	3	4.53	6.83
2	1	2.5	550	4	6.92	3.58
3	1	3.0	650	4	3.86	6.34
4	1.5	2.0	550	2	4.65	7.56
5	1.5	2.5	650	6	5.61	5.56
6	1.5	3.0	450	5	7.83	4.47
7	2	2.0	650	3	6.79	5.48
8	2	2.5	450	6	5.56	7.64
9	2	3.0	550	4	4.95	5.68

Table 3 Normalized values, computed relative efficiency, and S/N ratio of responses

S. No.	Bevel angle	Dross width	Dross height	Relative efficiency	S/N Ratio
1	0.66667	0.85210	0.89398	0.72836	−2.75306
2	0.50000	0.55780	0.46859	0.58321	−4.68352
3	0.50000	1.00000	0.82984	0.57611	−4.78992
4	1.00000	0.83011	0.98953	0.82757	−1.64394
5	0.33333	0.68806	0.72775	0.73429	−2.68269
6	0.40000	0.49298	0.58508	0.82394	−1.68209
7	0.66667	0.56848	0.71728	0.87596	−1.15034
8	0.33333	0.69424	1.00000	1.00000	0.00000
9	0.50000	0.77980	0.74346	0.66189	−3.58432

Table 4 Model coefficients for S/N ratios

Term	Coef.	SE Coef.	*T*	*P*
Constant	−2.55221	0.2500	−10.210	0.009
Nozzle s 1.0	−1.52329	0.3535	−4.309	0.050
Nozzle s 1.5	0.54930	0.3535	1.554	0.260
Torch he 2.0	0.70310	0.3535	1.989	0.185
Torch he 2.5	0.09681	0.3535	0.274	0.810
Oxy-fuel 450	1.07382	0.3535	3.038	0.093
Oxy-fuel 550	−0.75172	0.3535	−2.127	0.167
Constant	−2.55221	0.2500	−10.210	0.009

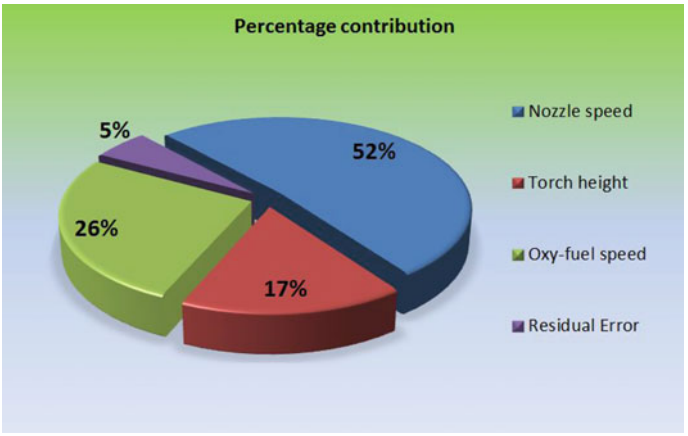

Fig. 2 Percentage contribution of machining parameters

Table 5 ANOVA for relative efficiency

Factors	DOF	Adj. SS	Adj. MS	*F*-test	Percentage contribution
Nozzle speed	2	10.712	5.3562	9.53	51.66
Torch height	2	3.431	1.7153	3.05	16.54
Oxy-fuel speed	2	5.466	2.7329	4.86	26.36
Residual Error	2	1.125	0.5623		5.42
Total	8	20.734			100

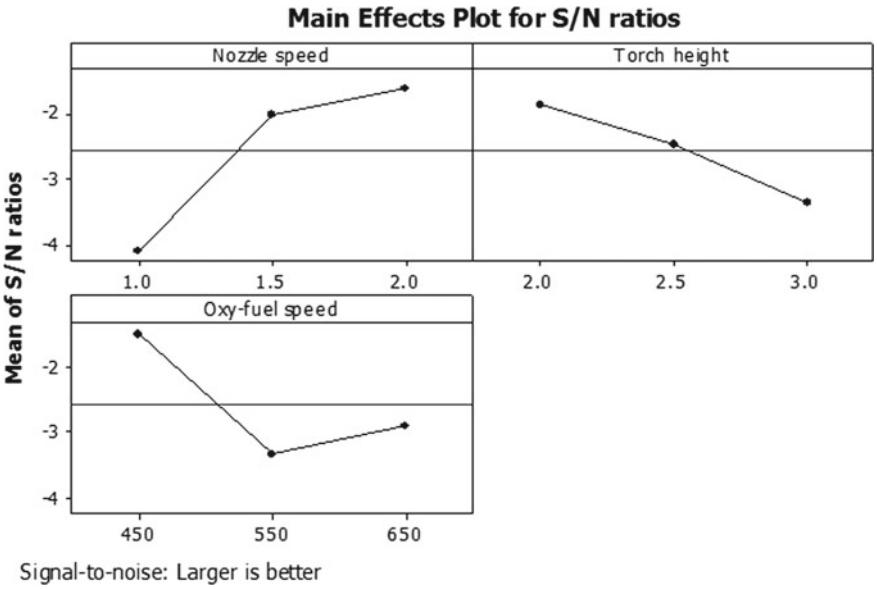

Fig. 3 Main effect plot of relative efficiency

The ANOVA analysis of input parameters of the cutting process is shown in Table 5. It shows that nozzle speed has the highest contribution of 51.66% which affects the cutting followed by oxy-fuel speed and torch height.

$$S = 0.7499,\ R{-}sq = 94.6\%,\ R{-}sq\ (\text{adj}) = 78.3\%$$

3.1 Confirmatory Test

Confirmation testing is necessary to validate the model. Once the optimal combination of oxy-fuel gas cutting constraints is carefully chosen to foretell and confirm the

Table 6 Response table for S/N ratios

0	Nozzle speed	Torch height	Oxy-fuel speed
1	−4.076	−1.849	−1.478
2	−2.003	−2.455	−3.304
3	−1.578	−3.352	−2.874
Delta	2.497	1.503	1.826
Rank	1	3	2

Table 7 Confirmatory test results

No. of experiment	Nozzle speed (m/min)	Torch height (mm)	Oxy-fuel speed (mm/min)	Relative efficiency
1	2	2	450	0.7346
2	2	2	450	0.7189
3	2	2	450	0.7197

Table 8 Analysis of a confirmatory test

Performance characteristics	Optimal setting level	Predicted optimal values	95% confidence interval	Actual confirmation experimental value
Relative efficiency	A3-B1-C1	0.19942	$-0.20127 < \eta_{obs} < 3.60011$	−2.80043

expected response through the confirmation experiment. However, there is no need to run the confirmation test if the optimal oxy-fuel gas cutting parameter combination is already included in the OA. It can be found that the optimal gas cutting levels combination (A3B1C1) was not included in the experiment matrix (Table 2). The predicted S/N ratio ($\hat{\eta}_{opt}$) can be calculated as [11]:

$$\hat{\eta}_{opt} = \bar{\eta} + \sum_{i=1}^{p} \left(\eta_{i,opt}^{-} - \eta^{-} \right) \tag{11}$$

where $\eta_{i,opt}^{-}$ is the mean S/N ratio for ith parameter at the optimal level, p is the number of parameters. In order to statistically judge the intimacy of the projected ($\eta_{i,opt}^{-}$) and experiential value of S/N ratio (η_{obs}), the confidence intervals (CIs) were determined. The CI is given by:

$$CI = \sqrt{F_{\alpha;1,\vartheta_e} V_{error} \left[\left(\frac{1}{n_{eff}} \right) + \left(\frac{1}{r} \right) \right]} \tag{12}$$

where $F_{\alpha;1,\vartheta_e} = 18.51$ is the F value from statistic table at a 95% confidence level, $\vartheta_e = 2$ is the degrees of freedom for the error, Verror $= 0.5623$ is the mean square of error, $r = 3$ is the validation test trial number, and n_{eff} is defined as:

$$n_{\text{eff}} = \frac{N}{1 + \vartheta_{\text{total}}} \tag{13}$$

where $N = 9$ is the total number of experiments and $\vartheta_{\text{total}} = 6$ is the total degrees of freedom of all parameters. By substituting these values in Eq. (13), n_{eff} value obtained as 1.2857. Similarly, CI is obtained as 3.40069 by using Eq. (12). If the difference between $\hat{\eta}_{\text{opt}}$ and η_{obs} is within the CI value, then the optimum oxy-fuel cutting parameter level combinations are valid. From Table 7, it can be observed that the calculated values of the prediction errors are within the 95% confidence interval, and Table 8 shows the computed S/N ratio of predicted optimum setting and observed confirmation test value.

4 Conclusion

The current investigation has done by applying DEA based on Taguchi's optimization technique for determining optimal machining conditions in the CNC oxy-fuel gas cutting processes on SAE/AISI–4140 Chromoly steel. It was found that

- Nozzle speed is the most influencing parameter in the CNC oxy-fuel gas cutting process as its contribution to the experiment is 51.6639% which is the maximum than the other two parameters.
- The preeminent possible optimum settings of this process are at 2 m/min of nozzle speed, 2.0 mm of torch height, and 450 mm/min of oxy-fuel speed, respectively.
- Confirmatory test results are found incredibly good agreement with those predicted.

Acknowledgements This research work is jointly supported by National Institute of Technology, Rourkela, India and Government College of Engineering Kalahandi, Bhawanipatna, Odisha, India.

References

1. Vora FR, Trivedi JH (2011) CNC profile gas cutting machine—application with nesting software and computer aided programming mechanism. In: National conference on recent trends in engineering & technology, pp 1–4
2. Zhou B, Liu Y-J, Tan S-K (2013) Efficient simulation of oxygen cutting using a composite heat source model. Int J Heat Mass Transf 57:304–311
3. Chen S-L (1999) The effects of high-pressure assistant-gas flow on high-power CO_2 laser cutting. J Mater Process Technol 88:57–66

4. Chen S-L (1998) The effects of gas composition on the CO_2 laser cutting of mild steel. J Mater Process Technol 73:147–159
5. Maity KP, Bagal DK (2015) Effect of process parameters on cut quality of stainless steel of plasma arc cutting using hybrid approach. Int J Adv Manuf Technol 78:161–175
6. Kumar A, Sahu J, Datta S, Mahapatra SS (2012) DEA based taguchi approach for multi-objective optimization in machining polymers: a case study
7. Madić MJ, Radovanović MR (2013) Identification of the robust conditions for minimization of the HAZ and burr in CO_2 laser cutting. FME Trans 41:130–137
8. Ahmadi B, Torkamany M, Jaleh B, Sabaghzadeh J (2009) Theoretical comparison of oxygen assisted cutting by CO_2 and Yb: YAG fiber lasers. Chin J Phys 47:465–475
9. Charnes A, Cooper WW, Rhodes E (1978) Measuring the efficiency of decision making units. Eur J Oper Res 2:429–444
10. Adler N, Friedman L, Sinuany-Stern Z (2002) Review of ranking methods in the data envelopment analysis context. Eur J Oper Res 140:249–265
11. Lanyi M (2000) Discussion on steel burning in oxygen (from a steelmaking metallurgist's perspective). In: Ninth international symposium on flammability and sensitivity of materials in oxygen-enriched atmospheres, pp 163–178

Utility Function Approach Integrated with Fuzzy for Optimization in Milling Glass Fiber Reinforced Epoxy Composites

Chirag Bagada, Himanshu Damor, Vishalkumar Prajapati and Kumar Abhishek

Abstract The glass fiber reinforced polymer (GFRP) composites are popular nowadays due to their widespread applications in aerospace and automobile industries. This is mainly because of their lightweight and high strength properties. But these materials need to be machined for any assembly or application. Therefore, it becomes crucial for manufacturers to maintain the required product quality without affecting the rate of productivity. In order to get effective machining, it is necessary to find favorable machining combinations. Hence, in this paper, the utility function based on fuzzy logic has been adapted with the purpose of assessing the favorable machining combination amid the end milling of GFRP composites.

Keywords GFRP · Milling · Utility function · Fuzzy rule · Optimization

1 Introduction

Nowadays, GFRP is widely utilized in several industrial fields, particularly in aviation and self-propelled vehicle industries because of their outstanding physical and mechanical properties, namely lightweight, significant stiffness, and superior strength-to-weight ratio [1]. Therefore, understanding the machinability aspects of such materials becomes essential. However, the machining of these materials is formidable due to their anisotropic nature. The foremost hindrances amid the machining of these materials comprised of fiber pull-out, burring, surface finish, and delamination. Hence, various works have been carried out to enhance the applicability of these composites.

Kavada et al. (2014) performed drilling operation on GFRP composites and assessed the impact of machining parameters, namely feed rate, tool material, and cutting speed on the delamination damage of the material. Sivasankaran et al. [2] executed CNC turning using a polycrystalline diamond (PCD) tool on the pipes made up

C. Bagada · H. Damor · V. Prajapati · K. Abhishek (✉)
Department of Mechanical Engineering, Institute of Infrastructure, Technology, Research and Management, Ahmedabad 380026, India
e-mail: krabhishek1987@gmail.com

A. K. Parwani and PL. Ramkumar (eds.), *Recent Advances in Mechanical Infrastructure*, Lecture Notes in Intelligent Transportation and Infrastructure,
https://doi.org/10.1007/978-981-32-9971-9_10

of GFRP composites and studied the importance of machining process parameters, namely cutting speed (N), feed rate (f), and depth of cut (d) on the surface roughness. Sahu et al. [3] applied full factorial design integrated CNSGA-II algorithm to assess the way of process parameters, viz. feed rate, speed, and drill diameter on the thrust and the torque in GFRP micro-drilling process. Vankanti and Ganta [4] scrutinized the influence of machining parameters, viz. cutting edge, feed, chisel edge width and point angle on the thrust force, and the torque GFRP composites drilling by means of ANOVA method. Result concluded that feed is a more influential factor to thrust force, whereas cutting speed affects torque more.

Parida and Bhuyan [5] adopted response surface methodology in the view of establishing a mathematical model for surface roughness and inspected the outcomes of machining variables amid drilling operation of GFRP composite. The machining variables are spindle speed (N), feed (f), and diameter of the drill bit (d) have been taken into consideration. Chaudhari et al. [7] used adoptive neuro-fuzzy interface system (ANFIS) to predict delamination factor in the drilling of GFRP composites. It has been noticed that root-mean-square error for delamination factor at entry and exit is 1.4732% and 2.9277%, respectively. Chavana et al. [6] discovered the consequences of filler material and process parameters like feed, spindle speed, diameter of the drill bit on the thrust force, and torque during GFRP composites drilling. The study concluded that the parameters, namely the thrust force and the torque, have been mainly affected by feed with a share of 97.72% and 82.70%, respectively. Akil et al. [8] adopted Taguchi-grey relational analysis methodology and optimized a number of drilling parameters for GFRP composites with multiple objectives of delamination factor and surface roughness. Shunmugesh [9] utilized the grey-fuzzy logic method and optimized the drilling process parameters of GFRP composites. Taguchi orthogonal array (L27) and ANOVA have been used for experimentation and analyzation, respectively, and discovered that the feed rate influences the delamination factor and surface roughness of the material.

Aforementioned literature highlights the factor affecting the performance amid the machining operation of GFRP composite materials. Nevertheless, it was noted that less effort has been emphasized to explore the machinability aspects of aforesaid composites during the milling operation. Therefore, the present study adopts the concept of utility function integrated with the fuzzy approach with the purpose of assessing the optimal parametric combination.

2 Experimental Part

2.1 Workpiece Material

GFRP composite plates of 1004 × 104.5 × 11 mm have been taken as the workpiece material.

Table 1 Input parameters with their respective levels

Parameters	Units	Levels			
		1	2	3	4
Spindle speed	RPM	1500	2000	2500	3000
Feed	mm/min	200	300	400	500
DOC	mm	1.0	1.5	2.0	2.5

2.2 Tool Material

Solid carbide (end mill tool) has been utilized as a cutting tool.

2.3 Experimental Setup

The experimentation has been executed on the CNC Vertical Milling Center (Mitsubishi V544).

2.4 Design of Experiments (DOE)

For milling of GFRP composite, input machining variables: RPM of spindle, feed, and DOC have been selected. Four different levels (Table 1) have also been decided by the literature study used in the machining process of the industry. The study utilizes the L_{16} orthogonal array (Table 2) for an experimental procedure to check the influence of milling variables to evaluate the optimal condition.

2.5 Output Responses

A stylus-type profilometer made up of Talysurf (Taylor Hobson, Surtronic 3+) has been employed to measure the average surface roughness (Ra) of the machined glass fiber reinforced epoxy. Cutting force has been measured using the dynamometer.

2.6 Experimental Part

Initially, the output responses, namely surface roughness and cutting forces, have been converted into individual utility degree (sometimes called as a preference number). In order to assess the individual utility index (presented in Table 3) for aforesaid

Table 2 L_{16} orthogonal array

S. No.	N (rpm)	f (mm/min)	d (mm)
1	1500	200	1
2	1500	300	1.5
3	1500	400	2
4	1500	500	2.5
5	2000	200	1.5
6	2000	300	1
7	2000	400	2.5
8	2000	500	2
9	2500	200	2
10	2500	300	2.5
11	2500	400	1
12	2500	500	1.5
13	3000	200	2.5
14	3000	300	2
15	3000	400	1.5
16	3000	500	1

Table 3 Experimental data and their corresponding utility index

S. No.	Ra (μm)	Cutting force (N)	U_{Ra}	U_{Fr}
1	2.1	71.99307	3.735343	5.523982
2	2.2	111.987	3.131315	3.820343
3	2.03	120.01	4.17553	3.553534
4	2	125.6512	4.368848	3.376408
5	2.5667	119.2778	1.129611	3.577132
6	2	95.65605	4.368848	4.428143
7	2.066	171.9567	3.947285	2.166648
8	1.4	151.7389	9.000014	2.648964
9	2.8	208.6587	0	1.420673
10	1.8	254.3508	5.736878	0.657124
11	2.4	29.22778	2.001535	8.999995
12	2.225	146.266	2.984598	2.790613
13	1.93	301.6084	4.831441	0
14	2.3	262.9954	2.554141	0.528248
15	1.8	197.1872	5.736878	1.638717
16	2.1667	92.23575	3.329352	4.568545

characteristic following equations have been used:

For evaluating the preference number of roughness average and cutting force:

$$A = \frac{9}{\log \frac{X_{\text{Lower}}}{X_{\text{Higher}}}} \tag{1}$$

The preference number (P_i) can be articulated on a logarithmic scale like this:

$$U_i = A \times \log \frac{X_i}{X_{\text{Higher}}} \tag{2}$$

These aforesaid assessed utility indices have been put in the fuzzy inference system (FIS) which utilizes fuzzy logic reasoning to aggregate the multiple input parameters into a single entity called multi-performance characteristic index (MPCI). The output MPCI has been assessed by categorizing each input factor into five linguistic variables, i.e., very low (vl), low (l), medium (m), high (h), and very high (vh) as exhibited in Fig. 1. Here, the crisp inputs have been converted into fuzzy values by means of the triangular membership function. Then, the fuzzy inference reason-

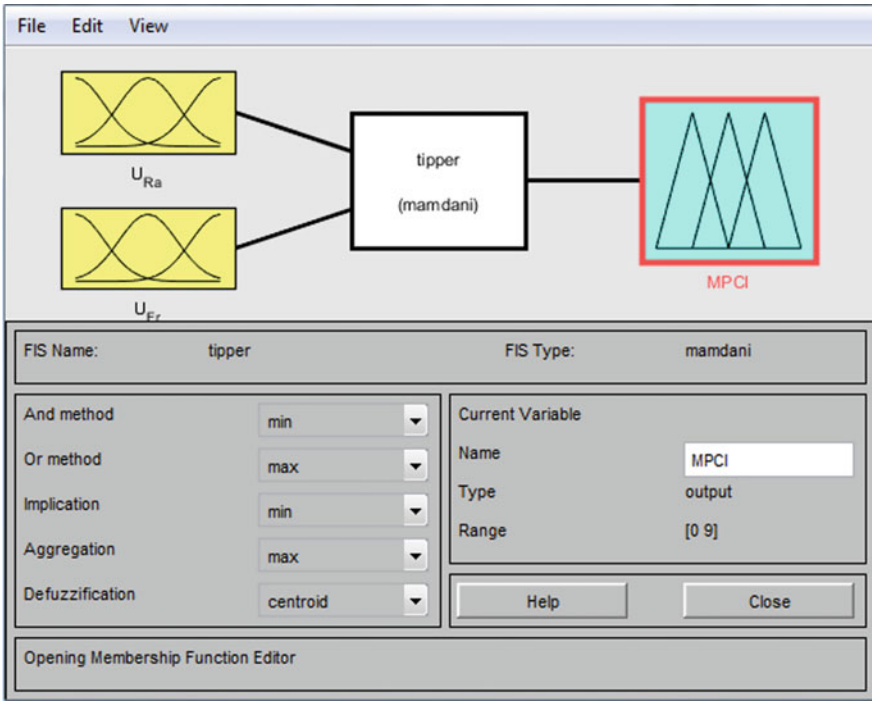

Fig. 1 Fuzzy inference system

ing has been accomplished by utilizing Mamdani implication method based on fuzzy rules. The Taguchi method has been lastly applied to assess the optimal combination.

The S/N ratio, as shown in Fig. 2, has been computed based on Higher-is-Better (HB) criterion (Table 4).

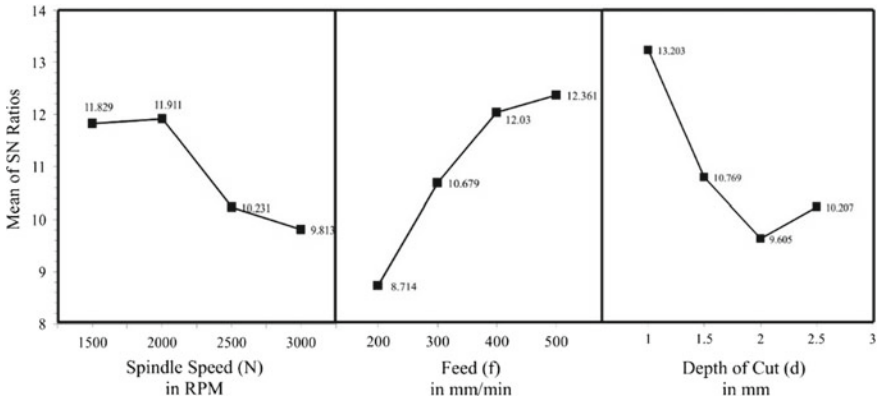

Fig. 2 S/N ratio plot for spindle speed, feed, and depth of cut

Table 4 MPCI with corresponding S/N ratios and expected S/N ratios

S. No.	MPCI	S/N ratio	Expected S/N ratio
1	4.63	13.3116	15.5830
2	3.7	11.3640	
3	3.52	10.9309	
4	3.85	11.7092	
5	2.85	9.0969	
6	4.4	12.8691	
7	3.32	10.4228	
8	5.79	15.2536	
9	1.69	4.5577	
10	3.47	10.8066	
11	5.53	14.8545	
12	3.43	10.7059	
13	2.48	7.8890	
14	2.42	7.6763	
15	3.94	11.9099	
16	3.88	11.7766	

$$\eta_{ij} = -10 \log \left(\frac{1}{n} \sum_{j-1}^{n} \frac{1}{y_{ij}^2} \right) \tag{3}$$

3 Conclusion

This work utilizes utility fuzzy-based Taguchi methodology to evaluate the optimal machining condition in milling of GFRP composites. It has been concluded that at the spindle speed of 2000 RPM, feed of 500 mm/min, and depth of cut of 1 mm, optimum surface roughness and cutting force are obtained.

References

1. Azmi I, Lin RJT, Bhattacharyya D (2012) Experimental study of machinability of GFRP composites by end milling. Mater Manuf Processes 27:1045–1050
2. Sivasankarana S, Harisagar P, Saminathan E, Siddharth S, Sasikumar P (2014) Effect of process parameters in surface roughness during turning of GFRP pipes using PCD insert tool. Procedia Eng 97:64–71
3. Sahu S, Nayak D, Rana H (2014) Thrust, torque analyses and optimization in micro drilling of GFRP using full factorial design integrated CNSGA-II algorithm, procedia. Mater Sci 6:967–974
4. Vankanti V, Ganta V (2014) Optimization of process parameters in drilling of GFRP composite using Taguchi method. J Mater Res Technol 3(1):35–41
5. Parida A, Bhuyan R (2015) Surface roughness model and parametric optimization in machining of GFRP composite: taguchi and response surface methodology approach. Mater Today: Proc 2:3065–3074
6. Chavana V, Dinesh K, Veeresh K, Algur V, Shettare M (2017) Taguchi's orthogonal array approach to evaluate drilling of GFRP particulate composites. Mater Today: Proc 4:11245–11250
7. Chaudhari A, Chaudhary V, Gohil P, Patel K (2016) Investigation of delamination factor in high speed drilling chopped GFRP using ANFIS. Procedia Technol 23:272–279
8. Akhil KT, Shunmugesh K, Aravind S, Pramodkumar M (2017) Optimization of drilling characteristics using grey relational analysis (GRA) in glass fibre reinforced polymer (GFRP). Mater Today: Proc 4:1812–1819
9. Shunmugesh K, Akhil KT, Aravind S, Pramodkumar M (2017) Optimization of drilling characteristics using Grey-Fuzzy logic in glass fibre reinforced polymer (GFRP). Mater Today: Proc 4:8938–8947

Design, Analytical Analysis and Manufacturing of 5-Cylinder Hydraulic Fixture with Rotary Table for Machining Case on VMC EZ5

Nirav P. Maniar, Niraj J. Sanghani, Hardik A. Khunt, Sudhir Thaker and Pradeep Thanki

Abstract Most of the research papers present theoretical aspects of fixture design. The present volume of this research work satisfies the demand of functional approach by applying theoretical principles of fixture design for industrial component. The component is case of motor body widely used in automobile industry. The research includes design, analytical analysis and manufacturing of a hydraulic fixture with unique concept of rotary table for machining five operations on various faces of component in one setup on VMC EZ5. The innovative use of rotary table eliminates the needs of multiple setup of fixture and thus results in huge cost saving. Fixture is not only designed but manufactured also, and it sets the classical example of design for manufacturing.

Keywords Fixture · Hydraulic · Design for manufacturing · Rotary table · Analytical analysis · Manufacturing infrastructure

1 Introduction

This paper includes the unique aspect of designing and manufacturing 5-cylinder hydraulic fixture for machining case of motor body on VMC EZ5 of pallet size 600 mm × 400 mm. The present research work formalizes the use of hydraulics in

N. P. Maniar (✉) · N. J. Sanghani · H. A. Khunt
V. V. P. Engineering College, Virda-Vajdi, Opposite Motel the Village, Kalawad Road, Rajkot, Gujarat 360005, India
e-mail: nirav.maniar.me@vvpedulink.ac.in

H. A. Khunt
e-mail: hardik.khunt.me@vvpedulink.ac.in

S. Thaker · P. Thanki
M/S Supra Technology, 51 a Bhakti Nagar Industrial Estate, Behind Shaktivan Manufacturers, Rajkot, Gujarat 360002, India
e-mail: sudhir@supratechnology.in

P. Thanki
e-mail: pradeep@supratechnology.in

A. K. Parwani and PL. Ramkumar (eds.), *Recent Advances in Mechanical Infrastructure*, Lecture Notes in Intelligent Transportation and Infrastructure,
https://doi.org/10.1007/978-981-32-9971-9_11

fixture and reduces nonproductive time. The research work also represents the unique concept of use of rotary table and analytical analysis under dynamic machining. Use of rotary table is an innovative aspect to eliminate the number of setups at various angles. Components are clamped in the same location in each cycle eliminating the variability in part deflection from clamping forces. So, offsetting is required only once when workpiece is mounted first time. Use of hydraulic fixture saves the offsetting time. Fixture is not only designed, but manufactured also, and it sets the classical example of design for manufacturing.

2 Literature

Studies in the fixturing began in the 1940s. Several manuals on jig and fixture design were developed such as Houghton and Wilson [1, 2], Henriksen [3] and Boyes [4]. Costa et al. [5] developed a clamping methodology to ease operations for complicated workpieces. Meyer and Liou [6] considered dynamic machining for fixture design methodology. Deiaba and Elbestawi [7] performed experiments for contact characteristics of workpiece and fixture. Papastathisa et al. [8] proposed an innovative concept of adaptive machining fixtures for controlling holding forces and dynamic layout. Yanga et al. [9] presented hydraulic clamping system of a special CNC machine tool for guide disk.

The following section presents the real-time research work of designing and manufacturing 5-cylinder hydraulic fixture for machining rear flange on VMC EZ5 of pallet size 600 mm × 400 mm. The innovative use of rotary table eliminates the need of multiple setup of fixture and thus results in huge cost saving.

3 Design, Analytical Analysis and Manufacturing of Hydraulic Fixture

3.1 Problem Definition

"Design and manufacturing of hydraulic fixture for machining case of motor body on VMC EZ5 of pallet size 600 mm × 400 mm. The major operations to be performed are drilling, boring and grooving."

3.2 Component Description

The component is case of motor body widely used in automobile industry, made up of aluminum ADC12, and overall dimensions are 231-mm diameter and 31.5-mm

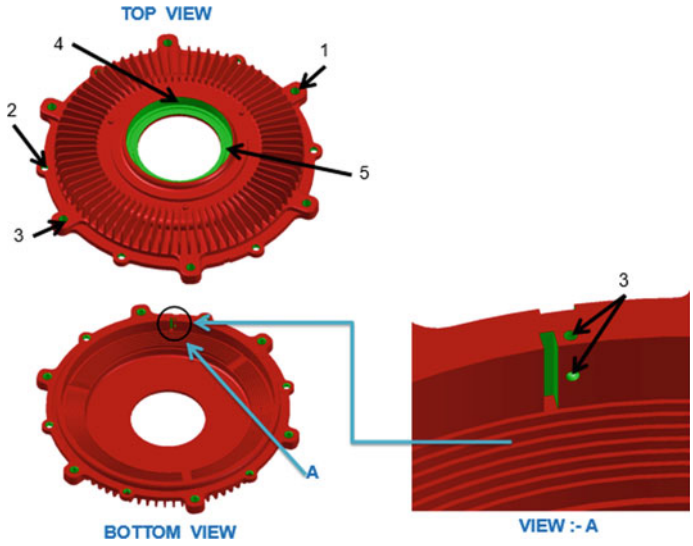

Fig. 1 Three-dimensional view of component

height, weighing 700 g. The raw component is made by high-pressure die casting process, and then turning of all required faces is performed. The geometry is circular, so all diametric faces are machined by using turning center. Moreover, as the material is soft, if drilling is done without pre-hole, the geometry will deform due to impact force of cutting tool. So, pre-holes are created using core during casting process to avoid deformation. Machining operations are to be performed on three faces—two sides from top and bottom face.

The list of operations to be performed is as under:

1. Drilling of 6 holes on PCD 214 mm (Ø7 mm, through depth)
2. Drilling of 6 holes on PCD 205 mm (Ø6 mm, through depth)
3. Drilling of 1 hole on side and bottom face as shown in view A of Fig. 1. (Ø2 mm)
4. Boring at center (Ø81.3, 9.9 mm depth)
5. ID grooving (2.6 mm).

Figure 1 shows component geometry with markings 1–5 as indicators of above operations.

3.3 Design of Fixture

According to very basic principle of location, machined surface should be used for location, so bottom face of the component is used for location as it is received finished by turning process after casting. The complete location is achieved using base plate, one rest pad, one retractable orientation pin and four poka-yoke nylon

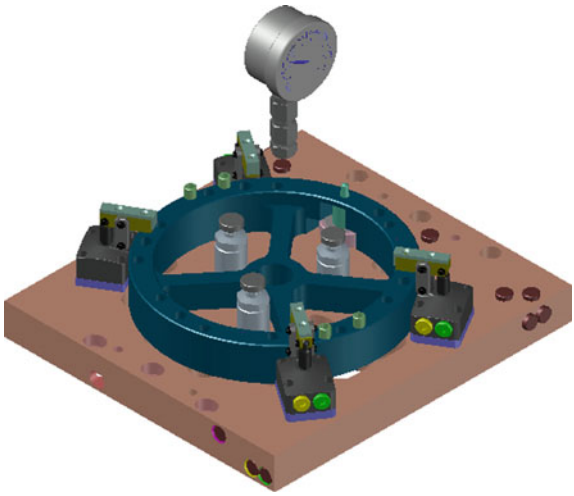

Fig. 2 Three-dimensional view of fixture without workpiece and rotary table

pins. Base plate provides the support to all components of fixture as well as piping for hydraulic fluid to operate hydraulic clamps as well as retractable orientation pin. Using principle of mutually perpendicular planes, rest pad and orientation pin are used to locate the component. Orientation pin locates a hole where drilling is required. So, a push–pull cylinder is provided to retract orientation pin after clamping to allow machining process. Four hydraulic clamps are used to clamp the component. Totally, five cylinders are required to operate four hydraulic clamps and one orientation pin. Operations 1, 2, 4 and 5 mentioned in the list of operations are performed for horizontal position of workpiece, but operation 3 is on vertical surface. So, workpiece will be rotated by 90° using a unique concept of rotary table for drilling 2-mm diameter hole eliminating the need of multiple setup of fixture and thus resulting in huge cost saving. Figures 2 and 3 show 3D view of fixture assembly without workpiece and rotary table as well as with workpiece and rotary table. Figure 4 shows photograph of manufactured fixture.

3.4 Analytical Calculations

Analytical calculations are carried out to decide the number of clamps required to clamp workpiece rigidly during operations.

Calculating cutting force for drilling hole of 7 mm,
Diameter, $D = 7$ mm,
Feed per revolution, $S = 0.18$ mm/revolution,
Material factor, $K = 0.55$,
T_h is the cutting force.

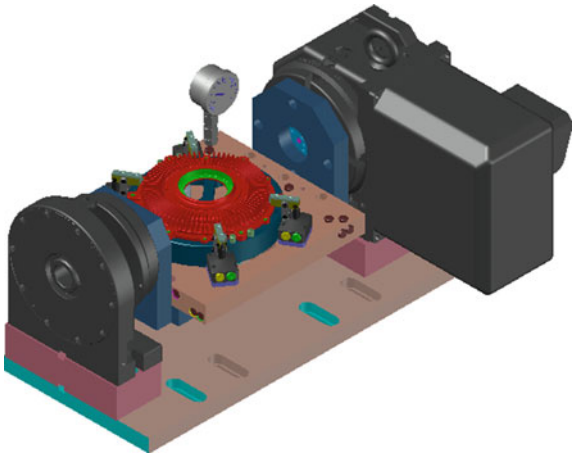

Fig. 3 Three-dimensional view of fixture with workpiece and rotary table

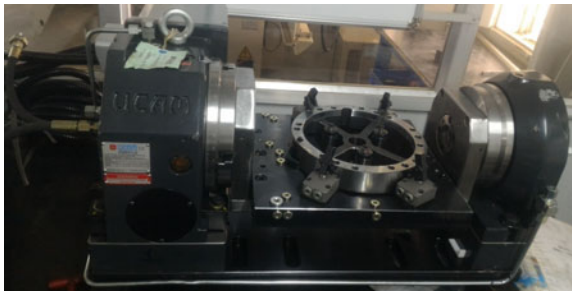

Fig. 4 Photograph of manufactured fixture with rotary table

$$T_h = \frac{1.17\,\mathrm{KD}}{(100\mathrm{S})^{0.85}} = 0.3828\,\mathrm{kgf} = 3.7538\,\mathrm{N} \quad (1)$$

Calculating cutting force for ID grooving of 2.6 mm,
End milling is used for grooving,
Width of cut, $b = 2.6$ mm,
Depth of cut, $t = 0.1$ mm,
$D = 2.6$ mm,
$N = 4000$ rpm,
Feed per tooth, $S_z = 0.02$ mm/teeth,
Number of teeth, $Z = 3$,
Unit power, $U = 12$ kw cm^{-1} min^{-1},
Flank wear correction factor, $K_h = 1$,
Rake angle correction factor, $K_\gamma = 0.93$ (for $\gamma = +15$)

$$v = \frac{\Pi\, D\, n}{1000} = 32.6725\ \text{mm/min} \tag{2}$$

$$S_m = \text{Sz Z n} = 240\ \text{mm/min} \tag{3}$$

$$Q = \frac{b\, t\, S_m}{1000} = 0.0624\ \text{cm}^3/\text{min} \tag{4}$$

$$\text{N} = \text{U K}_\text{h}\, \text{K}_\gamma\, \text{Q} = 0.6964\ \text{kW} \tag{5}$$

Tangential cutting force,

$$P_z = \frac{6120\, N}{v} = 130.4421\ \text{kgf} = 1.28\ \text{kN} \tag{6}$$

Now follows the analytical calculation for selection of link clamp.

Maximum sustainable force for the component is required to be calculated for selection of link clamp such that clamping force of each link clamp must be less than sustainable force.

For material ADC 12, $\sigma_{\text{yield}} = 165$ MPa.

Considering factor of safety = 1.75 and minimum contact area between workpiece and link clamp = 0.1 mm^2,

Maximum pressure which can withstand by material (ADC12) without deformation,

$$\sigma\text{max} = \frac{\sigma_{\text{yield}}}{\text{Factor of safety}} = 94.2857\ \text{MPa} \tag{7}$$

Maximum substantial force which can withstand by material (ADC12) without deformation

$$\text{P}_\text{max} = \frac{\sigma\text{max}}{\text{Area}} = 942.857\ \text{N} \tag{8}$$

Table 1 Analytical comparison for different work materials for drilling operation

Work material	K	T_h (N)
Copper alloys	0.55	3.7538
Stainless steel	1.56	10.6504
Mild steel	1.07	7.3051
Gray cast iron	1	6.8272

Table 2 Analytical comparison for different process parameters for end milling operation

T (mm)	S_z (mm/teeth)	γ	K_γ		P_z (kN)
0.1	0.02	15^0	0.93		1.28
0.2	0.03	15^0	0.93		3.32
0.1	0.02	10^0	1.00		1.42
0.2	0.03	10^0	1.00		4.26

Therefore, link clamp force must not be higher than 0.95 kN.

Standards of hydraulics suggest the use of following clamp specifications:

Hydraulic pressure = 2.5 MPa,

Cylinder force = 1.2 kN, lever length = 33.5 mm, clamping force = 0.8 kN. Now follows the calculation of the number of link clamps required for each component.

Considering $\mu = 0.45$,

$$\text{Number of link clamps} = \frac{P_z}{\text{Clamping force } x\ \mu} = 3.56 \tag{9}$$

So, four link clamps are required to clamp each component.

Table 1 shows analytical comparison of cutting force for different work materials for drilling operation. Table 2 shows analytical comparison of tangential cutting force for different process parameters for end milling operation at constant speed.

4 Conclusions

The present research work uses comprehensive approach of fixture design and manufacturing for industrial component. Manual clamping and offsetting require minimum 3 min to clamp the workpiece. But in case of hydraulic fixture, the clamping time for 5-cylinder hydraulic fixture is 3 s and declamping time is 2 s. Adding 10 s time for mounting and unmounting of workpiece, maximum time required in hydraulic fixture is 15 s. More than 2.5 min is saved in each cycle of operations, which will result in higher productivity as well as cost saving in effective amount. Moreover, every

link clamp provides uniform clamping force of 0.8 kN during each cycle which will improve process stability. Hydraulic fixture favors automated clamping and provides uniform clamping force with high operational efficiency.

References

1. Houghton SP (1956) Jigs and fixture design. Chapman & Hall
2. Wilson F (1962) Handbook of fixture design. McGraw-Hill, New York
3. Henriksen KE (1973) Jig and fixture design manual. Industrial Press, New York
4. Boyes W, Bakerjian R (1989) Handbook of jig and fixture design. Society of Manufacturing Engineers, MI, Dearborn
5. Costa C, Silva F, Gouveia R, Martinho R (2018) Development of hydraulic clamping tools for the machining of complex shape mechanical components. Procedia Manuf 17:563–570
6. Meyer R, Liou F (2013) Fixture analysis under dynamic machining. Int J Prod Res 35:1471–1489
7. Deiab I, Elbestawi M (2005) Experimental determination of the friction coefficient on the workpiece-fixture contact surface in workholding applications. Int J Mach Tools & Manuf 45:705–712
8. Papastathis T, Bakker O, Ratechev S, Popov A (2012) Design methodology for mechatronic active fixtures with movable clamps. Procedia CIRP 3:323–328
9. Yang K, Guan S, Wang C (2011) The design & calculation for hydraulic cylinder of workpiece hydraulic clamping system of a special CNC machine for guide disc. Procedia Eng 16:418–422

Design Modification for Multi-material Printing with Fused Deposition Modeling

Tarun Rijwani, PL. Ramkumar, Rahul Asnani and Nandan Patel

Abstract Fused deposition modeling 3D printers have wide future scope as most of FDM printers are small enough to qualify for desktop printer and easy to be operated by a layman, which enables its opportunity to become a consumer product for common people in coming future. On top of that, addition of multi-material printing feature at desktop-level 3D printers will be an attractive feature as 3D printing with multiple materials unleashes the various advantages whether it be printing with multiple colors or printing with different types of materials. Printing soluble supports with polyvinyl alcohol (PVA), printing pre-assembled complex structures, getting different combination of properties in a single part, etc. will be possible for desktop 3D printers. In this chapter, currently available techniques for multimaterial printing are reviewed thoroughly with the advantages and disadvantages of each as well a better alternative approach is proposed.

Keywords Fused deposition modeling · Multi-material printing · 3D printing · Multi-extrusion · Bowden extruder

1 Introduction

Three-dimensional printing technology enables the creation of physical objects from digital CAD files, and various types of materials can be used for 3D printing catered by various technologies like SLS and SLM for metal alloys and powder polymers, DLP and SLA for photopolymer resins, FDM for thermoplastics, metal clays, edible materials, etc. As per Forbes 93% of companies who adopted 3D printing in 2018 resulted in get more advantage in terms of the competitive market by reducing prototyping time and launching products early in the market. FDM-based 3D printers

T. Rijwani (✉) · PL. Ramkumar · R. Asnani · N. Patel
Mechanical Engineering Department, Institute of Infrastructure, Technology, Research and Management, Ahmedabad, Gujarat, India
e-mail: tarunrijwani1111@gmail.com

PL. Ramkumar
e-mail: pl.ramkumar@iitram.ac.in

A. K. Parwani and PL. Ramkumar (eds.), *Recent Advances in Mechanical Infrastructure*, Lecture Notes in Intelligent Transportation and Infrastructure,
https://doi.org/10.1007/978-981-32-9971-9_12

constitute the market share of 46% among total printers in the market [1]. Whereas multi-material technology in FDM leads to the addition of features, there are various methods to print using multiple materials we have analyzed available methods and proposed a better alternative to swap the material while printing.

2 Available Techniques for Multi-Material Printing

2.1 Dual Extruder

This is one of the most common techniques currently used in the 3D printers available in the market to print with multiple materials at a time, using an additional set of nozzle and extruder within the existing system (see Fig. 1). This kind of setup allows a user to print with two different materials, and mostly, it is used for printing of soluble supports using Polyvinyl Alcohol (PVA) or printing with same materials of two different colors [2]. This type of system is simple and easy to use, and two materials with a great difference in melting temperatures can also be printed easily and also avoid start and stop of the printer while changing filament reducing downtime. While limitations of this system are reduced the printable area of printer, offset of both the nozzle should always remain constant even after a change of temperatures arises various defects such as oozing, stringing, and layer shift, which hamper the quality of product and purge tower needs to be printed [3].

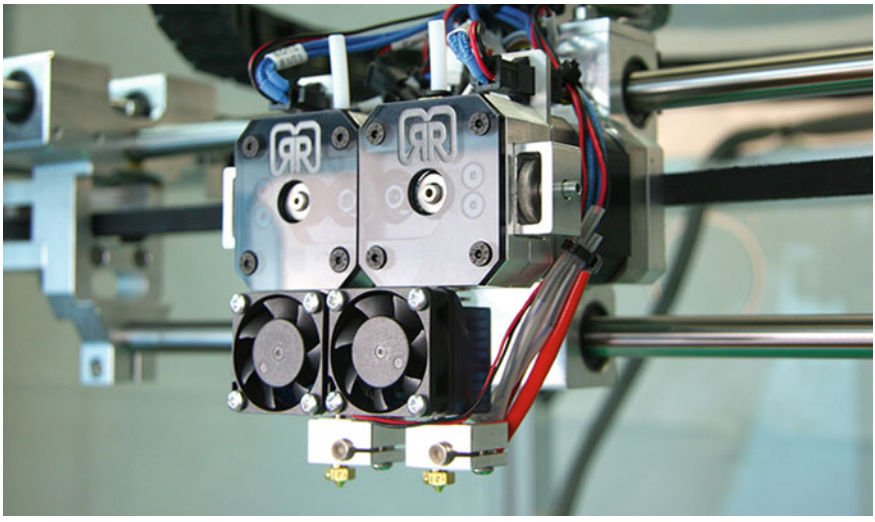

Fig. 1 Dual extruder [4]

2.2 Manual Way

Manual way for multi-material printing is simply by pausing the print in between where filament needs to be changed and resuming it after changing the filament, pause and resume functions can be controlled from the control interface while printing or can be modified in the G-code to reach away from the part and hold for the given time duration before continuing the print, but this method is complex and needs to seek human interference. No extra cost is involved for this method, a various number of materials can be used in a single print, no need to compromise with printing area, no need to print purge tower, and there is less number of defects as no additional mechanically complex devices are there. While this method needs human intervention and its complex to change filament manually in between of print, increase in downtime of the printer and any movement of the axis due to manual intervention can lead to a defective product [5].

2.3 Color 3D Printer

If the motor behind multi-material printing is to just get a part with multiple colors, color 3D printing technology is capable of doing it by combining FDM technology with inkjet printing. One of the best printers in the market with this technology is Da Vinci Color from XYZ printing (see Fig. 2). It uses special kind of filaments which absorbs the color pigments sprayed through jet while printing the part and results in a colored product, it uses pigments similar to an inkjet printer, generally four pigments are used CMYK (Cyan, Magenta, Yellow, Black), and different color combinations are made by mixing them in different proportions. Thus, different multiple colors and shades can be easily printed, this method is also simple and easy to use, and also, there is no need to print purge tower thus no downtime while printing. While color 3D printers need special purpose filaments which can absorb the color pigments and it is not possible to print with multiple different types of material such as Polylactic acid (PLA), Acrylonitrile Butadiene Styrene (ABS), Polyvinyl alcohol (PVA), etc. [6].

2.4 Palette from Mosaic Manufacturing

Palette is a 3D printer accessory from mosaic manufacturing, and it allows users to print with multiple materials and can be clubbed with any available single nozzle and single extruder based printer without any modification in the printer, so it is even compatible with warranty terms of most 3D printer manufacturers, palette has multiple extruders built in its system, and currently, it deals with four filaments as an intake and can cut, slice, and join the filaments back in the right order and

Fig. 2 XYZ printing Da Vinci Color 3D printer [6]

length required according to the part which is about to be printed; thus, it produces a single filament with multi-colored sections in it, which is then guided to the printer for printing, and it makes a normal single nozzle printer capable of printing with multiple different colored materials (see Fig. 3). This system can be combined with any normal single nozzle printer without any compromise with the printable area, and once setup is done, it is easy to operate [7]. While the additional cost of this palette is $700 which needs to be spent apart from the printer cost, and currently, it is only available for 1.75 mm diameter filaments [8].

3 Scope of Innovation

After analyzing these various methods for multi-material printing, we realized that there is plenty of room for developing something low cost, easy to use, and adoptable for existing single nozzle printers without affecting the warranty. As most of the printers in the market have already very low print volume, this was the major issue, and the new technique should not reduce the printable volume. Also, largely available printers in the market are using ATmega based controller board such as Arduino with RAMPS, MKS Gen boards or Geeetech GT2560 board. All of these boards have provision for connection of addition stepper motor for extruder, while the firmware

Fig. 3 Mosaic palette 2 [8]

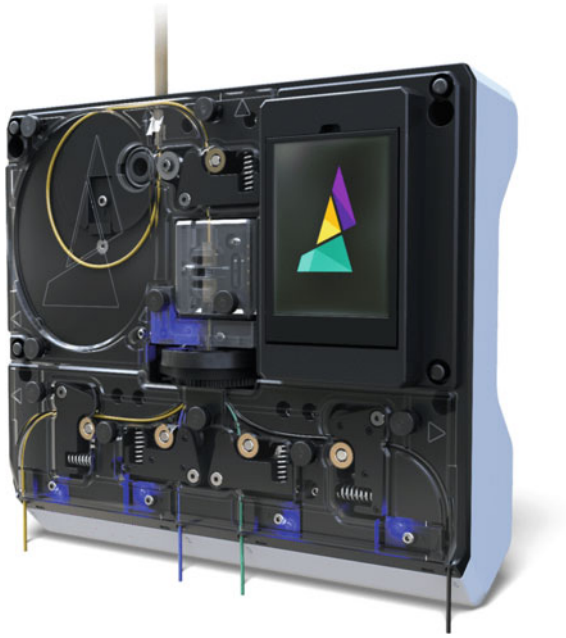

used by the printers is either open sourced or custom developed but these boards are capable of running with almost any firmware; so, there are ample of possibilities for developing a new technology and solving the existing problems.

4 Concept Generation

The initial step toward the generation of any concept is a collection of vital information from numerous sources available so that initiation of concept generation occurs in our mind. The usual sources of information are Internet, books, journals, government agencies, surveys, etc. [9]. For our innovation, we had got help from various journals available and Internet as well. Experts were not possible to reach in such a short period of time. Also for generating ideas, we constantly kept on searching for best-suited solutions which overcome the disadvantages of currently available methods.

Basic Requirements which should be satisfied by the concept:

1. Low cost and easy to use.
2. Can be clubbed with existing printer.
3. Should not affect the warranty terms.
4. Should not affect the print area.
5. Print quality should not get affected.
6. Requirement of printing purge tower.

Fig. 4 Turret [10]

4.1 Concept No. 1

This concept was developed getting inspired by the turret mechanism, the way CNC machine deals with a various number of tools in the turret (see Fig. 4). In similar, fashion multiple nozzles can be fixed on a turret which will be controlled by a servo motor and can be placed on the axis of 3D printer in place of a single nozzle. Thus, various materials can be printed using this technology all at different temperatures, the drawbacks of this method will be reduced print area, complex to set up, and requirement of multiple nozzles will lead to increase in cost, while mostly available 3D printer controllers have auxiliary pulse width modulation (PWM) pin to control servo motor of turret, still there will be need of an additional controller to apply PID and control the temperatures of different nozzles.

4.2 Concept No. 2

The concept no. 2 is based on the dual extruder method mentioned above in methods, the idea is to raise the secondary print nozzle to a certain height using a servo motor, this will eliminate the quality defects such as stringing and oozing which arise in dual nozzle printing, and however, adding this method in a preexisting printer will be quite tricky, but still it is possible to add it as mostly 3D printer controllers have an

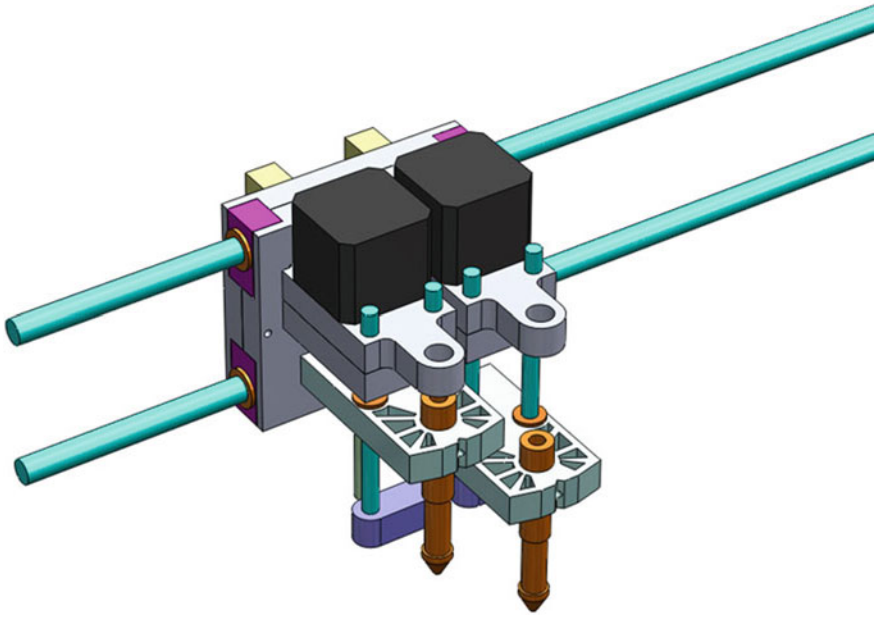

Fig. 5 Lifting extruder [11]

option for secondary nozzle temperature control and an auxiliary pin to control the servo used for raising the nozzle (see Fig. 5). Cost of this may be little high because good quality servo would be required to get quality prints and tough part will be to maintain the offset between both nozzles.

4.3 Concept No. 3

The concept no. 3 is to combine the dual extruders into a single body with one nozzle, a single heat block with two inputs of filament, and a single nozzle output (see Fig. 6). This will have very less effect on reduction in printable area and will be highly suitable for Bowden style extruders, cost of such system will be comparatively less, and also, the quality defect such as oozing and stringing arising because of secondary nozzle will not be there, no need to maintain the offsets also. After searching about this concept on the Internet, we found that this kind of setup for extruder is already available by E3D named as Cyclops+, but we found that major drawback for this kind of system is that both materials as input should be available on the time even though we are only printing with one material because if the inlet of secondary filament is kept empty, it will start oozing out the primary material, and this drawback existed because both the inlets and the nozzle were in the heat block of extruder.

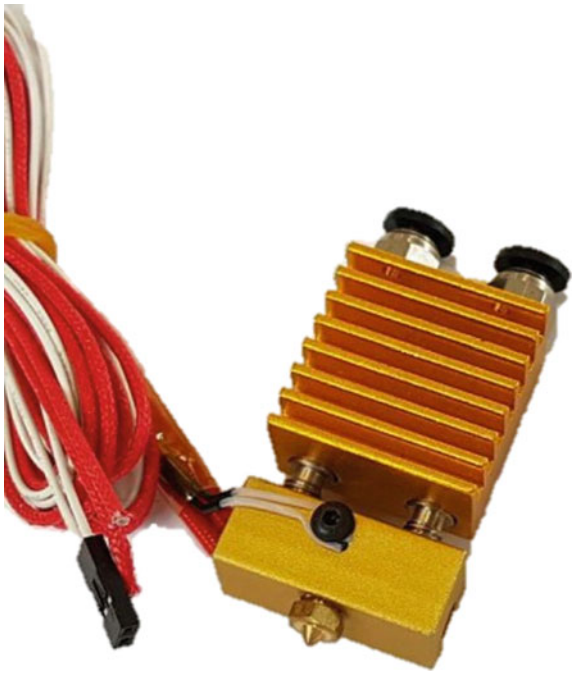

Fig. 6 E3D Cyclops [12]

4.4 Concept No. 4

After developing few concepts, we were quite clear that what kind of requirements should be fulfilled, we were thinking of something that has advantages from all these techniques avoiding the drawbacks which made concept generation more critical. For this concept, our inspiration was a multi-color pen the way it deals with multiple refills in a single cylinder and pushes out the required colored refill from the nozzle; our idea was to deal with multiple filaments in a similar manner, but if multiple filaments were combined at the place of heat block or nozzle, it would again result into a complex system idea was to keep it simple and easily adoptable so we thought of managing the filament change before heat end, thus making the system Bowden extruder type.

So the concept no. 4 was to develop a converging nozzle type of structure to guide various filaments toward a single output, to make this smooth and simple inner side of this will have PTFE tube lining with couplers at the ends, the major advantage of this system is that the converging filament guide can also be printed on the existing single nozzle extruder itself (refer Fig. 7). With this, multiple materials could be printed easily without compromising with printable volume, using a single nozzle only and it can be adopted for existing single nozzle printers as well.

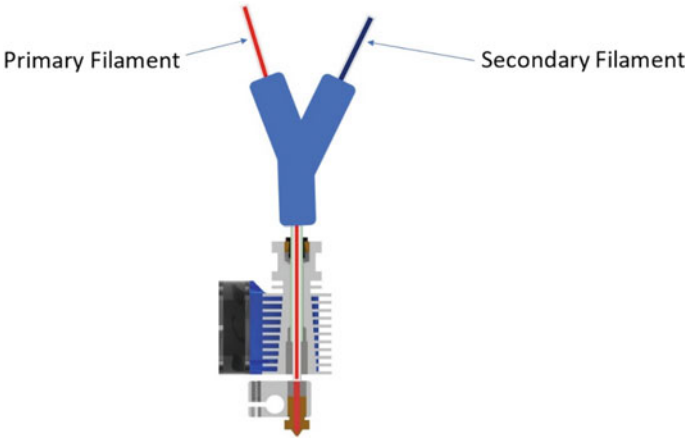

Fig. 7 Concept of multi-material printing with filament guide

5 Concept Selection

In the later phase of 1990s, the National Air and Space Agency (NASA) had developed various concepts for the mission of low-cost crafts in space. Many technologies used for the purpose of sensing, transmitting, and storage needed to be evaluated and selected to perform in various power sources and storage axillaries of the spacecraft. These different technologies further developed into various concepts, which needed to be evaluated before each deep space mission. Such decisions which involve the selection are quite risky because the concepts do not completely represent the technology, a characteristic of all concept selection problems in design. Methods which involve the structured evaluation of various concepts are needed to make the selection more effective [9]. The evaluation of all the available concepts was done by the method called "PUGH'S CONCEPT SELECTION CHARTS" (refer Table 1). The process was developed by PUGH in 1990 for using along with decision-making tools. The method is based on the minimum evaluation scale and it uses three metrics for the purpose of ranking, as developed by PUGH, and this method is termed as Pugh's chart. This method turns out to be a great help in the primary concept selection of a process when minimal information quality is available for any product. The more information quality available, the more effective this method becomes. This method refines the selection scale, as the quality of information available increases. The main objection of any concept selection process is to evaluate each concept and gather information and details of each concept as time and resources available to the selector [9].

Table 1 Pugh's chart

		Concepts							
		Concept no. 1		Concept no. 2		Concept no. 3		Concept no. 4	
Selection criteria	Weight (%)	Rating	Weighted score	Rating	Weighted score	Rating	Weighted score	Rating	Weighted score
Should not reduce the print area	15	2	0.30	2	0.3	3	0.45	5	0.75
Cost efficient	20	3	0.6	3	0.6	4	0.8	4	0.8
Can be clubbed with existing printer	15	1	0.15	3	0.45	3	0.45	3	0.45
Ease of use	15	3	0.45	2	0.30	3	0.45	4	0.6
Print quality should not get reduced	20	4	0.8	3	0.6	4	0.8	5	1
No requirement of printing purge tower	15	4	0.6	1	0.15	3	0.45	3	0.45
Total score		2.9		2.4		3.4		4.05	
Rank		3		4		2		1	
Continue		No		No		No		Develop	

6 Prototyping the Selected Concept

The emphasis is laid on the overall architecture of the product and then dealing with each component details while working on the configuration design. The design of the product is shown over here having the various features as mentioned before. The features of identified parts from configuration design available now turn into a design variable for preparing the parametric design.

Initially, we tried to design this system for two materials the steps involved in prototyping this system were:

(1) *Designing the filament guide*
(2) *Printing the designed guide*
(3) *Assembling the system*
(4) *Modifying firmware*
(5) *Testing the system.*

We followed these steps to get our first model, but it took us six iterations of design to reach our target and make a working system of this.

As the system also needed the modification in firmware, we added the filament changing code such that if filament change is required the filament in use will be retracted for the specified length, once retraction is complete, new filament will be fed ahead meanwhile the temperature of nozzle will be changed as per new material to be used. The concept is to use a similar kind of system for multiple materials also, and the only problem is the compatibility of the controller board to run multiple extruders.

Working of this concept is simply dependent on the filament guide adapter which is responsible for guiding different filaments into a single channel, and the forward and backward motion of these filaments is done by Bowden extruder and controlled by the G-codes provided; thus, if filament change is required the filament in use will get retracted till its end point reaches inside the top portion of guide and then second filament will be feed into the channel, this process is highly dependent on the G-codes. Length of these guides is used to calculate the amount of forward and backward movement of filament, while change is done. Currently, we have prototyped this system for two different materials, while a similar kind of system can also be used for multiple materials if hardware facility is available (see Fig. 8). Sample part is printed with two different filaments translucent red and white using this filament guide (see Fig. 9).

7 Conclusion

The attempt to overcome the problems of currently existing multi-material printing methods in a simply efficient and cost-effective way was successful after various iterations of designs, and we conclude to the concept which is cost-effective and

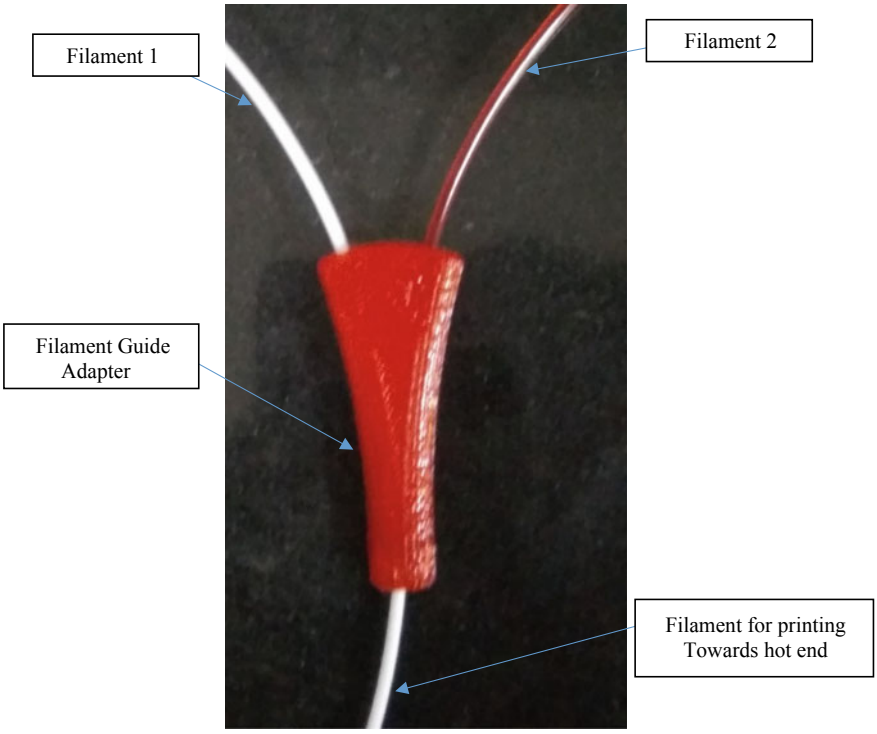

Fig. 8 Setup of filament guide for multi-material printing with single nozzle

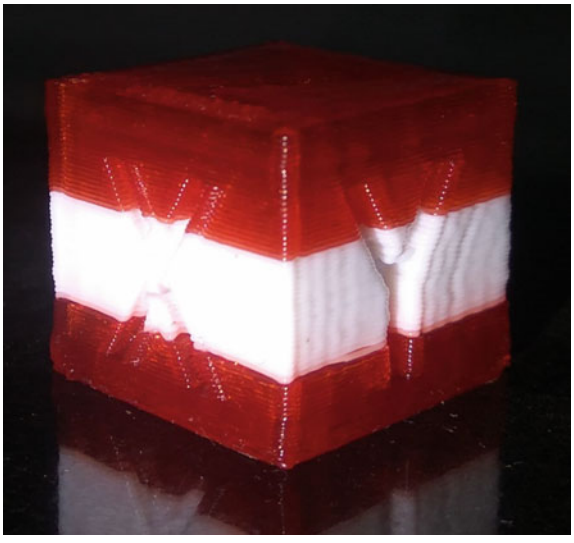

Fig. 9 Part 3D printed in dual colors translucent red and white using this concept

can be easily adopted by manufacturers as well as preexisting 3D printer owners for upgradation. The filament guide can be printed by the user on single extruder printer itself (see Fig. 8), CAD files required for this upgrade are submitted open source by us on Thingiverse. PTFE tubing needs to be inserted in the guide as a liner for smooth movement of filament. One side of the guide has inlet for multiple filaments and after converging there is outlet for single filament which goes to hot end for printing, the filament changing process happens inside the guide, and the complexity part of multi-material printing is now shifted to the program used to control this mechanism; hence, necessary firmware changes were also made and tested, now with this method multiple materials can be printed easily without reduction in printable area and at low cost.

References

1. Forbes (2019) The state of 3D printing. www.forbes.com/sites/louiscolumbus/2018/05/30/the-state-of-3d-printing-2018/#164ab18c7b0a. Last accessed 11 Feb 2019
2. 3DPrinterPrices (2019) Dual extruder 3D printers what you need to know. www.3dprinterprices.net/dual-extruder-3d-printers-what-you-need-to-know/. Last accessed 17 Feb 2019
3. 3D Printing Board (2019) Dual extruders are they worth it. www.3dprintboard.com/showthread.php?18159-Dual-Extruders-are-they-worth-it. Last accessed 13 Feb 2019
4. 3D Natives (2019) Dual extruder 3D printer. www.3dnatives.com/en/dual-extruder-3d-printer-171020174/. Last accessed 18 Feb 2019
5. All3DP, Multi Material 3D Printing 2018 Overview. www.all3dp.com/2/multi-material-3d-printing-an-overview/. Last accessed 13 Feb 2019
6. XYZPrinting, Da Vinci Color. www.xyzprinting.com/en-US/product/da-vinci-color. Last accessed 19 Feb 2019
7. All3DP (2019) Mosaic manufacturing launches palette 2 multi-material printing solution. www.all3dp.com/4/mosaic-manufacturing-launches-palette-2-multi-material-filament-solution/. Last accessed 21 Feb 2019
8. Mosaicmfg homepage (2019) www.mosaicmfg.com/. Last accessed 24 Feb 2019
9. Otto K, Wood K (2003) Product design—technique in reverse engineering and new product development. Pearson Publications
10. Incobeta (2019) Turret 35724 10 coolant nozzle for turret pack of 10. www.incobeta.com/turret/turret-35724-10-coolant-nozzle-for-turret-pack-of-10/. Last accessed 24 Feb 2019
11. Mit fab labs the multi process lathe 3D copy machine. www.fab.cba.mit.edu/classes/S62.12/people/yoav.sterman/evolution.html. Last accessed 23 Feb 2019
12. E3D Cyclops (2019) www.e3d-online.com/cyclops. Last accessed 26 Feb 2019

Comparative Evaluation for Studying the Parametric Influences on Quality of Electrode Using Taguchi Method Coupled with MOORA, DFA, and TOPSIS Method for Electrochemical Machining

Surya Narayan Panda, Dilip Kumar Bagal, Ajit kumar Pattanaik, Dulu Patnaik, Abhishek Barua, Siddharth Jeet, Biswajit Parida and Bibekananda Naik

Abstract The selection of optimal parameters of electrochemical machining (ECM) processes plays a noteworthy part in optimizing the measures of process parameters. Hence, evaluation of material removal rate and surface roughness is of enormously important in ECM. Developed in this paper is the application of Taguchi-based MOORA technique, desirability function analysis, and TOPSIS method for optimizing the responses of chromoly steel with the help of hexagonal-shaped brass electrode and brine solution. Multi-objective optimization has been done to investigate the influence of process parameters, i.e., voltage, tool feed rate, and signal on MRR and surface roughness. Optimal factor setting obtained from each optimization technique was compared, and confirmation test was done to validate the results obtained from electrochemical machining.

Keywords ECM · MRR · Surface roughness · Taguchi approach · Taguchi · MOORA · Desirability function analysis · TOPSIS

S. N. Panda (✉)
Birsa Institute of Technology Sindri, Dhanbad, Jharkhand, India
e-mail: suryanarayan.uce@gmail.com

D. K. Bagal · A. Pattanaik · D. Patnaik
Government College of Engineering, Kalahandi, Bhawanipatna, Odisha, India

A. Barua · S. Jeet · B. Parida
Centre for Advanced Post Graduate Studies, BPUT, Rourkela, Odisha, India

B. Naik
Biju Patnaik Institute of Technology, Phulbani, Odisha, India

A. K. Parwani and PL. Ramkumar (eds.), *Recent Advances in Mechanical Infrastructure*, Lecture Notes in Intelligent Transportation and Infrastructure,
https://doi.org/10.1007/978-981-32-9971-9_13

1 Introduction

In recent trend, nonconventional machining processes are gaining popularity day by day. Electrochemical machining technique is an alternative efficient nonconventional method for machining of advanced very hard materials. In this process, the workpiece can be worked upon without contact and thermal or mechanical impact [1]. The working principle of ECM is the material removal takes place in the stated process by anodic dissolution, which does not produce any residual stress, i.e., no thermomechancial property change for the workpiece. It is carried out by passing an electric current through an electrolyte in the gap of tool and workpiece [1–4]. In some investigations [5–7], it has been concluded that electrochemical machining gives a novel efficient method for achieving high-quality products for high obstruction and incredibly hard to machine materials. The process efficiency can be studied by analyzing the improvement of output characteristics like surface roughness, dimensional accuracy, rate of material removal, and the process cost [8, 9]. The fundamental rule of ECM activity depends on the controllable anodic disintegration system of work material taken as a hub with the device taken as cathode in an electrolytic arrangement [10–16].

In this study, optimization of process parameters like signal, voltage applied, and feed rate considering the multiple characteristics including rate of material removal and surface roughness by different optimization techniques. Taguchi-based MOORA technique, desirability function analysis, and TOPSIS method fare are used for optimizing the responses of chromoly steel as workpiece using a brass electrode of hexagonal shape and brine solution as electrolyte. Optimal factor setting obtained from each optimization techniques was compared, and confirmation test was done to validate the findings concluded from the stated analysis.

2 Experimental Setup and Methodology

The experiments were executed on machining of EN-19 chromoly steel to study the effects of input process parameters on output characteristics as surface roughness and rate of material removal. The experimental runs were carried out on an ECM setup from Meta-Tech. The machining process achieved using a solution of 10% NaCl as electrolyte. The experimental setup of ECM is displayed in Fig. 1.

2.1 Machining Parameter Selection

In this experimental analysis, three input process parameters viz. voltage, feed rate, and signal are taken. L_{18} orthogonal array is taken as the design of experiments. The input parameters taken are shown in Table 1.

Fig. 1 Experiment setup (Electrochemical machine)

Table 1 ECM process parameters

Input parameters	Code	Levels	L(1)	L(2)	L(3)
Signal	A	2	1	2	
Voltage	B	3	8 V	10 V	12 V
Feed rate	C	3	0.1 mm/min	0.3 mm/min	0.5 mm/min

3 MOORA Technique

The MOORA method (Multi-objective optimization based on ratio analysis) has been utilized to ignore unsatisfactory substitutions by choosing the most appropriates gathering the determination parameter. It is a decision strategy, where the goals were limited for each proclamation of results from a lot of accessible options. The MOORA method can be functional in numerous forms of complex multi-objective optimization problems. In MOORA method, the recital of the diverse output responses is arranged in a decision matrix as specified in Eq. (1) [6–8].

$$X = \begin{bmatrix} x_{11} & x_{12} & \cdots & x_{1n} \\ x_{21} & x_{22} & \cdots & x_{2n} \\ \cdots & \cdots & \cdots & \cdots \\ x_{m1} & x_{m1} & \cdots & x_{mn} \end{bmatrix} \tag{1}$$

where performance measure of the i-th alternative on j-th attribute is x_{ij}, m and n are the number of alternatives and attributes, respectively.

A ratio system will be formed by normalizing the data of the formed decision matrix using Eq. (2).

$$x_{ij}^{*} = x_{ij} / \left[\sum_{i=0}^{m} x_{ij}^{2} \right]^{\frac{1}{2}} \quad (j = 1, 2, \ldots, n) \tag{2}$$

where the normalized value lies between 0 and 1 is presented by x_{ij}^{*} for x value in i-th alternative on j-th attribute.

After that, for maximization problem, the normalized value will be added or in case for minimization problems subtracted. Now and again, a portion of the properties have more significance than others, and to convey significantly more significance to these characteristics, they are increased by their relating weight. After the consideration of weight, the equation will be:

$$y_i = \sum_{j=1}^{g} w_j x_{ij}^{*} - \sum_{j=g+1}^{g} w_j x_{ij}^{*} \tag{3}$$

where g is the maximized number of attribute and w_i is the weight of j-th attribute. The normalized assessment values presented by y_i for the i-th alternative relating to all the j-th attributes. After calculation of normalized assessment value, ranking of y_i is done from highest to lowest value to know the best alternate among the entire attributes. Thus, maximal y_i value is the best alternative among all since ranking of the y_i is the final preference [17, 18].

4 Desirability Function Analysis

Here, the initial step is to change every reaction into their relating attractive quality esteem otherwise desirable values. The quality esteem changes in the zero to one which is liable to the favored exhibit of the reactions and the objective incentive to be achieved. In the event that the response touches its target value, which is the most desired condition, its desirability is consigned as a union. If the significance of the response falls outer the recommended tolerance rage, which is not wanted, its desirability value is implicit as zero. Consequently, desirability value may vary within zero to unity. Derringer and Suich in 1980 suggested the formulae to calculate the desirability of each response liable upon the condition of the target value. For the equivalent responses, each individual desirability index (d_i) can be calculated using two forms of the desirability functions according to the requirement of the response characteristics [18].

A. *Smaller-the better*

The desirability function of smaller-the-better characteristics can be defined as specified in Eq. (4) [18]:

$$d_i = \begin{cases} 1 & \hat{y} \le y_{\min} \\ \left(\frac{\hat{y}-y_{\max}}{y_{\min}-y_{\max}}\right)^{r}, & y_{\min} \le y \le y_{\max}, r \ge 0 \\ 0 & \hat{y} \ge y_{\min} \end{cases} \tag{4}$$

where the $y_{\min}$ and $y_{\max}$ signifies the lower and the upper tolerance limit of $\hat{y}$ and r denotes the weight. If the equivalent response is liable to be nearer to the target, the higher value of the weight is set; or else, it is fixed to smaller value.

B. *Larger-the better*

The desirability function of the larger-the better characteristics can be defined as specified in Equation (5) [9, 10]:

$$d_i = \begin{cases} 0 & \hat{y} \le y_{\min} \\ \left(\frac{\hat{y}-y_{\min}}{y_{\max}-y_{\min}}\right)^r, & y_{\min} \le \hat{y} \le y_{\max}, r \ge 0 \\ 1 & \hat{y} \ge y_{\min} \end{cases} \tag{5}$$

where the $y_{\min}$ signifies the minor tolerance limit of $\hat{y}$, the $y_{\max}$ represents the major tolerance limit of $\hat{y}$ and r signifies the weight.

In the subsequent stage, the individual desirability index of all the responses is pooled to form a single value known as composite desirability D_0 by the following specified Eq. (6):

$$D_0 = (d_1^{w1} d_2^{w2} \ldots d_n^{wn})^{\frac{1}{w}} \tag{6}$$

where the individual desirability value is represented by d_i for each y_i and is the individual desirability of the asset y_i, w_i is the weight in the composite desirability and W is the sum of the distinct weights.

5 TOPSIS Method

TOPSIS method (Technique in order of preference by similarity to ideal solution) is used for estimating the substitutions earlier the various characteristic decision making; established on statistics that chosen ancillary ought to have the smallest separation distance from the positive ideal solution and the most remote separation distance from the negative ideal solution. Positive ideal solution defines the best performance values established by any substitute for each characteristic; however, negative ideal solution can be demarcated as worst performance values [19–21]. Following steps can be used for TOPSIS method execution.

In the first step, the decision matrix is formed:

$$D = \begin{matrix} A_1 \\ A_2 \\ \cdots \\ A_i \\ \cdots \\ A_m \end{matrix} \begin{bmatrix} x_{11} & x_{12} & \ldots & x_{1j} & x_{1n} \\ x_{21} & x_{22} & \ldots & x_{2j} & x_{2n} \\ \cdots & \cdots & \cdots & \cdots & \cdots \\ x_{i1} & x_{i2} & \ldots & x_{1j} & \ldots \\ \cdots & \cdots & \cdots & \cdots & \cdots \\ x_{m1} & x_{m2} & \ldots & x_{mj} & x_{mn} \end{bmatrix} \tag{7}$$

Here, conceivable alternatives represented by A_i (i = 1, 2, …, m), aspects linking to alternative performance are presented by x_j (j = 1, 2, …, n) and the performance of A_i with respect to attribute x_j is x_{ij}.

In the subsequent step, normalization matrix is done using Eq. (8):

$$r_{ij} = \frac{x_{ij}}{\sqrt{\sum_{i=1}^{m} x_{ij}^2}} \tag{8}$$

where r_{ij} signifies the normalized performance of A_i relating to attribute x_j.

In the third step, weighted decision matrix is formed using Eq. (9):

$$V = \lfloor v_{ij} \rfloor V = w_j r_{ij} \tag{9}$$

$$D = \begin{bmatrix} y_{11} & y_{11} & \cdots & y_{1i} & y_{1n} \\ y_{21} & y_{22} & \cdots & y_{2j} & y_{2n} \\ \cdots & \cdots & \cdots & \cdots & \cdots \\ y_{i1} & y_{i2} & \cdots & y_{1j} & \cdots \\ \cdots & \cdots & \cdots & \cdots & \cdots \\ y_{m1} & y_{m2} & \cdots & y_{mj} & y_{mn} \end{bmatrix} \tag{10}$$

Here, $\sum_{j=1}^{n} w_j = 1$

The fourth step involves the calculation of ideal solution values for both positive and negative, respectively.

(a) For positive ideal solution values:

$$\begin{aligned} A^+ &= \left\{ \left(\max_i y_{ij} | j \in J \right), \left(\min_i y_{ij} | j \in J | i = 1, 2, \ldots, m \right) \right\} \\ &= \{ y_1^+, y_2^+, \ldots, y_j^+, \ldots, y_n^+ \} \end{aligned} \tag{11}$$

(b) For negative ideal solution values:

$$A^+ = \left\{ \left(\min_i y_{ij} | j \in J \right), \left(\max_i y_{ij} | j \in J | i = 1, 2, \ldots, m \right) \right\}$$

$$= \{y_1^-, y_2^-, \ldots, y_j^-, \ldots, y_n^-\} \tag{12}$$

Here,

$J = \{j = 1, 2, \ldots, n|j\}$ and $J' = \{j = 1, 2, \ldots, n|j\}$: Associated with beneficial and nonbeneficial attributes.

In the fifth step, separation measures are determined. In this prospect, the distance of individual alternatives from the ideal solution is calculated by n-dimensional Euclidean distance using Eqs. (13) and (14).

$$S_i^+ = \sqrt{\sum_{j=1}^{n} (y_{ij} - y_j^+)^2 i = 1, 2, \ldots, m} \tag{13}$$

$$S_i^+ = \sqrt{\sum_{j=1}^{n} (y_{ij} - y_j^-)^2 i = 1, 2, \ldots, m} \tag{14}$$

The final step involves the determination of performance coefficient overall, which is closest to the ideal solution using the following Eq. (15).

$$C_i^+ = \frac{s_i}{s_i^+ + s_i^-}, i = 1, 2, \ldots, m; \quad 0 \leq C_i^+ \leq 1 \tag{15}$$

6 Result and Discussion

Table 2 represents the detail experimental data with respect to L_{18} orthogonal array considering Taguchi design of experiments. The values of MRR and surface roughness have been noted with different levels of inputs viz. signal, voltage, and feed rate.

6.1 Optimization Using MOORA Technique, Desirability Function Analysis, and TOPSIS Method

First, MOORA optimization method is applied to find out the optimal parameters. The normalization of the output characteristics is conferred to Eq. (2). After that, the normalized assessment values were calculated. An equal percentage of weight is considered for MRR, surface roughness, and the sum of all the weights will be 1. The MOORA overall assessment value is calculated using Eq. (3) and ranked according to the highest value of the overall assessment value. Table 3 shows the value overall assessment value and their ranking according to the highest value. Second, desirability function analysis was done. The individual desirability values (d_i) for MRR is calculated using larger-the-better criterion as in Eq. (5) and smaller-the-better

Table 2 Taguchi design of L_{18} with input and output values

Run. No.	Signal	Voltage	Feed rate	MRR	Surface roughness
1	1	8	0.1	0.039822	3.3600
2	1	8	0.3	0.011312	2.3333
3	1	8	0.5	0.021325	3.5333
4	1	10	0.1	0.002548	5.7333
5	1	10	0.3	0.063439	11.2000
6	1	10	0.5	0.036331	4.6667
7	1	12	0.1	0.012357	3.2667
8	1	12	0.3	0.037656	3.2667
9	1	12	0.5	0.071363	4.9333
10	2	8	0.1	0.025350	3.1000
11	2	8	0.3	0.079032	6.1333
12	2	8	0.5	0.100127	5.8667
13	2	10	0.1	0.004408	4.0000
14	2	10	0.3	0.035389	1.6667
15	2	10	0.5	0.039236	7.8667
16	2	12	0.1	0.003108	7.5333
17	2	12	0.3	0.008408	2.8000
18	2	12	0.5	0.037172	0.5333

criterion for surface roughness as in Eq. (4). After calculating individual desirability, the composite desirability (d_0) is calculated using Eq. (6). Third, TOPSIS method was used. The normalization of output characteristics has been done between 0 and 1 so to achieve output a single dimensionless scale. Here, each response parameters has been allotted with equal weight priority by considering equally significant. The separation distance has been calculated considering both positive and negative ideal solution values, respectively. Finally, the performance index overall (OPI) has been calculated and tabulated in Table 3.

6.2 Best Experimental Run

A. *MOORA technique*: In the above table, it can be seen that by using the MOORA method, for a particular values of input parameter, experiment number 16 has the highest value of the overall assessment value. Hence, experiment number 16 which is having the factor setting A2 B3 C1, i.e., signal of 2, voltage of 12 V, and feed rate of 0.1 mm/min is the optimal parameter combination for ECM.
B. *Desirability function analysis*: Fig. 2 shows the main effect plot for the composite desirability value for the levels of the MRR and surface roughness. Essentially,

Table 3 Overall assessment value, composite desirability/ and overall performance coefficient

Run. No.	MOORA		Desirability Function	TOPSIS
	Overall assessment value, y_i	Rank	Composite desirability, d_0	Overall performance coefficient, C+
1	0.0294	13	0.4025	0.2829
2	−0.0231	9	0.5911	0.3862
3	−0.0238	8	0.6313	0.4501
4	−0.1238	2	0.0000	0.2982
5	−0.0864	3	0.4848	0.4015
6	−0.0097	10	0.5250	0.4653
7	−0.0415	6	0.2645	0.2045
8	0.0257	12	0.4530	0.3079
9	0.0774	16	0.4932	0.3717
10	−0.0032	11	0.3465	0.2999
11	0.0705	15	0.5351	0.4033
12	0.1326	18	0.5753	0.4671
13	−0.0794	4	0.2403	0.3152
14	0.0561	14	0.4288	0.4185
15	−0.0748	5	0.4690	0.4823
16	−0.1633	1	0.2085	0.2215
17	−0.0414	7	0.3971	0.3249
18	0.0867	17	0.4373	0.3887

the smaller the composite desirability, the better is the multiple performance characteristics. In Fig. 2, the combination of A1 B1 C3 shows the smallest value of the mean-effect plot for the factors A, B, and C, respectively. Therefore, A1 B1 C3, i.e., signal of 1, voltage of 10 V, and feed rate of 0.5 mm/min is the optimal parameter combination for ECM. The residual plot for *S/N* ratio also has been presented in Fig. 3. For each individual parameter level, response for signal to noise ratios for composite desirability has been tabulated in Table 4.

C. *TOPSIS method*: In Fig. 4, the combination of A2B2C3 shows the smallest value of the S/N ratio for the factors A, B, and C, respectively. Therefore, A2B2C3, i.e., signal of 2, voltage of 10 V, and feed rate of 0.5 mm/min is the optimal parameter combination for ECM. The residual plot for S/N ratio also has been presented in Fig. 5. For each individual parameter level, response for signal to noise ratios for composite desirability has been tabulated in Table 5.

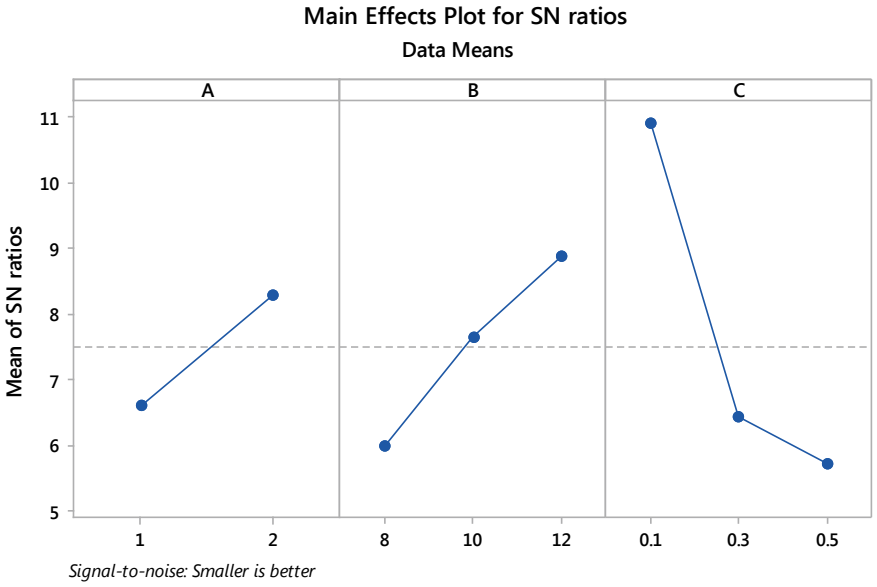

Fig. 2 Main-effect plot for S/N ratio of composite desirability

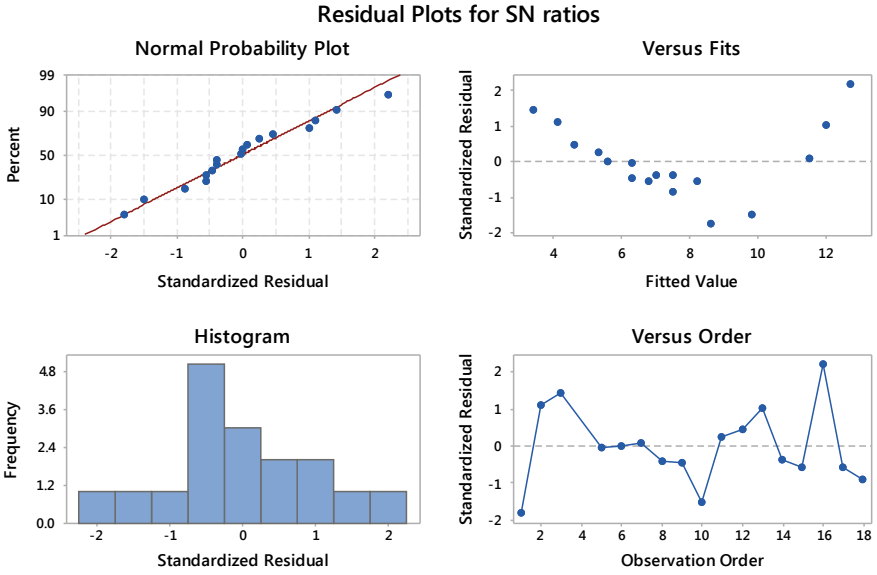

Fig. 3 Residual plot for S/N ratio of composite desirability

Table 4 Response table for signal to noise ratios for composite desirability

Level	A	B	C
1	6.615	5.984	10.933
2	8.287	7.640	6.423
3		8.899	5.716
Delta	1.672	2.915	5.218

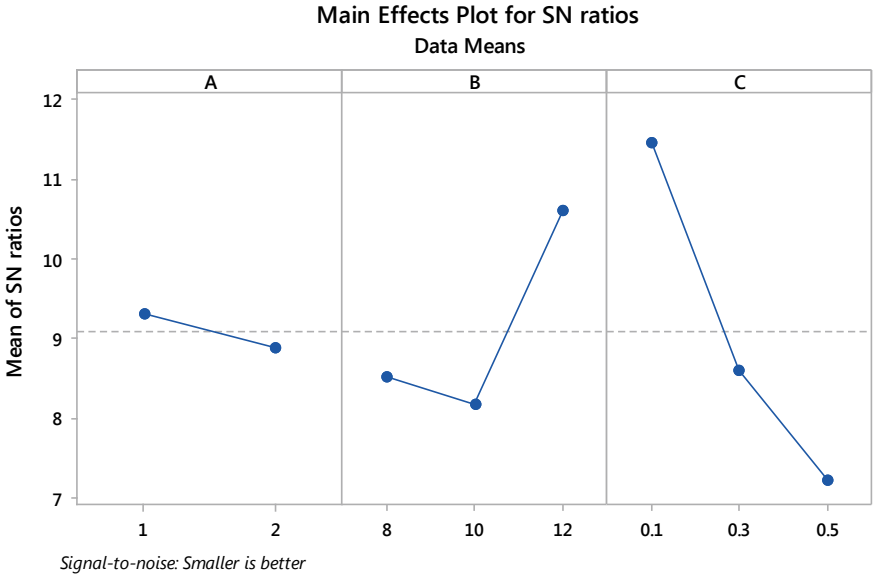

Fig. 4 Main-effect plot for S/N ratio of overall performance coefficient

6.3 Most Influential Factor

Tables 6 and 7 give the results of the analysis of variance (ANOVA) calculated values from the composite desirability overall performance coefficient, respectively. According to Table 5, factor C, the feed rate with 67.14% of contribution, is the most significant controlled parameters for ECM followed by factor B, the voltage with 22.4% of total contributions and factor A, the signal with 4.98% if the minimization of MRR and surface roughness are simultaneously considered. Similarly, from Table 6, factor C, the feed rate with 71.18% of total contributions, is the most significant controlled parameters for ECM followed by factor B, the voltage with 26.42% of total contributions and factor A, the signal with 1.07% if the minimization of MRR and surface roughness are simultaneously considered.

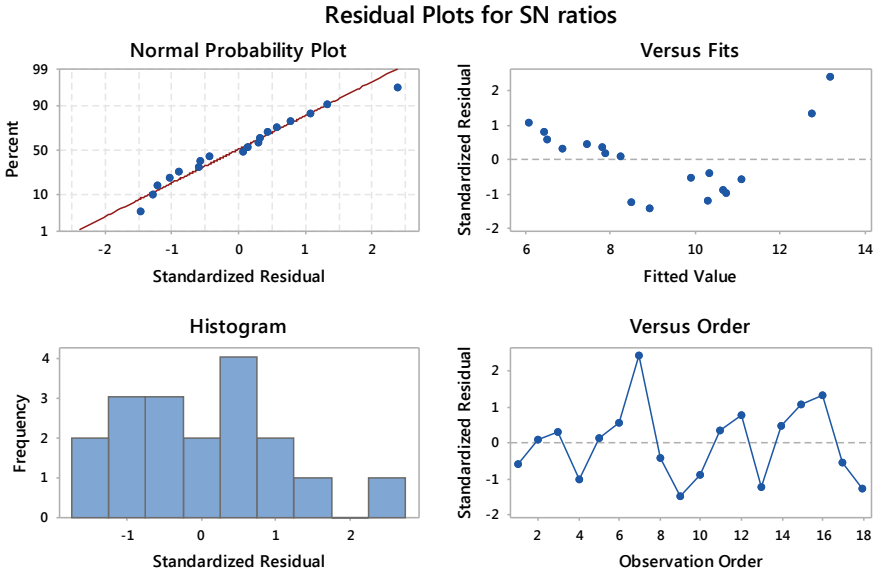

Fig. 5 Residual plot for S/N ratio of overall performance coefficient

Table 5 Response table for signal to noise ratios for overall performance coefficient

Level	A	B	C
1	9.318	8.521	11.474
2	8.607	8.884	8.168
3		10.613	7.221
Delta	0.434	2.445	4.253

Table 6 ANOVA results for composite desirability

Source	DF	Adj SS	Adj MS	*F*-Value	*P*-Value	% Contribution
A	1	6.062	6.0619	24.71	0.000	4.98
B	2	27.286	13.6430	55.62	0.000	22.40
C	2	81.801	40.9003	166.74	0.000	67.14
Error	11	2.698	0.2453			2.21
Total	16	121.830				100

$S = 0.4953$; R-Sq $= 97.8\%$; R-Sq(adj) $= 96.8\%$

Table 7 ANOVA result for overall performance coefficient

Source	DF	Adj SS	Adj MS	*F*-Value	*P*-Value	% Contribution
A	1	0.8477	0.8477	9.62	0.009	1.07
B	2	20.9563	10.4781	118.96	0.000	26.42
C	2	56.4683	28.2341	320.53	0.000	71.18
Error	12	1.0570	0.0881			1.33
Total	17	79.3293				100.00

$S = 0.2968$; R-Sq = 98.7%; R-Sq(adj) = 98.1%

6.4 Confirmatory Experiment

The confirmatory experiments were done using the optimal machining parameters combination obtained from desirability function analysis and TOPSIS method, Table 8. These confirmatory experiments were used to calculate and authenticate the enhancement in the feature of performance characteristics for machining of EN-19 chromoly steel. The optimal conditions using desirability function analysis and TOPSIS are A1 B1 C3 and A2 B2 C3, respectively. The estimated composite desirability and overall performance coefficient can be calculated using the most optimum parameters as in Eq. (16).

$$\mu_{\text{predicted}} = a_{2m} + b_{1m} - 3\mu_{\text{mean}} \tag{16}$$

where a_{2m} and b_{1m} are the individual mean values of the composite desirability and overall performance coefficient with optimum level values of each parameter, and μ_{mean} is the overall mean of composite desirability and overall performance coefficient. The predicted mean ($\mu_{\text{predicted}}$) at optimal setting for desirability function analysis and TOPSIS are 6.07162 and 3.41312, respectively.

From the confirmation experiment performed with the same experimental setup, there is a better covenant between the predicted optimal S/N ratio and experimental optimal S/N ratio for both approaches. Hence, both the parameter settings of the electrochemical machining process were canned as optimal.

Table 8 Confirmatory test results

Optimization technique	Optimal setting	Predicted optimal *S/N* ratio	Experimental optimal *S/N* ratio
Desirability function analysis	A1 B1 C3	6.07162	5.98799
TOPSIS	A2 B2 C3	3.41312	3.29879

Table 9 Optimal cut parameters using three optimization methods

Algorithm	Optimal setting	Signal	Voltage (V)	Feed rate (mm/min)
MOORA	A2 B3 C1	2	12	0.1
Desirability function analysis	A1 B1 C3	1	8	0.5
TOPSIS	A2 B2 C3	2	10	0.5

7 Conclusion

In this study, the influence of the machining parameters is investigated using different optimization techniques which lead to fulfill different contradictory objectives of the output responses as MRR has to be maximized while surface roughness is to be minimized. After applying multi-objective optimization for both the output responses for getting the desired optimal settings, it was concluded as:

- The feed rate is the most influencing parameter in the electrochemical machining process as its contribution to the experiment is the maximum than other two parameters from ANOVA.
- Optimal factor setting for ECM using three optimization methods is stated in Table 9.
- Confirmatory test results are found incredibly good agreement with those predicted.
- The methods stated above can also be applied efficiently for other engineering problems for finding the optimal alternatives.

References

1. Nayak KC, Tripathy RK (2012) Taguchi integrated least square support vector machine an alternative to artificial neural network analysis of electrochemical machining process. IOSR J Mech Civ Eng 1:01–10
2. Goutam RK (2012) Optimization and experimental investigation on EN19 using hexagonal shaped electrode in ECM. BTech thesis. National Institute of Technology, Rourkela
3. Kumar KS (2013) Experimental investigation of MRR and surface roughness of EN-18 steel in ECM. BTech thesis. National Institute of Technology, Rourkela
4. Ranganathan S, Senthilvelan T (2011) Multi-response optimization of machining parameters in hot turning using grey analysis. Int J Adv Manuf Technol 56:455–462
5. Jiang B, Lan S, Ni J, Zhang Z (2014) Experimental investigation of spark generation in electrochemical discharge machining of non-conducting materials. J Mater Process Technol 214:892–898
6. Za G, Povr O, Hrapavosti I (2010) Use of grey based Taguchi method in ball burnishing process for the optimization of surface roughness and microhardness of AA 7075 aluminum alloy. Mater Technol 44:129–135
7. Qu N, Fang X, Li W (2013) Wire electrochemical machining with axial electrolyte flushing for titanium alloy. Chin J Aeronaut 26:224–229

8. Sahu SN, Nayak D, Rana HK (2013) Optimization of ECM process parameter by using simulated annealing approach. Int J Adv Trends Comput Sci Eng 2:18–21
9. Lu J, Riedl G, Kiniger B, Werner E (2014) Three-dimensional tool design for steady-state electrochemical machining by continuous adjoint-based shape optimization. Chem Eng Sci 106:198–210
10. Mukherjee R, Chakraborty S (2012) Selection of the optimal electrochemical machining process parameters using biogeography-based optimization algorithm. Int J Adv Manuf Technol 64:781–791
11. Chakradhar D, Gopal AV (2011) Multi-objective optimization of electrochemical machining of EN31 steel by grey relational analysis. Int J Model Optim 1:113–117
12. Rama Rao S, Padmanabhan G (2012) Application of Taguchi methods and ANOVA in optimization of process parameters for metal removal rate in electrochemical machining of Al5%SiC composites. Int J Eng Res Appl 2:192–197
13. Das AK, Saha P (2013) Analysis on fabrication of micro-tools by micro-electrochemical machining process. Int J Nanomanuf 9:66–76
14. Rao SR, Padmanabhan G (2013) Linear modeling of the electrochemical machining process using full factorial design of experiments. J Adv Mech Eng VII:13–23
15. Tang L, Guo YF (2013) Experimental study of special purpose stainless steel on electrochemical machining of electrolyte composition. Mater Manuf Process 28:457–462
16. Kamaraj AB, Sundaram MM (2013) Mathematical modeling and verification of pulse electrochemical micromachining of microtools. Int J Adv Manuf Technol 68:1055–1061
17. Khan A, Maity KP (2016) Parametric optimization of some non-conventional machining processes using MOORA method. Int J Eng Res Afr 20:19–40
18. Barua A, Jeet S, Parida B, Samantray A, Bagal DK (2018) Comparative evaluation and optimization of 4-cylinder CI engine camshaft material using finite element analysis: a hybrid MOORA technique and Taguchi based desirability function analysis approach. Int J Tech Innov Mod Eng Sci 4:105–114
19. Barua A, Jeet S, Parida B, Sahoo BB, Bagal DK, Samantray A (2018) Virtual optimization of motorcycle sprocket material by using FEA and Taguchi coupled TOPSIS-GA-SA. Int J Adv Sci Res Manage 3:54–63
20. Jeet S, Barua A, Parida B, Sahoo BB, Bagal DK (2018) Multi-objective optimization of welding parameters in GMAW for stainless steel and low carbon steel using hybrid RSM-TOPSIS-GA-SA approach. Int J Tech Innov Mod Eng Sci 4:683–692
21. Parida B, Barua A, Jeet S, Bagal DK (2018) Fabrication and mechanical characterization of jute-glass-silk fiber polymer composites based on hybrid RSM-GRA-FIS and RSM-TOPSIS approach. Int J Res Eng Appl Manage 4:25–33

Recent Advances in Thermal Infrastructure

Computational Study of Mist Jet Impingement Heat Transfer on a Flat Plate with Slotted Nozzle

Bikram Kumar Pani and Dushyant Singh

Abstract The work presents the numerical investigation of a slot mist jet impingement cooling on an isothermal flat plate surface at three different temperatures 323, 350 and 363 K. A two-dimensional model was analyzed with mist (air and water) as working fluid. The distance from nozzle exit to the surface of the heated plate is varied from $h/S = 4$ and 8. The numerical analysis was carried out for jet Reynolds number $Re_s = 2750$ varying the volume fraction, vof 1–10% and size of droplet from 1 to 300 micron. Addition of mist causes significant increase of heat transfer coefficient as compared to the single-phase heat transfer coefficient. The numerical result of local heat transfer coefficient is compared with the experimental results of Gardon and Akfirat [1]. Also, the effect of heat transfer coefficient varying the distance from nozzle to plate spacing is shown. The turbulence models $k - \varepsilon$ and $k - \omega$ SST were considered for the study, and their differences are also presented.

Keywords Jet impingement · Mist · Droplet · Volume fraction

Nomenclature

S	Slot width (m)
h	Slot height from plate (m)
X	Length of the plate (m)
q''	Heat flux (W/m^2)
H	Heat transfer coefficient (W/m^{2}K)
T_w	Temperature of plate (K)
T_j	Temperature of jet (K)
U	Average velocity (m/s)
K	Turbulent kinetic energy (m^2/s^2)
P	Pressure (pa)

B. K. Pani · D. Singh (✉)
National Institute of Technology Manipur, Langol 795004, Manipur, India
e-mail: dushyant@nitmanipur.ac.in

A. K. Parwani and PL. Ramkumar (eds.), *Recent Advances in Mechanical Infrastructure*, Lecture Notes in Intelligent Transportation and Infrastructure,
https://doi.org/10.1007/978-981-32-9971-9_14

D	Diameter of droplet (m)
N	Component
I	Mass transfer rate (Kg/s)
i, j, k	Indices
g	Gravitational acceleration (m/s^2)
F	Interactive force per unit volume (N/m^3)
Q	Rate of heat transfer per unit mass (W/Kg)
W	Rate of work done per unit mass (J/kg)
E	Total internal energy per unit mass (J/kg)
TI	Turbulence intensity
D_0	Diameter of the jet (m)
T	Temperature of the jet (K)
e^*	Total internal energy per unit mass
vof	Volume fraction

Greek Symbols

μ	Dynamic viscosity (Pas)
ρ	Mass density (kg/m^3)
α	Volume fraction
ε	Turbulent dissipation rate (m^2/S^3)
ω	Specific dissipation rate
ν	Kinematic viscosity
σ_c	Phase stress tensor (Pa)

Notations

$\partial/\partial t$ $\partial/\partial x$	Partial derivative

Non-dimensional Numbers

Re_S	Reynolds number [ρUS/μ]

1 Introduction

Jet impingement heat transfer has always been a topic of interest in many engineering applications such as cooling of metals during heat treatment processes, gas turbine, drying of paper, textiles industry, cooling in grinding process and cooling of laser weapons. This flow is used extensively in process engineering applications that involve cooling, coating and drying operations.

In slot air jet impingement, Gardon and Akfirat [1] have experimentally concluded the relationship of various factors, like Reynolds number, nozzle to plate spacing and how it affects heat transfer coefficient. They found that the heat transfer coefficient forms a bell-shaped curve for nozzle to plate spacing greater than 14 slot width. There are a number of experimental and numerical studies done on slot air jet impingement [2–4].

Multiphase jet impingement gives higher heat transfer coefficient as compared to single-phase air jet impingement. Pakhomov et al. [5] numerically studied on two-phase mist jet impingements on flat surface and concluded that the heat transfer rate is increasing several times as compared to single phase due to the droplet effect of mist. There are very few number of experimental studies done on both coaxial [6] and round [7, 8] mist jet impingement.

In the present study, the experimental result of Gardon and Akfirat [1] is numerically simulated using CFD codes. Here, the working fluid used is mist (air + water) with various α and different droplet diameter (D_0) to predict the heat transfer behavior by using different turbulence models. The effect of heat transfer for multiphase jet impingement is compared to that of experimental results for the single-phase jet impingement.

2 Content

In this present study, slot jet impingement of mist on an isothermal flat plate is numerically investigated. The nozzle to plate spacing, $h/S = 4$, for a flow of $Re_s = 2750$ impinging on a flat plate is considered for the present numerical study [1]. The slot width of the nozzle S is 0.0015875 m, and the size of the plate is X, 0.1524 m in length. The different volume fractions are 1, 5 and 10%, and the different droplet diameters (D_0) are 1, 30, 50, 100 and 300 μm. along with three different temperatures at 323, 350 and 363 K. The same analysis is carried out for $h/S = 8$. Geometry of domain is as shown in Fig. 1.

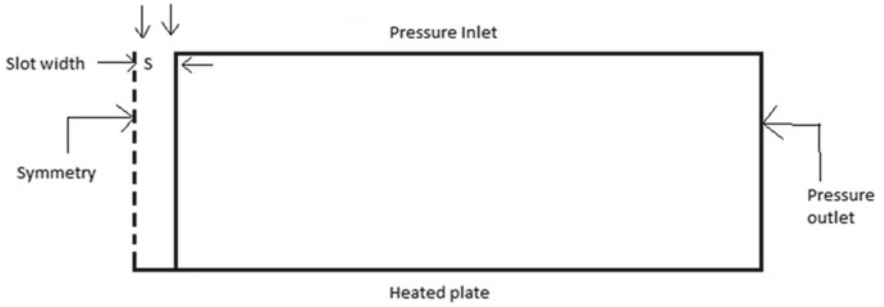

Fig. 1 Geometry of domain

2.1 Numerical Method

In this present study, the numerical simulations are carried out using the CFD source code, OpenFOAM [9] done for unsteady state, symmetric, turbulent slot jet impingement problem with different volume fractions at 1, 5 and 10%, different droplet diameters such as 1, 30 50, 100 and 300 μm, at different temperatures 323, 350 and 363 K and two different nozzles to plate spacing such as $h/S = 4$ and $h/S = 8$. The PIMPLE algorithm combines the PISO with the SIMPLE algorithm was used for pressure and velocity coupling. Second-order upwind scheme was used for spatial discretization of convective terms. Temporal term is discretized by second order accurate fully implicit central differencing technique, i.e., Euler

2.2 Equations

$$\frac{\partial}{\partial t}(\rho_N \alpha_N) + \frac{\partial}{\partial x_i}(\rho_N j_{Ni}) = I_N \tag{1}$$

Equation 1 indicates the Individual Phase Continuity Equation (IPME).

$$\frac{\partial}{\partial t}(\rho_N \alpha_N U_{Nk}) + \frac{\partial}{\partial x_i}(\rho_N j_{Ni} U_{Ni} U_{Nk}) = \alpha_N \rho_N g_k + F_{Nk} - \delta_N \left\{ \frac{\partial p}{\partial x_k} - \frac{\partial \sigma^D_{Cki}}{\partial x_j} \right\} \tag{2}$$

Equation 2 indicates the Individual Phase Momentum Equation (IPME).

$$\frac{\partial}{\partial t}(\rho_N \alpha_N e^*_N) + \frac{\partial}{\partial x_i}(\rho_N j_{Ni} U_{Ni} e^*_N) = Q_N + W_N + QI_N + WI_N + \delta_N \frac{\partial}{\partial x}(U_{Ci} \sigma_{Cij}) \tag{3}$$

Table 1 Boundary condition of the simulation

Boundary name	Boundary condition
Inlet	Uniform velocity distribution is considered at $Re = 2750$ and at 300 K temperature. The α vary at 1, 5, 10% and the bubble diameter (D_0) vary from 1 micron to 300 micron
Plate	Isothermal heated plate with no-slip condition is considered
Symmetry	Symmetry
Outlet	Both pressure inlet and pressure outlet are open sides of the domain at 300 K

Equation 3 indicates the Individual Phase Energy Equation (IPEE).

$$Re_s = \frac{uS}{v} \tag{4}$$

Equation 4 indicates the Equation of Reynolds Number wrt S.

$$H = \frac{q''}{(T_w - T_j)} \tag{5}$$

Equation 5 indicates the Equation of Heat Transfer Coefficient.

2.3 Boundary Condition

Table 1 shows the boundary condition of the simulation.

2.4 Grid Independence Test and Turbulence Test

Grid independence test was done by using three different grid dimensions (x, y): 225 × 100, 280 × 150 and 340 × 200 as shown in Fig. 2. Hence the grid 280 × 150 was chosen for further studies. Grid was made sufficiently fine so as to ensure a $y+$ below unity. For the calculation of turbulence intensity, two different RANS turbulence models were used as shown in Fig. 3. The results of two turbulence models were comparable near the stagnation point.

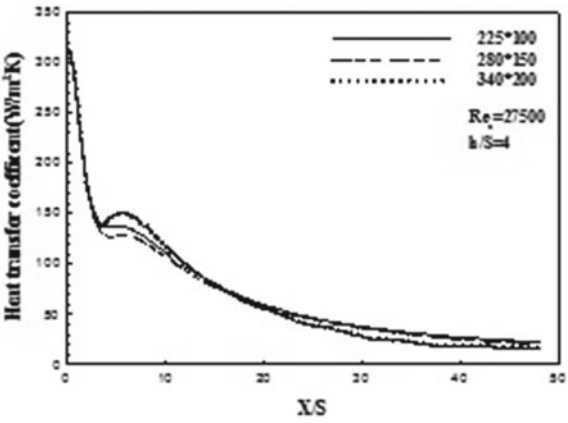

Fig. 2 Grid independence test

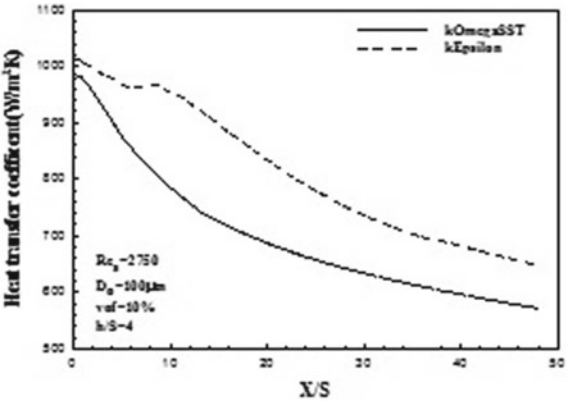

Fig. 3 Turbulence model test

3 Results and Discussions

3.1 Effect of Volume Fraction

Figure 4 shows heat transfer coefficient over the flat surface for the different volume fractions of mist. From Fig. 4, it can be observed that the numerical result of heat transfer coefficient shows a close agreement with the available experimental data. The mist injection with 1 and 5% shows nearly 200 and 240% increase in heat transfer coefficient near the stagnation point as compared to single-phase air jet impingement, respectively. However, at high vof, significant increase in heat transfer coefficient is not observed as the air jet impingement result. In Fig. 4 show that increase in volume fraction increases the heat transfer coefficient and, it may be due to by increasing volume fraction a thin layer will be generated over the flat surface and because of

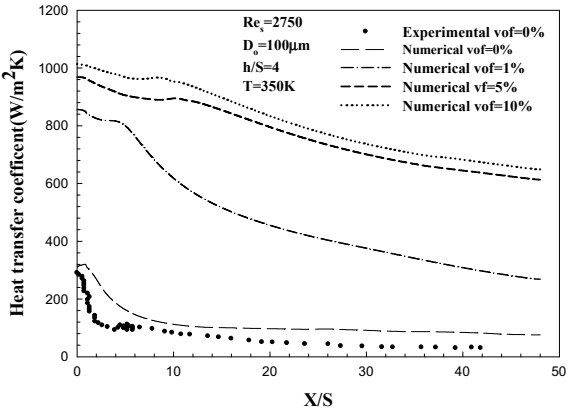

Fig. 4 Variation of heat transfer coefficient for different volume fractions

thin boundary layer generation heat transfer rate will increase by evaporation and convection cooling.

3.2 Effect of Bubble Diameter

Figure 5a shows that at 1 micron droplet the heat transfer coefficient at the stagnation point is more as compared to the 30 and 50 micron. But the overall heat transfer rate increases for higher droplet size. In Fig. 5b, the heat transfer coefficients are nearly similar at the stagnation point up to $X/S = 10$, after which the heat transfer coefficient is higher for 300-micron droplet diameter.

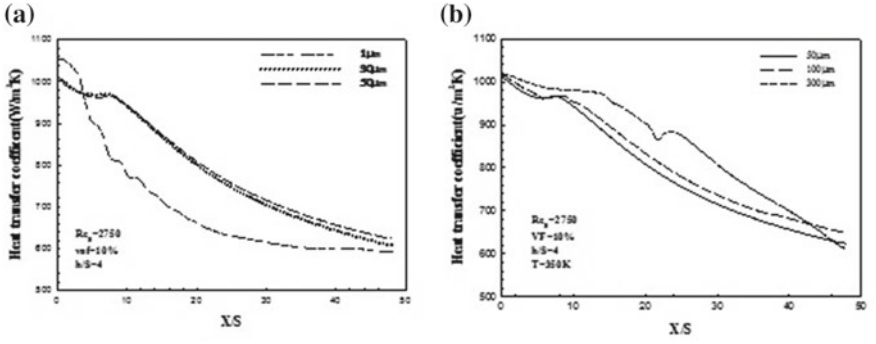

Fig. 5 Variation of heat transfer coefficient for the droplet size. **a** 1 μm, 30 μm, 50 μm and **b** droplet size, **a** 50 μm, 100 μm and 300 μm

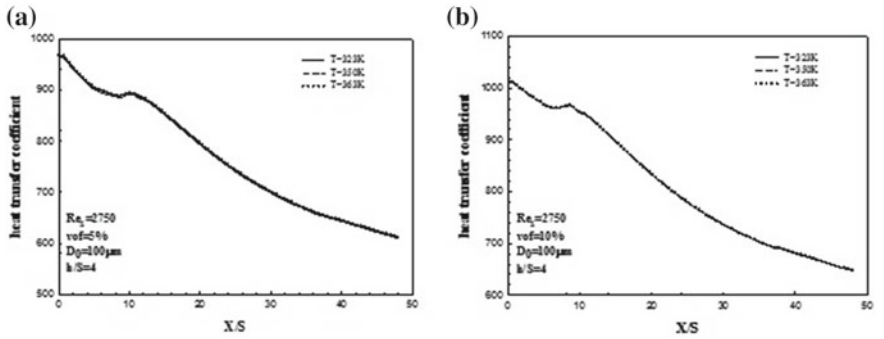

Fig. 6 Heat transfer coefficient at different plate temperatures

3.3 Effect of Temperature

From Fig. 6, it can be clearly seen that heat transfer coefficient does not change with varying plate temperature (323, 350 and 363 K) at $h/S = 4$ for both volume fractions of 5 and 10% because the ratio of q'' to the $(T_w - T_j)$ always remains constant.

3.4 Effect of Nozzle to Plate Height

In Fig. 7a, b, at constant volume fraction of 1%, heat transfer coefficient decreases around 50% at the stagnation point region by increasing the nozzle to plate spacing from $h/S = 4$ to $h/S = 8$. However, for vof 1%, the effect of nozzle to plate height is significant till $X/S = 20$, but after that there is a very small difference. In case of vof 5%, the effect of nozzle to plate height is observed throughout the length of the flat plate.

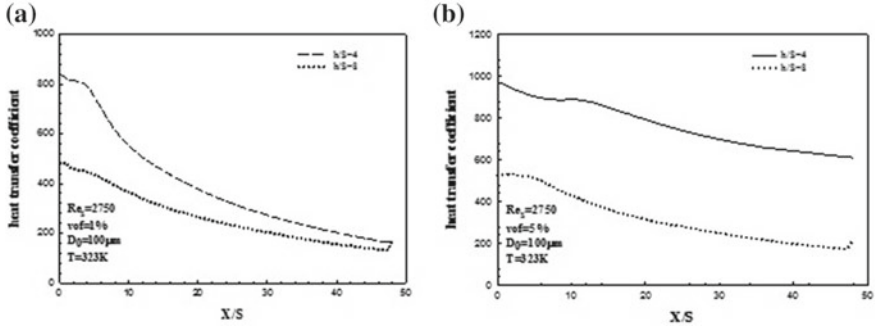

Fig. 7 Heat transfer coefficient at different nozzles to plate space

4 Conclusion

Mist addition causes the substantial increase in heat transfer rate (several times) compared with single-phase air jet impingement due to thin boundary layer generation on surface. By increasing droplet diameter, the heat transfer coefficients can also be increased.

Variation in plate temperature has no effect on the heat transfer coefficient.

The effect of nozzle to plate spacing is distinctly observed. The heat transfer coefficient increases with decrease in nozzle to plate spacing.

References

1. Gardon R, Akfirat JC (1966) Heat transfer characteristics of impinging two dimensional jets, Trans ASME (1966)
2. Dutta R, Dewan A, Srinivasan B (2013) Comparison of various integration to wall (ITW) RANS models for predicting turbulent slot jet impingement heat transfer. Int J Heat Mass Transf 65:750–764
3. Zhe J, Modi V (2001) Near wall measurements for a turbulent impinging slot jet. Transa ASME 123:112–120
4. Narayanan V, Seyed-Yagoobi J, Page RH (2004) An experimental study of fluid mechanics and heat transfer in an impinging slot jet flow. Int J Heat Mass Transf 47:1827–1845
5. Pakhomov MA, Terekhov VI (2010) Enhancement of an impingement heat transfer between turbulent mist jet and flat surface. Int J Heat Mass Transf 53:3156–3165
6. Quinn C, Murray DB, Persoons T (2017) Heat transfer behaviour of a dilute impinging air water mist jet at low wall temperatures. Int J Heat Mass Transf 11:1234–1249
7. Kanamori A, Hiwada M, Mimatsu J, Sugimoto H (2009) Control of impingement heat transfer using mist. J Therm Sci Technol 4(2):202–213
8. Graham KM, Ramadhyani S (1996) Experimental and theoretical studies of mist jet impingement cooling. J Heat Transfer 118(2):343–349
9. OpenFOAM user guide version [5.0] (2017)

Generation and Characterization of Bio-oil Through Slow Pyrolysis Process from *Jatropha Curcas* Shell

Vikram Rajai, Hiren Shah, Dhaval Patel, Himanshu Patel and Subarna Maiti

Abstract In this era of twenty-first century, demand of energy is growing everyday. Out of all the energy resources, petroleum products are the major influencing parameters. But, these petroleum products are now at their basal levels. To get an alternative solution, renewable energy sector is highly focused, to get rid of this trouble. There are various methodologies which are used for the generation of alternative fuels and one of them is pyrolysis. Pyrolysis is a decomposition process which occurs in thermo-chemical approach in the absence of oxygen. This paper shows the pyrolysis of *jatropha curcas* shell which is a complete wastage after the production of bio-diesel from jatropha seeds. *Jatropha curcas* shell was heated in a fixed bed reactor around 500 °C in the absence of oxygen and after the dehydration, bio-oil was obtained. The density of the bio-oil was observed as 957.8 kg/m^3, viscosity 3.152 cP at 25.2 °C, calorific value 29.07 MJ/kg and refractive index 1.4557 at 26.55 °C. The pour point and fire point were observed as −38 °C and 28.5 °C, respectively. Apart from these, the ultimate analysis of the bio-oil presents that it contains carbon 61.09% (wt%), hydrogen 7.22% (wt%), nitrogen 3.51% (wt%), oxygen 28.17% (wt%) and sulphur 819 ppm. The higher oxygen content in this bio-oil helps the base fuel inside the internal combustion engine to burn more efficiently.

Keywords Bio-oil · Dehydration · *Jatropha curcas* · Pyrolysis · Refractive index · Thermo-chemical

V. Rajai (✉) · H. Shah · D. Patel
Chhotubhai Gopalbhai Patel Institute of Technology, Uka Tarsadia University, Gopal-Vidyanagar, Maliba Campus, Surat 394350, Gujarat, India
e-mail: vikram.rajai@utu.ac.in

H. Patel · S. Maiti
Process Design & Engineering Cell, CSIR-Central Salt & Marine Chemicals Research Institute, G.B Marg, Bhavnagar 364002, Gujarat, India

A. K. Parwani and PL. Ramkumar (eds.), *Recent Advances in Mechanical Infrastructure*, Lecture Notes in Intelligent Transportation and Infrastructure,
https://doi.org/10.1007/978-981-32-9971-9_15

1 Introduction

India is 3rd largest consumer of hydrocarbon products in this globe after the USA and China. The fuel consumption of India is 4.1 million barrel/day and most of the energy resources are imported from foreign countries [1]. Statistical data suggests that India's consumption of the energy resources is almost five times higher than the production [2]. The effect of accretion in the price of petroleum products affects Indian economy a lot.

The utilization of petroleum products is one of the most affecting parameters on the environmental degradation in developing as well as developed countries. Petroleum products possess trivial amount of sulphur and nitrogen also and they react with the environmental gases which are converted into harmful gases like sulphur oxides (SO_x) and nitrogen oxides (NO_x) to cause acid rain. Various other harmful gases like carbon monoxide (CO), carbon dioxide (CO_2) and particulate matters are emitted during the operation of internal combustion (IC) engine.

Considering both the factors, i.e. pollution and insufficient petroleum resources, researchers are working on many alternative ways to fulfil the demand of consumption in such a way that the solution of the air pollution can also be solved and bio-fuel is one of them. There are many alternatives which are available for bio-fuel production like jatropha, jojoba, animal fats, algae, fungi, seaweed, etc. Various processes like pyrolysis, transesterification, carbon fixation, etc., are used for the generation of bio-fuel. Out of these, pyrolysis is widely adopted method which is generally utilized for carbonic materials. The amount of generation of solid waste in India is more than 960 million tonnes per year and out of this 350 million tonnes are agricultural wastes [3]. This carbonic waste can be used as feed in the case of pyrolysis process. According to National Bio-diesel Mission (NBM) of Government of India, base fuel will be blended 20% with bio-fuels. To reach this target, we require 97.14 MT of jatropha fruit. A jatropha fruit contains 65% weight of jatropha seed and rest 35% weight is of jatropha shell [4]. So, approximately 34.09 MT of jatropha shell will be generated as a waste. This shell can be fed as a raw material for a pyrolyser to generate a bio-oil. Apart from bio-oil which is condensable portion of the pyrolysis output, we are also getting solid char and non-condensable gases from it.

Further considering the rate of heating, pyrolysis process is classified into slow pyrolysis and fast pyrolysis. The rate of heating in slow pyrolysis is in the range of 5–20 °C/min and that for fast pyrolysis is in the range of 40–300 °C/min. Table 1

Table 1 Fast versus slow pyrolysis

Type of pyrolysis	Yield of bio-oil (%)	Yield of char (%)	Energy efficiency (%)
Fast pyrolysis (max. temperature 500 °C)	75	8.5	70.3
Slow pyrolysis (max. temperature 500 °C)	52.8	31.9	37.5

gives the comparison between the yields of various products in the case of fast as well as slow pyrolysis [5].

From this table, we can observe that we are getting higher yield of bio-oil in the case of fast pyrolysis compared to slow pyrolysis and higher yield of char in the case of slow pyrolysis compared to fast pyrolysis. But heat rate ultimately depends on the capacity of the set-up.

Prasanta Das et al. conducted thermo gravimetric analysis (TGA) on *jatropha curcas* shell which is shown by solid line in the graph (Fig. 1). From this experimentation, it is observed that the weight loss for the shell is almost constant after 500 °C [6]. This study suggests that we should heat the *jatropha curcas* shell up to 500 °C as after that weight loss of the material is almost negligible. Moreover, derivative gravimetric analysis(DTG) which is presented by dotted line in the graph shows that weight loss per minute is maximum around 290 °C and further increasing temperature, weight loss rate decreases. The calorific value of the bio-oil was obtained as 30.67 MJ/kg which can be upgraded by reduction process with hydrazine up to 48.92 MJ/kg and it is higher than the pure diesel.

Channiwala et al. gave the relation of higher heating value (HHV) for any hydrocarbon fuel as the following equation [7]. Following equation gives an idea about how the calorific value of any fuel is varying along its constituent's proportion. This relation plays a key role while investigating the performance parameters of an engine.

$$\mathrm{HHV} = 0.3491 * \mathrm{C} + 1.1783 * \mathrm{H} + 0.1005 * \mathrm{S} - 0.1034 * \mathrm{O} - 0.0151 * \mathrm{N} \quad (1)$$

Here, C, H, N, S and O are the percentage constituents inside the fuel. From this equation, we can observe that oxygen and nitrogen have the negative impact on the overall effect of calorific value. This is the reason for the lower calorific value of the bio-oil.

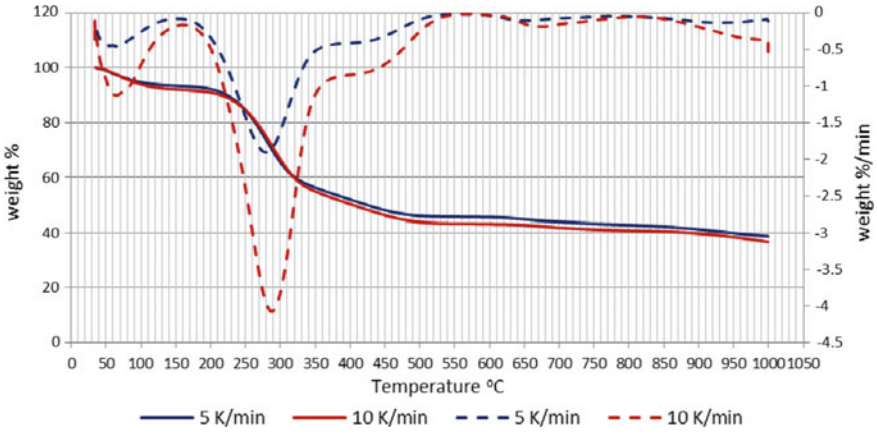

Fig. 1 Thermo gravimetric analysis

Putun et al. carried out pyrolysis of cotton seed at different temperatures along with the effect of sweeping gas. Cotton seed cakes were collected from various sources and they were crushed. The sole purpose of sweeping gas is to push the processed gases inside the chamber of a reactor and to stop any further reaction inside it [8].

S. Murugan et al. observed the variation of break thermal efficiency of an engine (η_{bth}) for tire pyrolysis oil blended with diesel which suggests that η_{bth} increases as we blend the base fuel with bio-oil [9]. It is because of better mixing of the fuel inside the chamber and higher content of the oxygen in bio-oil which increases the chances of complete combustion.

The higher viscosity of the bio-fuels causes loss in engine power. Higher the viscosity of the fuel, lesser the homogenous mixture will take place inside the chamber which will cause an incomplete combustion [10]. On the other side, Gumus et al. observed that break specific fuel consumption (BSFC) of an engine will reduce as we are mixing the base fuel with bio-fuel because of the higher oxygen content in the fuel [11].

Engine emission also gets affected by the blending. As we blend bio-fuel with the base fuel amount of carbon dioxide (CO_2) and carbon monoxide (CO)decrease as bio-fuel contains lower carbon content and higher oxygen content with respect to petroleum products [12, 13]. Engine performance and emission data suggest that *jatropha curcas* shell bio-oil can be used as an alternative fuel for compression ignition engine without any major modification [14].

2 Production Methodology

Jatropha curcas shell is used as a raw material for the production of oil. Jatropha seeds are used for the production of bio-diesel by transesterification and its shell is dried to remove the excessive moisture content. The density of shell may vary from 80 to 100 kg/m^3. After drying, feedstock was fed inside the reactor horizontally. Vacuum was created with the help of vacuum pump to remove the excessive oxygen from the chamber and to create a pressure drop as well. Chamber was heated up to 500 °C approximately with the heating rate of 7 °C/min. The holding time of this process was 150 min. Condensable gases were collected inside the oil sump which was kept inside the ice bath. Coil type heat exchangers were used to condense the gases generated through the process. Non-condensable gases were released to the atmosphere and char was collected to generate a fertilizer from it. The following flow diagram (Fig. 2) shows the path of the process.

Figure 3a, b shows the pictorial view of raw material and produced oil as well. Here, feedstock can be crushed also to increase the amount of oil generated. But in that way also energy input to generate the fuel will be increased which ultimately

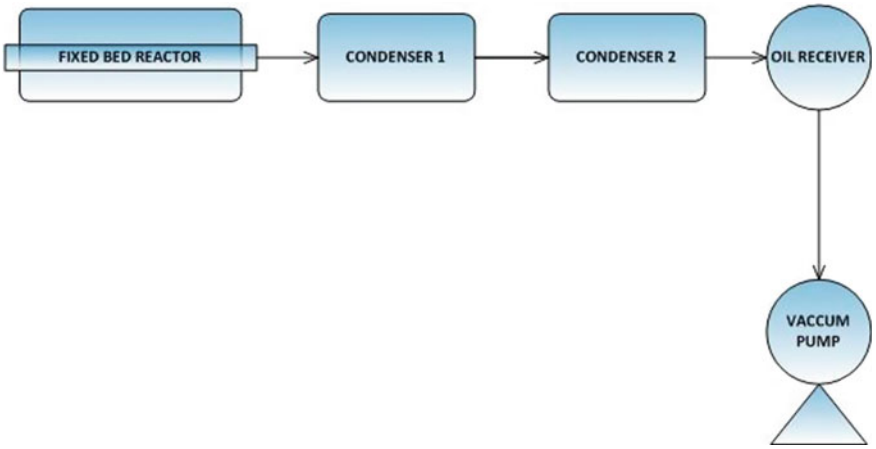

Fig. 2 Process layout

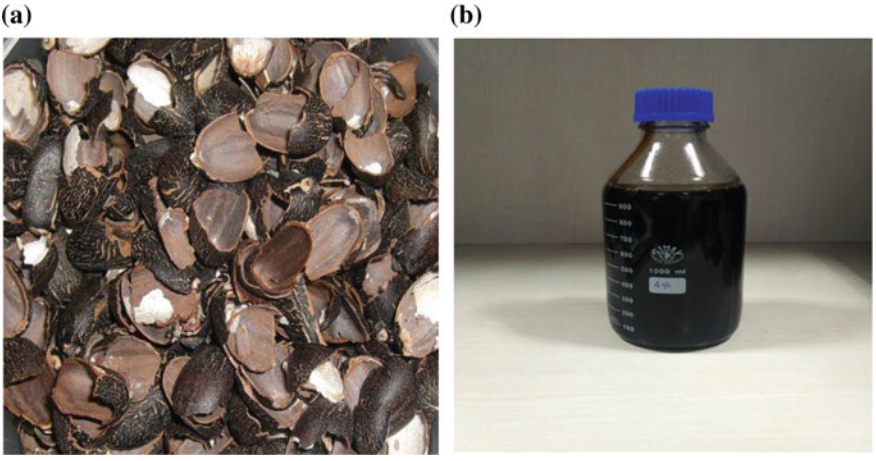

Fig. 3 **a** *Jatropha curcas* shell, **b** bio-oil blended diesel

decreases energy efficiency. To dry the shell, solar drier can also be used to give a provision to renewable energy.

Here, nitrogen gas can also be used as a sweeping gas to push the generated gases through outlet. It can be beneficial for pushing the gases, as well as it can act as an inert gas . For simplicity, a vacuum pump was used to suck the air at initially and processed gases as process starts.

3 Characterization of the Bio-oil

Characterization of the bio-oil was carried out on the basis of its physical properties, fuel properties and ultimate analysis.

3.1 Physical Properties

Table 2 gives the comparison between the physical properties of the bio-oil and diesel which includes density, viscosity, calorific value, refractive index and moisture content.

Above table shows that the viscosity of the bio-oil is slightly higher compared to pure diesel which can be beneficial in the case of lubrication of the engine. But on the other hand, it can create heterogeneous mixture inside the chamber which decreases the combustion efficiency of the fuel [15]. The density difference between both the fuels is negligible which makes them a perfect blend. The calorific value of the bio-oil is almost 35% lower than the pure diesel because of higher oxygen content inside it. But its calorific value can be enhanced by upgradation through reduction process.

3.2 Fuel Properties

Table 3 gives various fuel properties of the bio-oil compared to the diesel.

Pour point of any fuel is a temperature below which liquid fuel is converted into semi solid form and loses its fluid properties. Whereas cloud point is a temperature

Table 2 Physical properties

Property	Bio-oil	Diesel
Viscosity (cP)	3.152 (25.2 °C)	2.823 (25.2 °C)
Density (kg/m^3)	957.8 (26.4 °C)	823.3(26.4 °C)
Refractive index	1.4557 (26.5 °C)	1.4603 (26.7 °C)
Calorific value (MJ/kg)	29.07	44.28
Moisture content (wt%)	<0.5	–

Table 3 Fuel properties

Property	Bio-oil (°C)	Diesel (°C)
Fire point	28.5	44
Pour point	−38	−23
Cloud point	–	−5

Table 4 Ultimate analysis

Constituents	Bio-oil	Diesel
Carbon (wt%)	61.09	85.72
Hydrogen (wt%)	7.22	13.2
Nitrogen (wt%)	3.51	0.18
Oxygen (wt%)	28.17	0.6
Sulphur (ppm)	819	409

at which fuel is converted into cloudy form. Fire point is a minimum temperature at which vapour of a fuel will burn at least 5 s after combustion. Lower fire point of the bio-oil can be an important parameter to improve the brake thermal efficiency of the engine [16].

3.3 Ultimate Analysis

This analysis gives the information about the constituents present into the bio-oil.

From Table 4, we can observe that carbon content is lower in the case of bio-oil compared to diesel which can be the reason for lower carbon monoxide emission for blended fuel. Moreover, oxygen content is higher inside the bio-oil which diminishes the calorific value of the fuel and increases the break specific fuel consumption. But this excessive oxygen helps the base fuel for complete combustion. Apart from this, sulphur content is higher in bio-oil which enhances the emission of various sulphur oxides (SO_x).

3.4 Effect of Blending on Calorific Value

As we know that due to higher oxygen content, bio-oil has lower calorific value as compared to diesel. So, as we increase the amount of bio-oil in blending, its overall calorific value decreases accordingly. Table 5 and graph (Fig. 4) explain this phenomena conveniently. Here, four different samples of the fuels were prepared which contained different amount of fuels, i.e. 0, 4, 8, 12 and 16% of bio-oil and rest was pure diesel. The calorific values of these samples were analysed in a Bomb calorimeter.

Table 5 Calorific value versus blend

Blend proportion (%)	0	4	8	12	16
Calorific value (MJ/kg)	45.682	44.753	44.058	43.547	42.863

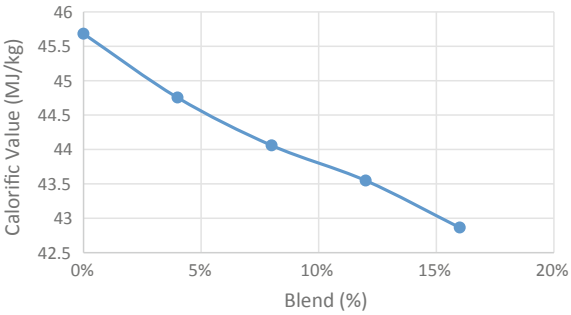

Fig. 4 Calorific value versus blend

From this graph, we can conclude that as the blend proportion increases, the overall calorific value of the fuel decreases because of higher oxygen content in the fuel.

4 Conclusion

In this study, pyrolysis of *jatropha curcas* shell was carried out at the temperature around 500 °C at the heat rate of 7 °C/min in the fixed bed reactor. It can be observed that the pyrolysis of shell is completed at this particular temperature because beyond this temperature, the gas output was almost negligible. The density and viscosity of the moisture-free bio-oil are nearer to that of pure diesel which makes it perfect soluble in it. On the other hand, the calorific value of the oil is around 65% of the pure diesel which increases the specific fuel consumption. The ultimate analysis of oil suggests that it contains higher amount of oxygen and because of that this oil works as an oxidizer inside the chamber which enhances combustion efficiency of the fuel. Pour point of the bio-oil is −38 °C which is much lower than diesel (−23 °C) and it can be beneficial for cold starting condition of the engine.

Acknowledgements We are thankful to CSIR-CSMCRI, Bhavnagar to provide us the experimental facility for pyrolysis. We also feel grateful for the support of the whole staff of Process Design and Engineering Cell(PDEC) Department, CSIR-CSMCRI.

References

1. Forbes website. https://www.forbes.com/sites/judeclemente/2015/08/07/indias-rise-to-3rd-place-in-oil-demand/#25ad4a9a1dc7. Accessed on 7 Aug 2015
2. Indexmundi website. https://www.indexmundi.com/factbook/topics/energy. Accessed on 2016
3. Jackson FR (1977) Recycling and reclaiming of municipal solid wastes. Conserv Recycl 1(2):235

4. Committee on Development of Biofuel (2008) Under the auspices of the Planning Comission of India (Courtesy 'case study' *Jatropha curcas* by GFU)
5. Bridgwater A, Carson P, Coulson M (2007) A comparison of fast and slow pyrolysis liquids from mallee. Int J Glob Energy Issues 27(2):204
6. Das P, Dinda M, Gosai N, Maiti S (2015) High energy density bio-oil via slow pyrolysis of *jatropha curcas* shells. Energy Fuels 29(7):4311–4320
7. Channiwala S, Parikh P (2002) A unified correlation for estimating HHV of solid, liquid and gaseous fuels. Fuel 81(8):1051–1063
8. Pütün E, Uzun BB, Pütün AE (2006) Fixed-bed catalytic pyrolysis of cotton-seed cake: effects of pyrolysis temperature, natural zeolite content and sweeping gas flow rate. Biores Technol 97(5):701–710
9. Murugan S, Ramaswamy M, Nagarajan G (2008) The use of tyre pyrolysis oil in diesel engines. Waste Manag 28(12):2743–2749
10. Öner C, Altun Ş (2009) Biodiesel production from inedible animal tallow and an experimental investigation of its use as alternative fuel in a direct injection diesel engine. Appl Energy 86(10):2114–2120
11. Gumus M, Kasifoglu S (2010) Performance and emission evaluation of a compression ignition engine using a biodiesel (apricot seed kernel oil methyl ester) and its blends with diesel fuel. Biomass Bioenergy 34(1):134–139
12. Kalam M, Husnawan M, Masjuki H (2003) Exhaust emission and combustion evaluation of coconut oil-powered indirect injection diesel engine. Renew Energy 28(15):2405–2415
13. Xue J, Grift TE, Hansen AC (2011) Effect of biodiesel on engine performances and emissions. Renew Sustain Energy Rev 15(2):1098–1116
14. Patel H, Rajai V, Das P, Charola S, Mudgal A, Maiti S (2018) Study of *jatropha curcas* shell bio-oil-diesel blend in VCR CI engine using RSM. Renew Energy 122:310–322
15. Agarwal AK (2007) Biofuels (alcohols and biodiesel) applications as fuels for internal combustion engines. Prog Energy Combust Sci 33(3):233–271
16. Agarwal D, Agarwal AK (2007) Performance and emissions characteristics of jatropha oil (preheated and blends) in a direct injection compression ignition engine. Appl Therm Eng 27:2314–2323

Feasibility Analysis of Photovoltaic (PV) Grid Tied System for Indian Military Station Considering Economic & Grid Cyber-Security Aspects

Ashish Sharma, V. Chintala and Suresh Kumar

Abstract The Indian Government in its pursuant towards building energy infrastructure is providing special stimulus towards utilization of renewable energy sources. India is not only bestowed with abundant sustainable resources but also possesses the second-largest army in the world having defence establishments spread all over the country. Employment of sustainable energy in defence sector has its own constraints. The current study looks into the feasibility case study of implementing a PV grid tied system for an Indian military station. The Solar potential for the chosen military station is studied and technical potential of roof top solar panels is determined by carrying out the site survey of available infrastructure of the Indian military station. The study explains the cyber-threats by connecting PV systems with grid. A unified threat management security system is incorporated and a comprehensive feasibility analysis including the economic viability of implementing the system in a military station is carried out.

Keywords Feasibility study · Photovoltaic · Grid cyber-security · Levelized cost

1 Introduction

Energy security is arguably the most vital element for accomplishment of military operations. The paradigm technological shift and revolution in military affairs have made military prowess of a nation exceedingly reliant on energy [1]. Energy security customarily was a means of fortifying protection from interruptions of essential energy systems [2]. The speedy growth of sustainable energy sources and shrinking of energy reserves and fossil fuels no longer hold the symbiotic affiliation with energy security [3]. Indian government over the years has incentivized the use of renewable

A. Sharma (✉)
Indian Defence Service, Vayusenabad MB Road, New Delhi, India
e-mail: ashishsharma2508@gmail.com

V. Chintala · S. Kumar
Mechanical Engineering Department, School of Engineering, Centre for Energy Research Centre (CAER), University of Petroleum and Energy Studies (UPES), Dehradun, India

A. K. Parwani and PL. Ramkumar (eds.), *Recent Advances in Mechanical Infrastructure*, Lecture Notes in Intelligent Transportation and Infrastructure,
https://doi.org/10.1007/978-981-32-9971-9_16

energy [4]. The percentage share of sustainable energy has risen steadily in India. However, India with its diverse demography and vast defence establishments, which are spread over the country, has plentiful unexplored opportunities of using sustainable energy in defence sector. The Ministry of New and Renewable Energy (MNRE) is bestowed with the responsibility of enhancing India's renewable energy capacity [5]. Since its inception MNRE has given tremendous impetus towards renewable sources, which now constitute 18% of total installed capacity [6]. In India, the MNRE cooperated with Ministry of Defence (MoD) in the year 2015 for reconnoitring the opportunities of utilizing renewable energy by setting up 300 MW of grid-connected solar photovoltaic power projects under viability gap funding (VGF) scheme [7].

Employing renewable energy for defence applications has tremendous opportunities but present equal challenges in terms of grid security. The PV power plant when connected to grid has to be protected in terms of threats against soft kills by cyber-attacks. Military establishment and military-technical equipment require reliable energy sources, however, use of grid tied Solar PV system for military station will be vulnerable to cyber-attacks [8–13] While investigating the challenges for using renewable energy for defence, the anatomy of cyber-threats on military power grids is to be analysed. With these considerations, efforts have been made to carry out a comprehensive feasibility study for realizing photovoltaic power system for an Indian military station. The following are the contributions in this paper:

- The study identifies one Indian military station and carries out the site survey for determining the roof top photovoltaic potential.
- With the help of simulations, financial viability analysis of the PV power plant is carried out.
- The study caters for special security military requirements and suggests a mitigation solution for cyber-threats.
- The study carries a comprehensive feasibility study of employing PV power system for an Indian military station.

2 Case Study: Employment of PV System for Indian Military Station

2.1 Resource Potential

A military station in India is chosen for carrying out the feasibility study. The site survey did not involve any security-sensitive areas of military station. The first step before undertaking the feasibility analysis is the determination of solar potential at the envisaged site. The theoretical solar potential was assessed by using the National Renewable Energy Laboratory (NREL) System Advisor Model. The System Adviser is an energy analysis software tool developed by National Renewable Energy Laboratory (NREL) which is operated by the US Department of Energy (DoE). The

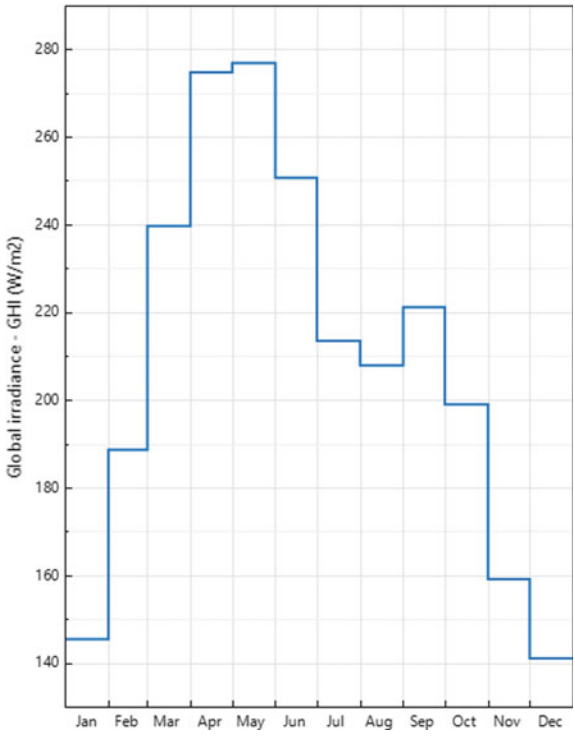

Fig. 1 Monthly GHI for site under study

monthly GHI Global Irradiance ($W/m^{2)}$ for the military station is shown in Fig. 1. The average GHI for the months of April, May and June is more than 6 $kWh/m^2/d$. The annual solar average is 5.06 $kWh/m^2/d$, making the chosen military station as an apt site for employing PV systems. The analysis of climatic data suggests employment of solar energy as the most effectual choice of energy for the chosen military station under study.

2.2 Technical Potential

In order to determine the potential for employing roof top solar panels with the available infrastructure, a site survey was undertaken at the available building infrastructure. PV modules of capacity per module 250 kWp multi-crystalline modules with efficiency >15% are selected to determine the peak power of the PV power plant project. The site survey involved the identification of usable infrastructure, area (Sqm) of usable space for mounting solar panels. The available barracks, workshops and residential buildings in the military station were identified for calculating the potential generation. The estimated PV potential is depicted in Table 1.

Table 1 Roof top PV potential of existing infrastructure

Sl no.	Building type	Roof area (Sqm)	Effective area (Sqm)	Solar panels (@250 W per 2 Sqm)	Power generation (W)
1	Hangers (08 Nos.)	22,728	14,206	7103	1,775,750
2	Training areas	1170	756	373	93,250
3	Storage area (03 Nos.)	4700	2970	1485	371,250
4	Fire point	210	150	75	18,750
5	Transport bay	160	100	50	12,500
6	Cafeteria	165	110	55	13,750
7	Office area	1100	739	369	92,375
8	Type 1 qtr (15 Nos.)	1200	750	375	93,750
9	Type 2 qtr (20 Nos.)	1890	800	400	100,000
10	Type 3 qtr (25 Nos.)	1180	750	375	93,750
11	Type 4 qtr (40 Nos.)	1800	800	400	100,000
12	Type 5 qtr (40 Nos.)	1100	600	300	75,000
13	Commercial areas	5500	3950	1975	493,750
14	Officers' mess	400	275	137	34,375
15	Mess canteen	380	225	112	28,000
Total generation capacity = 3,396,250 W					

The PV simulation and analysis is carried out with the help of NREL System Advisor. The DC system power rating of the photovoltaic array in kilowatts (kW) is chosen as 3300 kW. The DC to AC ratio used is 1.2, this is the ratio of inverter's AC rated size with array's rated DC size. The nominal rated DC to AC conversion efficiency is taken as 96%. The array type is fixed array roof type with a tilt of 33°. The ratio of photovoltaic area to the ground area is taken as 0.4. The total losses including soiling, shading, mismatch and other miscellaneous losses are taken at 14.08%.

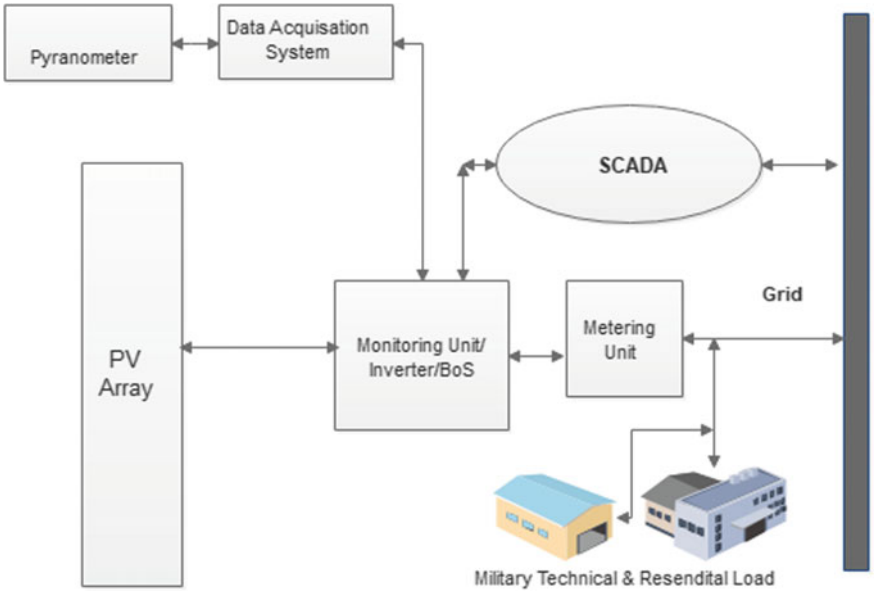

Fig. 2 Block diagram of PV system under the study

3 Cyber Vulnerability of Grid Tied PV System

3.1 SCADA Utility for PV Plant

Supervisory Control and Data Acquisition (SCADA) system is utilized for the grid automation system for power system utility. The grid-connected photovoltaic system considered in our study consists of PV panel, cables, inverters and energy management system as depicted in Fig. 2.

SCADA system is the heart of the energy management system. The vulnerability of SCADA system is mainly due to communication security. The SCADA vulnerability is explained in succeeding paragraphs, this is particularly important to understand in order to design the security for PV system under evaluation.

3.2 Identifying the Vulnerabilities in SCADA

SCADA system is used to automate the power plant utility system and control functions of plants. The monitoring and control sensors track the activity which includes network state monitoring and optimization. Forecasting, scheduling, linked to Programmable Logic Controllers (PLC) or remote sensors for automatically carrying the required tasks. The SCADA systems and the electric grid servers are net-

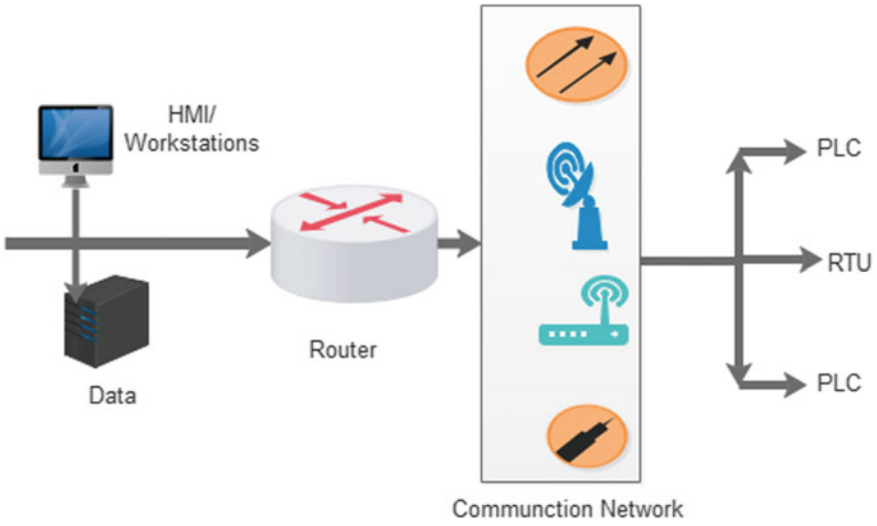

Fig. 3 SCADA communication network

worked as depicted in Fig. 3. The networking can be carried using media redundancy of wired and wireless system, optical fibre network, etc. In our case study, we have considered communication network using Ethernet and Transmission Control Protocol/Internet Protocol (TCP/IP) which can also be exploited like any other communication network [14].

The SCADA network can be secured with firewalls and antivirus systems. The antivirus protection is usually not proactive. The antivirus signatures are updated only after the vulnerabilities are exposed. For example, it was only after Stuxnet exploited the SCADA vulnerabilities, that the antivirus companies developed updates against such attacks. To attack the SCADA network once the vulnerabilities are identified, the next step is to attack the software, which can be done by an attack on Open System Interconnection (OSI) model. Diagnostic server attack using the User Diagram Protocol (UDP) port can be attacked in the network layer attack. In this type of network layer attack, the attacker can send UDP requests for diagnostic on the router. This is a phony request to consume the resources using the router ports which are enabled for the TCP and UDP requests. The SCADA systems employing TCP/IP can be attacked on the transport layer by injecting malware packets to take control of the controllers. Once the security has been breached and malware implanted, the PLC and sensors can be controlled. These sensors can be told to behave the instruments as per the malicious code to achieve the desired results. The process of exploiting the SCADA vulnerabilty is depicted in Fig. 4.

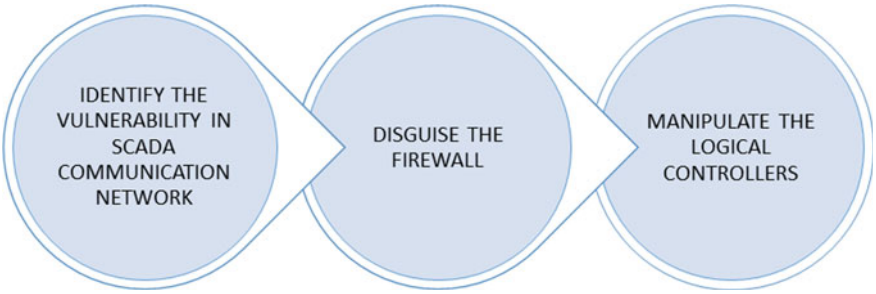

Fig. 4 Exploiting the SCADA vulnerability

4 Mitigation Methodology Employed in PV System Under Study

It is a well known fact that security comes with a cost; however, security and reliability are also one of the fundamentals pillars for military systems. The vulnerability of SCADA can be handled by employing security protocols. A secure redundant network for packet exchange over various distributed utilities is suggested as described in Fig. 5. Unified Threat Management (UTM) system is suggested to obviate the cyber-threats.

Unified Threat Management (UTM). The suggested network employs unified threat management systems which will include Firewalls, Antivirus Intrusion Prevention System (IPS), content filtering, encryption, etc. The UTM will have the following security specifications:

- **Perimeter Security**: Perimeter security devices are installed in the network, these consist of Firewalls and IPS between Layer-3 and access router. The IPS will

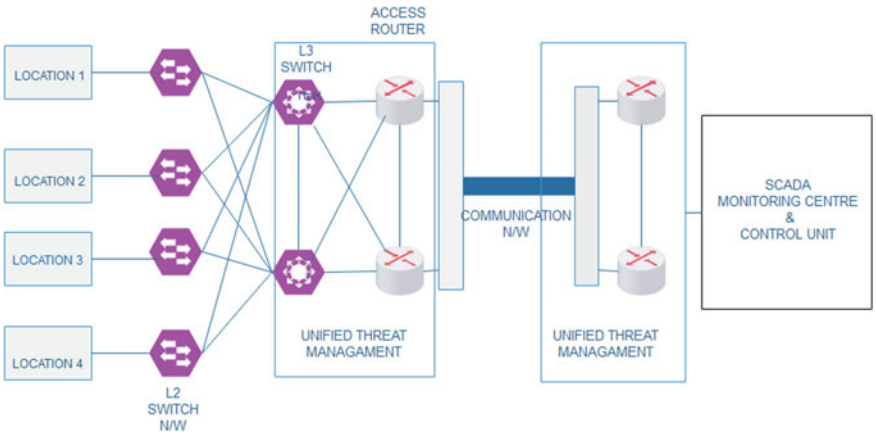

Fig. 5 SCADA network security employing UTM

do signature-based protection, proactive network-based behaviour analysis and proactive user-based behaviour analysis protection. Bulk encryption is employed after core routers.

- **Authentication, Authorization and Audit**: Every authenticated user will only have access. Databases of users of the network and their role specifications are configurable.
- **Customised Operating system**. Desktops using Internet domains mostly employ MS Windows The widely used operating system are most vulnerable to attacks. To overcome this, a customized operating system which provides secure browsing environment is suggested.

The implementation model in our simulation employs Digital Subscriber Line Access Multiplexer (DSLAM), ADSL modems, screening routers, firewalls, proxy servers and switches.

5 Financial Analysis

In order to carry out the financial analysis, the system costs are taken from the benchmarked cost of solar energy by Indian government. Additional security equipment cost is also catered into financial analysis. The system cost includes direct capital costs and indirect capital costs. The main constituents of capital costs include the cost of PV modules, cost of inverter, cost of cables and switchgears, cost of balance equipment, construction and labour cost. As a special case to cater for the military cyber-security, the additional cost of Intrusion Detection Systems (IDS), Bulk cryptographic apparatus is also added as additional cyber-security protection for grid-connected SCADA systems. The day-to-day cyber-security cost is also included in the operation & maintenance (O&M) costs for the power system. The financial parameters are evaluated for a life time of 25 years. Degradation rate is assumed at 0.5% per year. For carrying out the financial viability of the chosen project, the levelized cost of energy (LCOE) is calculated. LCOE is economic assessment for the setup of power plants by visually assuming the effective values such as initial cost, lifetime period of power plant, which are required after considering various economic subsidies given by government. LCOE is the minimum amount for the institution of the PV plant at which the energy must be sold after the establishment of the power plant [15]. The summary of evaluated parameters including the Levelized cost of energy is listed in Table 2. The nominal LCOE is 9.47 cents/kWh which is equal to 6.69 Indian Rupees (INR) with current exchange of 1USD equal to 70 INR.

Table 2 Financial evaluation of PV project

Metric	Value
Annual energy (year 1)	4,639,162 kWh
Capacity factor (year 1)	16%
Energy yield (year 1)	1406 kWh/kW
PPA price (year 1)	9.04 €/kWh
PPA price escalation	1%/year
Levelized PPA price (nominal)	9.71 €/kWh
Levelized PPA price (real)	6.87 €/kWh
Levelized COE (nominal)	6.47 €/kWh
Levelized COE (real)	6.70 €/kWh
Net present value	$93,746
Internal rate of return (IRR)	13.70%
IRR at the end of project	19.66%
Net capital cost	$2,817,887
Equity	$846,083
Size of debt	$1,971,804
Minimum DSCR	0.72

6 Summary and Conclusion

The feasibility study of employing PV systems for a military station in New Delhi, India has been presented in the study. The PV potential was calculated for already existing infrastructure buildings in the military station. With an annual average GHI of 5.06 kWh/m^2/d, the simulation results showed a production of 4,639,162 kWh energy for first year. The study suggested a secure communication network employing unified threat management scheme employing separate security layers. After comparison with the benchmarking cost of energy set by Indian government for various sustainable energy projects, the levelized cost of energy (LCOE) for the case study shows that solar energy is viable option. In addition, the cost of cyber-security in the grid tied PV system is arguably the most efficient source of renewable energy for the military station under study.

References

1. Nuttall WJ, Samaras C, Bazilian M (2017) Energy and the military: convergence of security, economic, and environmental decision-making, vol 30
2. Abrhám J, Britchenko I, Jankovic M, Garškaitė-Milvydienė K (2018) Energy security issues in contemporary Europe. J Secur Sustain Issues 7. https://doi.org/10.9770/jssi.2018.7.3(1)
3. Valentine SV (2011) Emerging symbiosis: renewable energy and energy security. Renew Sustain Energy Rev 15:4572–4578. https://doi.org/10.1016/j.rser.2011.07.095

4. Singh R (2018) Energy sufficiency aspirations of India and the role of renewable resources: scenarios for future. Renew Sustain Energy Rev 81:2783–2795. https://doi.org/10.1016/j.rser.2017.06.083
5. Ministry of new and renewable energy, Government of India strategic plan for new and renewable energy sector for the period 2011–17 Feb 2011. https://mnre.gov.in/file-manager/UserFiles/strategic_plan_mnre_2011_17.pdf. Accessed on 21 July 2018
6. Government of India MNRE annual report 2017–18. https://mnre.gov.in/file-manager/annual-report/2017-2018/EN/pdf/chapter-1.pdf. Accessed on 7 Nov 2018
7. MNRE, Order No 30/60/2013–14/NSM(Pt) Govt of India Implementation of Scheme for setting up over 300 MW of Grid-Connected & Off-grid Solar PV Power Projects by defence Establishments under Ministry of Defence and Para Military Forces (under MHA) with Viability Gap Funding (VGF) under Phase-II/III of JNNSM during 2014–15 and onwards
8. Prehoda EW, Schelly C, Pearce JM (2017) U.S. strategic solar photovoltaic-powered microgrid deployment for enhanced national security. Renew Sustain Energy Rev 78:167–175. https://doi.org/10.1016/j.rser.2017.04.094
9. Chlela M, Joos G, Kassouf M (2016) Impact of cyber-attacks on islanded microgrid operation. ACM Press, pp 1–5
10. Moreira N, Molina E, Lázaro J et al (2016) Cyber-security in substation automation systems. Renew Sustain Energy Rev 54:1552–1562. https://doi.org/10.1016/j.rser.2015.10.124
11. Arghandeh R, von Meier A, Mehrmanesh L, Mili L (2016) On the definition of cyber-physical resilience in power systems. Renew Sustain Energy Rev 58:1060–1069. https://doi.org/10.1016/j.rser.2015.12.193
12. Salmeron J, Wood K, Baldick R (2004) Analysis of electric grid security under terrorist threat. IEEE Trans Power Syst 19:905–912. https://doi.org/10.1109/TPWRS.2004.825888
13. Kushner D (2013) The real story of stuxnet. https://spectrum.ieee.org/telecom/security/the-real-story-of-stuxnet. Accessed on 15 Oct 2018
14. Zhu B, Joseph A, Sastry S (2011) A taxonomy of cyber attacks on SCADA systems. In: 2011 International conference on internet of things and 4th international conference on cyber, physical and social computing. IEEE, Dalian, China, pp 380–388
15. Short W, Packey DJ, Holt T (1995) A manual for the economic evaluation of energy efficiency and renewable energy technologies

Inlet and Outlet Geometrical Condition for Optimal Installation of Gravitational Water Vortex Power Plant with Conical Basin Structure

Rabin Dhakal, Sirapa Shrestha, Hari Neupane, Sunil Adhikari and Triratna Bajracharya

Abstract This paper focuses on micro-hydropower called gravitational water vortex power plant (GWVPP) which operates in ultra-low-head requirement (0.7–3 m) and is used in off-grid energy generation in rural areas. GWVPP is a new type of hydropower system in which a channel and a basin structure are used to form a water vortex, where the rotational energy from the water is extracted from runner at the center of the vortex. In this study, inlet and outlet geometrical conditions, specifically basin diameter and outlet diameter, of a recently acclaimed efficient conical basin design are found out. Different geometrical CAD models are developed by using SolidWorks software, and simulation is done with the help of commercial CFD code ANSYS CFX. Then, the geometrical relationship among these parameters is also analyzed and established. This result is finally validated through experimental testing of four different types of basin with distinct geometry.

Keywords Geometrical condition · Rural electrification · CFD · Micro-hydropower

1 Introduction

Gravitational water vortex power plant (GWVPP) is a relatively new micro-hydropower technology in which a rotation tank (basin) converts potential energy into kinetic energy, and a turbine, placed at the center of a water vortex, extracts this kinetic energy of water. An exit hole is made at the bottom of the basin through which the water vortex discharges [1]. GWVPP (Fig. 1) does not need a large head unlike other hydroelectric power plants: They can operate on heads as low as 0.7 m [2]. The

R. Dhakal (✉) · S. Shrestha · H. Neupane
School of Engineering, Kathmandu University, Kavre, Nepal
e-mail: rbndhakal@gmail.com

R. Dhakal · S. Adhikari
Institute of Engineering, Tribhuvan University, Thapathali Campus, Kathmandu, Nepal

T. Bajracharya
Institute of Engineering, Tribhuvan University, Pulchowk Campus, Lalitpur, Nepal

A. K. Parwani and PL. Ramkumar (eds.), *Recent Advances in Mechanical Infrastructure*, Lecture Notes in Intelligent Transportation and Infrastructure,
https://doi.org/10.1007/978-981-32-9971-9_17

Fig. 1 Gravitational water vortex power plant [2]

construction costs are relatively small which makes them suitable for Nepal in order to electrify rural communities. This has the possibility of removing the need for mega hydropower stations [3]. The installation of GWVPP can act as an exemplar project that can have huge environmental benefits with no negative environmental impact. Thus, for a developing country, like Nepal, this micro-hydropower technology is a boon to eradicate energy crisis [4].

Austrian engineer Franz Zotlöterer developed GWVPP technology, the method of initiating and extracting energy from water vortices for micro-hydropower generation [5]. More than 50 GWVPPs have already been installed in Europe since 2007 with more under construction. However, only a few of them are installed in other parts of the world [5–7]. Compared to other hydroelectricity generation technologies, the GWVPP has the greatest potential at low-head sites, and unlike conventional reaction and impulse turbines, they have the potential for maintaining high efficiencies even as the head approaches nearly zero. This is because the sole purpose of head is to create an artificial vortex in this system [8]. Also, unlike most of the micro-hydropower technologies, fish and small debris can pass through an operating GWVPP without causing damage to the turbine or harm to the fish. The GWVPP has several further advantages such as improving dissolved oxygen concentration through creation of vortex, homogenously disseminating contaminants in the water and increasing the heat of evaporation of water so that it can reduce its temperature itself during summer [5].

There have been many research works going on related to GWVPP technology around the world, and those works have contributed to minimize the cost of civil works. This has been incorporated from the early patent of Zotlöterer's to the latest patent of Kauris. There are different research articles based on the cost issues of civil works and the proposed solutions to reduce the cost. For instance, in 2015 Dhakal et al. [9] proposed a conical basin structure to develop an artificial vortex which solves

this cost issue. Conical basin increases the vortex strength and ultimately optimizes the basin size which results in reduction of civil works' cost associated with the construction of basin. However, demerit of the conical basin is that the geometry is quite complex to build. The complexity increases if concrete is used to build the basin thus adding to the cost of civil works. But the conical basin could be suitable for Kouris's system or any similar system where the power plant is small in size. Thus, a study to find out optimum dimension of the basin diameter and the outlet diameter is crucial in determining the plant size for the GWVPP.

2 Study of Past Researches

A number of researches have been carried out on GWVPP, focusing on the optimization of the basin structure design for the formation of the water vortex. Wanchat et al. [10, 11] indicated the important parameters that determine kinetic energy of free water vortex, namely head of water in the canal, outlet tube diameter, condition of inlet, and geometry of basin. They proposed a cylindrical tank having a plate to guide the incoming flow and an outlet tube at the bottom center to create the kinetic energy as the optimum design.

Mulligan et al. [1] studied the ratio between the basin diameter and the outlet tube diameter, concluding that the maximum the power output in cylindrical basin is obtained when the ratio of outlet tube diameter to basin diameter should be within 14–18%. In addition, the research conducted at Tribhuvan University, Nepal [12, 13], concluded that the vortex created by the use of conical basin structure having optimal position of runner results in improved output power and efficiency compared to cylindrical basin structure. Moreover, the research also concluded that the different geometrical parameters that determine the design of conical basin of GWVPP for a given flow and head are inlet width, basin diameter, notch length, canal height, and cone angle [9], which are shown in Fig. 2.

A team from Trinity College, Dublin [14], investigated operating conditions of GWVPP. The inlet flow rates, inlet water height, runner blade sizes, and blade numbers were all varied experimentally while recording turbine rotational speed, vortex height, and output torque for each setting using Prony brake dynamometer. It was found that turbine efficiency increases with increase in blade area and blade number for the blade configurations tested. Finally, of three inlet heights (height of water in the basin) tested, a height of 25 cm above the tank base (35% of the overall tank height) was found to be optimum for turbine performance. A maximum measured efficiency of 15.1% was found in these tests; however, the system was not optimized for this operation.

The research on runner design has lately been carried out by Dhakal et al. [15]. Computational fluid dynamics (CFD) analysis, similar to the research of Parajuli et al. [16], was carried out on three different runner designs with straight, twisted, and curved blade profiles. ANSYS CFX was used to analyze the fluid flow through channel, basin, turbine hub and blade, and results were used to evaluate efficiency

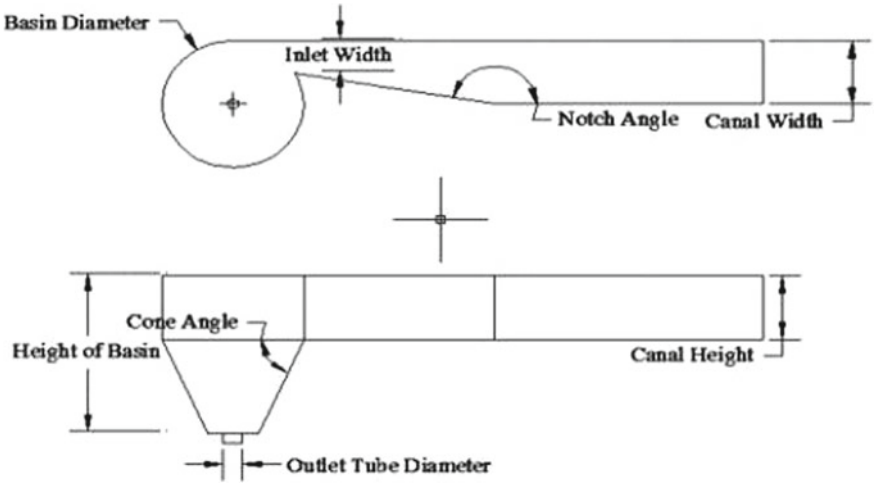

Fig. 2 Various geometrical parameter of basin structure taken for the study in the previous research [19]

of each of the runner designs. The CFD analysis showed curved blade profile to be the most efficient profile, with a peak efficiency of 82%, compared to 46% for the straight blade runner and 63% for the twisted blade. In order to validate the runner analysis, an experimental test of the turbine system was carried out in a scaled version of GWVPP. The testing showed that the runner behaved as predicted from the CFD analysis and had a peak efficiency point of 71% at 0.5 m head.

Current researches have solely focused on parameters that govern the design of basin structure conducting experimental and computational studies on GWVPP turbine system. However, no research has been published on inlet and outlet geometrical parameters for conical basin design. Therefore, this paper presents a numerical and experimental study that has been conducted on GWVPP system to select suitable inlet and outlet geometrical conditions for conical basin design using ANSYS CFX validated by an experimental study.

3 Numerical Analysis of Geometry

Computational fluid dynamics (CFD) deduces complex governing equations of a fluid system into a set of simpler algebraic equations which are easier to solve [17]. A CFD process includes three steps: preprocessing to specify boundary conditions, solver to define convergence criteria, and post-processing to analyze the results. The steady flow of water vortex is assumed in this paper. Moreover, the vortex is also assumed axisymmetric and incompressible. The following equation gives the continuity equation and the Navier–Stokes equations in cylindrical coordinates,

which is governing equation of flow.

$$\frac{\partial V_r}{\partial r} + \frac{\partial V_z}{\partial z} + \frac{V_r}{r} = 0 \tag{1}$$

$$V_r \frac{\partial V_\theta}{\partial r} + V_z \frac{\partial V_\theta}{\partial z} - \frac{V_r V_\theta}{r} = \nu\left(\frac{\partial^2 V_\theta}{\partial r^2} + \frac{\partial V_\theta}{r\partial r} - \frac{V_\theta}{r^2} + \frac{\partial^2 V_\theta}{\partial z^2}\right) \tag{2}$$

$$V_r \frac{\partial V_r}{\partial r} + V_z \frac{\partial V_r}{\partial z} - \frac{V_\theta^2}{r} + \frac{\partial \rho}{\rho \partial z} = \nu\left(\frac{\partial^2 V_r}{\partial r^2} + \frac{\partial V_r}{r\partial r} - \frac{V_r}{r^2} + \frac{\partial^2 V_r}{\partial z^2}\right) \tag{3}$$

$$V_r \frac{\partial V_z}{\partial r} + V_z \frac{\partial V_z}{\partial z} - \frac{\partial \rho}{\rho \partial z} = g + \nu\left(\frac{\partial^2 V_z}{\partial r^2} + \frac{\partial V_z}{r\partial r} + \frac{\partial^2 V_r}{\partial z^2}\right) \tag{4}$$

where V_θ, V_r, and V_z are tangential, radial, and axial velocity components, respectively, and ν is kinematic viscosity [18].

Due to the complexity of the above equations, it is impossible to get an analytical solution directly. Therefore, CFD method is used to approximate a solution to these equations. In this study, flow visualization in the basins and velocity distribution at height 60–70% of total height of basin as suggested by Dhakal et al. [9] is obtained through simulation. Simulation is done in commercial CFD code ANSYS CFX after modeling of fluid domain as shown in Fig. 3 using CAD software SolidWorks.

After modeling, meshing of the proposed model was done using software ICEM CFD for fluid analysis. For optimization of the meshing process, denser mesh was taken near wall, and at air-core region, at first but later the grid was refined and uniformly dense mesh was generated. It is to be done as the maximum vortex velocity is obtained in region between the air core and the wall. The canal and outlet region were meshed with cut cell mesh, and tetrahedron was used for meshing of basin.

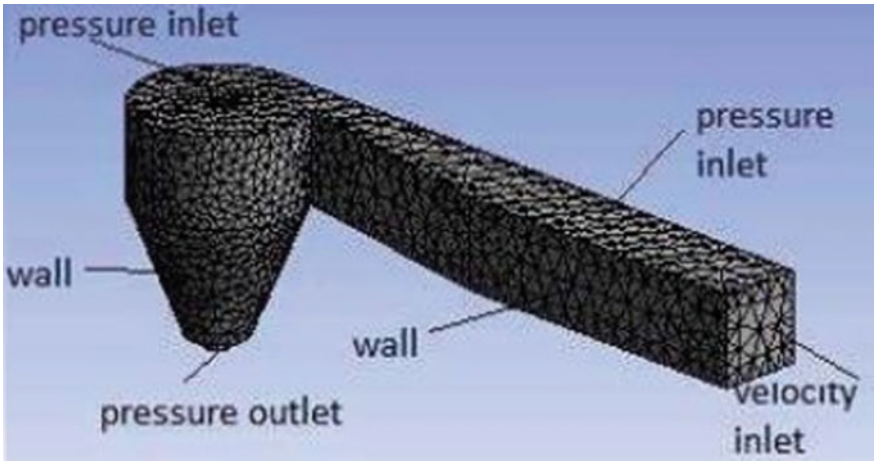

Fig. 3 Boundary conditions for CFD simulation

The simulation was run at condition of no-slip at the wall and pressure outlet condition at the outlet. The initial velocity at the inlet of fluid (water) flow was set to be 0.1 m/s. The upper surface was subjected to atmospheric pressure. Conical basin was simulated considering closed channel flow as the vortex structure does not significantly change for both open and closed canal flow. The hydraulic diameter of 0.2667 m is assumed for fluid flow, and the number of elements in the final computational domain used for the simulation was 308,851, and minimum and maximum element sizes were 3105 m and 6102 m, respectively. The grid convergence graph is shown in Fig. 4.

Discretization of the governing equations is done by the finite volume method (FVM) with suitable discretization schemes using the commercial CFD package ANSYS FLUENT 14.5. Steady pressure-based segregated solver with double precision and implicit scheme was used to solve the discretization equation. The steady terms and discretized equation were solved by separate method, i.e., second-order method for the steady terms and a simple method for the discretized equations. Discretization of the momentum equation and other equations is done by the use of second-order upwinding method as this method gives a proper visualization of the physics of flow. The convergence criterion for all of the equations was taken as 10^{-4}.

For the process of finding optimum inlet and outlet geometrical condition, at first simulation of basins having different basin diameter (D) and outlet diameter (d) was done. Viewing the streamline distribution (Fig. 5) and the contour of velocity (Fig. 6), the tangential velocity at the position where the turbine gets maximum power is noted. It was seen that the maximum velocity measured was 0.8 m/s for basin having d/D ratio of 22.5%. We can see from the flow simulation that the average velocity increases while increasing the d/D ratio from 15 to 22.5% and then it start decreasing. So it can be concluded from the graph (Fig. 7) that the conical basin is efficient in power production in the range of d/D ratio of 20–25%.

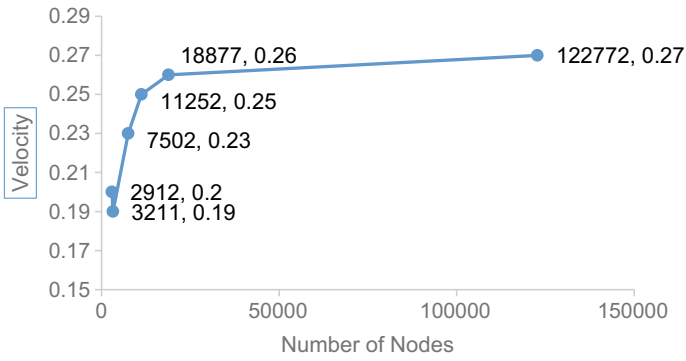

Fig. 4 Grid convergence

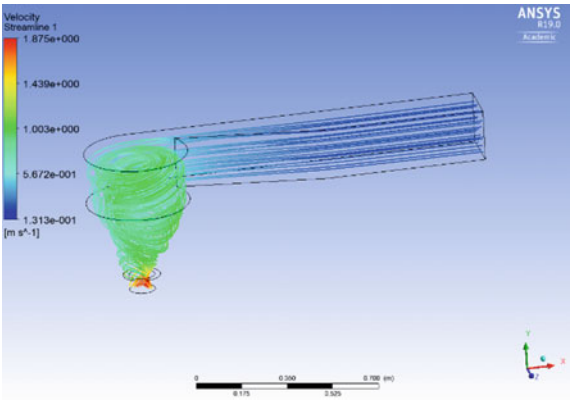

Fig. 5 Streamlines flow in basin

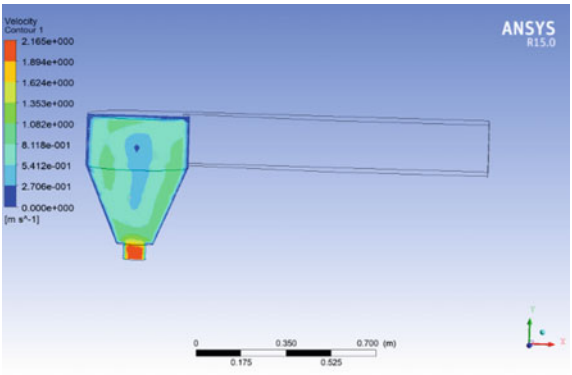

Fig. 6 Contour of velocity

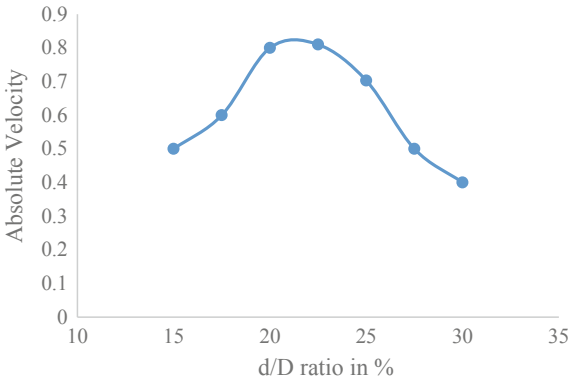

Fig. 7 Variation of absolute velocity with change in *d*/*D* ratio

4 Experimental Testing

A reduced scale model of GWVPP was constructed, following the rules for geometric, kinetic, and dynamic similarities. The laboratory setup is shown in Fig. 8. It has basin diameter of 400 mm, canal height of 200 mm, notch angle of 10°, and cone angle of approximately 23° [19]. The system has a total head of 0.5 m and operates with a flow rate of 0.004 m^3/s, which is provided by a pump recirculating the water flow. The canal is 880 mm long and 200 mm wide.

Float method is used to measure the inlet velocity. A light object was dropped into the canal to float and move in direction of flow, and time taken by the floating object to cover a distance of 0.5 m was measured. This process was repeated five times to calculate average velocity. Considering smooth walls of canal with correction factor of 0.85 [20], mean inlet velocity was calculated to be 0.03 m/s.

Following the previous work, where the maximum output power was found; when runner is placed at position of 65–75% of total height of basin from top position [9], the runner position for these tests was taken 400 mm from the bottom of the basin. A Prony brake dynamometer, which consists of a pulley of 110 mm diameter fitted to the output shaft and rope of 7 mm diameter connected to two-digital weight balance through the pulley, as shown in Fig. 9, was used for the measurement of torque. One weight balance is suspended through a small pulley carrying weight, and another is fixed at top of the basin. The load at the weight balance is increased gradually to apply the load on the output shaft, and corresponding value of speed is noted.

Fig. 8 Fabricated experimental setup

Fig. 9 Prony brake dynamometer system

The output power from the turbine can then be calculated using the following equation:

$$P_{\text{Shaft}} = \frac{2\pi g r_{\text{pulley}} n}{60}\left(M_{\text{weight}} - M_{\text{counterweight}}\right) \tag{5}$$

where r_{pulley} is the pulley radius, M_{weight} is the mass on one side of Prony brake dynamometer, and $M_{\text{counterweight}}$ is the mass on the other side of Prony brake dynamometer. The experimental readings of four types of basin having different d/D ratio (Fig. 10) show that the basin having d/D ratio of 20 and 25% have higher efficiency compared to 16 and 30% d/D ratio (Table 1).

Fig. 10 Four different basins having different inlet and outlet geometry

Table 1 Readings of experimental study

d/*D* ratio (%)	Torque measurement			Power output		Power input			Efficiency (%)
	W_1 (kg)	W_2 (kg)	Torque (N m)	W (rpm)	P_{out} (wat)	Head (h)	Flow rate Q (m^3/s)	P_{in}	
16	0.6	0.1	0.24	150	3.8	0.5	0.004	19.62	19.36
25	1.1	0.2	0.57	146	8.5	0.5	0.004	19.62	43.32
20	1.3	0.2	0.65	140	9.53	0.5	0.004	19.62	48.57
30	0.9	0.2	0.44	142	6.36	0.5	0.004	19.62	32.24

5 Conclusion

In this research, the CFD analysis of different types of basin having different inlet and outlet geometry is studied. The CFD analysis shows that the basins having *d*/*D* ratio in the range of 20–25% gives maximum output power as the simulation result shows maximum tangential velocity of the streamlines and contour. Moreover, the experimental testing conducted on the basin having *d*/*D* ratio of 16, 20, 25, and 30% shows that the two basins having *d*/*D* ratio of 20 and 25% give maximum output power in comparison with basins having *d*/*D* ratio of 16 and 30%. Hence, it can be concluded that the basin having *d*/*D* ratio between 20 and 25% is efficient for power production.

Acknowledgements Authors would like to acknowledge the financial support from American Society of Nepalese Engineers (ASNEgrs). The authors would also like to thank Center of Energy Studies under Institute of Engineering of Tribhuvan University, Turbine Testing Lab of Kathmandu University, and Alternative Energy Promotion Center Nepal for their support in completing this article.

References

1. Mulligan S, Casserly J (2010) The hydraulic design and optimisation of a free water vortex for the purpose of power extraction. BE Project Report Institute of Technology, Sligo
2. Zotloterer F (2018) Zotloterer—smart energy system. Available: http://www.zotloeterer.com/welcome/gravitation-water-vortex-power-plants/. Accessed on 19 Nov 2018
3. Dhakal R, Chaulagain RK, Bajracharya T, Shrestha S (2015) Economic feasibility study of gravitational water vortex power plant for the rural electrification of low head region of nepal and its comparative study with other low head power plant. In: Conference proceeding of the 11th international conference on ASEAN knowledge networks for the economy, society, culture, and environmental stability, Kathmandu
4. Vortex Energy Solution Pvt. Ltd. (2019) A concept proposal for 10 kw GWVPP installation in nepal for rural electrification. Vortex Energy Solution Pvt. Ltd. Available: https://vortexenergysolution.com/2018/12/09/a-concept-proposal-for-10-kw-gwvpp-installation-in-nepal-for-rural-electrification/. Accessed on 9 Feb 2019
5. Available: http://www.zotloeterer.com/welcome/gravitation-water-vortex-power-plants/. Accessed on 30 July 2017
6. Genossenschatt Wasserwribe —Home Page. Available: http://gwwk.ch/. Accessed on 23 June 2016
7. KourisPower Ltd. (2016) Home Page. Available: http://www.kourispower.com/. Accessed on 23 June 2016
8. Yaakob OB, Ahmed YM, Elbatran AH, Shabara HM (2014) A review on micro hydro gravitational vortex power and turbine systems. Jurnal Teknologi 69:1–7
9. Dhakal S, Timilsina AB, Dhakal R, Fuyal D, Bajracharya TR, Pandit HP, Amatya N, Nakarmi AM (2015) Comparision of conical basin and cylindrical basin with optimum position of runner: gravitational water vortex power plant. Renew Sustain Energy Rev 48:662–669
10. Wanchat S, Suntivarakorn R (2005) Preliminary design of a vortex pool for electrical generation
11. Wanchat S, Suntivarakorn R, Tonmit K, Kayanyiem P (2013) A parametric study of gravitational water vortex power plant. Adv Mater Res 805–806:811–17

12. Bajracharya TR, Chaulagain RK (2012) Developing innovative low head water turbine for free-flowing streams suitable for micro-hydropower in flat (Terai) regions in Nepal. In: Center for Applied Research and Development(CARD), Central Campus, Institute of Engineering, Tribhuvan University, Kathmandu, Nepal
13. Dhakal S, Nakarmi S, Pun P, Thapa AB, Bajracharya TR (2013) Devlopment and testing of runner and conical basin for gravitational water vortex power plant. In: Center for Applied Research and Devlopment (CARD), IOE, Tribhuvan University, Kathmandu
14. Power C, McNabola A, Coughlan P (2016) A parametric experimental investigation of the operating conditions of gravitational vortex hydropower (GVHP). J Clean Energy Technol 4(2):112–119 (2016)
15. Dhakal R, Bajracharya TR, Shakya SR, Kumal B, Khanal K, Williamson SJ, Gautam S, Ghale DP (2017) Computational and experimental investigation of runner for gravitational water vortex power plant. In: 6th international conference on renewable energy research and application, San Diego, CA, USA
16. Parajuli P, Koirala P, Pokharel N, Neopane HP, Chitrakar S, Maskey RK (2016) Computational and experimental study of an ultra-low head turbine. In: 4th International conference on the development in the in renewable energy technology (ICDRET), Dhulikhel, Nepal
17. Sayma A (2009) Computational fluid dynamics. Bookboon
18. Young DF, Munson BR, Okiishi TH, Huebsch WW (2006) Fundamental of fluid mechanics. AMES, IOWA: Wiley (2006)
19. Dhakal S, Timilsina AB, Dhakal R, Fuyal D, Bajracharya TR, Pandit HP (2014) Effect of dominant parameters for conical basin: gravitational water vortex power plant. In: Proceedings of IOE graduate conference 2014, Centre for Applied Research and Development, IOE Pulchowk, Lalitpur, Nepal
20. Massey BS, Ward-Smith J (1998) Mechanics of fluid. CRC Press, London (1998)

An Exergy Analysis and Effect of Condenser and Evaporator Temperature on Ice Production Plant

Shobhit Varshney, Hiren Shah and Vikram Rajai

Abstract In this study, an exergy analysis of an ice production plant was carried out. The exergy formulas were written and solved based on actual plant data to point out the thermodynamics inutility. For the analysis, the necessary data are obtained from an ice production plant situated at GIDC Navsari, Gujarat, India. The plant included ammonia refrigerant vapor compression refrigeration system having 24 tonnes of ice manufacturing capacity per day, including Kirloskar-4 cylinder reciprocating compressor, shell and tube condenser, induced draft counter flow cooling tower with fill- and flooded-type evaporator. Here the effect of condenser and evaporator temperature on exergy efficiency of components, compressor work and on COP, was also discussed. It is found that the significant amount of exergy drop is happened in compressor out of numerous parts of the ice plant, and it depends on evaporating temperature, condensing temperature, and geographical conditions. To measure the exergy loss (irreversibility) of the ice production procedure, an effort was also formed. So, to get the knowledge about the potential location for the plant execution refinement, an important detail can be obtained with the help of the exergetic study and its subsidiary derivatives.

Keywords Coefficient of performance · Compressor work · Condenser temperature · Evaporator temperature · Exergy analysis · Ice production process · Refrigeration system

1 Introduction

As the industrial rebellion increase in the mid of the twentieth century, the application of the latest technology also increases in our routine life. This leads to further utilization of energy and made it an entangled part of life. Moreover, in the progress of the countries, the rate of utilization of energy consumption plays a vital role in

S. Varshney · H. Shah (✉) · V. Rajai
Chhotubhai Gopalbhai Patel Institute of Technology, Uka Tarsadia University, Gopal-Vidyanagar, Maliba Campus, Surat, Gujarat 394350, India
e-mail: hirenshah29@hotmail.com

A. K. Parwani and PL. Ramkumar (eds.), *Recent Advances in Mechanical Infrastructure*, Lecture Notes in Intelligent Transportation and Infrastructure,
https://doi.org/10.1007/978-981-32-9971-9_18

success. To meet the increasing demand of the society with the energy, it is required to have an enough amount of pursuit and productivity in this field [1].

For these reasons, the modern approach uses the exergy analysis to process analysis, which gives a close practical perspective of the procedure. For the engineering process estimation, the exergy analysis is used as a new and advanced thermodynamic technique [2, 3]. The exergy analysis is depending on both the first and second laws of thermodynamics, whereas the energy analysis depends on the first law of thermodynamics. Both analyses utilize the material balance for the system considerably.

The first law is bothered only with the conservation of energy. It does not give an idea about how, where, and why the performances are reduced. As compared to the energy balance with the help of the exergy calculation, it can give the deeper information about the process as well as the new unpredicted suggestions for the refinement [4]. Dincer [5] shows the relationship between the environment and exergy, energy and exergy, energy and energy policy evolution details. The principles and methodologies of exergy analysis are well-signifies [6–8]. An exergy analysis is usually aimed to determine the maximum performance of the system and to the sites of exergy loss (irreversibility) [9].

In this paper, exergy analysis is applied to the vapor compression refrigeration cycle. The declaration for the exergy efficiency and exergy loses (lost works) for the separate procedure builds up the cycle as well as the coefficient of performance (COP), and second law of efficiency for the whole cycle is analyzed. Results of evaporating and condensing temperatures on the exergy losses, $\dot{W}_{\text{comp,}}$ COP, and second law efficiency, are carried out. Vapor compression refrigeration systems are broadly used in air-conditioning and refrigerator systems. But everywhere, exergy as well as energy analysis is necessary to get maximum output and system with high performance.

The main objective of the present study is to analyze and evaluate the energy use and its efficiency. Thermodynamic relations and its derivatives are used to perform energy and exergy analysis. The classification of studies conducted and the approaches applied are then investigated; finally, it summarized that the study and analysis of exergy are necessary for vapor compression system.

2 Materials and Methods

2.1 Capacity, Process Cycle, and Its Layout

The necessary data and details for exergy analysis were acquired from an ice production shad factory located in GIDC, Navsari, Gujarat, India. The utmost ice production capacity of the plant was 24 tonnes per day. An actual flow illustration of the considered ice production factory is shown in Fig. 1.

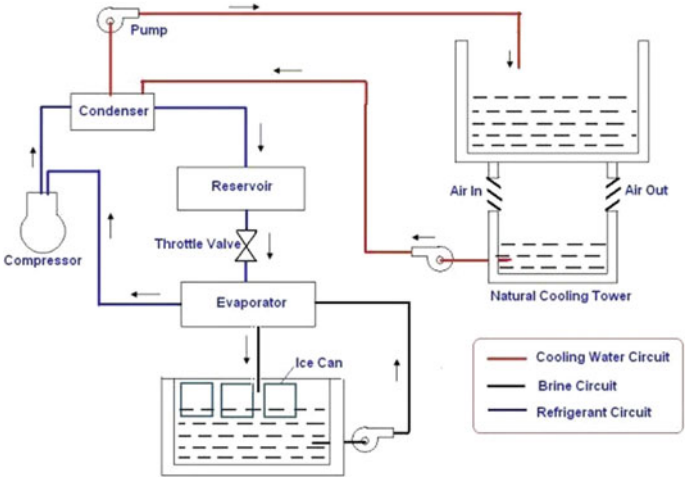

Fig. 1 Line diagram of 24 TR ice production plant

The ice manufacturing plant consisted of an ice manufacturing line and vapor compression refrigeration system. The real functioning data are recorded from the plant panel and control systems which are used for the exergetic computations of the factory and its major subparts. The exergetic analysis of the system was calculated by considering the average values of the noted data (Fig. 2 and Table 1).

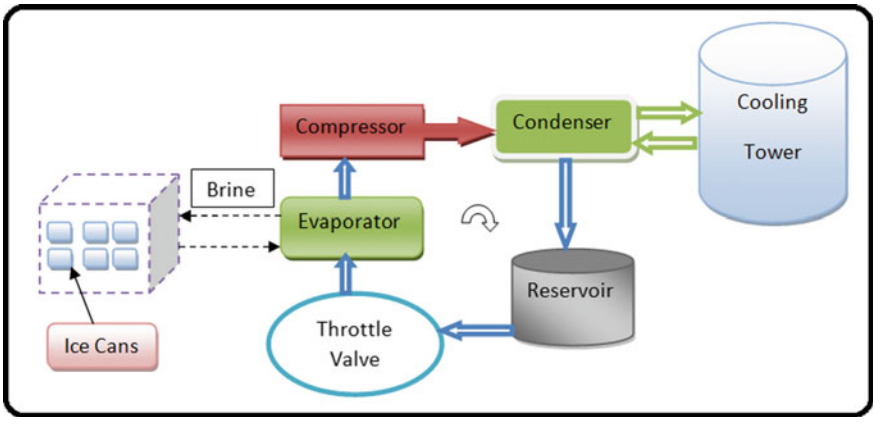

Fig. 2 Flow diagram of 24 TR ice production plant

Table 1 Description of plant components

Parameter	Significant
Compressor	Kirloskar-4 cylinder (KC-4)
Condenser	Shell and tube
Cooling tower	Induced draft counter flow cooling tower with fill
Evaporator	Flooded type
Freezing tank	6 mm thickness M.S. sheet
Ice cans	120 kg (size: $10'' \times 21'' \times 48''$)
No of ice cans	390
Refrigerant	Ammonia
Refrigerant gas pipeline	'C' class pipe
Brine	Sodium chloride

2.2 Plant Description

With the development of the modern refrigeration equipment, the demand for block ice is increasing in the market day-by-day. The uses of an ice are in hospitals, chemical pharmaceutical, fishery and commercially used in different industrial applications. Refrigeration is defined as the removal of heat energy so that a material or space is cooler than its surrounding atmosphere. An ice plant works on the same principle as a simple refrigeration system.

All VCR equipments consist of four main parts: evaporator coils, compressor, condenser, and throttle valve. The low-pressure vapor of refrigerant is converted into high pressure of refrigerant vapor with the help of compressor, and it conveys to the condenser. Here, the refrigerant vapor is condensed by rejecting the heat into atmosphere and converted into the high-pressure liquid, which is converted into low-pressure liquid by throttle valve [10].

From here, the liquid is conveyed to the evaporator coils, which are placed into the rectangular tank, where ice is formed due to the occurrence of heat exchanging process. This is one complete refrigeration cycle. The total capacity of this plant is to manufacture 390 ice blocks, and the mass of each block is 120 kg. The time required to freeze all these ice blocks are 44 h. In this plant, there is no ice storage facility so half of the ice blocks are sold-out per day to meet the demand of another day.

The main problem associated with the plant is power consumption incorporated with manufacturing of ice which ultimately increases the running cost of the plant. So the main objective of the analysis is to increase the COP, lower the losses and power consumption and enhance the efficiency of the plant. If it enhances the effectiveness of the energy at an industrial sector, then notably the greenhouse gas emissions and the operating costs associated with the energy use is decreased. For saving the maximum energy which dissipated from the large industry during the complex process, many engineering and scientific methodologies are available and many more are continuously progressing. The methods used depend on engineering assessment,

Table 2 Exergetic formulations [12]

Components	Exergy destruction	Exergy Efficiency
Compressor	$\dot{E}_{d,\text{comp}} = \dot{E}_{\text{suc}} - \dot{E}_{\text{disc}} + \dot{W}_{\text{comp}}$ $\dot{E}_{\text{suc}} =$ $\dot{m}_{\text{ref}}[h_{\text{suc}} - h_o] - T_o[S_{\text{suc}} - S_o]$	$\acute{\eta}_{\text{ex,comp}} = 1 - (\dot{E}_{\text{comp}}/\dot{W}_{\text{comp}})$
Condenser	$\dot{E}_{d,\text{cond}} =$ $(\dot{E}_{\text{in}} - \dot{E}_{\text{out}})_{\text{cond}} + (\dot{E}_{\text{in}} - \dot{E}_{\text{out}})_{\text{water}}$ $\dot{E}_{\text{in,cond}} =$ $\dot{m}_{\text{ref}}[h_{\text{in}} - h_o] - T_o[S_{\text{in}} - S_o]$ $\dot{E}_{\text{out,cond}} =$ $\dot{m}_{\text{ref}}[h_{\text{out}} - h_o] - T_o[S_{\text{out}} - S_o]$ $\dot{E}_{\text{in,water}} =$ $\dot{m}_{\text{ref}}[h_{\text{in}} - h_o] - T_o[S_{\text{in}} - S_o]$	$\acute{\eta}_{\text{ex,cond}} = 1 - (\dot{E}_{\text{cond}}/(\dot{E}_{\text{in}} - \dot{E}_{\text{out}})_{\text{cond}}$
TXV	$\dot{E}_{d,\text{TXV}} = (\dot{E}_{\text{in}} - \dot{E}_{\text{out}})_{\text{TXV}}$ $\dot{E}_{\text{in,TXV}} =$ $\dot{m}_{\text{ref}}[h_{\text{in}} - h_o] - T_o[S_{\text{in}} - S_o]$	$\acute{\eta}_{\text{ex,TXV}} = 1 - (\dot{E}_{\text{TXV}}/\dot{E}_{\text{in,TXV}})$
Evaporator	$\dot{E}_{d,\text{evap}} =$ $(\dot{E}_{\text{in}} - \dot{E}_{\text{out}})_{\text{evap}} + (\dot{E}_{\text{in}} - \dot{E}_{\text{out}})_{\text{brine}}$ $\dot{E}_{\text{in,evap}} =$ $\dot{m}_{\text{ref}}[h_{\text{in}} - h_o] - T_o[S_{\text{in}} - S_o]$ $\dot{E}_{\text{out,evap}} =$ $\dot{m}_{\text{ref}}[h_{\text{out}} - h_o] - T_o[S_{\text{out}} - S_o]$ $\dot{E}_{\text{in,brine}} =$ $\dot{m}_{\text{brine}}[h_{\text{in}} - h_o] - T_o[S_{\text{in}} - S_o]$	$\acute{\eta}_{\text{ex,evap}} = 1 - (\dot{E}_{\text{evap}}/\dot{E}_{\text{in}} - \dot{E}_{\text{out}})_{\text{evap}}$

energy and exergy analysis. By exergy analysis, both qualitative and quantitative result can be obtained as compared with energy analysis which gives only quantitative result. In present paper, the effect of condensing and evaporative temperature on $\dot{W}_{\text{comp}}$, COP, exergy loss, and exergy efficiency is analyzed.

In the past couple of decades, the modification, design, optimization of the manufacturing, and production process have the relation with exergy analysis due to their special ideational character to provide detail knowledge regarding ecological, thermodynamics, and physical cost. Hence, it is very useful for the analysis of the plant to get the optimum result for the given input parameters [11] (Tables 2, 3).

2.3 Cooling Load Calculation [13]

Sensible heat required to lower temperature of water from its raw temperature to its freezing temperature

$$Q_1 = M_{\text{wf}} * (C_p)_{\text{water}} * \Delta T$$

Table 3 Plant operating parameter

Refrigerant	Ammonia
Environmental temperature	30 °C
Temperature of cold chamber	−1.5 °C
Evaporator temperature	−10 °C
Compressor outlet temperature	110 °C
Condenser temperature	40 °C
Brine temperature	−8.5 °C
Compressor inlet pressure	0.29 Mpa
Compressor outlet pressure	1.55 Mpa
Electric motor efficiency [13]	0.8
Compressor mechanical efficiency [13]	0.8
Specific isobaric heat capacity of brine [13]	2.85 kJ/kgK
Specific heat capacity of brine [13]	2.093 kJ/kgK
C_P of ammonia [10]	3.0 kJ/kgK
Mass of water to be freeze per day	23,400 kg/day
Latent heat of water [10]	355 kJ/kg
Specific heat of water [10]	4.187 kJ/kgK
Brine temperature	−8.5 °C
Raw water temperature	27 °C
Ice temperature	−1.5 °C
Freezing temperature	0 °C

Changing the latent heat of water at its freezing temperature from liquid to solid.

$$Q_2 = M_{\text{wf}} * L_f$$

Raising the temperature of water from its freezing temperature to the brine temperature.

$$Q_3 = M_{\text{wf}} * (C_p)_{\text{brine}} * \Delta T$$

Total heat load

$$Q_T = Q_1 + Q_2 + Q_3$$

For typical ice plant, there is 15% of allowance [13]; therefore

$$Q_C = 1.15\, Q_T$$

2.4 P-H and T-S Diagram of Ice Plant Based on Actual Data

See Figs. 3, 4 and Tables 4, 5.

$$S_{22'} = S_2 + \mathrm{Cp}\ln(T_{22'}/T_2)$$
$$h_{22'} = h_2 + \mathrm{Cp}(h_{22'} - T_2)$$
$$\dot{m}_{\mathrm{ref}} = Q_C/(h_1 - h_4)$$
$$\dot{W}_{\mathrm{comp}} = \dot{m}_{\mathrm{ref}}\,(h_{22'} - h_1)/\dot{\eta}_{\mathrm{mech}} * \dot{\eta}_{\mathrm{elec}}$$
$$\mathrm{COP} = Q_c/\dot{W}_{\mathrm{comp}}$$

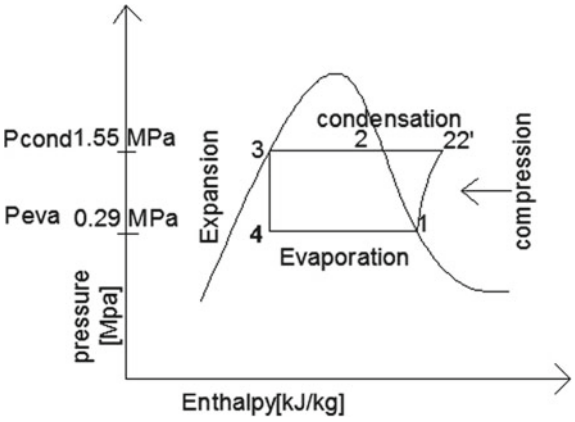

Fig. 3 Pressure–enthalpy diagram

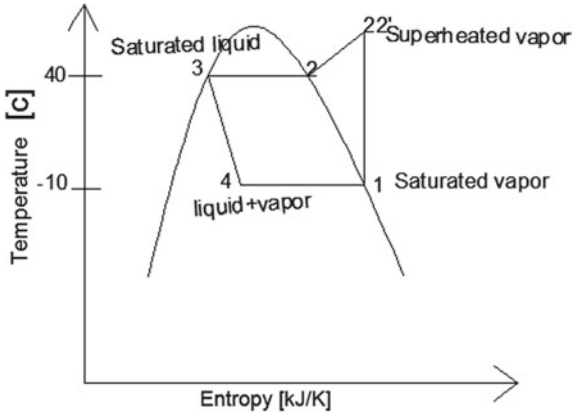

Fig. 4 Temperature–entropy diagram

Table 4 Property of refrigerant [10]

$h_1 = h_g$(kJ/kg)	h_2(kJ/kg)	$h_3 = h_f$(kJ/kg)	S_1(kJ/K)	S_2(kJ/K)	S_3(kJ/K)
1450	1490	390	5.7559	5.1546	1.64

Table 5 Computed parameters of proposed ice plant

S. No.	Parameters	Value
1	Q_1	30.61 kW
2	Q_2	96.14 kW
3	Q_3	4.81 kW
4	Q_T	131.56 kW
5	Q_c	152 kW
6	$\dot{m}_{\text{ref}}$	0.1433 kg/s
7	$\dot{W}_{\text{comp}}$	55.56 kW
8	COP	2.71

3 Results and Discussions

In the given experiment, exergy analysis has been done using EES software. Exergy efficiency and exergy destruction of each subunit have been calculated. It is shown that condensing temperature and evaporating temperature have a large effect on the exergy efficiency of the plant as well as on the compressor work. Here the effect of condensing temperature and evaporating temperature on compressor work, exergetic efficiency, COP, and total exergy destruction of plant is shown. Most of the research paper shows that most of the exergy loss occurs in compressor out of the all parts of VCR system (Table 6).

Table 6 Exergy efficiency of component, COP, power required to run compressor at varying condensing temperature

Condenser temperature (°C)	$\dot{\eta}_{\text{comp}}$	$\dot{\eta}_{\text{cond}}$	$\dot{\eta}_{\text{TXV}}$	$\dot{\eta}_{\text{evap}}$	COP	$\dot{W}_{\text{comp}}$ (kW)	Irreversibility (kW)
48	0.5469	0.5710	0.6675	0.6952	2.318	65.56	45.30
44	0.5519	0.6043	0.6923	0.7125	2.427	62.63	42.22
40	0.5645	0.6487	0.7485	0.7303	2.736	55.56	35.89
36	0.5771	0.8419	0.7974	0.7491	3.112	48.85	29.40
32	0.5848	0.9428	0.8235	0.7689	3.379	44.98	26.03

3.1 *Performance of Condenser Temperature on Exergy Loss, $\dot{W}_{comp}$, COP, η_{II}*

The effect of condenser temperature plays a vital role in exergy of the VCR system. Kabul et al. [14] show that condenser temperature has a contradictory effect from the temperature of evaporator. If it raises the temperature of condenser, the effect of COP, second law efficiency ratio, and exergy efficiency were declined, while the total irreversibility rate was enhanced.

In Fig. 5, the COP of the plant increases while $\dot{W}_{comp}$ reduces with reducing the condensing temperature. The main cause behind it is that with reducing the condenser temperature the specific volume for compressor work will reduce which ultimately reduces $\dot{W}_{comp}$. It is shown in Fig. 6 that exergetic efficiency decreases for all the subunits of plants with an increase in condensing temperature, while Fig. 7 shows that exergy loss (irreversibility) enhances with raising the temperature of condenser. The higher exergy loss occurs, because of the high temperature difference between system and surrounding. Ozgur and Bayrakci [15] also noticed that the losses of exergy are directly proportional to the temperature of condenser. If the temperature of condenser rises, then the chance of irreversibility access may be high. From the study, Jabardo et al. [16] also show the relations between the temperature of condenser, losses of exergy, and second law efficiency. Saravanan and Kalaiselvam [17] also have done many researches for the various refrigerants to indicate the relations between the

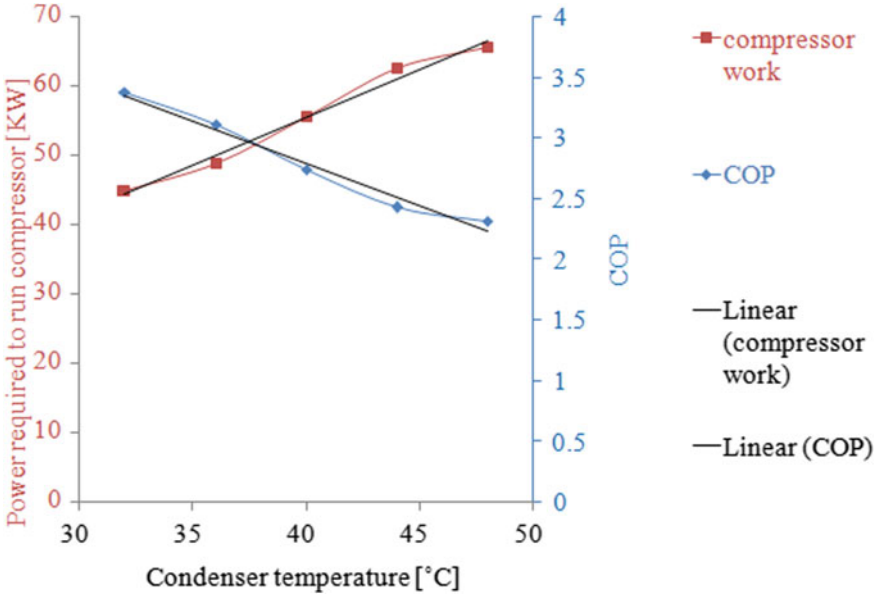

Fig. 5 COP, $\dot{W}_{comp}$ versus condenser temperature

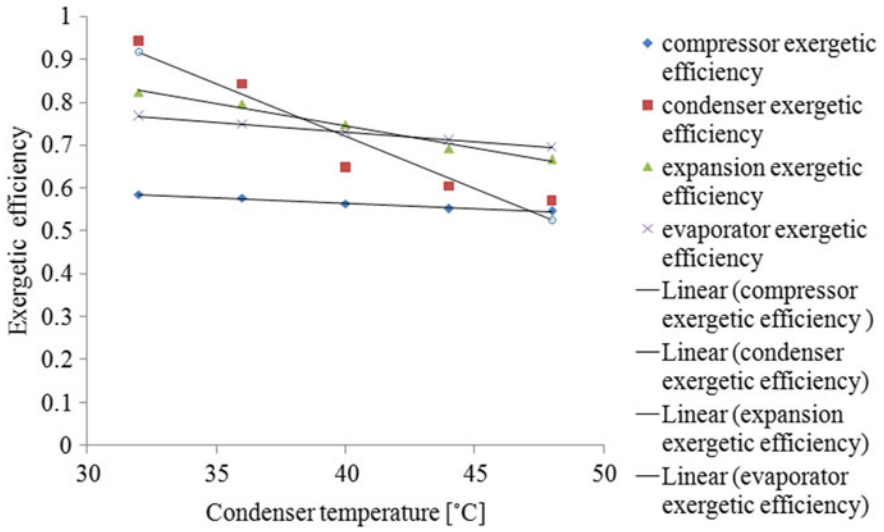

Fig. 6 Exergetic efficiency versus condenser temperature

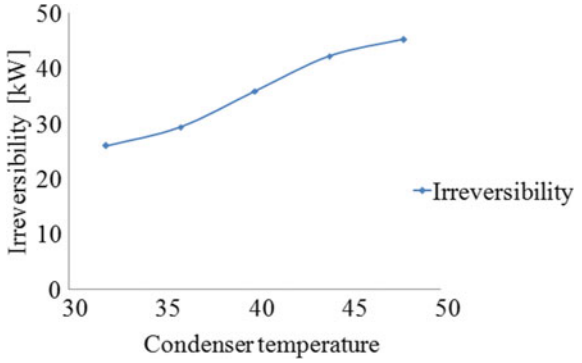

Fig. 7 Irreversibility versus condenser temperature

condenser and evaporator temperature and effect on the exergy, COP, and on the efficiency of the various components of the VCR system (Table 7).

3.2 Performance of Evaporator Temperature on Exergy Loss, $\dot{W}_{comp}$, COP, η_{II}

The losses of exergy were computed for the VCR system. From the throttle valve, the liquid refrigerant enters into evaporator coils. As the refrigerant in the form of

Table 7 Exergy efficiency of component, COP, power required to run compressor at varying evaporator temperature

Evaporator temperature (°C)	$\dot{\eta}_{comp}$	$\dot{\eta}_{cond}$	$\dot{\eta}_{TXV}$	$\dot{\eta}_{evap}$	COP	W_{comp} (kW)	Irreversibility (kW)
−20	0.5534	0.6407	0.6298	0.5463	2.101	72.33	52.66
−15	0.5590	0.6448	0.6928	0.6268	2.389	63.63	43.96
−10	0.5645	0.6487	0.7485	0.7303	2.736	55.56	35.89
−5	0.5697	0.6524	0.7975	0.8683	3.161	48.08	28.41

liquid goes through the coils of evaporator, the refrigerant sucks up the heat from the evaporator and convert it into vapor form during this process surrounding becomes cool. So, as the liquid refrigerant vaporizes and continuously producing a cooling effect at the end of evaporator coils, only vapour form of refrigerant enters from the suction valve of the compressor. The loss of exergy is less at a high temperature of evaporator, and more as the temperature of evaporator decreases. Figures 8 and 9 show that, with rise in the temperature of evaporator, the values of COP and exergy efficiency enhance, while the overall irreversibility rate and $\dot{W}_{comp}$ reduced. In short, the system performance is affected positively as the temperature of evaporator increased. $\dot{W}_{comp}$ also reduces as the temperature of evaporator increases because of the specific volume reduces as well as the enthalpy difference between the compressor inlet and outlet condition also reduces which ultimately reduces the compressor power work.

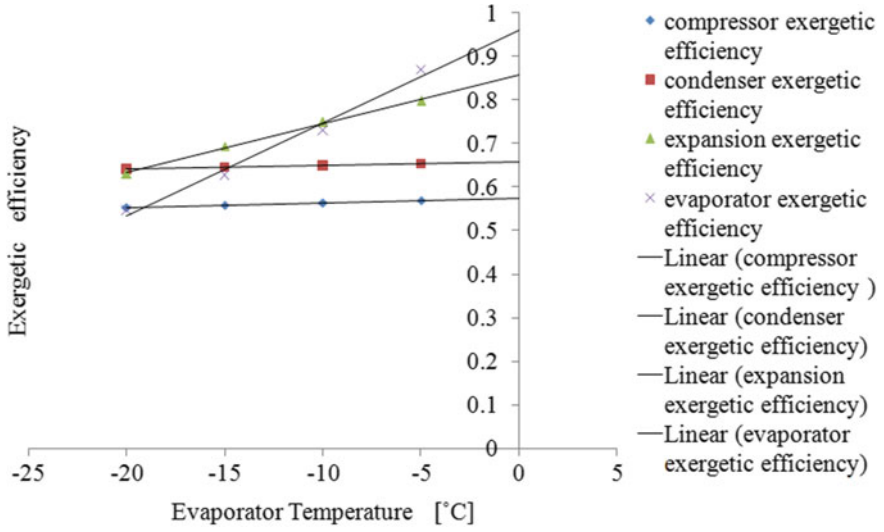

Fig. 8 COP, $\dot{W}_{comp}$ versus evaporator temperature

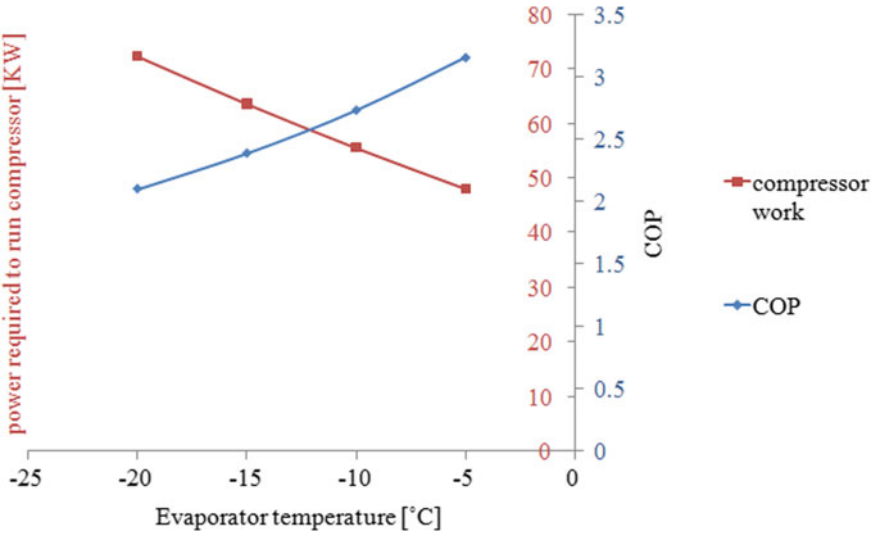

Fig. 9 Exergetic efficiency versus evaporator temperature

To analyze the performance of ammonia refrigerant and VCR system for different evaporator and condenser temperature and for study exergy analysis, one computational modal was prepared [17]. The overall loss of exergy decrease as raise the temperature of evaporating and a reverse effect shows for the second law efficiency. Saravanan and Kalaiselvam [17] noticed that exergy losses decreased with the increase in the evaporator temperature. Figure 10 shows the relation between the irreversibility and the evaporator temperature. The reason behind the relationship is

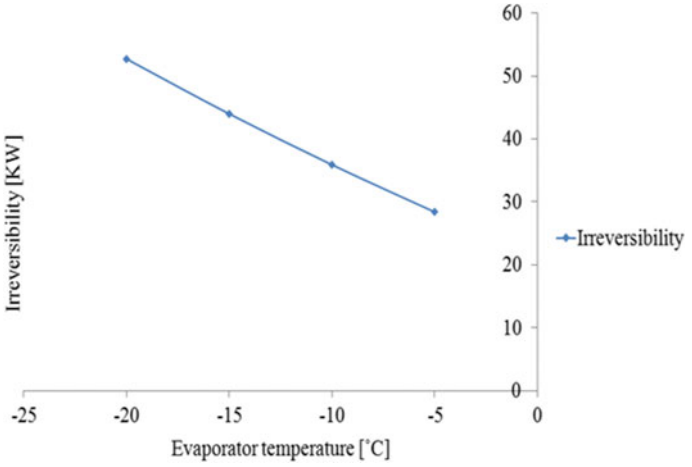

Fig. 10 Irreversibility versus evaporator temperature

that with increased refrigerating effect, the exergy loss declines. As the temperature of evaporator increases; due to the less temperature difference between system and surrounding, the heat transfer from system increases and which is responsible for the higher refrigerating effect.

4 Conclusion

Here, a particular exergy analysis of an ice production plant was calculated based on real operating plant inputs. Some concluding remarks could be listed as follows.

The functional exergetic efficiency of the KC4 reciprocating compressor, shell and tube condenser, expansion valve, and evaporator coil were determined at 56.45%, 64.87%, 74.85%, and 73.03% correspondingly. The total exergy efficiency of the plant was seen 36.4%, whereas the total irreversibility was measured 35.89 kW. It is recommended to operate plant at 35 °C of condenser temperature and −8 °C of evaporator temperature. In reality, it gives meaningful notifications for the better change in the plant execution as well as potential locations for the performance improvement in the plant by the study of exergy analysis and its solutions.

From the exergetic analysis, it is concluded that the compressor has the least exergetic efficiency. If it reduced the condenser temperature, power consumption of the plant is reduced and exergetic efficiency is increased . If we reduce the evaporator temperature, power consumption of plant is increased, and exergetic efficiency is reduced.

Acknowledgements The authors gratefully acknowledge the support of the engineers of Harsiddhi Ice Factory located at GIDC, Navsari, for providing the necessary facilities as well as the crucial comments given by reviewers regarding paper quality is appreciated.

References

1. Brown S (1996) Single-site and industrial-scale schemes. Appl Energy 53:149–155
2. Szargut D, Petela R (1965) Egzergia. WNT
3. Szargut J, Morris D, Steward F (1998) Exergy analysis of thermal, chemical and metallurgical processes. Hemisphere Publishing Corporation, New York
4. Saidur R, Masjuki HH, Jamaluddin MY (2007) An application of energy and exergy analysis in residential sector in Malaysia. Energy Policy 35:1050–1063
5. Dincer I (2002) On energetic, exergetic and environmental aspects of drying systems. Int J Energy Res 26(8):717–727
6. Gaggioli RA (1998) Available energy and exergy. Int J Appl Thermodyn 1:1–8
7. Wark KJ (1995) Advanced thermodynamics for engineers. McGraw-Hill, New York
8. Bejan A (1988) Advanced engineering thermodynamics. Wiley, New York
9. Saidur R, Ahamed JU, Masjuki HH (2010) Energy, exergy and economic analysis of industrial boilers. Energy Policy 38(5):1188–1197
10. Arora SC, Domkundwar S (1989) A course in refrigeration and air conditioning, 5th edn. Dhanpat Rai and Sons, Delhi

11. Ozahi E, Demir H (2013) A model for the thermodynamic analysis in a batch type fluidized bed dryer. Energy 59:617–624
12. Mota-Babiloni Adrián, Belman-Flores JM, Makhnatch Pavel, Navarro-Esbrí Joaquín, Barroso-Maldonado JM (2018) Experimental exergy analysis of R513A to replace R134a in a small capacity refrigeration system. Energy 162(C):99–110 Elsevier
13. Kotas TJ (1995) The exergy method of thermal plant analysis, Reprint edn. Krieger Publishing Company, Malabar
14. Kabul A, Kizilkan O, Yakut AK (2008) Performance and exergetic analysis of vapor compression refrigeration system with an internal heat exchanger using a hydrocarbon, isobutane (R600a). Int J Energy Res 32:824–836
15. Bayrakci HC, Ozgur AE (2009) Energy and exergy analysis of vapor compression refrigeration system using pure hydrocarbon refrigerants. Int J Energy Res 1538. https://doi.org/10.1002/er.1538
16. Jabardo JMS, Mamani WG, Ianalla MR (2002) Modelling and experimental evaluation of an automotive air conditioning system with a variable capacity compressor. Int J Refrig 25:1157–1172
17. Kalaiselvam S, Saravanan R (2009) Exergy analysis of scroll compressors working with R22, R407 and R717 as refrigerant for HVAC system. Therm Sci 13:175–184

Direct Steam Generation by an Enclosed Solar Parabolic Trough for Enhanced Oil Recovery

V. K. Ramesh, V. Chintala and Suresh Kumar

Abstract Steam generation for industrial applications by harnessing solar energy has picked up momentum in recent years. One of the major applications for steam in crude oil extraction industries is thermal enhanced oil recovery (EOR). In the current study, direct steam was generated by enclosed parabolic troughs for improved crude oil recovery. For such a plant, effect of direct normal irradiance (DNI) on the steam generation parameters was assessed. Further, the outlet steam temperature and pressure were also addressed in the study. Maximum DNI in a day was in the range of 1120–1185 w/m^2 and the maximum steam generation was 1.1–1.3 kg/s. Finally, it is concluded that enclosed solar troughs are promising option for solar direct steam generation.

Keywords Enclosed trough · DNI · EOR · Direct steam generation

1 Introduction

The enhanced oil recovery (EOR) refers to a method used to recover additional oil from a reservoir than by primary and secondary recoveries. The purpose of EOR is to increase recovery factor of the reservoir by moving the unmovable oil. Thermal EOR refers to a process of increasing the temperature of the reservoir fluid by means of thermal applications and thus reduce the viscosity and make the oil more movable. In solar thermal EOR, high-pressure and high-temperature steam is produced with the help of concentrated solar power (CSP) and injected into the oil-bearing reservoirs. The solar energy is concentrated on to receiver tubes which carries water, and due to continuous heat transfer from sun rays to receiver tube surface, water inside the tubes

V. K. Ramesh (✉)
Petroleum Development Oman LLC, PO Box 81, PC 100 Mina al Fahal, Sultanate of Oman
e-mail: VK.Ramesh.Nair@gmail.com

V. K. Ramesh · V. Chintala · S. Kumar
Department of Mechanical Engineering, School of Engineering, University of Petroleum and Energy Studies (UPES), Dehradun 248007, India

A. K. Parwani and PL. Ramkumar (eds.), *Recent Advances in Mechanical Infrastructure*, Lecture Notes in Intelligent Transportation and Infrastructure,
https://doi.org/10.1007/978-981-32-9971-9_19

get converted into steam. This steam is injected into the reservoir, which will help the oil viscosity to come down and make the oil more mobile, and aids in more oil recovery. The potential for solar energy for thermal EOR was discussed in research papers as early as 1982, in anticipation of the steam generated using solar thermal methods; the work was published in 1982 on the "Anticipated effect of diurnal injection on steam drive efficiency" [1]. Subsequently, there were several conceptual, theoretical and modelling studies carried out. As of now, the commercial viability of the solar thermal EOR has been established. Solar tower technology and enclosed trough technologies have been proven for steam production. Enclosed trough technology was introduced by M/s Glasspoint Solar, Inc. and some previous works have been already available [2–6]. Enclosed trough technology has been adopted for thermal EOR operation of one of the heavy oil fields in south Oman and such facility is operational. The historical operational data of the facility pertaining to the steam generation and CSP module have been collected and the same are being analysed on an empirical basis in this paper. Such an analysis of the operational parameters of direct steam generation using CSP technologies is very unique and has not been published so far.

2 Materials and Methods

As shown in Fig. 1, in enclosed trough technology, parabolic reflectors are mounted inside a glasshouse. The glasshouse will help to avoid wind load and dust on the mirrors. Water is pumped through the tube receivers, from one side and on the other side steam is generated and the same is taken to the injector wells through steam header.

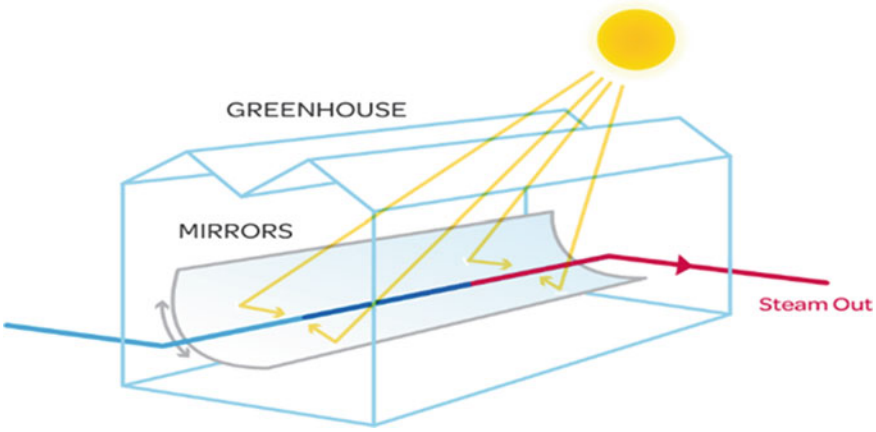

Fig. 1 Enclosed trough concepts (*Source* Glasspoint) [7, 8]

The actual solar steam generator system under study is an installation in south Oman and consists of a standard module containing multiple individual solar block glasshouse structures designed to provide steam to the injection wells. Each solar block glasshouse structure also referred as solar block can deliver a heat transfer rate equivalent to either 45 or 36 Tons of Steam Per Hour (TSPH). The system will generate steam using a once-through steam generator configuration made up of evaporator solar arrays to generate 80% quality steam up at to 95 barg at the tie-in point.

As shown in Fig. 2, the solar EOR system's key components are a nominal multi-acre solar field of solar collectors, weather station, feed water charging systems, air handling unit (AHU) for humidity control inside the glasshouse, associated piping, valves, instruments, controllers, and safety devices. The control methodology for operation of all solar blocks is the same. Process control of each individual solar block is independent from the others, but a common source of water supply provided by feed water storage tank will be shared by all solar blocks. The system will operate in automated mode during normal operation with all solar blocks being managed by the programmable logic control (PLC) system, with signals exchanged with the oil field operations existing field control system. For the purpose of the experimental analysis, the operational parameters of one evaporator solar array are studied in detail. Each evaporator solar array loop is configured as 8 rows of 3 solar collectors per row, 24 collectors in total per loop. Size of each collector is 60 m $\times$ 8 m. The total length of the receiver tube for one loop is 1440 m. The tubes are 2″ size. Tubes are externally coated with special black paint to increase the thermal absorption. Once-through solar steam generator evaporator solar arrays will heat the feed water coming from feed water transfer pump to produce wet steam, 80% steam quality w/w.

The plant has got high level of automation; the operating parameters are recorded on a historian server on real-time basis. The data required for analysis is retrieved from server and used as appropriate.

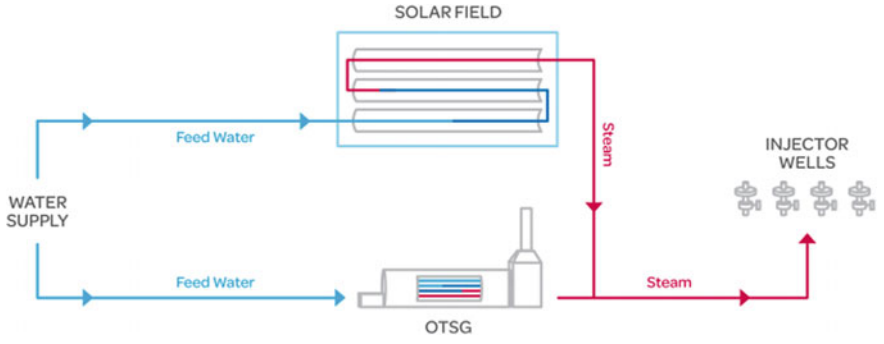

Fig. 2 Solar EOR based on enclosed trough technology (*Source* Glasspoint) [7, 8]

3 Level of Automation and Data Acquisition

There is an automation mechanism to alter the angle of the solar collectors, so that the sun rays will fall on the mirror in normal direction and the mirrors can focus the sun rays to the receiver tube always. Such system is called sun tracking system, and the algorithm of the program is made based on the coordinates of the solar collectors and the actual date of operation. Another interlock for automation is that, whenever the DNI measured at the weather station goes beyond the minimum preset value, the system will automatically go on shut down mode and the mirrors will move to the park mode, in which the mirrors reflective surface will not face the sun. The following parameters can be measured or calculated as per the current design of the plant.

- **The energy from sun**: Direct normal irradiance (DNI) in W/m^2 is measured at weather station. It is nothing but a rotating shadow band radiometer. This instrument consists of a silicon photodiode pyranometer and a motor driven band that momentarily shades it from direct sunlight in order to make a measurement. The depth of the shadow and the solar zenith angle can be used to calculate direct normal irradiance (DNI) and diffuse horizontal irradiance (DHI), the two components of sunlight necessary to calculate its effect on non-horizontal surfaces.
- **Water inlet parameters**: The boiler feed quality water is fed to the evaporator solar array receiver tubes from nitrogen blanketed feed water storage tank. Just before entering the water to the solar receiver tubes, the water parameters like temperature, pressure and flow rate are measured using a multi-variable flow transmitter. Such measurements are continuously being recorded.
- **Steam outlet parameters**: The receiver tube outlet steam, when it comes out after receiving solar energy from the eight-row of solar collector, it goes through a multi-variable flow transmitter, which records parameters like temperature, pressure and flow rate.
- **Steam quality measurement**: Steam quality is calculated by the James quality equation. It calculates the quality of steam (mass fraction of vapour in wet steam) produced by each evaporator loop by measuring the pressure drop of wet steam across a fixed orifice downstream of the steam generator and comparing it to the total flow measured upstream of the steam generator.
- **Additional data available**: The receiver tubes inside the glasshouse are equipped with additional resistance temperature detectors (RTD), temperature measuring sensors. There are RTDs, each placed after every row, means after every 180 m length at the crossover location from one row to the other. These parameters are also getting recorded on continuous basis.

4 Results and Discussion

For the purpose of analysis, various operational data were collected starting from 01 January 2018 for about 10 months. The database thus generated is being used for analysis. The main data collected are direct normal irradiance (DNI) in watts per square meter, receiver tube water inlet parameters like mass flow rate in kilogram per second, temperature in degree celsius, pressure in kilo pascal, receiver tube steam outlet parameters like mass flow rate in kilogram per second, temperature in degree celsius, pressure in kilo pascal. Attempt is made to plot their interdependence, which is discussed in this section.

4.1 DNI Variations for the Area

- **DNI Variation for a day**: DNI at the plant area (18°19′30.9″N 55°40′24.6″E) is measured using a weather station pyranometer, mounted outside the solar fields, on 15 January 2018 from morning 06:00 h to evening 18:00 h. The date is selected on an arbitrary basis. The data collection interval was set as 10 min. The pattern of DNI variation is plotted with time on *x*-axis and DNI on *y*-axis. As shown in Fig. 3, the shape of plot is that of bell curve. DNI increases as time passes, reaches the peek at around 12:00 h and then decreases with time, reaches zero at around 18:00 h. Maximum DNI was in the range of 1120–1185 W/m^2 and the average DNI range was 825–827 W/m^2.

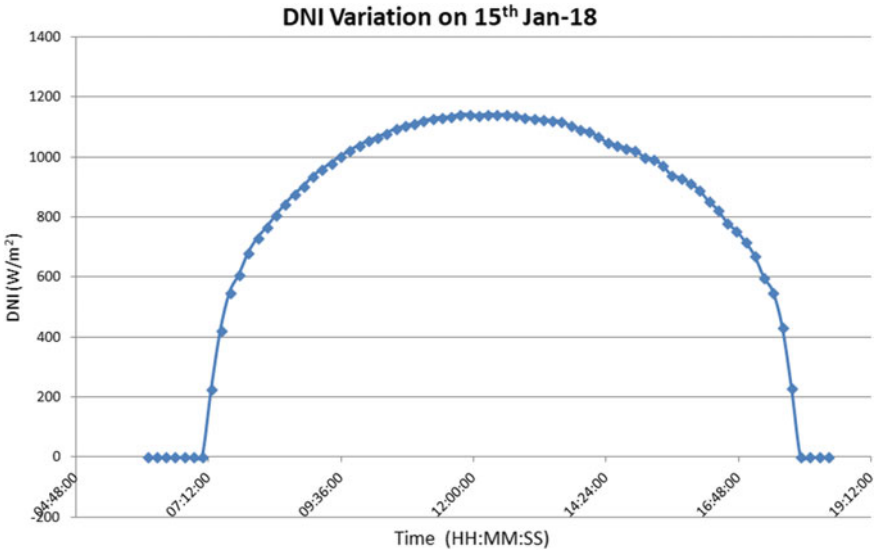

Fig. 3 DNI variation for a day

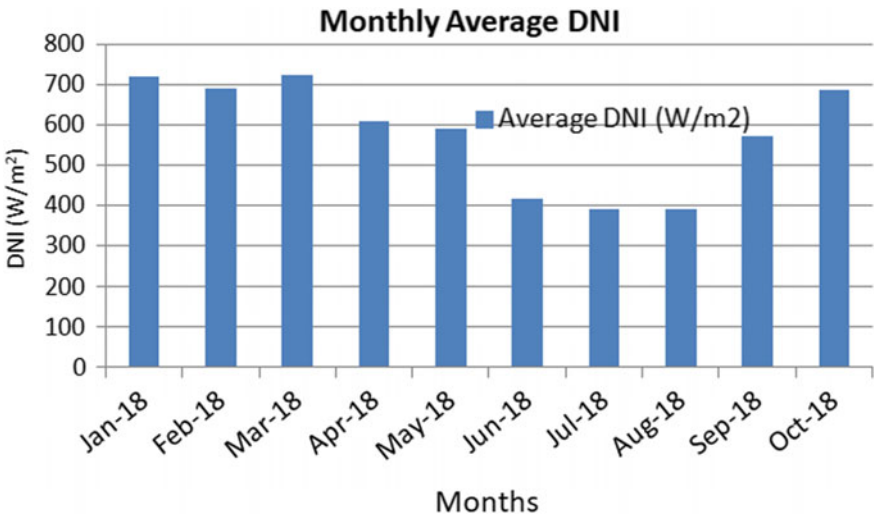

Fig. 4 Monthly average DNI

- **Monthly average DNI**: Average DNI for each month from January 2018 to October 2018 is calculated for the day time and the same is plotted as shown in Fig. 4. DNI values less than 50 W/m^2 are not considered in the calculation.

4.2 Inlet and Outlet Mass Flow with Respect to Time

Inlet and outlet mass flow rates were measured using multi-variable flow transmitters from morning to evening on 15 January 2018. The data was recorded in every 10 min. The results of their variation with time are plotted as shown in Fig. 5. It may be noted that, as time passes, as DNI increases, more steam is generated, inlet and outlet mass flow rates increase accordingly. Though the two curves not falling on top of the other exactly, both follow the same pattern. Further study and analysis are required for understanding why there is difference between inlet and outlet mass flow rates.

4.3 Effect of DNI on Inlet and Outlet Temperatures

Inlet and outlet temperatures were measured using multi-variable flow transmitters, in every 10 min from morning to evening on 15 January 2018. The results of their variation with time are plotted as shown in Fig. 6. DNI is also plotted to have a better inference. It may be noted that, as time passes, the inlet water temperature remains almost constant. This is because the water is sourced from a tank. However, outlet

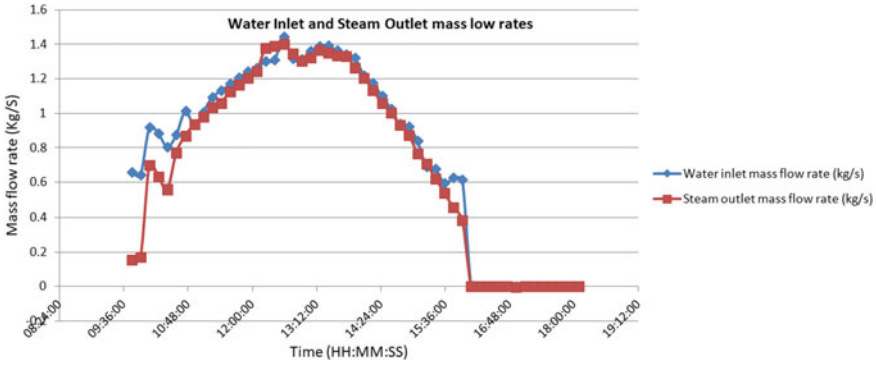

Fig. 5 Mass flow rate variation with time

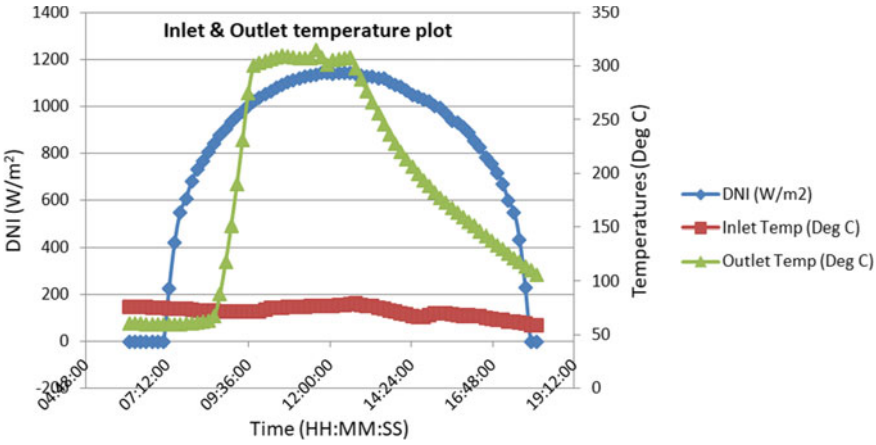

Fig. 6 DNI, inlet and outlet temperature variation with time

temperature changes with time and shows a pattern. As DNI increases, water inside the receiver tubes is converted to steam, and temperature of the steam increases to maximum, when DNI reaches peak and then drops. When DNI is at its peak, the temperature of water inside the tube reaches to about 300 °C and is already converted into steam. Every day evening, once the DNI drops to a level where in the steam production is not practically possible, the water from the tank is still pumped to the tubes in circulation mode for pre-heating of the water to the extent possible. Thus, the inlet water temperature in the plot is showing a slightly negative slope. The inference related to lower steam temperature during the start of the day, compared to inlet water temperature to be studied and analyzed further.

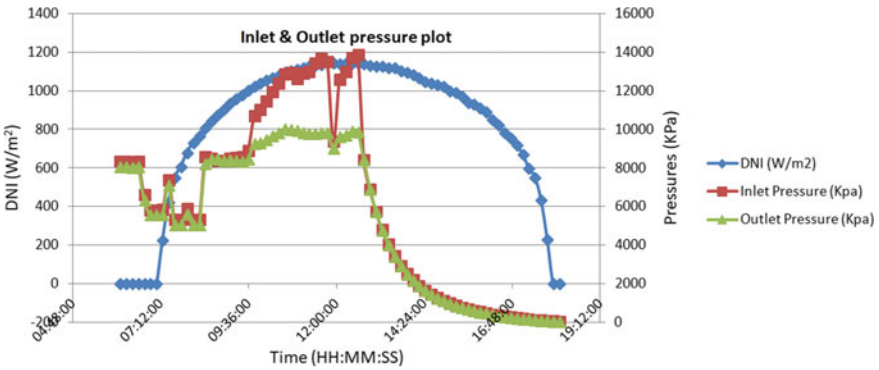

Fig. 7 Inlet and outlet pressure variation with time

4.4 Effect of DNI on Inlet and Outlet Pressures

Inlet and outlet pressures were measured using multi-variable flow transmitters from morning to evening on 15 January 2018 in every 10 min. The results of their variation with time are plotted as shown in Fig. 7. DNI is also plotted to have a better inference. It may be noted that, as time passes, the inlet water pressure fluctuates. The fluctuation mainly depends on the downstream draw off, or it could be because of some influence of the parameter external to the system under consideration like tank level, pump performance, valve positions, fluctuation in draw off water by other loops, etc. However, it hardly depends on DNI as water is pumped from a tank. Initially, with time outlet pressure also follows the same pattern as of inlet pressure. In this region, the water inside the receiver tubes is still liquid. As DNI increases, water inside the receiver tubes get converted to steam and the changes in the inlet water pressure has less sensitivity on the steam outlet pressure, due to compressibility associated with steam. As DNI decrease, the fluid inside receiver tube is again predominantly water. In this region, the inlet and outlet pressure follows the same pattern of fluctuation.

4.5 Effect of DNI on Temperature Variation Along the Receiver Tube Surface

The total length of the receiver tube is 1440 m. In order to measure the surface temperature of the tube at intermediate locations, RTDs have been installed at the "U" shaped bend area of the loops. The location of RTD installation is selected in such a way that the flow restriction is reduced to a minimum. These RTD are measuring the temperatures as "seen" by its sensor. The flow is expected to be turbulent as phase change is also happening inside the tube. Such intermediate temperatures were measured using RTDs from morning to evening on 15 January 2018. The time

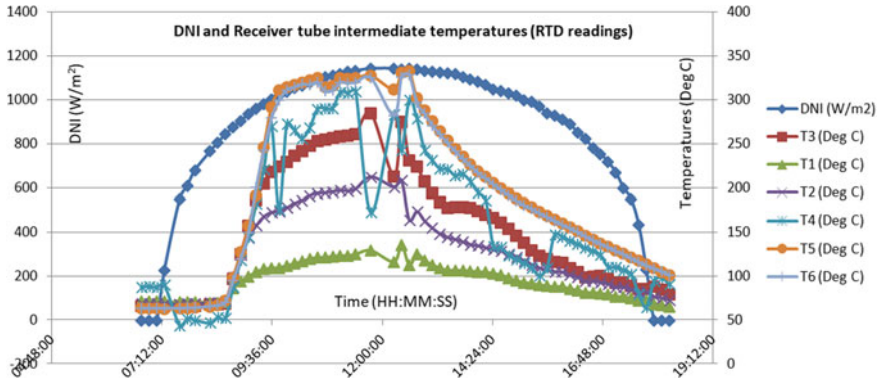

Fig. 8 Temperature variation along the receiver tube surface

duration between two readings was kept as 10 min. The readings of each RTD has been noted and the same is plotted as below in Fig. 8. DNI is also plotted to have better inference. T1, T2, T3, T4, T5 and T6 denotes the RTDs, T1 being closest to the inlet water side T6 being closest to the steam outlet side. It may be noted that the heavy fluctuation for T1, T2, T3 and T4 during the peak DNI region is expected to be due to the phase change happening inside the tube. Inside the tube, when water is expanded to steam, more heat is being absorbed from the tube surface to cater for latent heat requirements, same time continuous flow of fluid is taking place. Bubbles will be generated and broken, which makes the flow very turbulent and can cause fluctuations in temperature. Fluctuation is comparatively less for T5 and T6, because, when the fluid reaches to that section of the tube, it is already in steam phase.

5 Conclusions

Performance of the enclosed trough technology was reported earlier for a pilot plant [4]. Detailed operational data are now available for further studies and analysis. Based on the above analysis of the data on empirical basis, enclosed solar parabolic trough technology is a promising option to produce direct steam in places where abundant solar energy is available. The steam generated is used for enhancing the oil recovery in the current example, which is called solar thermal EOR. It was explored that the success of the deployment of enclosed trough direct steam generation system is strongly dependent on direct normal irradiance (DNI) of the area of deployment.

Acknowledgements Authors would like to thank M/s Glasspoint Solar, Inc. for providing access to the data required for the analysis.

References

1. Doscher TM, Ghassemi F (1982) The anticipated effect of diurnal injection on steamdrive efficiency. J Pet Technol
2. Bierman B, ODonnell J, Burke R, McCormick M, Lindsay W (2014) Construction of an enclosed trough EOR system in South Oman. Energy Procedia 49:1756–1765
3. Chaar M, Venetos M, Dargin J, Palmer D (2014) Economics of steam generation for thermal EOR. In: Abu Dhabi International Petroleum Exhibition & Conferenceno. SPE 172004 MS, pp 1–18
4. Bierman B et al (2014) Performance of an enclosed Trough EOR system in South Oman. Energy Procedia 49:1269–1278
5. Glasspoint Solar (2018) One gigawatt solar thermal project generating steam for oil production—project overview. [Online] Available: www.glasspoint.com. Accessed on 07 Oct 2018
6. Glasspoint Solar (2015) How big is Miraah. [Online] Available: www.glasspoint.com//miraah. Accessed on 07 Oct 2018
7. Glasspoint Solar (2015) Operating CSP in desert conditions. Enclosed trough technology. In: MENASOL 2015. Available: https://www.glasspoint.com/news/in-the-news/archives/page/6/. Accessed on 07 Oct 2018
8. Solar Thermal Technology, Solar Steam Generator, GlassPoint Enclosed Trough. [Online] Available: https://www.glasspoint.com/technology/. Accessed on 12 Jan 2019

Fluid Flow Study of Circular Jet Impingement on Flat Plate

Dushyant Singh and Saurabh Kango

Abstract In this present study, the round jet impingement on flat plate is analyzed numerically using four different RANS turbulence models. The four turbulence models considered are k-ω SST, realizable k-ε, RNG k-ε and v^2f. The numerical results in terms of turbulent kinetic energy have been compared with the previously published experimental results for the purpose of validation. It has been observed that v^2f model predicted the variation in turbulent kinetic energy accurately in the wall jet region above the near wall as compared with other models.

Keywords Circular jet impingement · RANS turbulence models · Turbulent kinetic energy

Nomenclature

$C\mu$	Model constant
d	Nozzle diameter
f	Elliptic relaxation function
h	Nozzle to plate spacing
I	Turbulent intensity
K	Turbulent kinetic energy
K_{f}	Thermal conductivity of the fluid
$\dot{m}$	Mass flow rate
P_r	Prandtl number
T_{j}	Jet exit air temperature

D. Singh (✉)
Department of Mechanical Engineering, National Institute of Technology Manipur, Imphal 795004, India
e-mail: dushyant7raghu@gmail.com

S. Kango
Department of Mechanical Engineering, National Institute of Technology Jalandhar, Jalandhar, India

A. K. Parwani and PL. Ramkumar (eds.), *Recent Advances in Mechanical Infrastructure*, Lecture Notes in Intelligent Transportation and Infrastructure,
https://doi.org/10.1007/978-981-32-9971-9_20

T_w	Local wall temperature
T_∞	Ambient temperature
v^2	Velocity variance scale
X and Y	Radial distance from stagnation point
Z	Vertical distance from the plate

Greek Letters

ε	Turbulent dissipation rate
ε_{ss}	Emissivity of the stainless steel foil
μ	Dynamic viscosity of air
μ_t	Turbulent viscosity
ρ	Density of air
ω	Specific dissipation rate

1 Introduction

Impinging jet heat transfer is frequently used in engineering applications in industries due to its various features like localized and immediate cooling and when very high heat transfer rates are required. There are a lot of examples of jet impingement in industries like bakery ovens, in glass, paper and steel industry, etc. The flow exhibits complex flow physics due to turbulence kinetic energy produced by normal straining, strong stress anisotropy, streamline curvature and a radially spreading wall jet with near-wall separation [1]. The several applications of jet impingement in various industries have also encouraged the researchers to develop various computational models, with moderate system requirements. The heat transfer characteristics and flow behaviors can be easily predicted using such models. However, the accuracy of prediction depends upon the modeling of turbulence. Various turbulence models use different parameters to model turbulence of the flow. The accuracy of those models depends upon those parameters and nature of the problem. To simulate the turbulence, two (k-ω SST, realizable k-ε, RNG k-ε) and four (v^2f) equations (parameters) are used. Zukerman and Lior [2] reviewed the performance of various RANS model for round jet impingement on flat plate. Dewan et al. [3] have reviewed recent trends in the computation of turbulent jet heat transfer. There are many researches done on various aspects such as effect of nozzle geometry in confinement, chamfering of nozzle inlet, to gain more insight into the field of jet impingement. Their studies helped in understanding the heat transfer characteristics under various conditions [4, 5].

The predictions of flow by a turbulence model depend upon how well these models are able to capture the Reynolds stresses. The turbulent kinetic energy (k) calculated

by various RANS model uses only the normal Reynolds stresses [2]. The closure method approximates the turbulent kinetic energy (k) with only normal Reynolds stresses. Various RANS model uses turbulent kinetic energy as a parameter to predict the turbulent flow. The Reynolds stresses were experimentally analyzed by many researchers so as to obtain the nature of turbulence flow [6–8]. Cooper et al. [6] have conducted experimental analysis of Reynolds stresses on round jet impinging on a flat plate and presented their results. Turbulence flow in the near field of an axisymmetric jet was experimentally investigated by Tummers et al. [7] and found instantaneous flow reversal in the near-wall region, attributed to the formation of small secondary vortices. Yao et al. [8] have conducted studies on turbulent jet impingement on a flat surface, investigated on Reynolds stress and concluded that the mixing region in the free jet has the maximum kinetic energy. Numerical investigation of normal Reynolds stresses with RANS model is also done to get more insight into various aspects of turbulent flow. The comparative study done in this present work, with turbulent kinetic energy, was not previously done by many researchers.

2 Numerical Modeling

The problem of circular jet impinging on a flat plate was analyzed numerically assuming the flow to be steady, incompressible, turbulent and axisymmetric. Figure 1a, b shows the schematic diagram of flat plate and 3-D representation of the geometry. In this present study, the relative performance of different RANS turbulence models with varying nozzle to plate spacing (h/d) was determined.

The time-averaged continuity, momentum and energy equations solved during the simulation are as follows:

$$\frac{\partial u_i}{\partial x_i} = 0 \tag{1}$$

$$\rho u_j \frac{\partial u_i}{\partial x_j} = -\frac{\partial P}{\partial x_i} + \frac{\partial}{\partial x_j}\left[\mu\left(\frac{\partial u_i}{\partial x_j} + \frac{\partial u_j}{\partial x_i}\right) - \rho\overline{u_i' u_j'}\right] \tag{2}$$

The Reynolds stress was calculated using Boussinesq hypothesis.

$$\overline{u_i u_j} = \nu_t\left(\frac{\partial u_i}{\partial x_j} + \frac{\partial u_j}{\partial x_i}\right) - \frac{2}{3}k\delta_{ij} \tag{3}$$

ν_t is the turbulence viscosity, and k is the square of length scale. For detailed discussion of RANS turbulence models, the readers are advised to review studies of Singh et al. [9, 10], and Dutta et al. [11].

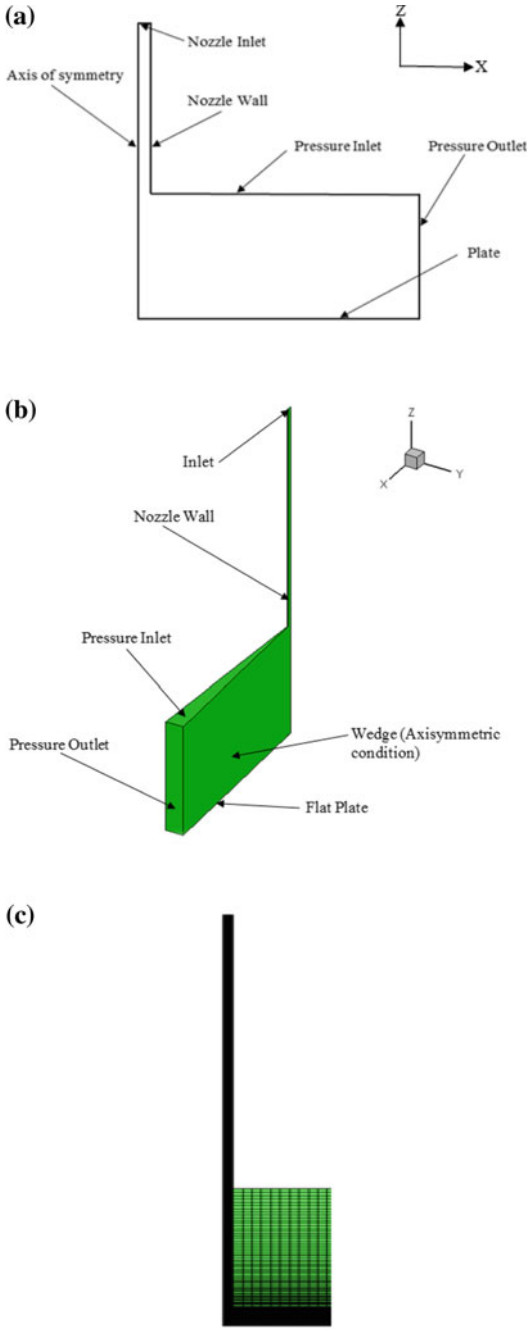

Fig. 1 **a** Cut section view of the plate, **b** 3-D view of domain geometry and **c** Mesh pattern of computational domain

3 Solution Methodology

The open-source CFD solver, OpenFOAM 5 was used to solve the continuity, momentum and energy equations as shown in Fig. 1c. Finite volume method is used by this solver to discretize the governing equations. Semi-implicit pressure linked equation (SIMPLE) algorithm is used to couple velocity and pressure [12]. Four RANS turbulence models, namely k-ω SST, realizable k-ε, RNG k-ε and v^2f were used to model turbulence. OpenFOAM supports variety of wall functions for different parameters [13]. Corresponding wall functions were used according to the input boundary conditions in order to capture the near-wall effects. When the residuals of continuity, velocity components and turbulence quantities fall below 10^{-6}, the solution is deemed to be converged. The values of density and dynamic viscosity were taken as 1.225 kg/m^3, 1.7894 $\times$ 10^{-5} kg/ms, respectively.

4 Boundary Conditions

A long channel was modeled so as to get a fully developed flow at the nozzle exit. Uniform velocity distribution was given as input at nozzle inlet while no slip condition was given at both the plate and nozzle walls. The sufficient grid refinement was near the target surface to obtain Y^+ value less than 1. Both pressure inlet and outlet are open sides of the domain with zero initial gauge pressure. Wedge boundary condition was applied at both front and back sides of the geometry as OpenFOAM demands the use of a wedge-shaped geometry for axisymmetric cases. Remaining boundary conditions were set using the following equations:

$$K = \frac{3}{2}(uI)^2, \varepsilon = C_\mu \frac{\rho K^2}{\mu}(\mu_t/\mu)^{-1}, \omega = \frac{\rho K}{\mu}(\mu_t/\mu)^{-1}, v^2 = \frac{2}{3}K \tag{4}$$

At pressure boundaries and inlet, the flux of K, ε, ω, v^2, f is set to zero. The values of k, ε, ω and v^2 at inlet were calculated from the above equations based on the values of turbulent intensity and eddy viscosity ratios.

5 Results and Discussions

In this present study, the turbulent kinetic energy was numerically simulated and compared with the experimental results of Reynolds stresses [7]. In the quest for an appropriate turbulence model, the simulations were carried out using k-ω SST, realizable k-ε, RNG k-ε and v^2f turbulence models at $Re_d = 23{,}000$, for various non-dimensional distance of the jet exit to flat plate, h/d ratio = 2. To predict turbulent kinetic energy k, RANS turbulence models use only the normal Reynolds stresses.

With the help of instantaneous velocity fluctuations perpendicular to each coordinate axis, at a particular point in the domain, the turbulent kinetic energy can be calculated. Turbulent kinetic energy is one of the parameter by which the turbulence flow is determined by these turbulence models. Figure 2 shows the turbulent kinetic energy predicted by the four turbulence models at various locations of the fluid flow domain, for nozzle to plate spacing, $h/d = 2$, compared with the experimental results obtained by Tummers et al. [7]. At the stagnation point, $Y/D = 0$, the near-wall turbulence kinetic energy predicted by both realizable k-ε and v^2f models is near to the experimental result, whereas RNG k-ε and k-ω SST models overpredicted the results as depicted in Fig. 2a. As explained, from the fluid flow results, both RNG k-ε and k-ω SST models overpredicted at the stagnation point while the predictions

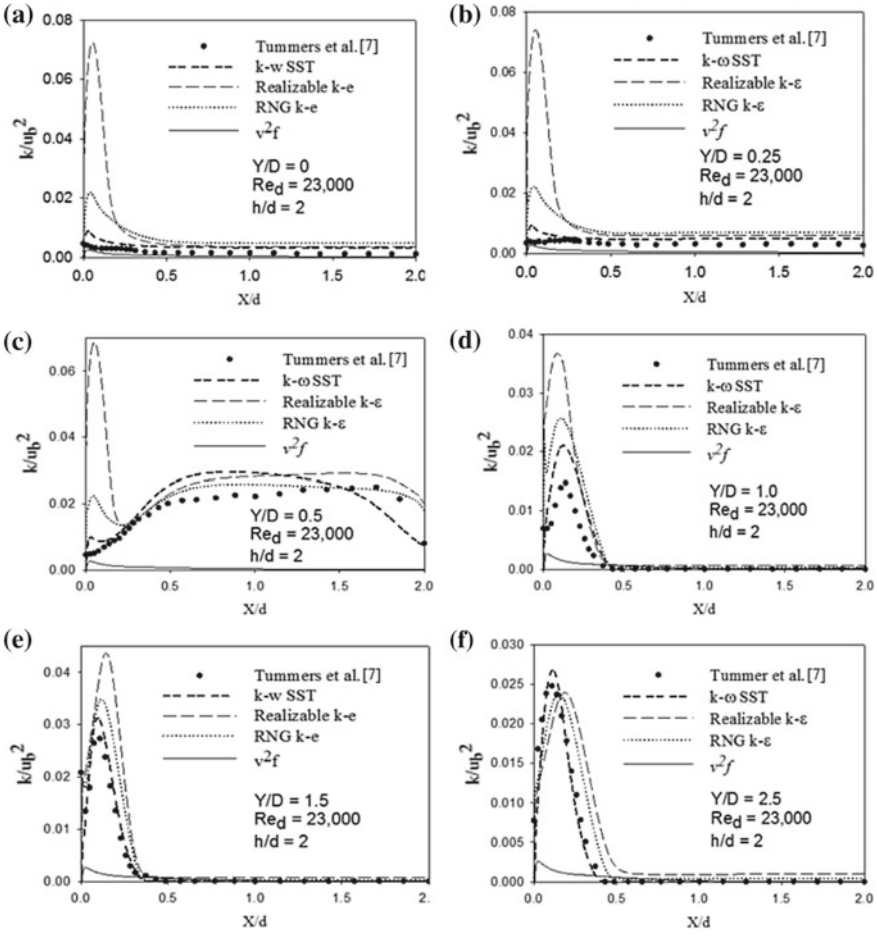

Fig. 2 Turbulent kinetic energy predicted by the four turbulence models at various locations of the fluid flow domain, compared with the experimental results obtained by Tummers et al. [7]

of realizable k-ε and v^2f models were close to the experimental results. However, realizable k-ε model overpredicted the turbulence kinetic energy after the near-wall region. Same trend in results was followed by all the turbulence models at Y/D = 0.25 as shown in Fig. 2b; however, the predictions by RNG k-ε and k-ω SST models almost matched with the experimental results further away from the near-wall region. From Fig. 2c, it is evident that v^2f model predicts close results with experimental values in the near-wall region, but all other models overpredict the result. The turbulent kinetic energy predicted by other models at stagnation point is very high compared with the prediction of v^2f model; hence, it is able to predict the accurate result at stagnation point. From Fig. 2d, it is clear that the predictions of both RNG k-ε and k-ω SST models matched the nature of the curve beyond the near-wall region, while only v^2f model underpredicted the results in the near-wall region. This explains why the Nusselt number was underpredicted by v^2f model in this region. The trend of the experimental result was captured by k-ω SST, Realizable k-ε and RNG k-ε, however v^2f model underpredicted the result at the near-wall region. At $Y/D = 1.5$, the variation in turbulent kinetic energy at near-wall region was captured by k-ω SST, while RNG k-ε and realizable k-ε overpredicted the results; however, v^2f model underpredicted the results as depicted in Fig. 2e.

The k-ω SST turbulence model's prediction matched with the experimental result accurately at $Y/D = 2.5$, in the near-wall region and beyond, while v^2f model followed the same trend and accurately matched with the experiment results only beyond near-wall region as shown in Fig. 2f. RNG k-ε and realizable k-ε also captured the trend of the curve but their result varied slightly from the experimental result. At the wall jet region, k-ω SST captured the behavior of the curve accurately. This explains the reason for the accurate prediction of Nusselt number in wall jet region by k-ω SST. In all the cases, realizable k-ε model tend to overpredict the result. The v^2f model is better in predicting the turbulent kinetic energy results at stagnation point, while both RNG k-ε and k-ω SST turbulence models predicted the nature of the curve in the vicinity of stagnation point.

6 Conclusion

In this present analysis, four different turbulence models were used in the analysis of turbulent kinetic energy using Reynolds stresses for nozzle to plate spacing at $h/d = 2$ and $Re_d = 10{,}000$. The v^2f model predicted the variation in turbulent kinetic energy accurately in the wall jet region above the near wall while it predicted with moderate accuracy in the stagnation region.

References

1. Geers LFG, Hanjalic K, Tummers MJ (2006) Wall imprint of turbulent structures and heat transfer in multiple impinging jet arrays. J Fluid Mech 546:255–284
2. Zuckerman N, Lion N (2006) Jet impingement heat transfer: physics, correlations, and numerical modeling. Adv Heat Transf 39:565–631
3. Dewan A, Dutta R, Srinivasan B (2012) Recent trends in computation of turbulent jet impingement heat transfer. Heat Transfer Eng 33(4–5):447–460
4. Colucci DW, Viskanta R (1996) Effect of nozzle geometry on local convective heat transfer to a confined impinging air jet. Exp Therm Fluid Sci 13:71–80
5. Brignoni LA, Garimella SV (2000) Effects of nozzle-inlet chamfering on pressure drop and heat transfer in confined air jet impingement. Int J Heat Mass Transf 43:1133–1139
6. Cooper D, Jackson DC, Launder BE, Liao GX (1993) Impinging jet studies for turbulence model assessment-l. Flow-field experiments. Int J Heat Mass Transf 36(10):2675–2684
7. Tummers MJ, Jacobse J, Voorbrood SGJ (2011) Turbulent flow in the near field of a round impinging jet. Int J Heat Mass Transf 54:4939–4948
8. Yao S, Guo Y, Jiang N, Liu J (2015) An experimental study of a turbulent jet impinging on a flat surface. Int J Heat Mass Transf 83:820–832
9. Singh D, Premachandran B, Kohli S (2013) Numerical simulation of the jet impingement cooling of a circular cylinder. Numer Heat Transf, Part A: Appl 64(2):153–185
10. Singh D, Premachandran B, Kohli S (2013) Experimental and numerical investigation of jet impingement cooling of a circular cylinder. Int J Heat Mass Transf 60:672–688
11. Dutta R, Dewan A, Srinivasan B (2013) Comparison of various integration to wall (ITW) RANS models for predicting turbulent slot jet impingement heat transfer. Int J Heat Mass Transf 65:750–764
12. Patankar SV (1980) Numerical heat transfer and fluid flow. Hemisphere, Washington DC
13. OpenFOAM 5 User guide

Techno-economic Assessment of Indian Power Plant Retrofitted with Calcium Carbonate Looping Capture Method

Pulkit Kumar and Ajit Kumar Parwani

Abstract The increase in concentration of carbon dioxide (CO_2) into the atmosphere has now become a serious threat to the world. Agriculture is now getting badly affected due to changes in weather pattern which is caused by the presence of huge amount of CO_2, a potential greenhouse gases (GHG). Developing country like India where agriculture and services play a major role in the GDP is more concerned about the global warming. Major source of CO_2 emission in India is thermal power plant, which accounts for almost 65% of CO_2 being emitted into the atmosphere. So implementation of CO_2 capture unit with minimum cost in thermal power plant is very necessary in order to cut the emission of CO_2. In this paper, techno-economic assessment of carbon capture unit in thermal power plant of India is performed using IECM software developed by the Department of Energy, Carnegie Mellon University, USA. It is estimated that the implementation of calcium carbonate looping combustion method of carbon capture will increase the total amount by almost Rs. 2687/MWh. This amount can be reduced by utilizing and selling the stored CO_2 to different industries.

Keywords Greenhouse gas · Calcium looping combustion · IECM · Techno-economic

1 Introduction

Global warming poses serious threat to sustenance of life on earth, be it the life of human beings or the other living creatures. The rapid pace of increasing human activity is an important reason behind increasing concentration of CO_2 which is currently 411.75 ppm (February, 2019). The implications of growing amount of CO_2 in atmosphere are elaborately discussed in literature [1, 2]. Effects of rise in global

P. Kumar · A. K. Parwani (✉)
Institute of Infrastructure Technology Research and Management, Maninagar, Ahmedabad, India
e-mail: ajitkumar.parwani@iitram.ac.in

A. K. Parwani and PL. Ramkumar (eds.), *Recent Advances in Mechanical Infrastructure*, Lecture Notes in Intelligent Transportation and Infrastructure,
https://doi.org/10.1007/978-981-32-9971-9_21

atmospheric CO_2 concentration and the resulting climate change (including global warming) are being experienced around the world.

Extreme weather effects are being experienced more often at many more places in the recent years. In India too, the frequency and unpredictability of such extreme weather effects have gone up in recent years, thus resulting in the loss of precious life and asset. The number of death in India due to heat stroke during the recent past is mentioned in Fig. 1 [3–7]. The possibility and frequency of occurrence of such extreme weather event are largely uniform for various different geographical locations around the world. However, the scale of damage due to such environmental disaster is dependent on the disaster preparedness of the local people, government and the available infrastructure. This is the reason behind the disproportionately large damage meted by the developing or the under-developed countries as compared to the developed world. Besides such disaster preparedness, there are many more developmental goals inspiring the local governments to work towards superior economic growth rate with the ultimate aim of achievement of better standard of living for their citizenry.

More often than not, such superior economic growth rate is achieved at the expense of intensive (and perhaps inefficient too) exploitation of natural resources. India accounts for 17% of world population of which 30% can be considered to be underprivileged. Since past several decades, the successive government in India have been targeting the gross domestic product (GDP) of 7% or higher. The intensity of the effect of global warming and global climate change are being felt around the world in affecting per capita income and standard of living in India, their dependence on

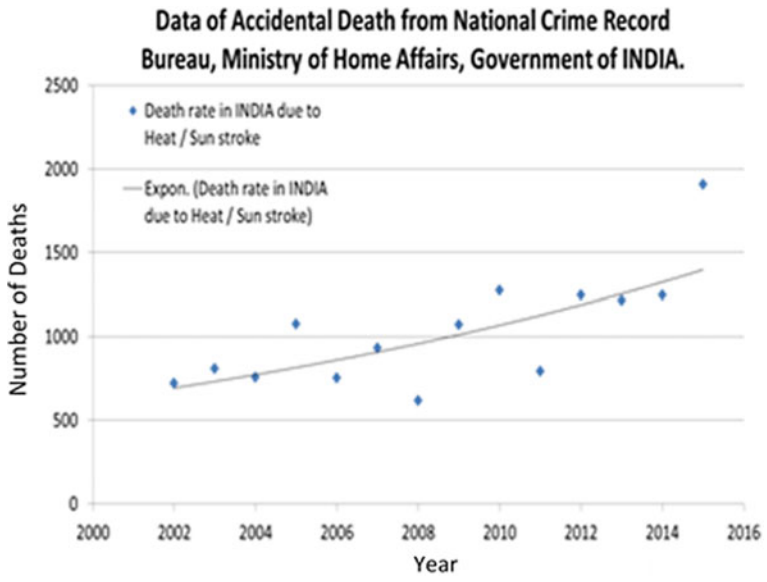

Fig. 1 Death rate due to heat/sun stroke in India [8]

electricity Current government has put forward the ambitious target of providing a secure home fulfilling the necessities of life to everyone in India by 2022. In addition, several other transportations, irrigation or amenities project are under various phase of planning or engineering or construction. These projects would demand large amount of power in the form of electricity. Power generation has grown rapidly in India with a growth rate of around 4.72% in electricity production over previous fiscal year. India is developing rapidly with expansion in industrial activities which will boost the demand of electricity. India ranks third in producing electricity and fifth in installed capacity of power generation globally [9].

Power consumption is estimated to increase from 1160.1 TWh in 2016 to 1894.7 TWh in 2022 with the production capacity of 1423 TWh. Almost 65.7% of the total power produced in India is contributed by thermal power plants with total installed capacity of 219.56 GW, out of which 193,821.50 MW is contributed by coal-based power plants. Due to increase in no. of thermal power plants, the problem of CO_2 emission is also increasing proportionally [10]. Considering these facts, it has now become mandatory for the thermal power plants to install a carbon capture unit in order to reduce the carbon dioxide emission. But installing the carbon capture unit will increase the cost of energy production which will cause energy penalty. So, techno-economic assessment of carbon capture is very important before installing such unit.

The Integrated Environmental Control Model (IECM) is a software, which is created for estimation of performance, emission and cost of fossil-fuel is used for analysis. This software was developed by the Carnegie Mellon University, United States Department of Energy. Pulverized coal power plants with carbon capture and storage plant can be simulated in the IECM environment. The base plant can be configured along with various emission characteristics of the flue gases and the stack. Through this IECM software, capital and total cost of the setup can be estimated with post-combustion CCS retrofitting [11].

In this paper, data has been taken from Wanakbori Thermal Power Station (WTPS), Gujarat State Electricity Corporation Limited (GSECL), Wanakbori, Gujarat. WTPS is a coal-based thermal power plant with seven working units of 210 MW each, as on April 2018. The data used in the analysis is of unit number 7 of WTPS. By using this data, we can perform techno-economic analysis for calcium carbonate looping (CCL) CO_2 capture unit retrofitted in power plant using IECM software.

1.1 Calcium Carbonate Looping

It is one of the post-combustion carbon capture methods in which calcium oxide (CaO) is used as sorbents to remove CO_2 from flue gases, which comes from power plant. Using this method concentrated stream of CO_2 is produced, which is suitable for storage and utilization. The CCL method depends on the reversible, exothermic reaction that happens in the carbonator at a temperature of 650 °C, where CO_2 in the flue gas is consumed by CaO to form calcium carbonate ($CaCO_3$). Now this $CaCO_3$

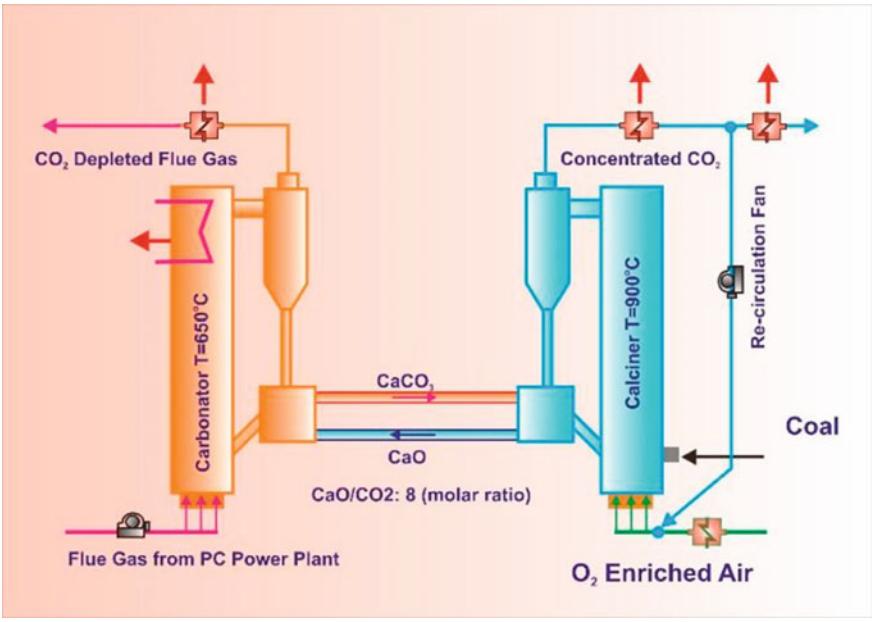

Fig. 2 Calcium carbonate looping [12]

is sent to calciner, where it gets converted to CO_2 and CaO at high temperature. In calciner, we get pure stream of CO_2. CaO left in the calciner is again sent to carbonator to take part in the reaction. The reversible reaction which takes place inside the carbonator and calciner is given by the Eq. 1

$$CaO(s) + CO_2(g) \Leftrightarrow CaCO_3(s) \tag{1}$$

So this treated and captured CO_2 is then stored which can be utilized for different purpose. Remaining flue gas is emitted to the atmosphere from the carbonator. Since this is an exothermic reaction, so the energy produced can be utilized in the secondary steam cycle to produce electricity. The principle of the CCL process is shown in Fig. 2.

2 Techno-Economic Analysis of Carbon Capture for 210 MW Power Plant Is as Under

IECM software is specifically built for power plant. In our study, we are analysing the amount of carbon dioxide emitting from 210 MW plant. Using the data of power plant in IECM software, cost of capturing carbon dioxide is calculated. The result obtained was in terms of dollar because the software gives the output considering

the currency of USA. The cost breakup associated with the installation of carbon capture unit is shown in Table 1.

From the result Table 1 it can be concluded that the capital required for the installation of carbon capture unit in WTPS is 655$/Kw-net. This cost includes almost all the cost necessary to retrofit in a working power plant. Table 2 gives comparison of the cost between with and without CO_2 capture in WTPS.

It also gives the details of total CO_2 emitted and captured along with the cost of capturing it. Cost of CO_2 captured is characterized as gradual levelized capture costs in a given year separated by the volume of CO_2 caught for a given year. It is commonly communicated as the change in levelized cost of electricity annually, between the capture case and the reference case, divided by the volume of CO_2 captured in a year. The standard formula is given by equation no. (1):

$$\left(\mathrm{COE}_{\mathrm{capture}} - \mathrm{COE}_{\mathrm{ref}}\right) \times \mathrm{MWh}_{\mathrm{capture}} / \mathrm{CO}_{2\mathrm{captured}} \tag{1}$$

While the cost of avoidance is defined as the gradual levelized capture costs annually by the change in intensities of reference and capture cases multiplied by the

Table 1 Capital required for installing CCS unit

CO_2 capture plant costs	Capital cost ($/kW-net)
Process facilities capital	325.4
General facilities capital	32.54
Engineering and home office fees	22.76
Process contingency cost	80.39
Project contingency cost	88.58
Interest charges (AFUDC)	83.66
Royalty fees	1.626
Preproduction (Start-up) cost	18.02
Inventory (Working) capital	2.747
Total capital requirement (TCR)	655.5

Table 2 Comparison of cost for CO_2 capture

	Without CO_2 capture	With CO_2 capture
Electricity generation capacity (MW)	210 MW	210 MW
CO_2 Emitted (kg/kWh)	1.12	0.03752
CO_2 Captured (kg/kWh)	0	0.7702
Cost of electricity (COE) ($/MWh)	53.27	91.01
Added cost of CCS ($/MWh)	0	37.74
Cost of CO_2 avoided ($/tonne)	0	34.87
Cost of CO_2 captured ($/tonne)	0	34.99

MWh created in the capture case. The denominator is basically the volume of CO_2 captured less the volume of CO_2 discharged by the frameworks required to capture the CO_2. It is calculated by using the standard formula given in equation no. (2):

$$\left(\mathrm{COE}_{\mathrm{capture}} - \mathrm{COE}_{\mathrm{ref}}\right) / \left(\mathrm{Intensity}_{\mathrm{ref}} - \mathrm{Intensity}_{\mathrm{capture}}\right) \tag{2}$$

After analysis, it was found that the added cost of carbon dioxide capture and storage unit is 37.74 $/MWh. It can be converted into Indian rupee considering the current value of dollar which is equal to Rs. 2686.90. Conversion of dollar into rupees is done considering the value of 1 dollar is Rs. 70.14 dated on 23 January 2019. So the total cost addition in unit production of electricity is almost equal to Rs. 2.7.

3 Conclusion

This article evaluates the cost of installing CLC technology for capturing CO_2 in a working power plant. Wanakbori Thermal Power Station (WTPS) situated in Wanakbori, Gujarat is chosen for the analysis purpose. IECM software version 11.2 is used in performing techno-economic analysis. From the result, it can be concluded that the cost of capturing CO_2 is Rs. 2.7/KWh which is a significant amount. It can be justified by the benefits of reducing the amount of CO_2 from the atmosphere. Also, the stored CO_2 can be reused in various applications or it can be sold to the industries like chemical industry, refrigeration industry, soda industry, etc. The revenue generated by selling the stored carbon dioxide to various industries will help to cut the cost of capturing CO_2.

Acknowledgements This work was possible because of the data shared by the WTPS, Wanakobri. The authors would like to thanks Mr. AD Gamit, Deputy Engineer (WTPS, GSECL) for providing the required data needed for analysis.

References

1. The current and future consequences of global change, Global Climate Change, National Aeronautics and Space Administration (NASA, USA). http://climate.nasa.gov/effects
2. Global Energy Assessment (GEA), by International Institute for Applied Systems Analysis (IIASA). http://www.globalenergyassessment.org/
3. Report from National Centers for Environmental Information (NOAA), State of the Climate: Global Climate Report for January 2019, published online February 2019, retrieved from https://www.ncdc.noaa.gov/sotc/global/201901/supplemental/page-1
4. India crippled by extreme weather as 100 million exposed to floods. https://www.theguardian.com/sustainable-business/2016/apr/21/india-drought-flooding-natural-disasters-risk-population-economy-insurance
5. National Centres for Environmental Information, USA. https://www.ncdc.noaa.gov/climate-information/extreme-events

6. Over 1600 died in India due to extreme weather conditions in 2016. http://www.hindustantimes.com/india-news/over-1-600-killed-due-to-extreme-weather-patterns-in-2016/story-ZXToWjowatrEYk81af2V4H.html
7. Extreme weather events in India in the past 10 years. http://www.downtoearth.org.in/news/extreme-weather-events-in-india-in-the-past-10-years-46450
8. Report Published by National Crime Record Bureau, Ministry of Home Affairs, Government of India, 2016
9. India is now the world's third-largest electricity producer, A report published by quartz India. https://qz.com/india/1237203/india-is-now-the-worlds-third-largest-electricity-producer
10. A regional assessment of the potential for CO_2 storage in the indian subcontinent, A technical study report Prepared by IEA, report no. 2008/2, May 2008
11. IECM 2012: Integrated environmental control model available at: http://www.cmu.edu/epp/iecm/
12. Angela R, Huang Y, Haaf M, Rezvani S, Dave A, Hewitt NJ (2017) Techno-economic and environmental analysis of calcium carbonate looping for CO_2 capture from a pulverised coal-fired power plant, 9th international conference on applied energy, ICAE 2017, pp 1876–6102

Estimation of Time-Varying Heat Flux for One-Dimensional Heat Conduction Problem by Hybrid Inverse Method

Sanil Shah and Ajit Kumar Parwani

Abstract Time-varying heat flux for one-dimensional heat conduction problem is estimated by inverse heat transfer method. The conjugate gradient method (CGM) and hybrid of JAYA-CGM algorithm are used for estimation. Finite volume method (FVM) is used to discretize one-dimensional problem domain for determining simulated temperature measurements. These temperature measurements are utilized in CGM and hybrid algorithm in order to estimate transient heat flux. Results show that hybrid algorithm estimates constant, linearly increasing, and linearly decreasing heat flux better than CGM.

Keywords Conjugate gradient method · Inverse heat transfer · Hybrid algorithm · JAYA

1 Introduction

Inverse heat transfer is the most widely used for estimation of thermal boundary conditions, thermophysical properties of material, location of source term in given domain, etc. Inverse heat transfer has a wide range of applications such as astrophysics, aeronautics, nuclear science, thermal science, etc. [1]. In direct heat transfer problem, values of quantities at boundaries are known and temperature field is obtained for design purpose. But in inverse technique, these boundary conditions are unknown and they are estimated by measuring the temperature data near to that boundary. In the most of cases, the measured temperature data is used for estimation of unknown quantity by minimizing the relevant objective function which makes it as an optimization problem. Since accuracy of inverse heat transfer problems (IHTP) highly depend upon measured temperature data, any error in measured temperature deteriorates the output which makes inverse heat transfer as ill-posed problems.

S. Shah · A. K. Parwani (✉)
Mechanical Engineering Department, Institute of Infrastructure Technology Research and Management, Ahmedabad, India
e-mail: ajitkumar.parwani@iitram.ac.in

A. K. Parwani and PL. Ramkumar (eds.), *Recent Advances in Mechanical Infrastructure*, Lecture Notes in Intelligent Transportation and Infrastructure,
https://doi.org/10.1007/978-981-32-9971-9_22

IHTP are ill-posed problems [1]; hence, they require mathematical treatment to stabilize. Tikhonov and Arsenin [2] introduced regularization procedure in which smoothing terms were added to modify the least-squares equation in order to reduce the effects of temperature measurement errors. Alifanov and Artyukhin [3] introduced iterative regularization principle in which solution improves by sequence. The stopping criterion for such iterative procedure is chosen so that the final solution is stabilized with respect to errors in the input data.

In most of inverse heat transfer problems, the solution is obtained by minimizing the least-square error between measured and estimated temperatures which id termed as objective function. For solving each problem, a well-defined algorithm is used in which each mathematical term is solved and objective function converges to a defined minimum value. There are many methods available for solving inverse heat transfer problems. Some of them are stochastic methods in which populations of solutions are randomly generated and the best fitted solution is chosen. Differential evolution (DE) algorithm, generic algorithm (GA),and particle swarm optimization (PSO) are some of the recommended stochastic methods [4]. These methods give accurate results but are very time-consuming which lead to higher computational cost.

Other methods are deterministic methods in which solution starts from any random input (most probably zero value of unknown quantity) and then approaches toward actual solution [1]. Newton–Gauss method, Levenberg–Marquardt's method, steepest descent method (SDM), conjugate gradient method (CGM), Quasi–Newton kmethod, etc. are examples of deterministic methods. These methods are fast in converging and also lead accurate results for better initial guess. However, sometimes the main algorithm converges at local minima and hence, these methods are less accurate for estimation of boundary conditions.

To take the advantage of accuracy of stochastic methods and convergence speed of deterministic methods, hybrid algorithms are used. In these algorithms, two methods are coupled and adjusted such a way that it gives results within specified accuracy and within particular time period. Parwani et al. [3] used hybrid method by the combination of CGM and DE for estimation of boundary condition in various heat transfer cases. They concluded that this hybrid algorithm is more accurate than CGM and faster than DE. The current work focuses on a new hybrid algorithm where a stochastic algorithm JAYA is coupled with deterministic method CGM.

2 JAYA Algorithm

JAYA is a multi-objective optimization algorithm developed by Rao [5]. In this algorithm, the steps are designed in such a way that solution approaches toward best solutions and far from worse solutions. Figure 1 shows flow chart of JAYA. As shown in Fig. 1, solution starts from initial random population and then best and worse solution is chosen. According to convergence criteria, the solution modifies and reaches toward the optimum value. The main advantage of this algorithm is that it can be used for constraint as well as unconstrained problems [5]. For optimiz-

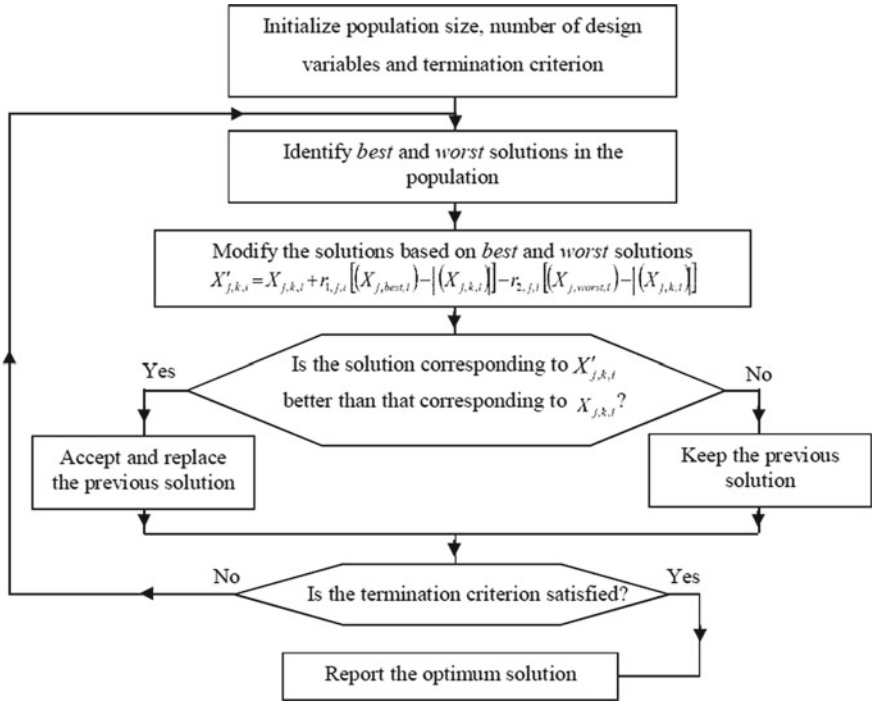

Fig. 1 JAYA algorithm

ing the different parameters, JAYA is successfully implemented [6, 7]. Since JAYA is stochastic-based method, it can be used for multiple objectives but still nobody ever tried it for inverse heat transfer problem where it is used for minimizing the least-square bases objective function by available measured temperature data.

Suppose, $f(x)$ is the objective function is to be minimized at ith iteration, assume that there are m numbers of design variables (i.e., $j = 1, 2 \ldots m$), n number of candidate solutions (i.e., population size $k = 1, 2, \ldots n$). Let, the best candidate *best* obtains the best value of $f(x)$ and the worst candidate *worst* obtains the worst value of $f(x)$ in the entire candidate solutions. If $X'_{i,j,k}$ is the value of the jth variable for the kth candidate during the ith iteration, then this value is modified as per the following Eq. (1):

$$X'_{j,k,i} = X_{j,k,i} + r_{1,j,i}\left(X_{j,\text{best},i} - \left|X_{j,k,i}\right|\right) - r_{2,j,i}\left(X_{j,\text{worst},i} - \left|X_{j,k,i}\right|\right) \quad (1)$$

where $r_{1,j,i}$ and $r_{2,j,i}$ are random numbers ranging from 0 to 1.

From Eq. 1, it is clear that the solution approaches near to best solutions and far away from worst ones. The termination criterion is the least value of an objective function (i.e., 10^{-3} to 10^{-6}). The objective function may vary for different problems.

3 Conjugate Gradient Method

CGM is a gradient-based method and most widely used method in inverse heat transfer problems. The authors had estimated strength of point source for one-dimensional heat conduction problem by CGM [8]. In CGM, the solution is obtained by minimizing the objective function:

$$S[\mathrm{qe}(t)] = \int_{t=0}^{t=t_f} \left\{ Y_m(x_{\mathrm{meas}}, t) - T\left[x_{\mathrm{meas}}, t, \mathrm{qe}(t)\right] \right\}^2 \mathrm{d}t \tag{2}$$

where $Y_m(x_{\mathrm{meas}}, t)$ are measured temperature values and $T\left[x_{\mathrm{meas}}, t, \mathrm{qe}(t)\right]$ are the estimated values at that measuring point (x_{meas}). Figure 2 shows computational domain for one-dimensional heat conduction problem where heat flux $q(t)$ is given at left boundary and right boundary is insulated.

The governing equation of this problem is:

$$\frac{\partial}{\partial x}\left(k\frac{\partial T}{\partial x}\right) = \rho c \frac{\partial T}{\partial t} \tag{3}$$

As the flux is applied on left boundary and right boundary is insulated which lead to following boundary conditions:

$$-k\frac{\partial T}{\partial x} = q(t) \text{at} \quad x = 0, t > 0 \tag{3a}$$

$$\frac{\partial T}{\partial x} = \text{at} \quad x = x, t > 0 \tag{3b}$$

In direct problem, $q(t)$ is known and temperature field $T(x, t)$ is obtained. In inverse problem, measured temperature values at measuring point x_{meas} are available and flux $(\mathrm{qe}(t))$ is estimated by CGM. Figure 3 shows CGM algorithm. As shown, the unknown quantity $\mathrm{qe}(t)$ is initially guessed and fed to algorithm.

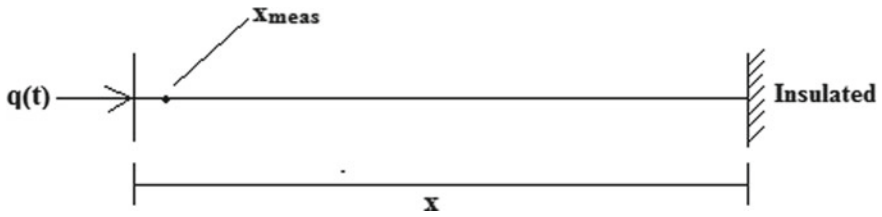

Fig. 2 Computational domain for one-dimensional heat conduction problem

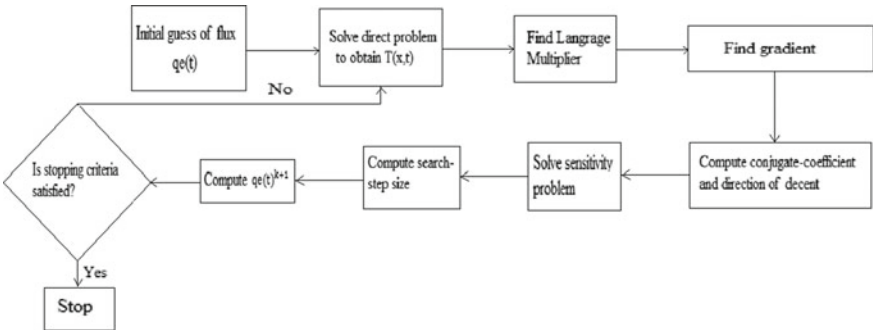

Fig. 3 CGM algorithm

In CGM, qe(t) is modified by following equation:

$$\text{qe}(t)^{k+1} = \text{qe}(t)^k - \beta^k d(t)^k \tag{4}$$

where $\text{qe}(t)^{k+1}$ is flux value at $k+1$ iteration and β^k is search step size and $d(t)^k$ is direction of decent. The value of qe(t) modifies until S[qe(t)] reaches particular minimum value. For current case, stopping criteria for CGM are $S[\text{qe}(t)] < 10^{-6}$. CGM is very fast method among all methods, and also it is a most recommended method; but sometimes due to lake of gradient, it converges at local minima and could not obtain the global minimum value of objective function especially for estimation of constant boundary condition [8].

4 Hybrid JAYA-CGM Algorithm

As mentioned earlier, JAYA is accurate but requires special treatment for inverse heat transfer problems; it can be used for providing better guess of unknown quantity as initial guess for CGM rather than zero or any random guess. This will give CGM a better initial input and hence, it will converge more accurately. Figure 4 shows combined JAYA-CGM algorithm. In first part, JAYA estimates optimum solution of problem and then that optimum value is fed to CGM as an initial guess.

For one-dimensional heat conduction problem, first random populations of qe(t) are generated and modified according to Eq. 1. After some iterations as solution converges to a particular limit, optimum value of qe(t) is fed to CGM as an initial guess and then conventional CGM starts. For the current case, domain length is 1 m, and domain is divided into 100 grid points. The heat flux q(t) is applied for 10 s on left boundary and time step taken for transient analysis is 0.2 s. Hence, total 50-time steps taken. The measuring point is 0.01 m away from left boundary where flux is applied and all the measured temperature data $Y(t)$ was taken at that point. For this case, numerical experiment is carried out where first, the known value of heat flux

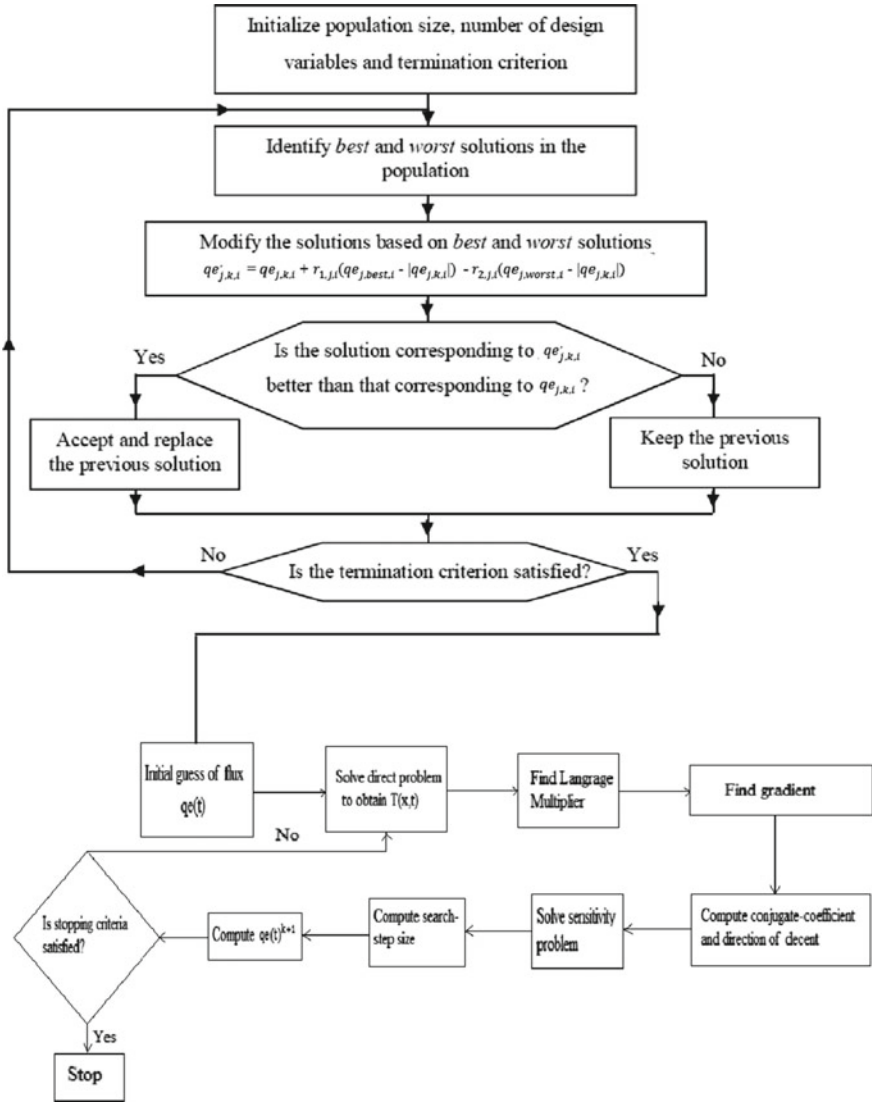

Fig. 4 Hybrid algorithm

$q(t)$ is applied and temperature field is obtained. The temperatures at measuring point x_{meas} are taken as measured values $Y(t)$. Then by inverse algorithms (both hybrid and CGM), the heat flux is estimated (qe(t)) by minimizing the objective function given in Eq. 2. The same stopping criteria are used for hybrid algorithm, i.e., S[qe(t)] $< 10^{-6}$. In this analysis, random errors of thermocouple measurements have not been considered in measured temperatures $Y(t)$.

5 Results

CGM does not update the heat flux value at the end time step and hence, it gives the same value of heat flux at every iteration at the end time step which was initially guessed during the start of algorithm. Due to these limitations, CGM gives poor results of estimation at the end of time steps and overall error increases. In hybrid algorithm, JAYA after some iterations gives optimum value to CGM as an initial guess and hence, the estimation will be improved. As the main objective of this work is to compare the two algorithms, the results of estimation of heat flux variations with time are shown in graphs. Figure 5 gives comparison of estimated heat flux by hybrid and CGM for linearly increasing profile. From Fig. 5, it is clear that hybrid algorithm gives more accurate profile than CGM. The same comparison of results is given in Fig. 6 but this time, the heat flux profile is linearly decreasing. For this case, hybrid algorithm gives better profile estimation than CGM. Figure 7 shows the comparison of estimation of constant heat flux profile by hybrid and CGM algorithms. It shows the hybrid algorithm can estimate the constant heat flux profile better than CGM.

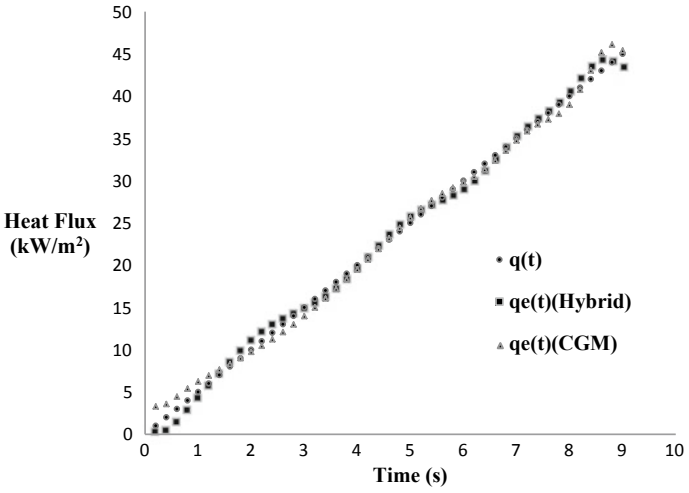

Fig. 5 Comparison of CGM and Hybrid algorithms for estimation of linearly increasing heat flux

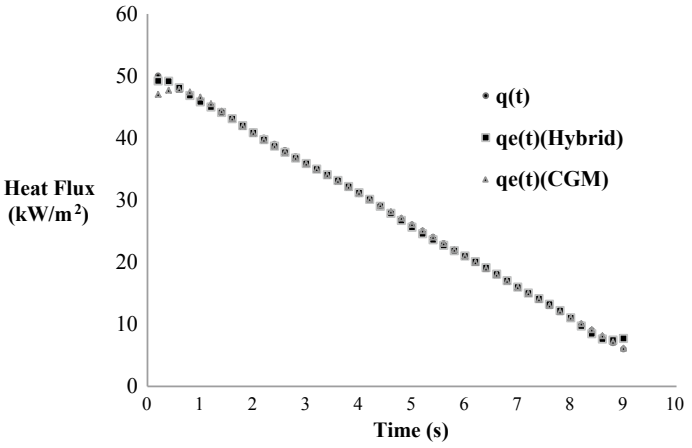

Fig. 6 Comparison of CGM and Hybrid algorithms for estimation of linearly decreasing heat flux

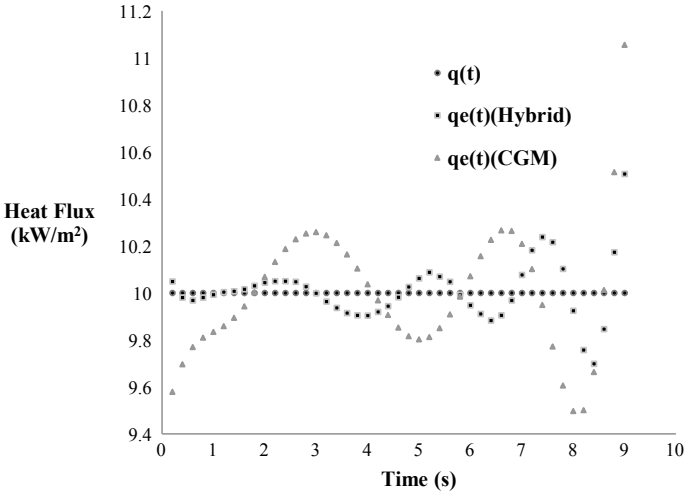

Fig. 7 Comparison of CGM and Hybrid algorithms for estimation of constant heat flux

RMS error for determining the accuracy of estimation is calculated by following equation:

$$\text{RMS} = \frac{1}{N}\sqrt{\sum_{i=1}^{N}\left[q(t) - \text{qe}(t)\right]^2} \tag{5}$$

where N is the total number of time steps. For this case, total 45-time steps were taken. $q(t)$ is the actual flux and qe(t) is the estimated flux.

Table 1 Comparison of RMS errors for CGM and hybrid algorithm

S. No.	$q(t)$	RMS error (CGM)	RMS error (Hybrid algorithm)	% decrease
1	Linearly increasing	137.73	117.83	14.43
2	Linearly decreasing	77.1256	52.8795	31.43
3	Constant	41.3	18.98	54.04

Table 1 shows three different cases of time-varying heat fluxes and values of RMS error. To quantify the accuracy of estimated results, root mean square (RMS) errors are used.

From Figures and Table 1, it is clear that hybrid algorithm gives better results than CGM for linearly increasing, linearly decreasing, and constant heat flux profiles. For constant heat flux, hybrid algorithm gives about 54% less RMS error than CGM. It shows that the CGM converges on local minima and can not converge beyond that. However, The estimation can be enhanced by taking temperatures at multiple points [1].

6 Conclusions

In the current work, inverse estimation of transient heat flux for one-dimensional heat conduction problem carried out by CGM and hybrid JAYA-CGM algorithm. For estimation, numerical experiment carried out in which three profiles of flux estimated: linearly increasing, constant, and linearly decreasing.

Following are the common conclusions drawn:

- Hybrid JAYA-CGM algorithm gives better estimation of for all heat flux profiles than CGM.
- Hybrid JAYA-CGM is better choice for estimation of constant heat flux profile than CGM as it gives 54% less RMS error than CGM.

Acknowledgements This work is supported by the fund of SERB division of Department of Science and Technology, Government of India. The financial support toward this research is greatly appreciated.

References

1. Ozisik MN, Orlande HRB (2000) Inverse heat transfer: fundamentals and applications. Taylor and Francis, New York
2. Tikhonov AN, Arsenin VY (1977) Solution of Ill-posed problems. Winston & Sons, Washington DC
3. Alifanow OM, Artyukhin EA (1975) Regularized numerical solution of nonlinear inverse heat conduction problem. Inzhenerno-Fizicheskii Zhurnal 29:159–164
4. Parwani AK, Talukdar P, Subbarao PMV (2013) Performance evaluation of hybrid differential evolution approach for the estimation of strength of heat source in radiatively participating medium. Int J Heat Mass Transf 56:552–560
5. Rao RV (2016) Jaya: a simple and new optimization algorithm for solving constrained and unconstrained optimization problems. Int J Ind Eng Conf 7:9–34
6. Rao RV (2017) Ankit saroj: constrained economic optimization of shell-and-tube heat exchanger using elitist JAYA algorithm. Energy 128:785–800
7. Rao RV, Rai DP, Ramkumar J, Balic J (2016) A new multi objective JAYA algorithm for optimization of modern machining process. Adv Prod Eng Manag 11:271–286
8. Shah S, Parwani AK (2019) Estimation of time-varying heat source for one-dimensional heat conduction by conjugate gradient method. In: Innovations in infrastructure. advances in intelligent systems and computing, vol 757. Springer (Book Chapter), Singapore pp 329–339

Numerical Simulation of Moving Surface Boundary-Layer Control Over Symmetric Aerofoil

Vipul Patel, Swapnil Parekh and Ajit Kumar Parwani

Abstract The objective of the current study is to increase the lift and decrease the drag for NACA 0012 aerofoil by moving surface boundary-layer control (MSBC). The numerical simulation of lift and drag for two moving surfaces of aerofoil is carried out with commercial software "Ansys Fluent." In the first configuration, one moving surface is considered of length 10% and other of length 15% of the chord length, both are at the upper side of the aerofoil. In the second configuration, both moving surfaces are considered of same length 10% of chord length but one is at the upper side, while other is at the lower side of the aerofoil. The results of both configurations are compared for different angle of attack and surface to free stream velocity ratio (U_c/U).

Keywords NACA · MSBC · Flow separation · Moving surface · Angle of attack

1 Introduction

The study to control the boundary layer with use of cylinders and rotating surfaces is known as the moving surface boundary-layer control (MSBC). Many studies to improve the fluid dynamic properties like lift, drag, and flow separation has been done in the past using rotating cylinders.

This concept has been studied for a wide range of applications including the improvement of the stall characteristics of wings of aircraft and for the drag reduction of semi-trailer trucks [1]. The history of the MSBC and an overview of previous work are provided in a comprehensive review by Modi and Deshpande [2]. Newton noticed this phenomenon of moving surface on the trajectory of a spinning ball [3]. Further, Magnus studied this effect and made ship with vorticity generation principle [4].

The concept of moving surface is implemented by momentum injection into the existing boundary layer [5]. The flow separation can be delayed by providing the

V. Patel · S. Parekh · A. K. Parwani (✉)
Department of Mechanical Engineering, Institute of Infrastructure Technology Research and Management, Ahmedabad, India
e-mail: ajitkumar.parwani@iitram.ac.in

A. K. Parwani and PL. Ramkumar (eds.), *Recent Advances in Mechanical Infrastructure*, Lecture Notes in Intelligent Transportation and Infrastructure,
https://doi.org/10.1007/978-981-32-9971-9_23

pseudo momentum to the boundary layer flow with moving surface. Usually, a rotating cylinder is used in the MSBC which causes the effect of momentum injection on the existing boundary layer near the surface of the object. This effect integrated with circulation control helps in drag reduction and increase in lift. The two effects, momentum injection and circulation control can be described as follows.

The flow over the aerofoil gets separated after a particular angle which is known as the stall angle. With the momentum injection, we try to impinge the velocity into the nearer boundary layer of the aerofoil with externally rotating the surface of the aerofoil. This provides an extra coupling force to delay the flow separation over aerofoil. This is possible due to the no-slip condition at the aerofoil surface. With injection of a momentum, the pressure gradient, where it becomes zero and then afterward negative, can be moved to the later part of aerofoil and thus improving the performance for the flow over aerofoil. When moving surface is added with the aerofoil to generate lift, it causes circulation. The rotating or moving surface changes the tangential component of velocity with the surface and thereby it changes the pressure distribution and stall angle of the aerofoil which increases the lift [6]. Different values for lift can be obtained with different speeds of moving surfaces and angle of attack.

In this study, numerical simulation has been performed over the symmetric aerofoil NACA 0012 with moving surfaces over two different types of configurations. For one case, two moving surfaces have been implemented over the upper side (low-pressure side) of an aerofoil and the other case considers two moving surfaces applied to the upper (low pressure) and lower (high pressure) one on each side. The aim of the study is to relate the boundary layer separation with the momentum injection and study how different boundary-layer control configurations affect the lift and drag values for the symmetric aerofoil.

2 Numerical Simulation

In the current study, NACA 0012 aerofoil is used which is a symmetric type Aerofoil and widely used in numerical analysis of lift and drag. The simulation is performed in Ansys Fluent 18.0 with air as a fluid. At a room temperature, air has a density $= 1.225$ kg/m^3 and viscosity $= 1.7894 \times 10^{-5}$ kg/ms. The flow is considered to be incompressible and turbulent. The transition SST (4 equations) model is taken which is based on the coupling of the SST k-omega transport equations and two other transport equations [7], one for intermittency and other for the transition onset criteria, in terms of the momentum-thickness Reynolds number.

2.1 Equations Used in Study

Continuity Equation [8, 9] :

$$\frac{\partial p}{\partial t} + V \cdot (\rho u) = 0 \tag{1}$$

Naiver–stokes momentum equation:

$$\frac{\partial u}{\partial t} + u \cdot \nabla u = -\frac{\nabla P}{\rho} + \vartheta \nabla^2 u \tag{2}$$

Transition SST (4 equations):

$$\frac{\partial(\rho k)}{\partial t} + \frac{\partial\left(\sigma u_j k\right)}{\partial x_j} = \widehat{P}_k - \widehat{D}_k + \frac{\partial}{\partial x_j}\left[(\mu + \sigma_k \mu_t)\frac{\partial k}{\partial x_j}\right] \tag{3}$$

$$\frac{\partial(\rho\omega)}{\partial t} + \frac{\partial\left(\rho u_j \omega\right)}{\partial x_j} = P_\omega - D_w + \frac{\partial}{\partial x_j}\left[\left(\mu + \sigma_\omega \mu_t \frac{\partial \omega}{\partial x_j}\right)\right] + 2(1 - F_1)\frac{\rho\sigma_{\omega 2}}{\omega}\frac{\partial k}{\partial x_j}\frac{\partial \omega}{\partial x_j} \tag{4}$$

$$\frac{\partial(\rho\gamma)}{\partial t} + \frac{\partial\left(\rho u_j \gamma\right)}{\partial x_j} = P_\gamma - E_\gamma + \frac{\partial}{\partial x_j}\left[\left(\mu + \frac{\mu_t}{\sigma_f}\right)\frac{\partial \gamma}{\partial x_j}\right] \tag{5}$$

$$\frac{\partial\left(\rho \widehat{R}_e \theta_t\right)}{\partial t} + \frac{\partial\left(\rho u_j \widehat{R}_e \theta_t\right)}{\partial x_j} = P_{\theta t} + \frac{\partial}{\partial x_j}\left[\sigma_{\theta t}(\mu + \mu_t)\frac{\partial \widehat{R}_e \theta_t}{\partial x_j}\right] \tag{6}$$

2.2 Geometry, Computational Domain and Meshing

The NACA0012 aerofoil with chord length of 1 m is considered in this study and it has maximum thickness of 12% of its chord length. Two configuration geometries are being considered. In Case 1, (Fig. 1) both the surfaces are at the upper side with one surface length is 10% of the chord length and second surface length is 15% of the chord length. In Case 2, (Fig. 2) it has two moving surfaces at trailing edge, one at upper side and other is at lower side with length of 10% of the chord length [10].

Figure 3 shows the computational domain and the mesh generated. The domain behaves as virtual wind tunnel for an aerofoil. Computational domain has dimensions 10 times larger than the aerofoil model. It has a semi-circular inlet which is used for generating flat velocity profile as equivalent to free stream velocity profile of external

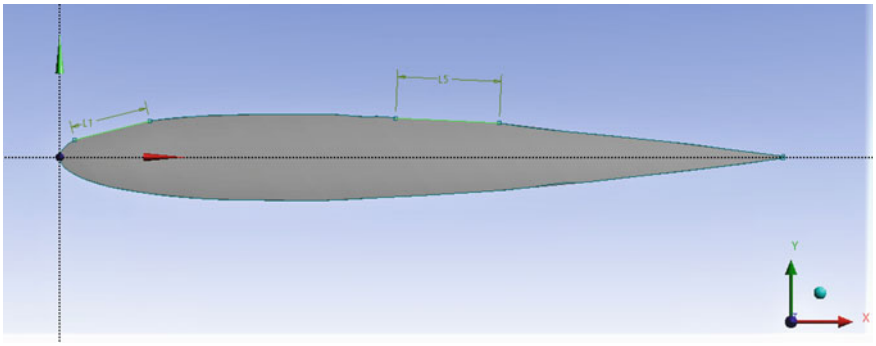

Fig. 1 Geometric profile of NACA 0012 aerofoil with both moving surfaces are at the upper side

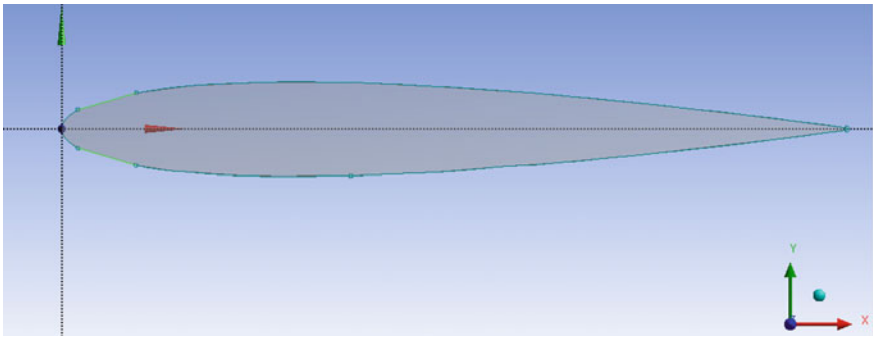

Fig. 2 Geometric profile of NACA 0012 aerofoil with one moving surface at upper side and second moving surface at lower side

flow. The pressure outlet is placed 10 times of aerofoil length away, while other two upper and lower boundaries are set as wall [11].

ICEM mesher available in ANSYS is used for meshing. Finite volume meshing is employed for discretizing the governing equations [12]. Both structured and unstructured meshes are used for the meshing of domain. The domain is divided into different parts where different mesh of different size employed. Inflated mesh used near wall of aerofoil to capture the boundary layer.

2.3 Boundary Conditions

Boundary conditions (Fig. 4) used in the runs for all the simulations are as follows [13, 14]:

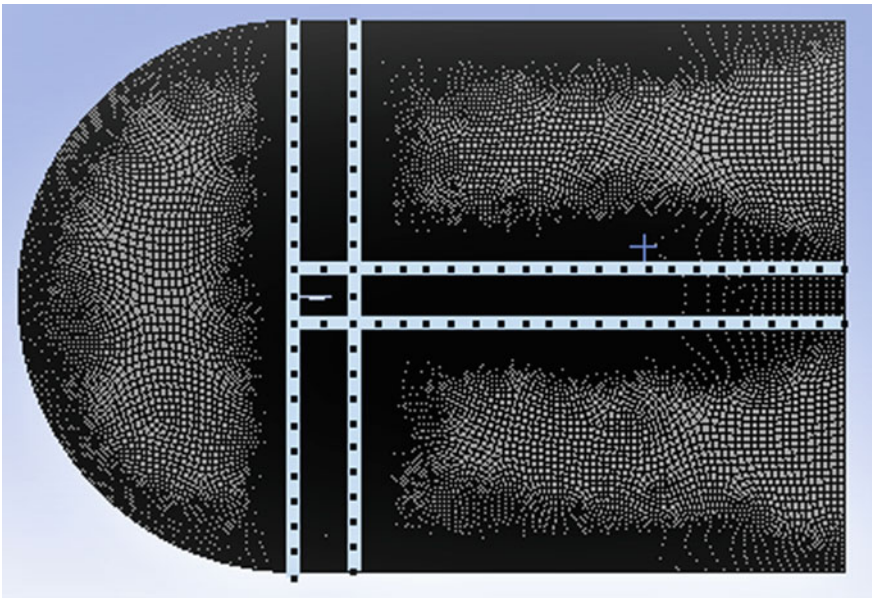

Fig. 3 Mesh generated over computational domain

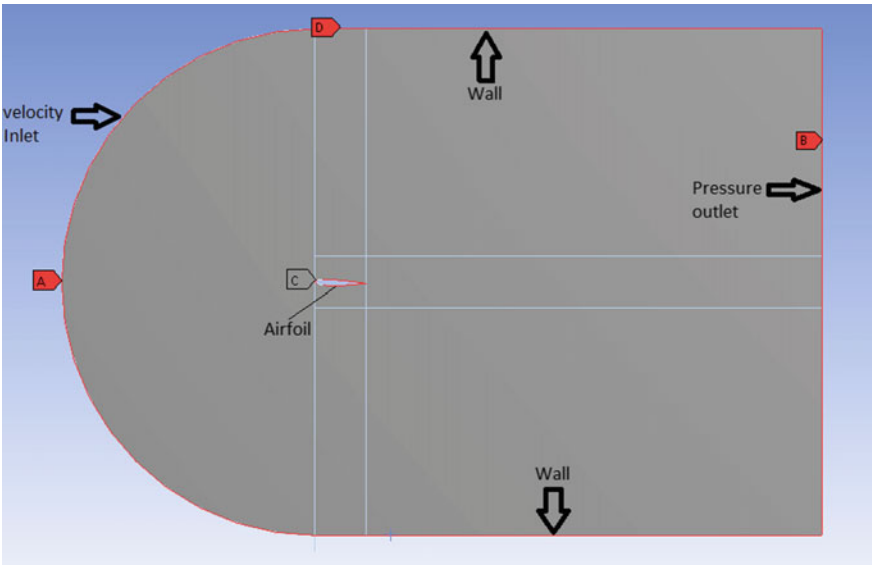

Fig. 4 Boundary conditions over computational domain

I. Velocity inlet—Free stream velocity in positive direction of flow in *X*-direction 10 m/s. Specification method used for turbulence as intermittency, intensity and hydraulic diameter with values 1, 0.5% and 1 m, respectively.
II. Pressure outlet—Gauge pressure-0 Pa, Backflow direction specification method-normal to boundary, Backflow pressure specification-total pressure. Specification method used for turbulence as intermittency, intensity and hydraulic diameter with values 1, 1.5% and 1 m, respectively.
III. Moving Wall—Variable moving wall velocities in positive direction of flow in *X*-direction ranging from 10 to 40 m/s with no-slip shear condition. Standard roughness model with roughness height 0 m and roughness constant 0.5 was used.
IV. Wall—stationary wall with no-slip condition. Standard roughness model with roughness height 0 m and roughness constant 0.5 was used as domain walls.

2.4 Grid Convergence Study

In order to get the optimum results compromising with time which is a usual method followed in industries, grid convergence study was performed with the drag coefficient. For different grids (say G1, G2, and G3) having different mesh points, if the parameters selected for observation shows the difference of less than 5% on going from grids G1 to G2 or G2 to G3, then the grid having less variation in parameters is selected [9].

Table 1 shows the study carried on different grids having different mesh points for the case of airfoil with angle of attack 2° with surface to free stream velocity ratio $(U_c/U) = 1$ at free stream velocity 10 m/s, are shown below.

From the above table, grid with 1,78,541 meshing elements was chosen as the optimum grid size as the change in drag coefficient from grid 4 to grid 5 are less than 5%. And for subsequent finer grids, the results for drag coefficient values do not change significantly. Thus, grid 4 with 1,78,541 meshing element is the optimum meshing size for the runs performed.

Table 1 Mesh points and drag coefficient values for different grids

Sr. no.	No. of elements	Drag coefficient
1	15,020	0.018505
2	24,830	0.016067
3	98,903	0.014937
4	1,78,541	0.014353
5	2,15,873	0.014120
6	3,34,826	0.014160
7	3,82,687	0.013952

3 Results and Discussions

The simulations on Ansys workbench are performed for the two cases at different angle of attacks and U_c/U ratios. For comparison, graphs are plotted between drag coefficients and lift coefficients versus surface velocity ratio at 2° and 6° angle of attack.

Figure 5 a, b shows the plots of drag and lift coefficient with U_c/U at angle of attack 2°. From the results, it is observed that for both the cases with increase of angle of attack the lift coefficient increases, while the drag coefficient decreases. For Case 1 (both the moving surfaces at the upper side) it is observed that the lift coefficient is higher than Case 2 (one moving surface at upper side and one at lower side) for angle of attack 2°. Also, for angle of attack 2°, the drag coefficient obtained for Case 1 is less than the drag coefficient obtained in Case 2.

Figure 6a, b shows the plots of drag and lift coefficient with U_c/U at angle of attack 6°. The results at angle of attack 6° shows higher lift coefficient for Case 2, as with increase in the angle of attack the pressure ratio between upper and lower side decreases. This leads to increase in lift coefficient. The drag coefficient in Case 2 is more than Case 1. For any angle of attack with increase in U_c/U ratios, the lift coefficient increases and drag coefficient decreases for both cases.

Figure 7a, b shows the plots of drag and lift coefficient with U_c/U at angle of attack 10°. The results show initially higher lift and lower drag for case-2 and as the U_c/U increases we get higher lift for case-1 while drag remains lower for case-2.

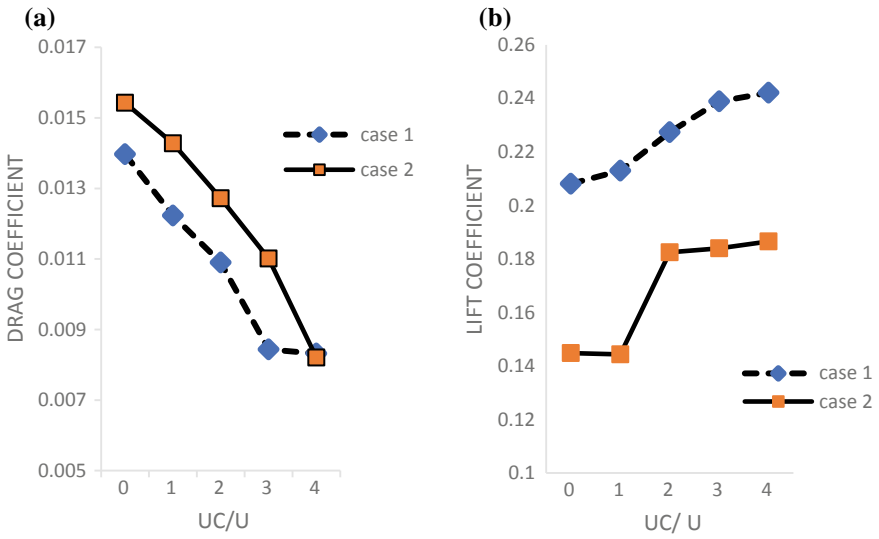

Fig. 5 Plot of **a** drag coefficient, **b** lift coefficient versus surface velocity ratio for angle of attack 2°

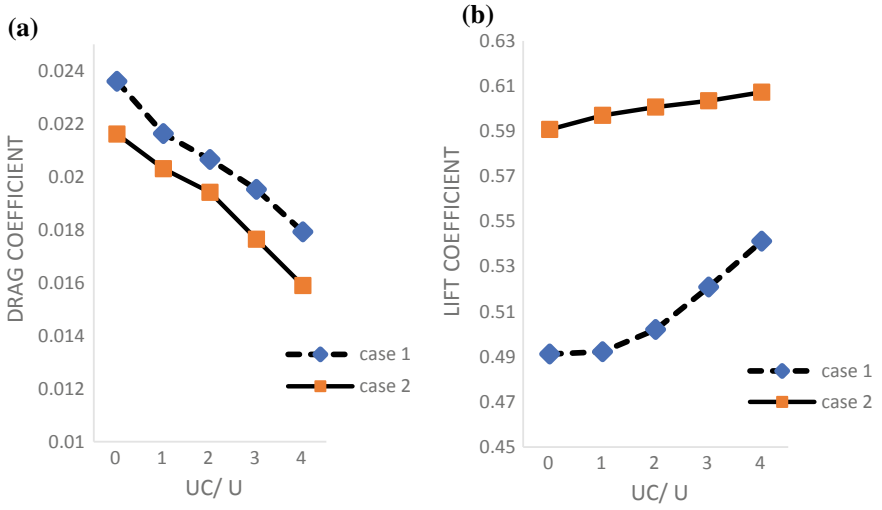

Fig. 6 Plot of **a** drag coefficient, **b** lift coefficient versus surface velocity ratio for angle of attack 6°

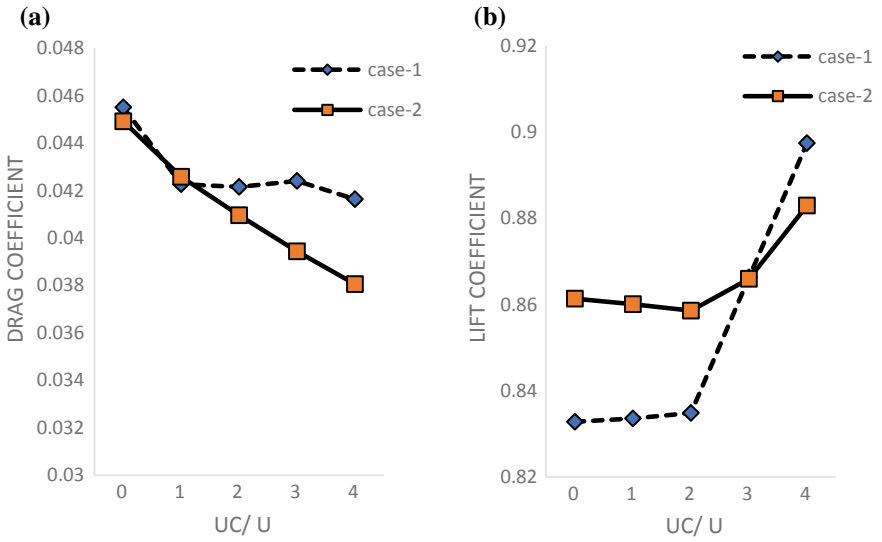

Fig. 7 Plot of **a** drag coefficient, **b** lift coefficient versus surface velocity ratio for angle of attack 10°

Comparison of both the cases shows that there is an increase in lift coefficient and reduction in drag coefficient for different type of configurations. For angle of attack 2°, the lift increase in Case 1 is 32.23% and reduction in drag coefficient is 16.75% compared to Case 2 and for angle of attack 6°, lift increase in Case 2 is 21.29% and reduction in drag coefficient is 6.13% than Case 1 for $U_c/U = 1$. For angle of attack 10° the lift coefficient in Case 2 is 3.426% higher than the case-1.

4 Conclusion

The results show that the moving surface injects the momentum into the flow, due to this, boundary layer separation is delayed which increases the lift coefficient and decreases the drag coefficient. For low angle of attack at 2°, Case 1 is more effective than Case 2, while for higher angle of attacks at 6° and 10°, Case 2 is more effective. For angle of attack 2°, the lift coefficient for Case 1 is 32.23% more than Case 2 for $U_c/U = 1$ and drag coefficient for Case 1 is 16.75% less than Case 2 for $U_c/U = 1$. For angle of attack 6° lift coefficient in Case 2 is 21.29% more than Case 1 and drag coefficient is 6.13% less than Case 1 for $U_c/U = 1$.

References

1. Modi VJ, Ying B, Yokomizo T (1991) An approach to design of the next generation of fuel efficient trucks through aerodynamic drag reduction. In: Proceedings of the ASME winter annual meeting, Atlanta, USA, vol DE 40, pp 465–482
2. Modi VJ, Deshpande VS (2000) A Joukowski aerofoil with momentum injection. In: AIAA-2000-4108, pp 445–451
3. Schlichting H (1968) Boundary layer theory, 3rd edn. McGraw-Hill, New York, pp 127–724
4. Modi VJ, Munshi SR, Mokhtarian F, Bandyopadhyay G, Yokomizo T (1994) Multielement aerofoils with moving surface boundary-layer control: wind tunnel, numerical and flow visualization studies. In: Proceeding of the 19th congress of the International Council of the Aeronautics Sciences, Anaheim, USA. AIAA Publisher, pp 80–103
5. Modi VJ, Fernando M, Yokomizo T (1991) Moving surface boundary-layer control as applied to two-dimensional and three-dimensional bluff bodies. J Wind Eng Ind Aerodyn 38:83–92
6. Jawahar HK, Qing A, Mahdi A (2018) Experimental and numerical investigation of aerodynamic performance for aerofoils with morphed trailing edges. Renew Energy 127:355–367
7. Douvi C, Athanasios TI, Dionissios MP (2012) Evaluation of the turbulence models for the simulation of the flow over a National Advisory Committee for Aeronautics (NACA) 0012 aerofoil. J Mech Eng Res 4(3):100–111
8. Rao TS, Mahapatra T, Chaitanya S (2018) Enhancement of lift-drag characteristics of NACA 0012. Mater Today: Proc 5:5328–5337
9. Sahu R, Patnaik BSV (2011) CFD simulation of momentum injection control past a streamlined body. Int J Numer Meth Heat Fluid Flow 21(8):980–1001
10. Md. Sadiqul I, Shaik MH, Mohammad A, Md. Quamrul I (2017) Numerical investigation on boundary layer control through moving surface in NACA 0012 aerofoil. In: AIP conference proceedings, vol 1851, 020111, pp 1–7
11. Shmilovich A, Yadlin Y (2006) Flow control for the systematic build-up of high-lift systems. In: 3rd AIAA flow control conference, vol 2855, pp 1–14

12. Salam A, Barman S, Atique A, Asif S, Probha NN, Faisal Kh (2015) A CFD based parametric study to investigate the moving surface effect on aerofoil boundary-layer control. Military Institute of Science and Technology, Dhaka
13. Modi VJ, Mokhtarian F, Fernando M (1989) Moving surface boundary-layer control as applied to two-dimensional aerofoils. J Aircr 28(2):104–112
14. Hassan A, Sankar LN (1989) Separation control using moving surface effects—A numerical solution. AIAA 89(0972):1–9

Transient Analysis of an Injection Mould with Conformal Cooling Channels

Shivsagar G. Sharma, Deepika Singh Singraur and D. S. S. Sudhakar

Abstract Injection moulding is a manufacturing process to create plastic parts and it consists of four major processes injection, packing, cooling and ejection. Cooling process takes almost half of the whole cycle time in injection moulding. Injection moulds were cooled by creating straight drilled channel in mould but that channel does not provide uniform and efficient cooling since it does not conform to the shape of the mould. Conformal cooling channel takes the exact shape of the mould cavity, and therefore it provides efficient cooling. Circular, profiled circular and trapezoidal profile cooling channels have been designed for injection mould. To optimize the effectiveness of the cooling, channels with constant heat transfer between mould and cooling channels, constant perimeter and different convective heat transfer coefficient have been taken. Thermal analysis has performed on Ansys 14.5 and Taguchi method has used to optimize the best cooling channel.

Keywords Conformal channels · Heat transfer · Constant perimeter · Taguchi

1 Introduction

In injection moulding, plastic parts are produced by injection of melted plastic granules into mould, which has two halves one is moveable and another is fixed one. Injection moulding process is capable of producing any intricate and complex design part with ease and precision [1]. Despite the various advantages and applications of injection moulding, there are various other factors like cooling channel design for mould, melt temperature, injection pressure, mould temperature and coolant temperature should be considered so that quality of the product can be improved [2]. Practically it has found that; out of total cycle time of injection moulding processes,

S. G. Sharma (✉)
Fr. Conceicao Rodrigues College of Engineering, Bandra, Mumbai, India
e-mail: shivsagarsharma9@gmail.com

D. S. Singraur · D. S. S. Sudhakar
Production Engineering Department, Fr. Conceicao Rodrigues College of Engineering, Bandra, Mumbai, India

A. K. Parwani and PL. Ramkumar (eds.), *Recent Advances in Mechanical Infrastructure*, Lecture Notes in Intelligent Transportation and Infrastructure,
https://doi.org/10.1007/978-981-32-9971-9_24

cooling process alone takes on an average 65–75% of cycle time. For complex shape which consists of curve surfaces, straight drilled channels do not provide uniform cooling [3]. So for uniform temperature distribution in mould, conformal cooling channels have been designed. Conformal cooling channels conform to the shape of the mould cavity [4]. It cools the mould uniformly and reduces warpage, shrinkage and sink marks [5, 6]. A plastic bucket part has been taken from Myco mould industry having thickness of 1.5 mm. The main objective of this research is to reduce cooling time by designing a mould with different cooling channel profiles. Thermal transient analysis and Taguchi method have been used to optimize the best cooling channel for efficient cooling of mould.

2 Methodology

Acrylonitrile butadiene styrene (ABS) plastic and structural steel materials have been used for plastic bucket and mould, respectively. Materials properties are shown in Table 1.

2.1 Moulds Design with Conformal Cooling Channels

SolidWorks 17 has been used for mould design with conformal channels. Mould cavity has been used for this research since mould core also gives almost the same result as cavity. Figure 1 shows the mould with different cooling channel profiles. To design cooling channel, the rule of thumb has been utilized [7]. Table 2 shows the parameters and its level for conformal cooling channel design.

The diameter of circular cooling channel has been taken as 7 mm and its perimeter has calculated. All cooling channels have been designed with constant perimeter having helical and spiral path for bucket vertical face and base of the bucket, respectively.

Table 1 Material properties for mould and plastic part

Materials	Structural steel	ABS plastic
Density (kg/m^3)	7850	1050
Specific heat (J/kg K)	434	1465
Thermal conductivity (W/m K)	60.5	0.25

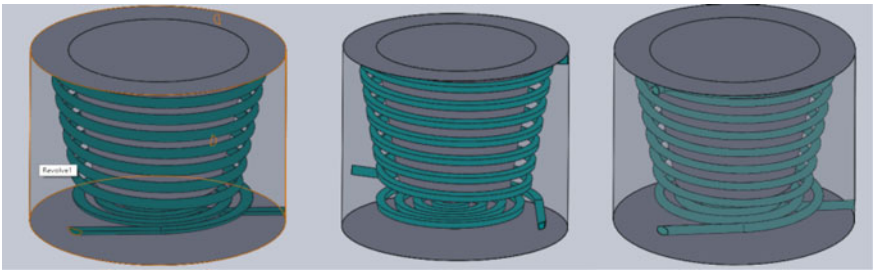

Fig. 1 Mould cavity with profiled circular, trapezoidal and circular cooling channels profile

Table 2 Cooling channels parameters and its levels

Parameters	Levels		
	1	2	3
Profile	Circular	Profiled circular	Trapezoidal
Centre-line distance (L), mm	9	12	15
Pitch (P), mm	12	15	18

2.2 Governing Equations of Injection Mould

In injection mould, there are four possible ways of heat transfer conduction, forced convection, free convection and radiation. Hydraulic diameters need to be found for profiled circular and trapezoidal channels. Convective heat transfer coefficient (h) for channels has been calculated using Dittus–Boetler equation [8] given by

$$h = 0.023 \frac{K}{D} \mathrm{Re}^{0.8} \mathrm{Pr}^{0.4}. \tag{1}$$

where K is thermal conductivity of coolant, D diameter of cooling channels, Re is Reynold's number and Pr is Prandtl number. Heat flux (q) at the interface of the melt and mould has calculated using an analytical formula [9, 10]

$$q(t) = \frac{\sqrt{\rho_\mathrm{p} c_\mathrm{p} k_\mathrm{p}} \times \sqrt{\rho_\mathrm{m} c_\mathrm{m} k_\mathrm{m}}}{\sqrt{\rho_\mathrm{p} c_\mathrm{p} k_\mathrm{p}} + \sqrt{\rho_\mathrm{m} c_\mathrm{m} k_\mathrm{m}}} \times \frac{1}{\sqrt{\pi t}} \times (T_\mathrm{melt} - T_\mathrm{mould}). \tag{2}$$

where ρ, c and k denote density, specific heat and thermal conductivity. Subscripts p and m are used for polymer and mould material. Plastic melt temperature and mould temperature are denoted by T_melt and T_mould, respectively. Melt meets the mould surface after the time period (t).

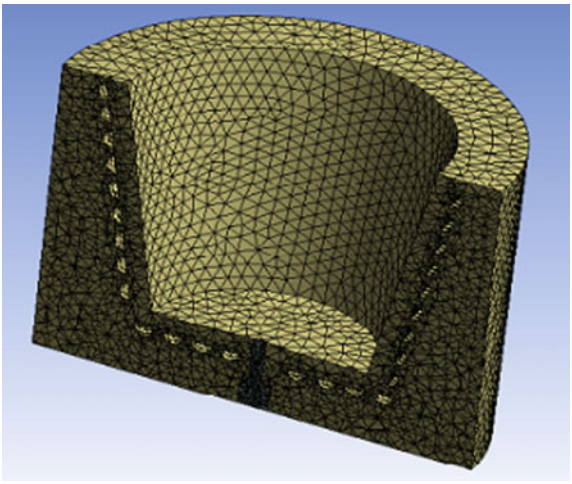

Fig. 2 Meshed mould cavity

2.3 Thermal Transient Analysis of Injection Mould

Mesh for mould cavities have been generated with medium smoothing, fast transition, minimum edge length 0.07 mm, transition ratio 0.272, maximum layer 5 and growth rate of 1.2. Ansys workbench has been used for meshing and is shown in Fig. 2. Tetrahedrons mesh with sizing 3 mm and 6 mm have been taken for sprue bush as well as cooling channel surface and mould cavity, respectively. Mesh generator generated mesh having 258,574 nodes and 168,911 elements.

A. **Boundary Conditions and Analysis Setting**

Thermal transient analysis has been performed since temperature of the mould is varying with time. Cooling water, plastic melt and mould temperatures are 25 °C, 230 °C and 50 °C, respectively. Input parameters are heat flux and convective heat transfer coefficient. Heat flux at the interface of the cavity and melt has been found using Eq. (2). Convective heat transfer for each channel has been found separately using Eq. (1). Heat flux calculated was 60,369 W/m^2 and convective heat transfer coefficients were 3168.79 W/m^2 °C, 4153.85 W/m^2 °C and 4241.22 W/m^2 °C for circular, trapezoidal and profiled circular cooling channels, respectively.

De-moulding temperature has been set to 55 °C and analysis has been run for 200 s to check the output parameters. The analysis time has been set for 200 s for all moulds since some moulds take 200 s to reach de-moulding temperature. The expected results for this analysis are minimum cooling time, minimum mould surface temperature and low von Mises stress. Von Mises stress should be as low as possible to avoid failure of the mould. The output parameters of interest are presented in Table 3. Von Mises stress is denoted by "$\sigma_{\text{Von-mises}}$".

Table 3 Mould analysis results

Sr. No.	Inputs			Outputs		
	Profile	L (mm)	P (mm)	Cooling time (s)	$(\sigma_{\text{Von-mises}})$max (Mpa)	Max-mould temp (°C)
1	Circular	9	12	15.39	59.53	48.74
2	Circular	9	15	27.66	59.82	50.09
3	Circular	9	18	45.97	62.97	51.39
4	Circular	12	12	34.4	70.76	51.09
5	Circular	12	15	56.83	67.45	52.42
6	Circular	12	18	92.96	73.48	53.68
7	Circular	15	12	75.09	77.44	53.39
8	Circular	15	15	132	83.06	54.53
9	Circular	15	18	200	80.79	55.84
10	Profiled circular	9	12	10.76	65.65	47.86
11	Profiled circular	9	15	19.13	65.68	48.83
12	Profiled circular	9	18	28.19	68.02	49.91
13	Profiled circular	12	12	26.37	74.1	50.38
14	Profiled circular	12	15	39.22	75.04	51.27

(continued)

Table 3 (continued)

Sr. No.	Inputs			Outputs		
	Profile	*L* (mm)	*P* (mm)	Cooling time (s)	$(\sigma_{\text{Von-mises}})$max (Mpa)	Max-mould temp (°C)
15	Profiled circular	12	18	55.81	76.2	52.29
16	Profiled circular	15	12	56.54	82.74	52.74
17	Profiled circular	15	15	78.12	83.57	53.54
18	Profiled circular	15	18	123.44	83.55	54.5
19	Trapezoidal	9	12	13.1	66.34	48.13
20	Trapezoidal	9	15	22.22	66.41	49.26
21	Trapezoidal	9	18	33.1	68.57	50.39
22	Trapezoidal	12	12	28.77	74.35	50.62
23	Trapezoidal	12	15	43.75	74.8	51.64
24	Trapezoidal	12	18	62.7	77.54	52.67
25	Trapezoidal	15	12	62.48	82.59	52.98
26	Trapezoidal	15	15	89.11	90.87	53.89
27	Trapezoidal	15	18	172.18	93.47	54.9

3 Taguchi Analysis

An L27 array has been used since there are three factors and three levels as mentioned in Table 2. Figure 3 shows the main effects plot for signal to noise ratio. Smaller the better signal to noise (S/N) ratio has been employed since objective is to minimize the cooling time, mould surface temperature and von Mises stress. Taguchi analysis shows that among all cooling channels, mould with profiled circular channel takes minimum time to reach de-moulding temperature.

Response Table 4 shows variation in outputs with pitch, centre-line distance (L) and profile. This analysis shows that centre-line distance is the most important factor for cooling of the mould. As centre-line distance increases, cooling time of the mould gets affected drastically. Channel profile affects the cooling time of mould the least.

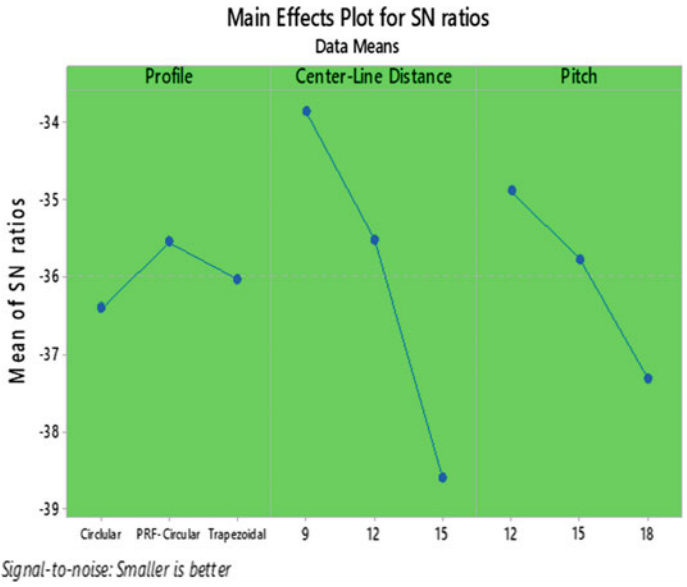

Fig. 3 Main effects plot for signal to noise ratio

Table 4 Analysis response table

Level	Profile	Centre-line distance	Pitch
1	−36.40	−33.86	−34.88
2	−35.55	−35.51	−35.77
3	−36.02	−38.60	−37.31
Delta	0.85	4.74	2.43
Rank	3	1	2

4 Results and Discussion

Thermal transient analyses of 27 models with circular, profiled circular and trapezoidal cooling channels have been performed on Ansys Workbench and subsequently Taguchi analysis has been performed with smaller the better *S/N* ratio.

Figure 4 shows the temperature and stress variation in mould with circular channel having centre-line distance 9 mm and pitch of 12 mm. The maximum temperature and stress after 200 s are 48.74 °C and 59.53 Mpa, respectively. Cooling time for all the moulds has been calculated by interpolation. Figure 5 shows temperature and stress variation of mould with trapezoidal cooling channel mould. Cooling times of the mould with circular and trapezoidal channels have been obtained as 15.39 s and 13.103 s, respectively. Lower the pitch of the cooling channel, faster will be the cooling of the mould.

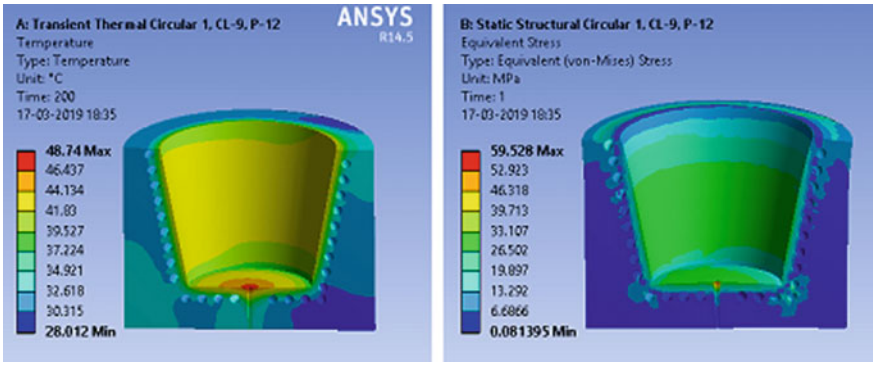

Fig. 4 Mould temperature (left) and stress variation (right) for circular cooling channel

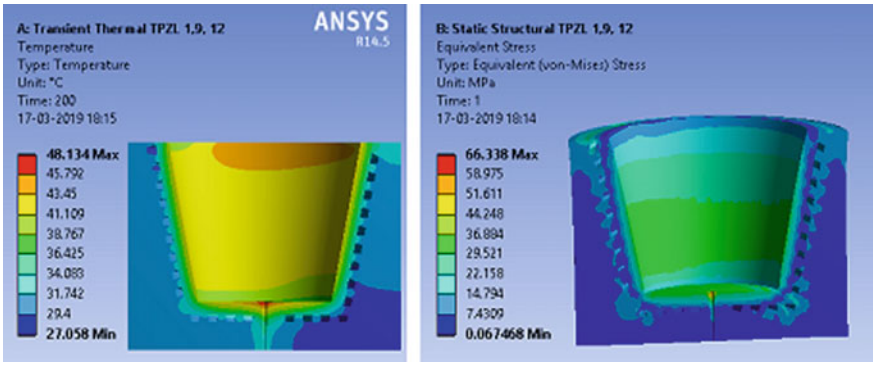

Fig. 5 Mould temperature (left) and stress variation (right) for trapezoidal cooling channel

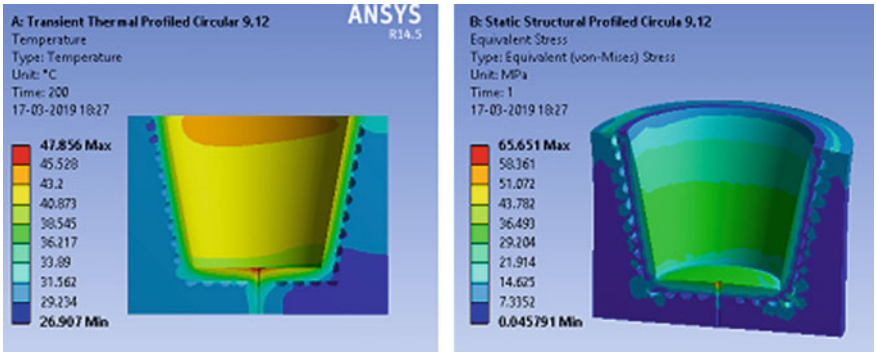

Fig. 6 Mould temperature (left) and stress variation (right) for Profiled circular cooling channel

The results show that the mould with profiled circular cooling channel takes minimum time to cool the mould and also it helps in minimizing the overall von Mises stress and maximum temperature on mould surface.

The cooling time of the mould is most affected by centre-line distance and less affected by the channel profile. Results show that as centre-line distance with pitch of the channel increases, cooling time also increases. Figure 6 shows that for centre-line distance 9 and 12 mm pitch with profiled circular profile, the maximum temperature and von Mises stress after 200 s is 47.854 °C and 65.651 MPa, respectively. So, decrease the cooling time of the mould centre-line distance should be kept small. Cooling channel profiles can give effective cooling if designed with appropriate pitch and centre-line distance.

5 Conclusion

In this research, conformal cooling channels with circular, profiled circular and trapezoidal cooling channels having equal perimeter with distinct convective heat transfer coefficient have been taken for thermal transient analysis. Analysis shows that with profiled circular cooling channel, cooling time of the mould can be reduced to some extent and it aids in increasing productivity. For constant perimeter channel, profiled circular channel takes 4.63 s less time than circular channel and 2.34 s less time than trapezoidal cooling channel. So to reduce cooling time of an injection mould and its associated defects, profiled circular and trapezoidal cooling channels can be preferred over circular cooling channel. Taguchi analysis shows that centre-line distance should be small for efficient cooling. It also shows that 12 mm pitch with 9 mm centre-line distance gives efficient cooling.

Acknowledgements I would like to express my special thanks to M. V. Rao sir and Santosh sir for their support and guidance throughout this research.

References

1. Tang SH et al (2006) Design and thermal analysis of plastic injection mould. J Mater Process Technol 171(2):259–267
2. Dang X-P, Park H-S (2011) Design of U-shape milled groove conformal cooling channels for plastic injection mold. Int J Precision Eng Manuf 12(1):73–84
3. Venkatesh G, Ravi Kumar Y (2017) Thermal analysis for conformal cooling channel. Mater Today 4(2):2592–2598
4. Singraur DS, Patil B (2016) Review on performance enhancement of plastic injection molding using conformal cooling channels. Int J Eng Res General Sci 4(4)
5. Vojnová E (2016) The benefits of a conforming cooling systems the molds in injection moulding process. Procedia Eng 149:535–543
6. Park H-S, Han Pham N (2009) Design of conformal cooling channels for an automotive part. Int J Autom Technol 10(1):87–93
7. Jahan SA et al (2017) Thermo-mechanical design optimization of conformal cooling channels using design of experiments approach. Procedia Manuf 10:898–911
8. Saifullah ABM, Masood SH, Sbarski I (2012) Thermal–structural analysis of bi-metallic conformal cooling for injection moulds. Int J Adv Manuf Technol 62(1–4):123–133
9. Carslaw HS, Jaeger JC (1959) Conduction of heat in solids, 2nd edn. Clarendon Press, Oxford, p 88
10. Kurosaki Y, Satoh I, Saito T (1996) Trans JSME 62–599C: 2864–2871

Emission Analysis of a Small Capacity Producer Gas Engine at Higher Hydrogen Concentration and Compression Ratios

M. Sreedhar Babu, Shibu Clement, N. K. S. Rajan and Tehsinraza Mulla

Abstract In this paper, the effect of hydrogen concentration (16–22% by volume) in producer gas-air mixtures at several engine compression ratios (11, 15 and 18:1) on emissions was analyzed and reported. The experiments were carried out using bottled producer gas, with fixed gas composition resembling close to the gas quality of an open top re-burn downdraft gasifier of IISc make. Engine was operated close to stoichiometry at a constant speed of 1500 rpm, under naturally aspirated mode. Hydrogen being a highly combustible component in a producer gas-air mixture, the dynamics of in-cylinder combustion process was expected to influence the emissions. The engine was found to operate knock free under all compression ratios and loads. The measured emission data was compared against CPCB-2016 norms in India. The comparative emission analysis reveals an increase in NO emission with increase in hydrogen concentration due to higher peak in-cylinder pressures at higher compression ratios. However, the overall emission trend was found to be in compliance with prescribed emission limits.

Keywords Emission · Producer gas · Hydrogen · Compression ratio

M. Sreedhar Babu · T. Mulla (✉)
Department of Mechanical Engineering, Jain College of Engineering,
Belagavi, Karnataka 590014, India
e-mail: tehsinraza1997@gmail.com

M. Sreedhar Babu
e-mail: sreedhar@jainbgm.in

S. Clement
Department of Mechanical Engineering, BITS Pilani,
K.K. Birla Goa Campus, Goa 403726, India
e-mail: shibu@goa.bits-pilani.ac.in

N. K. S. Rajan
Department of Aerospace Engineering, Indian Institute of Science,
Bengaluru, Karnataka 560012, India
e-mail: nksr@cgpl.iisc.ernet.in

A. K. Parwani and PL. Ramkumar (eds.), *Recent Advances in Mechanical Infrastructure*, Lecture Notes in Intelligent Transportation and Infrastructure,
https://doi.org/10.1007/978-981-32-9971-9_25

1 Introduction

Producer gas (PG) is a low energy density (4–6 MJ/Nm^3) gaseous fuel, produced from a biomass in a downdraft gasifier via gasification process [1]. PG is popularly used for power generation application [2] and it is ideally suited for decentralized power production [3]. Besides power generation application, the other advantages associated with PG fuel is its nature of being renewable (short carbon cycle) and also carbon neutral [4]. Lately, due to acute shortage in fossil fuel reserves (like oil, coal, and petroleum-based fuels) and environmental concern, a huge emphasis is laid on exploration and promotion of renewable fuels. Literature [5] depicts that, the potential of biomass derived energy in India stands at second highest, 17,538 MW, after wind energy potential, 49,130 MW. It is also reported [6, 7] that, researchers explored PG engine operation with higher compression ratios to study mostly the engine performance or engine knocking tendency. However, not much work is reported on influence of hydrogen in PG at higher compression ratio (CR) on emission front. Furthermore, with environmental concerns and also with available huge bio-energy potential, the literature stresses [8] the need for improvement in biomass energy systems through progress in combustion science. Thus, the possible advancements may primarily depend on (i) improving the existing engine design, (ii) cleaner in-cylinder combustion process, or (iii) utilization of renewable fuels and their blends. The present study is focused on utilization of PG fuel blends and its influence on engine emission at higher compression ratios for sustainable future.

2 Materials and Methods

The experimental setup used for the present work is shown in Fig. 1a. The list of engine specifications is set out in Table 1. The three PG fuel blends that were considered for the experimental study were formulated by following a mid-point approach as depicted in Table 2. The corresponding combustion properties of PG mixture blends and CNG fuel are listed in Table 3.

The desirable compression ratio (CR) on engine was achieved by varying thickness of the gasket on the cylinder head as shown in Fig. 1b. Furthermore, two pedestal fans were arranged externally to facilitate engine cooling. The engine was operated close to stoichiometry at a constant speed of 1500 rpm and under naturally aspirated mode. The engine was equipped with eddy current dynamometer with a loading capacity of 14 N-m and also with a modern data acquisition system to acquire engine combustion data. More details on engine fueling system and instrumentation are presented in [9, 10]. The exhaust from the engine was measured through a calibrated five gas analyzer (AVL-444). The principle used for measuring CO and CO_2 was the non-dispersive infrared (NDIR); HC was measured through flame ionization detector (FID); NO was measured through chemiluminescence detector (CLD), and for O_2, an electrochemical sensor was used. Further, the CO, CO_2, and O_2 were recorded in

(a) Experimental test rig

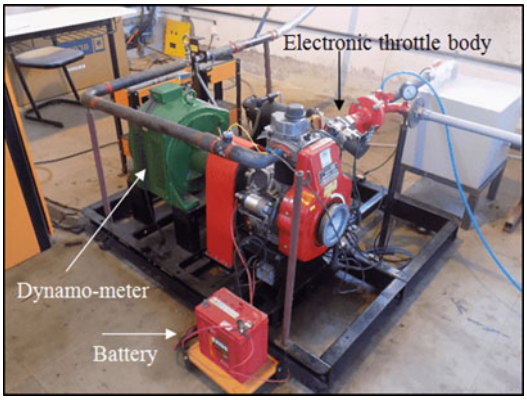

(b) Cylinder head

Fig. 1 **a** Experimental setup. **b** Cylinder head gasket

Table 1 List of PG engine specifications

Parameter	Specifications
Make and model	Greaves cotton Pvt. Ltd., #1533
Bore × stroke	82 × 68 mm, toroidal piston shape
Engine type	four-stroke, single cylinder, air-cooled type
Engine capacity	359 cm^3, converted from CI to SI mode

Table 2 Formulation of PG fuel blends in volume %

PG composition	PG-A	PG-B	PG-C	CNG
Hydrogen	16	19	22	–
Methane	2.5	2.5	2.5	95
Carbon-monoxide	18	18	18	–
Carbon-dioxide	12	12	12	–
Nitrogen	51.5	48.5	45.5	–
Ethane	–	–	–	5

Table 3 Calculated combustion properties of PG fuel blends and CNG fuel

Properties	PG-A	PG-B	PG-C	CNG
(A/F) stoichiometry ratio (kg/kg)	1.18:1	1.3:1	1.48:1	17:1
Adiabatic flame temperature (K)	1950	1980	2010	2230
Lower heating value (MJ/kg)	4.283	4.712	5.361	49.88

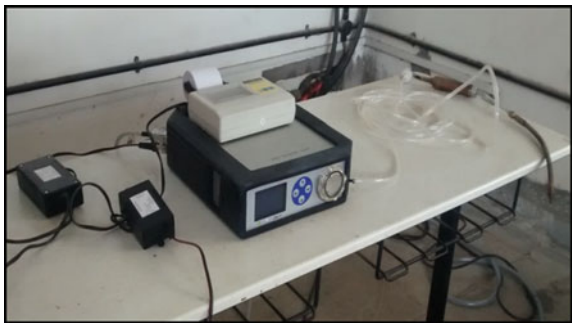

Fig. 2 Five gas analyzer (AVL-444)

volume percentage, whereas the HC and NO were recorded in ppm units. The five gas analyzer (AVL-444) is shown in Fig. 2.

3 Results and Discussion

The tailpipe emissions were measured after engine reached a steady operating condition at 50, 75% and full engine load. The engine exhaust gas was sampled through a sampling system designed and fabricated as per recommended ARAI standards. The sampling system would sample out (1/3rd volume) at any given time from an overall exhaust gas flow. The detailed discussion on emission trends at different engine load points is presented below.

3.1 Analysis of Emissions at 50% Engine Load Point

As presented in Fig. 3b, the production of NO was found to be increasing with increase in hydrogen concentration and compression ratio. This is attributed to higher in-cylinder temperatures owing to higher CRs and comparatively higher adiabatic flame temperatures of PG (shown in Table 3). Whereas, the production of HC was found to be in decreasing trend (approx. 90% lesser than CNG at CR:11), with increase in hydrogen and CR which generally indicates an efficient combustion process, and this trend is in good agreement with existing literature [11]. Referring to CO emission, the production of CO has shown a decreasing trend with increase in hydrogen content and CRs as shown in Fig. 3a. This may be due to higher turbulence levels near cylinder walls owing to higher CRs. However, in summary, all the emissions at 50% load were within prescribed limits of CPCB norms.

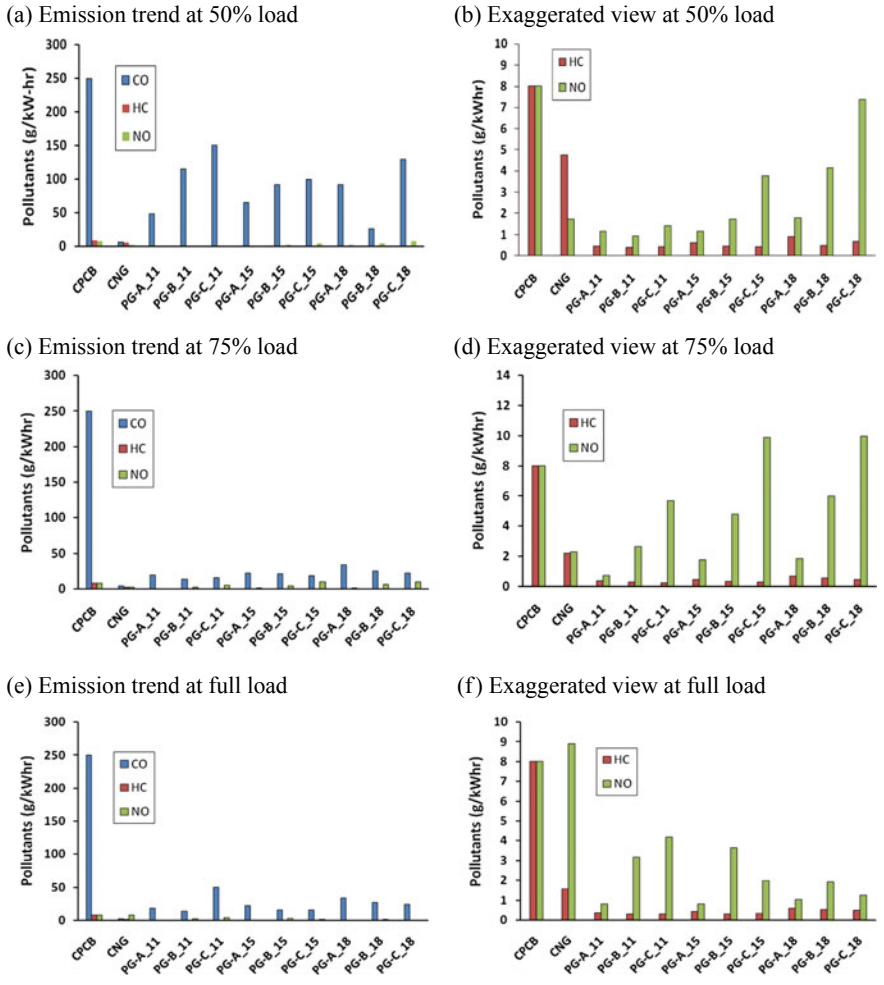

Fig. 3 Emission trend at 50% (**a**, **b**), 75% (**c**, **d**) and full engine load point (**e**, **f**)

3.2 Analysis of Emissions at 75% Engine Load Point

As shown in Fig. 3d, the production of NO was found to be 20% higher than the set limits of CPCB for PG-B and PG-C blends. This is attributed to higher average in-cylinder peak pressures (at CR: 11, 15 and 18:1–33, 40 and 55 bar, respectively). The overall HC production was found to be in decreasing trend with increase in CRs (approx. 88.5% lesser than CNG at CR:11), suggesting better combustion process due to maximum energy conversion load operating point. Further, the CO production was also found to be in decreasing trend as shown in Fig. 3c, with increase in hydrogen content, CRs and load. This may be attributed to rapid combustion process (with

an ability to consume end charge across cylinder walls) due to squish effect owing to toroidal piston shape—giving rise to higher turbulence levels at higher CRs and loads. For higher CR operation, suitable catalytic converter can be identified to limit the NO_x emissions.

3.3 Analysis of Emissions at Full Engine Load Point

As presented in Fig. 3e, the CO production has shown a decreasing trend comparatively with increasing loads and hydrogen concentration. Particularly, PG-B at CR:15 gave rise to 26% reduced CO production, against 75% engine load operation. However, the PG-C at CR:11 has shown an undesirable peak of CO, due to fuel-rich engine operation at full load. Referring to Fig. 3f, the HC production has shown similar trend as that of 75% loading condition, and no significant variation was observed. The NO production has shown a decreasing trend at CR:18, against 75% loading, for each of the PG blends, respectively. Further, poor load-carrying ability of engine was observed at CR:18 and higher levels of heat loss from cylinder walls. Maximum energy conversion (higher thermal efficiency) for present engine was obtained at CR:15 and 75% loading condition, more details on the same is reported by author in [12]. Thus, the present PG engine operation was satisfactory, when fueled with higher hydrogen content (up to 22% by volume) and higher compression ratios (up to CR:18), without any sign of knock.

4 Conclusions

A work was taken up to address the influence of producer gas fuel blends with hydrogen concentration (16–22%) on engine emissions at higher compression ratios (11–18:1). Based on the measured emission data, an increase in NO emission with increase in H_2 and CRs was observed, owing to higher in-cylinder peak pressures and thus temperatures. The unburnt HC emission has shown a substantial decreasing trend with increase in hydrogen content and compression ratio, indicating efficient combustion process owing to higher reactivity of hydrogen. The CO emissions were slightly dominant over NO and HC emissions but well within prescribed limits. In summary, the producer gas engine operation has showcased a possibility of reducing air pollution for sustainable human life and future.

Acknowledgements Author would like to thank BITS Pilani, KK Birla Goa Campus, and DST for providing experimental test rig facility. Thanks to Director & Principal of Jain College of Engineering, Belagavi for financial assistance.

References

1. Sridhar G, Sridhar HV, Dasappa S, Paul PJ, Rajan NKS, Mukunda HS (2005) Development of producer gas engines. IMechE Int J Automob Eng 219:423–438
2. Sridhar G, Dasappa S, Sridhar HV, Paul PJ, Rajan NKS (2005) Gaseous emissions using producer gas as a fuel in reciprocating engines. SAE technical paper, 2005-01-1732
3. Dasappa S, Sridhar G, Sridhar HV, Rajan NKS, Paul PJ, Upasani A (2007) Producer gas engines-proponent of clean energy technology. In: 15th European biomass conference & exhibition. Germany, 7–11 May 2007
4. Babu MS, Shibu C, Rajan NKS (2011) Biomass based green technologies—potential and sustainability. Bio-energy, India, MNRE, Government of India. 9&10, pp 20–23
5. Energy Statistics Report (2012) Ministry of statistics and programme implementation. Government of India
6. Sridhar G, Paul PJ, Mukunda HS (2001) Biomass derived producer gas as a reciprocating engine fuel—an experimental analysis. Int J Biomass Bioenergy 21:61–72
7. Ahrenfeldt J, Birk Henriksen U, Kvist T (2011) High compression ratio engine operation on biomass producer gas. SAE technical paper, 2011-01-2000
8. Bilger RB (2000) Future progress in turbulent combustion research. Int J Prog Energy Combust Sci 26:367–380
9. Babu MS, Clement S, Rajan NKS (2016) Development and testing of laboratory scale induction system fuelled with bottled producer gas. Int J Appl Mech Mater 852:659–665
10. Babu MS, Clement S, Rajan NKS (2016) Fuel conversion benefit of producer gas over gasoline. Energy Proc 100:203–210
11. Natarianto I, Sunil T, Prakashbhai RB, Raymond LH, Ajay K (2017) Engine power generation and emission performance of syngas generated from low density biomass. Int J Energy Convers Manag 148:593–603
12. Sreedhar Babu M (2017) Experimental investigations and modeling studies on performance of spark ignited engine with varied compositions of producer gas. Ph.D. thesis. BITS Pilani University

Recent Advances in Design Infrastructure

Finite Element Analysis of Conformal Cooling for Reduction of Cycle Time to Enhance Performance in Plastic Injection Molding Process

Deepika Singh Singraur, Bhushan T. Patil and Yogesh T. Rampariya

Abstract The use and improper placement of conventional cooling channels leads to uneven cooling of the mold surfaces, which results in defects like sink marks, warpage, and thermal residual stresses. The design variables considered for the cooling are mold and melt temperature, injection time, cooling time, cooling temperature, packing time, and packing pressure. Conformal cooling channels are used to improve the cooling system design and to reduce the defects. Temperature distribution along the mold cavity is studied in this paper. In the proposed design method, the cooling channel is produced by the design tool and the results have been compared with simulated results produced by ANSYS software. The transient thermal analysis in ANSYS workbench is performed to analyze the thermal response of rapid heating and cooling of mold to see the effects on mold heating and cooling efficiency and the cycle time of molding operation. The maximum temperature and minimum temperature were reduced by 18.78%. The analysis has been done for hot and cold runners.

Keywords Injection molding · Temperature distribution · Cooling efficiency · Conformal cooling

1 Introduction

Injection molding is one of the most important manufacturing processes available in plastic manufacturing industries. Since cooling of the injection mold takes most of the cycle time, reduced or minimum cooling time leads to increase in the productivity. Various researches focus on minimization of cycle time. The cooling system design comprises of the design of the cooling channel. The straight drilled cooling channel is the most common because of its simplicity in design and manufacturing. It is

D. S. Singraur (✉) · B. T. Patil
Fr. Conceicao Rodrigues College of Engineering, Mumbai, India
e-mail: deepika.singraur@gmail.com

Y. T. Rampariya
A. P. Shah Institute of Technology, Thane, India

A. K. Parwani and PL. Ramkumar (eds.), *Recent Advances in Mechanical Infrastructure*, Lecture Notes in Intelligent Transportation and Infrastructure,
https://doi.org/10.1007/978-981-32-9971-9_26

the cheapest type of cooling channel. It can be manufactured by drilling or boring operations. The optimum design involves design of channel in terms of cooling time, number of cooling channels, size of cooling channels, location of cooling channels, coolant temperature, and convective heat transfer between coolant and the wall. The cooling performance of the channels has been studied by Dang and Park [1], where they proposed U-shaped grooved channels. Sun et al. [2] proposed a milled groove insert method for cooling of the mold for a household iron part and generated milled groove in core and mold. Altaf et al. [3] investigated prototype production of profiled conformal cooling of injection mold using epoxy. Liu et al. [4] also proposed a rapid heat cycle molding (RHCM) in contrast to conventional injection molding process. Saifullah et al. [5] introduced thermal analysis of cooling channels for injection mold. The cycle time was reduced to 35% with case of square section compared to conventional straight cooling channels.

Due to non-uniformity in cooling stage, defects like shrinkage and warpage may occur. Thus, the design of conformal channels is such that it conforms to the shape of molded part keeping in view that the distance between the cooling channels and mold surface is uniform.

2 Methodology and Model

2.1 CAD Model

In this work, a plastic cup was taken up to express the whole optimizing process. The modeling is done by one of the modeling software SolidWorks. It is then imported to Autodesk Inventor and ANSYS to analyze the cooling/feeding time, to analyze the influences of each type of feeding and cooling system it was defined geometry similar to a cup with three sizes, in polypropylene PPC 3120 MU5, from Total Refining & Chemicals. The geometries are denominated as Part 1, Part 2, and Part 3 below as shown in Fig. 1.

To carry out various CAD-related analyses, finite element analysis is employed. Numerical method in combination with CAD can be used for solving subtlety related

Fig. 1 Parts dimensions for the cup

	Part 1	Part 2	Part 3
h [mm]	50	150	500
d_B *[mm]*	22.74	82.32	274.39
d_T *[mm]*	42.68	128.05	426.83

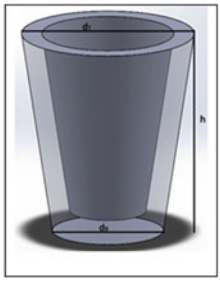

to engineering discipline due to availability and easy accessibility of high-end computers and various analysis softwares. A numerical description of geometry, boundary end conditions, material characteristic property, and loading conditions are various tools available under FE method. The FE method divides body under analysis into finite number of small elements and nodes to carryout subsequent mathematical analysis. The accuracy of FE analysis depends on number of nodes selected for analysis.

2.2 Governing Equation and Boundary Conditions

Equation governing the conduction analysis is given as:

$$\dot{Q}_m + \dot{Q}_c + \dot{Q}_e = 0 \quad \text{(i)} \tag{1}$$

where

$\dot{Q}_m$, $\dot{Q}_c$ and $\dot{Q}_e$, heat flux from molten plastic, heat flux exchange with coolant and heat flux exchange with surrounding.

$$\dot{Q}_m = \text{Total heat content of molten plastic}$$

$$\dot{Q}_m = mC_p(T_M - T_E)$$

$$\dot{Q}_c = \text{Heat lost by conduction and convection}$$

$$= \left(\frac{1}{h\pi d} + \frac{1}{k_{st}.S_e}\right)^{-1}(T_M - T_E)t_c$$

$$S_e = \text{effect of geometry on heat transfer}, \quad S_e = \frac{2\pi}{\ln\left[\frac{2x\sinh\left(2\pi\frac{y}{x}\right)}{\pi d}\right]}$$

where d = channel diameter, x = cooling channel pitch, y = distance of center of cooling channel to the mold surface

$$\textbf{Nusselt Number}, \ \text{Nu} = \frac{hl_c}{K} = \frac{hd}{K}$$

l_c = Characteristic length, h = convective heat transfer coefficient, K = thermal conductivity.

For forced convection heat transfer

$$\text{Nu} = 0.023 \times \text{Re}^{0.8}$$

Hence, $h = \frac{31.395}{d}\text{Re}^{0.8}$, where Re = Reynolds's Number, $\text{Re} = \frac{Vd}{\upsilon}$.

The boundary condition was applied to melt setting it at a temperature of 260 °C maintaining the mold temperature at 100 °C and injection pressure limit as 100 MPa. The average coolant flow rate has been maintained at 150 cc/s. The glass transition

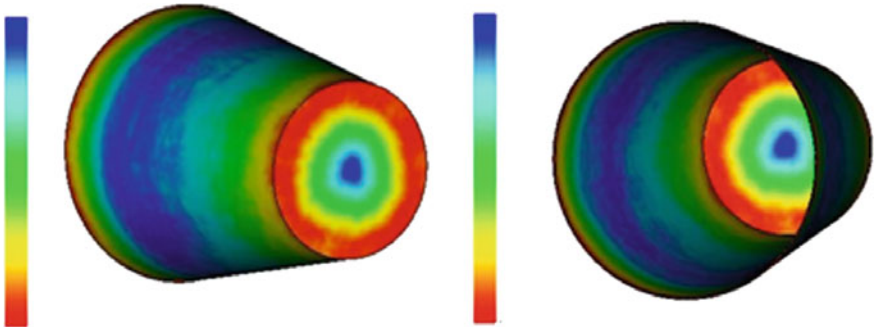

Fig. 2 Best gate locations; Part 1

temperature is 210 °C. The end time has been entered and the transient loads are indicated in terms of temperature, heat flux, heat generation rate, convection film coefficient, and heat flow. The mesh has been created with 3-D tetrahedral mesh element.

3 Result and Discussion

3.1 Gate Location

The gate location analysis evaluates that which are the best locations to place the gate in the part. Since the geometry of the parts is symmetrical according to *Z*-direction, it was expected that the best location to inject the material was in the bottom center of the cup as shown in Fig. 2. It is possible to see the flow resistance and that the bottom center of the cup has the lower flow resistance, so is the best location to place the gate too. The selected location to place the gate was the bottom center of the cup according to these two results.

3.2 Fill Analysis

Fill Analysis is the first parameter to be analyzed after gate setting. It helps to determine whether fill is balanced or not. Contour analysis shows equally spaced lines for balanced fill. Flow rate can be determined by space between lines. Flow fill analysis also helps to determine whether flow at extreme end reaches at same time or not. In the result shown, blue zone represent initially filled section, whereas red zone represents last filled section. As per analysis, it takes 1.291 s to fill whole part.

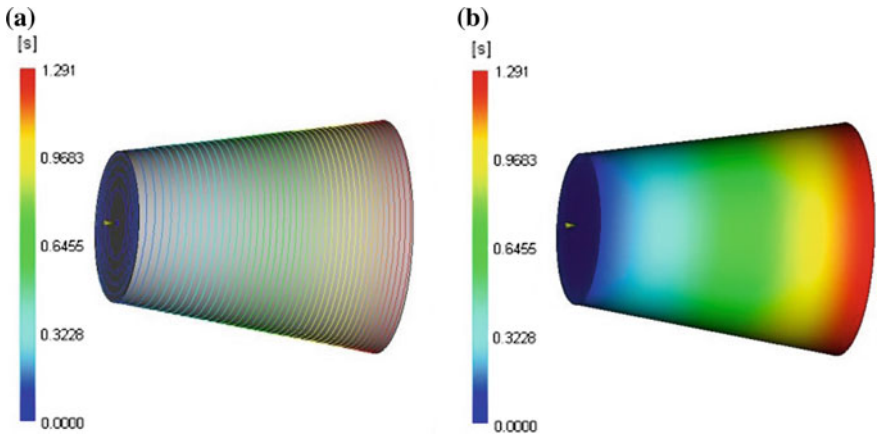

Fig. 3 Fill time result; **a** Contour; **b** Shading; Part 2

The flow of the material starts from the bottom root of the part and fill the part with symmetry along all direction. Figure 3a, b shows a fill time plot with outline and with shading.

3.3 Bulk Temperature

The other results analyzed were the bulk and flow front temperatures as shown in Fig. 4a, b. The Bulk temperature denotes weighted average temperature across thickness. The bulk mean temperature range limit has to be more than 20 °C and

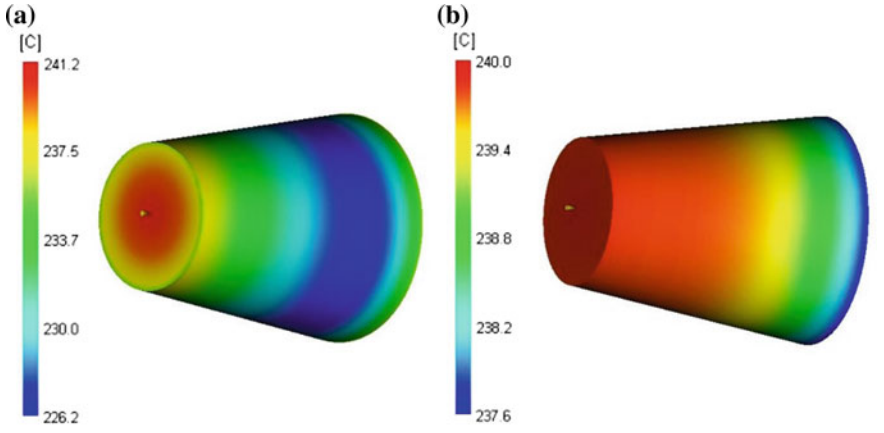

Fig. 4 **a** Bulk temperature; **b** Flow front temperature; Part 2

temperature range for flow front temperature should be more than 5 °C, and analysis results satisfy these criteria. In filling phase, one of the most important parameter need to be taken care is shear stress at wall. Wall shear stress should not exceed material stress limit, while analysis this criteria was maintained within permissible limit. Shear stress can be consulted in ANSYS database and for Polypropylene 3120 MU5 the maximum allowable shear stress is 0.26 MPa.

3.4 Cooling Analysis

It is the most important task to maintain uniform cooling temperature to achieve effective and efficient heat transfer. Hence, the following results were analysed—coolant temperature, coolant flow rate, average part temperature, maximum temperature, profile part temperature, mold temperature, and time to reach ejection (refer Table 1).

The coolant temperature was initially set at 25 °C for every design alternative. The inlet temperature was changed after in order to improve cooling of parts. Regarding range of temperature to accomplish, all the design mold alternative are in agreement with it. However, percentage of reduction varies due to difference in types of plastic, mold material, cooling channel layout, and shape and size of analysed part.

The coolant flow was set in order to keep Reynolds number up to 10,000 as shown in Fig. 5a, b. As heat transfer rate is optimum for turbulent flow as compared to laminar flow. Hence, the flow velocity of coolant was adjusted in order to achieve turbulent flow.

The Average Temperature is between mold temperature and ejection temperature for all parts. The maximum part temperature with cold runner is way below ejection temperature because of longer cycle time.

The Average temperature, part result (Fig. 5a) is between the mold temperature and the ejection temperature for all parts. The temperature, maximum, part result (Fig. 5b) for Part 2 and Part 3 with cold runners is way below the ejection temperature because of the longer cycle time that this type of feeding system imposes.

The temperature profile, part result is below the ejection temperature for all the parts and varies across the thickness less than 10 °C. The mold temperature should be within 10 °C for amorphous materials and within 5 °C for semi-crystalline materials, but this guideline is very difficult to achieve for most molds. The part temperature varies mostly in a 10 °C range over each mold face. Close to the gate location or in the top of the parts the temperature varies more than 10 °C. After improvements, the results of Part1 and Part2 have changed but Part3 has poor part and melt temperature results. The Part 3 as poor part and mould temperature results. The behavior of this result between the feeding systems is dependent on the melt temperatures.

Table 1 Comparision between conventional and conformal cooling

		Average T (°C)	Circuit coolant T (°C)	T, Max. (°C)	T, profile (°C)	T, mold (°C)	T, part (°C)	T, eject (s)
Part 1	Cold runners and normal cooling	72.89–85.35	25.01–25.98	102.2	102.2	35.16-54.26	42.06–64.47	9.016
	Cold runners and conformal cooling	75.55–83.38	25.00–26.30	105.9	105.9	30.74–43.71	37.84–55.01	8.574
	Hot runners and normal cooling	71.54–83.60	25.01–26.15	101.5	101.5	33.23–53.77	39.62–63.90	8.97
	Hot runners and conformal cooling	76.92–84.25	20.1–21.00 25.01–26.27	108.7	108.7	28.09–39.90	36.79–51.57	8.365
	Cold runners and normal cooling	30.04–41.06	25.01–25.81	41.74	41.74	25–38.96	28.19–41.74	8.33
Part 2	Cold runners and conformal cooling	34.39–39.14	25.01–27.47	41.77	41.77	25–39.03	28.24–41.77	8.312
	Hot runners and normal cooling	49.99–71.39	25.02–27.09	75.02	75.02	45.76–61.39	56.57–68.47	10.17

(continued)

Table 1 (continued)

		Average T (°C)	Circuit coolant T (°C)	T, Max. (°C)	T, profile (°C)	T, mold (°C)	T, part (°C)	T, eject (s)
	Hot runners and conformal cooling	53.81–67.87	25.01–29.5; 30.00–36.72	72.99	72.99	31.15–58.15	39.99–65.72	10.05
	Cold runners and normal cooling	36.86–46.92	25.02–25.50	48.46	48.46	27.06–47.46	28.46–48.46	8.849
Part 3	Cold runners and conformal cooling	30.96–40.34	25.01–27.69	45.93	45.93	25.35–44.46	26.32–44.84	8.304
	Hot runners and normal cooling	59.42–75.82	20.00–21.42	79.51	79.51	39.78-68.27	46.84–74.00	10.9
	Hot runners and conformal cooling	56.00–74.97	20–21.49; 15.03–27.96	84.62	84.62	36.64–79.22	44.09–84.62	11.14

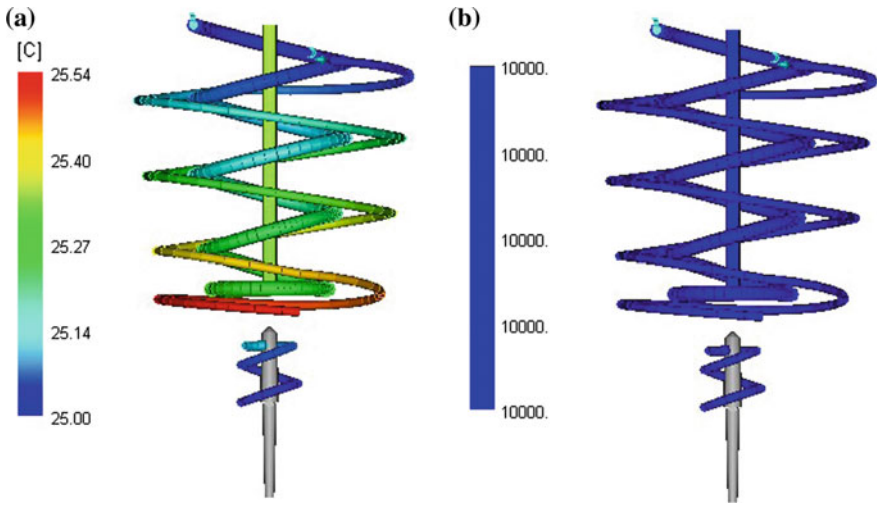

Fig. 5 Cooling results: **a** Coolant temperature; **b** Reynolds number; Part 2 CC

4 Conclusions

A comparative study has been conducted for conventional and channels that conform to the shape of the object through virtual prototypes. The results indicate that conformal channels proved to be effective in reducing cooling time and reduce product displacement. The study of flow behavior of coolant helps in understanding cooling efficiency and design of cooling channel.

Results showed the comparison between conventional and conformal channels for all the three parts using conventional and conformal cooling channels. The results were presented for different combinations such as conventional cooling employed with hot and cold runner. Similarly, conformal cooling results were represented for hot and cold runner. An increase in the average temperature was observed. The range between lowest and highest temperature of part is reduced by 18.78%. On the other hand, there is only a decrease of 3.8% for the maximum temperature in the interior of the cup. Conformal cooling in manufacturing achieves an improved heat transfer leading to a better part quality.

Conformal cooling channels lead to better heat dissipation and reduced cooling times. But these channels are difficult to fabricate by simple machining processes as they have a complex geometry. These channels are easily fabricated through direct metal laser sintering or selective laser sintering techniques but these methods are cost-effective. Hence, there is a scope of research in the area of easy fabrication of the conformal channels.

References

1. Dang XP, Park HS (2011) Design of U-shape milled groove conformal cooling channels for plastic injection mold. Int J Precis Eng Manuf 12(1):73–84
2. Sun YF, Lee KS, Nee AYC (2004) Design and FEM analysis of the milled groove insert method for cooling of plastic injection moulds. Int J Adv Manuf Technol 24(9–10):715–726
3. Altaf K, Majdi Abdul Rani A, Raghavan VR (2013) Prototype production and experimental analysis for circular and profiled conformal cooling channels in aluminium filled epoxy injection mould tools. Rapid Prototyp J 19(4):220–229
4. Liu C, Cai Z, Dai Y, Huang N, Xu F, Lao C (2018) Experimental comparison of the flow rate and cooling performance of internal cooling channels fabricated via selective laser melting and conventional drilling process. Int J Adv Manuf Technol 96(5–8):2757–2767
5. Saifullah ABM, Masood SH, Sbarski I (2012) Thermal-structural analysis of bi-metallic conformal cooling for injection moulds. Int J Adv Manuf Technol 62(1–4):123–133

Identification of Cracks Length by XFEM and Machine Learning Algorithm

Srinivasu Chadaram and Saurabh Kumar Yadav

Abstract In the paper a crack identification study is performed by using extended finite element method (XFEM) and Machine learning method. XFEM is widely used for the analysis of two dimensional and three dimensional crack simulations. XFEM is faster than the finite element method because, it removes the burden of remeshing as crack grows. To reduce the computational effort and cost, Machine learning based regression analysis has been performed and validated with the sample data. The proposed algorithm is used to find the accuracy in evaluating some benchmark problems in detection of crack length. The accuracy of the method is more than 90%.

Keywords XFEM · Identification of crack · Machine learning · Regression

1 Introduction

To promote better safety in service life, structural health monitoring (SHM) is very important. As shown in Fig. 1, model of cantilever equipped with sensors to SHM during service load. SHM is useful not only to detect the damage but also it gives characteristics of the damage, which is a significant observation [1]. In practical situation the damage in structures due to crack enhancement, SHM is performed continuously to monitor the crack developments during the life span of the structures in aircrafts, offshore and onshore ship buildings, oil refineries and nuclear reactors. Many experimental methods evolved replaced the nondestructive methods like ultrasonic tests, radiography analysis and electrical impedance tomography, which have some limitations.

In finding the remaining useful life (RUL) of a structure, Bayesian interface method based on Bayes's theorem is applied to calculate the equivalent damage growth. Crack growth model by Paris is a function of stress intensity factor which involved in finding RUL is complicate factor of applied loading, boundary condi-

S. Chadaram (✉) · S. K. Yadav
Department of Mechanical Engineering, Institute of Infrastructure Technology Research and Management (IITRAM), Ahmedabad, India
e-mail: chsrinivasu108@gmail.com

A. K. Parwani and PL. Ramkumar (eds.), *Recent Advances in Mechanical Infrastructure*, Lecture Notes in Intelligent Transportation and Infrastructure,
https://doi.org/10.1007/978-981-32-9971-9_27

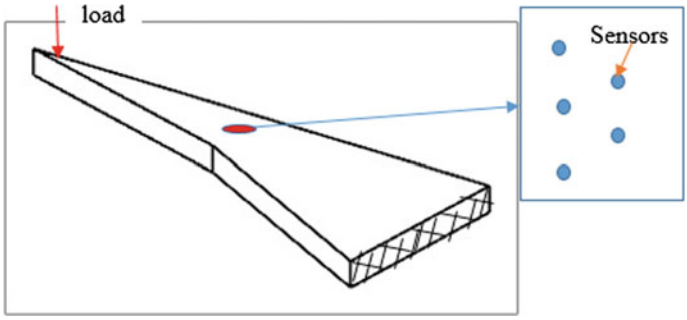

Fig. 1 Model of cantilever, showing the sensors arrangement

tions, position of crack and its geometry [2, 3]. Damage detection of structures by nondestructive method depends on the dynamic response of the structures which often requires the comparative study of damaged and undamaged structures [4]. Data driven computational mechanics is developed to ascertain the stress-strain relationship for nonlinear elastic materials. The strain fields are measured using digital image methods, which are time consuming and quite difficult to take the data from the image processed [5]. The identification of crack is required to predict the failure of the structure. Previously crack identification has been performed with the help of genetic algorithm and PSO method [6]. This method is quite time consuming.

In this paper we consider edge crack and center crack in a thin plate under mode I loading condition. In actual practice the damage sizes measured during health monitoring by onboard sensors and actuators, which detect the flaw size and location of flaw. Estimating damage size is complicate factor still, this research work is under development. In this paper synthetic data is used instead of actual monitored data. The model parameters are assumed, the crack modeling and simulation is performed by using XFEM. The displacement at some specified nodes on one edge with sensors as shown in Fig. 3a, b are generated with crack size as a varying parameter. In this paper a new approach for crack length detection, machine learning is presented. The measurements of displacements at specific nodal points are applied to this machine learning regression based algorithm. Forward XFEM problem is converted into inverse method. The result has been compared with some small test data.

2 XFEM Formulation for Crack

2.1 Governing Equation

In two dimensional elastic domain Ω shown in Fig. 2, the linear momentum equation for small deformation in static equilibrium is given as

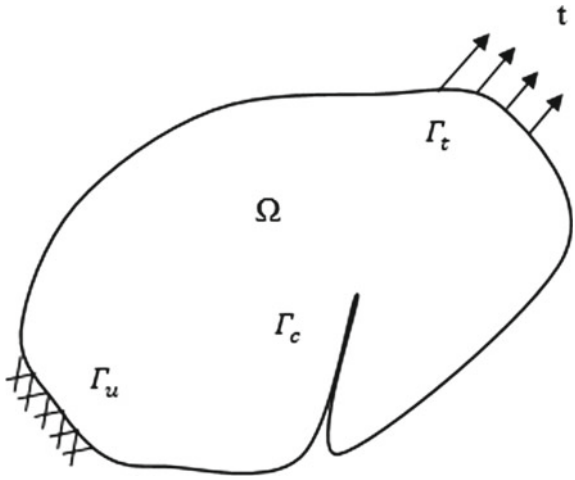

Fig. 2 A body with a traction free crack and external traction force

$$\Delta \cdot \boldsymbol{\sigma} + \boldsymbol{b} = 0 \text{ in } \Omega \tag{1}$$

where $\boldsymbol{\sigma}$ and $\boldsymbol{b}$ denotes the Cauchy stress tensors and body force vectors per unit volume respectively. With the following boundary conditions:

$$\boldsymbol{\sigma} \cdot \boldsymbol{n} = \bar{\boldsymbol{t}} \quad \text{external traction}(\Gamma_t) \tag{2}$$

$$\boldsymbol{\sigma} \cdot \boldsymbol{n} = 0 \quad \text{on crack surface}(\Gamma_c) \tag{3}$$

$$\boldsymbol{u} = \bar{\boldsymbol{u}} \quad \text{at}(\Gamma_u) \tag{4}$$

where Γ_c, Γ_t and Γ_u are the crack, traction and displacement boundaries respectively, $\boldsymbol{n}$ is the normal vector on the prescribed boundary at a point as shown in Fig. 2 $\bar{t}$ is traction force vector on the boundary Γ_t and $\bar{u}$ is the prescribed displacement on the boundary Γ_u.

2.2 XFEM Approximation

The idea of extended finite element method is developed by Ted Belytschko and team [7], which is used for modelling discontinuity or singularity in the arbitrary space without remeshing. The XFEM approximation to evaluate displacement at some specific point x in the domain of enrichment is given below.

$$u^{\mathrm{h}}(x) = u^{\mathrm{FE}} + u^{\mathrm{enr}} \tag{5}$$

$$u^{\mathrm{h}}(x) = \sum_{j=1}^{n} N_j(x) u_j + \sum_{k=1}^{m} N_k(x) \psi(x) a_k \tag{6}$$

$$\psi_{,i}(x) = \mathrm{sign}(\xi) \xi_{,i}(x) \tag{7}$$

where N_j, N_k are shape functions associated finite element (FE) and enriched (enr) nodes, u_j is number of degrees of freedom in regular finite element method, a_k is the additional enriched degrees of freedom, $\psi(x)$ is a set of enrichment functions associated with the enriched nodes in the domain of discontinuity, ξ indicates the perpendicular distance from the crack path, $\xi(x)$ is calculated from the derivatives of the shape functions. For displacement evaluation at some points in the model in practical situation, some sensors are placed as shown in XFEM model in Fig. 3a, b. The sensors automatically detect the nodal displacements with any increase in size of the flaw in working conditions. Therefore, this continuous health monitoring system (HMS) monitored the data in service life of any dynamic system at random environment for future predictions. The XFEM model Fig. 3a, b are generated with the material properties of stainless steel ASS304 [8] and geometric properties of mono material is preferred based on previous literature [9] mentioned in Table 1.

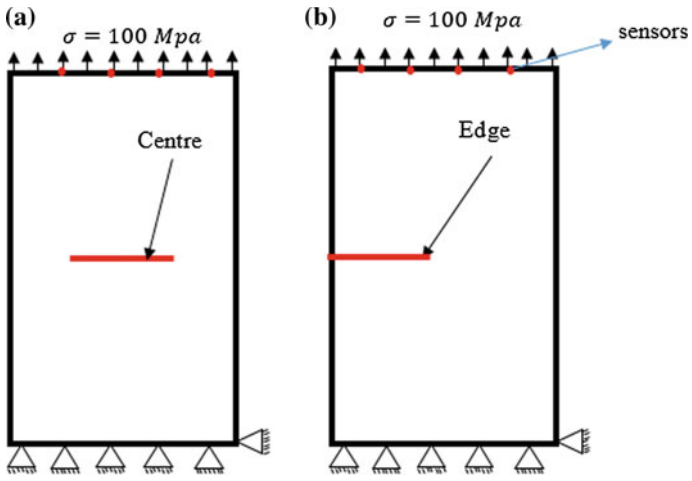

Fig. 3 **a** Centre crack inside plate, **b** Edge crack inside plate

Table 1 Material and geometric properties

	Parameter	Value
1	Young's modulus(MPa)	200
2	Poisson's ratio	0.3
3	Maximum fracture toughness(MPa $m^{1/2}$)	278
4	Rectangular plate dimensions(m × m)	0.1 × 0.2

3 Inverse Method

3.1 Regression Analysis and Classification in Machine Learning

Machine learning is able to produce useful prediction or outcomes by themselves from the past experience data. Regression problems are generally with infinite number of inputs and output is single number. In regression method the weight is obtained from the data obtained with the program. Both the regression and the classification are supervised learning problems where it has input x and output y. The input data is trained to map with given output data. The machine learning assumes a model up to certain parameters as shown in equation below [10].

$$\boldsymbol{Y} = g(\boldsymbol{X}/\boldsymbol{\theta}) \tag{8}$$

where $g(X/\theta)$ is a model, θ are its parameter and Y denotes the number regression values. In machine learning algorithm optimizes the parameters θ, such the minimal approximation error is achieved. Such our estimates come to closer exact value in the training data. Any linear or higher order polynomials can be used to best fit the input data.

4 Solution Procedure

The elements are identified to enrich along the crack path. The Laplace transforms are involved to transform the differential equations into algebraic equations in the domain Ω as shown in Fig. 2. Sub grids elements are generated on the enriched nodes.

1. The complete procedure for both XFEM and machine learning are briefly given in the following steps.
2. All the FEM elements enriched along crack surface are discretized to sub elements.
3. Finding approximate path of crack in the discretized domain.
4. The Dirichlet and essential boundary conditions are applied to generate the discontinuity in the domain.
5. The data of displacements in x and y direction are generated at some nodes on the edge using sensors as shown in Fig. 3.
6. Repeating above constructive steps for varying crack length for both edge crack and center crack to generate the data.
7. The data generated is fed to the machine learning regression algorithm to fit a model without any explicit algorithm.
8. Now the model is trained with given XFEM input and output data.

9. The accuracy of prediction is performed by giving know displacements with crack length an unknown.

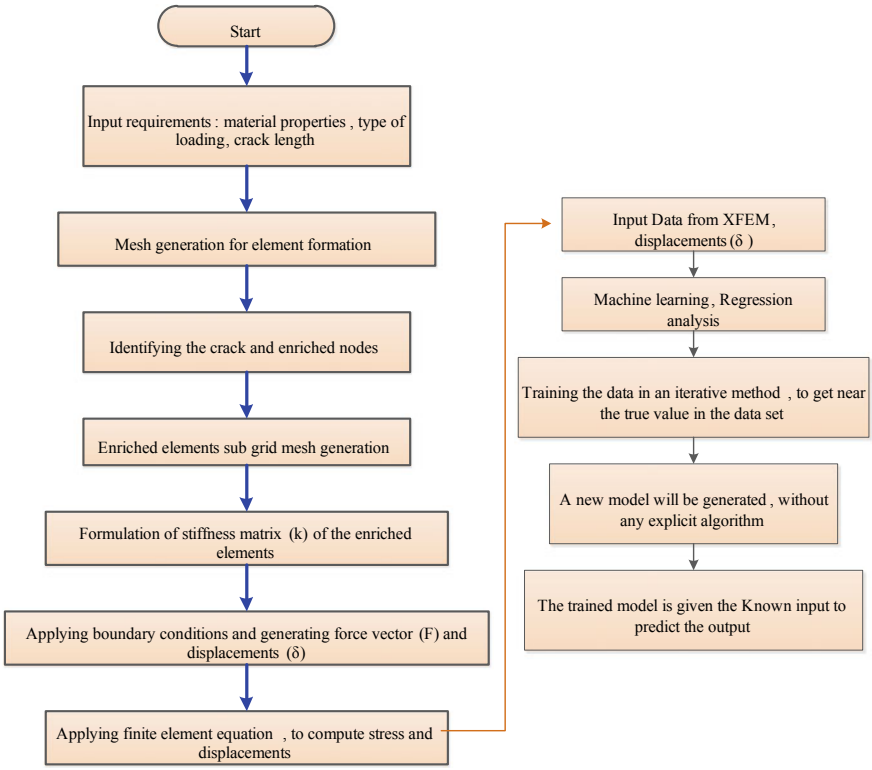

5 Results and Discussion

To get the result from above discussed formulation a MATLAB program has been developed with material properties mentioned in Table 1. The results of developed XFEM program has been validated with some bench mark problem. The accuracy of the edge crack and center crack is good. Further method is extended to implement the machine learning algorithm with regression method is implemented. On the top edge of the plate, displacement in x and y direction are measured for center crack and Edge crack. The data is trained by machine learning, regression analysis. The model generated by machine learning is able to predict the unknown crack length by know displacements with more than 90% accuracy. As shown in the Tables 2 and 3 the error percentage in both case of edge crack and center crack. Figure 4 shows the maximum stress in edge and center crack at 0.051 m crack length as 13.3665 MPa and 17.6578 MPa respectively.

Table 2 Comparison of Center crack length (XFEM) with machine learning

	XFEM	Machine learning	% error
1	0.051	0.0508	0.39
2	0.060	0.0617	2.8
3	0.069	0.0646	6.3
4	0.076	0.0786	3.4

Table 3 Comparison of Edge crack length (XFEM) with machine learning

	XFEM	Machine learning	% error
1	0.051	0.0517	1.3
2	0.060	0.0635	5.8
3	0.069	0.0689	0.1
4	0.076	0.0719	5.39

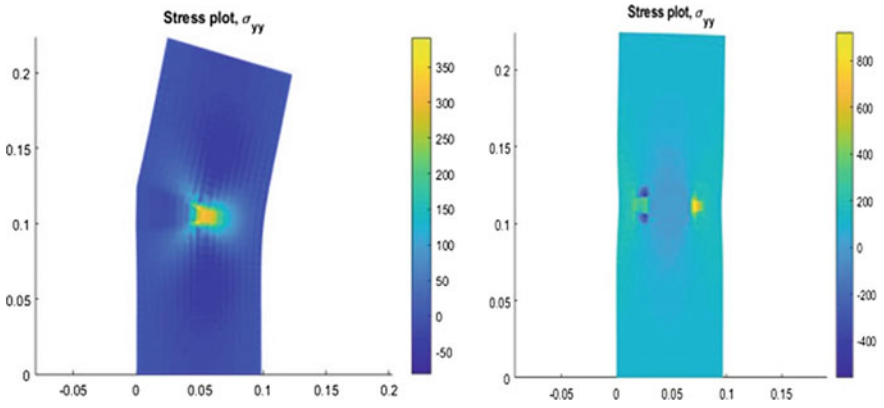

Fig. 4 XFEM stress model

6 Conclusion

In the present work, Crack identification has been done with the use of machine learning method. The present results show a great level of accuracy in the prediction of crack length. This method can be extended to predict the complex crack shape and to predict the SIF also. Figure 4, shows the XFEM stress plots at crack length 0.051 m, which I will extend in the future work to predict the stress intensity factor. The stress intensity calculation for two dimensional and three dimensional problems is a time consuming. The extension of present method will reduce the computation time. The accuracy of present method in crack length prediction is above 90% and time required to computation is extremely small if compared to PSO and genetic algorithm. The present method will be quite useful for the industry and academia community. It will help in designing algorithm to predict failure in the system.

References

1. Sohn H, Ferrar C, Hemez FM, Czarnecki J (2003) A review of structural health monitoring literature: 1996–2001. Struct Heal Monit, vol LA-13976-M, no. LA-13976-MS, pp 1996–2001
2. Pais MJ (2017) DETC2011-4, pp 1–12
3. Coppe A, Pais MJ, Haftka RT, Kim NH (2012) Using a simple crack growth model in predicting remaining useful life. J Aircr 49(6):1965–1973
4. Papila M, Haftka RT (2003) Implementation of a crack propagation constraint within a structural optimization software. Struct Multidiscip Optim 25(5–6):327–338
5. Methods C et al (2018) ScienceDirect data-based derivation of material response. Comput Methods Appl Mech Engrg 331:184–196
6. Livani MA, Khaji N, Zakian P (2018) Identification of multiple flaws in 2D structures using dynamic extended spectral finite element method with a universally enhanced meta-heuristic optimizer, pp 605–623
7. Belytschko T, Gracie R, Ventura G (2009) A review of extended/generalized finite element methods for material modelling
8. Srinivasu C, Singh SK, Jella G, Jayahari L, Kotkunde N (2017) Study of limiting dome height and temperature distribution in warm forming of ASS304 using finite element analysis. In: Materials today: proceedings, vol 4, no 2
9. Nasri K, Abbadi M, Zenasni M, Ghammouri M, Azari Z (2014) Double crack growth analysis in the presence of a bi-material interface using XFEM and FEM modelling. Eng Fract Mech 132:189–199
10. Alpaydin E (2010) Introduction to machine learning, 2nd edn

A Study of Occupant Injuries Classification in Automobile Accidents in Relation to Upper Extremities Bones

Kedar M. Hendre, Kiran D. Mali and Dhananjay M. Kulkarni

Abstract Occupant injuries in case of automotive accidents are a major concern from the point of view of human life and the costs associated with the medical treatments. The injuries associated with high-speed impacts are sometimes fatal in nature. The high-speed accidents occur above vehicle speed of 50 kmph, and the accident damage duration is about 100–150 ms. However, injuries from the low-speed impact are equally severe and they may not cause loss life to human life but cause injuries which are burden on medical costs. Restraint systems in the cars have the effect of saving human lives in high-speed impacts, but they are also known to be a cause of injuries to occupant. This study deals with the classification of injuries to human in case of automotive accidents and describes a mathematical way of assigning scores to human injuries. The injury measurement scales are studied—the Abbreviated Injury Scale (AIS), Injury Severity Score (ISS) and the Probability of Death Score (PODS). In relation to the human injuries, ample research is available for injuries to vital organs like brain, neck, chest, spine and lower extremities like thighs and knees. Very little literature is available for upper extremities such as forearms and shoulder. This paper describes the joints and bone structure for upper extremities and emphasizes the risk to upper extremities in accidents. It also describes the various types of bone fractures and the permissible loads for the fracture of bones of upper extremities.

Keywords Biomechanics · Upper extremity · Accidents · Injuries

K. M. Hendre (✉) · K. D. Mali · D. M. Kulkarni
Department of Mechanical Engineering, BITS-Pilani, K. K. Birla Goa Campus, NH 17 B, Zuarinagar, Goa 403726, India
e-mail: p20160025@goa.bits-pilani.ac.in

K. D. Mali
e-mail: kiranm@goa.bits-pilani.ac.in

D. M. Kulkarni
e-mail: dmk@goa.bits-pilani.ac.in

K. M. Hendre
Engineering, Research & Development Department, TATA Technologies, 25, Rajiv Gandhi Info Tech Park, Hinjewadi, Pune, India

A. K. Parwani and PL. Ramkumar (eds.), *Recent Advances in Mechanical Infrastructure*, Lecture Notes in Intelligent Transportation and Infrastructure,
https://doi.org/10.1007/978-981-32-9971-9_28

1 Introduction

Automobiles are a commonplace items in today's world and necessities for travel. They have gained popularity as the most common mode of personalized travel. The numbers of vehicles on the road are increasing day by day and so are the accidents associated with the vehicle movement. The nature of accidents and the injuries coming from the accidents have also changed over the years. This nature depends on the type/size of the vehicle and on the type of restraint system present in the vehicles. Vehicles in the 1950s started with seatbelts—the basic element of any restraint system. Today's vehicles have come a long way having as many as 16 airbags, collapsible steering column mechanisms and seatbelts with pretensioners. Thanks to these safety measures, the numbers of deaths on the roads have come down, but the same cannot be said about the injuries. Nature and severity of injuries have changed. A lot of injuries are caused by the impact on the accidents, and some are also caused by the restraints systems themselves [1]. Airbag explosions release a lot of energy into the cabin space which is a potential safety hazard in itself. The airbags reduce all fatal injuries to delicate organs like the head, neck, chest, and heart. However, inflation of airbag releases a lot of energy to the upper limbs and upper extremities of the body. This additional uncontrolled energy can cause injuries to any organ of the human body, but essentially to the upper extremities. Airbag deployment can cause injuries leading to permanent impairment of organs. The most common form of injuries caused by airbags is to the upper extremities. It is estimated that the non-fatal injuries to the upper limbs have increased by about 40% due to the use of efficient restraint system for saving lives [1]. This paper is an attempt to understand the biomechanics behind the injuries to the upper extremities. The bone structure of the clavicle, arm, elbow, forearm, wrist, hand and fingers has been explained. The breaking forces and moments on various bones have been collected based on the available research. Prior research has been done on the testing of the cadaver forearm using a 3-point bending test [2]. The general scales of injury measurement have been considered, viz. Abbreviated Injury Scale (AIS), the Injury Severity Score (ISS) and the Probability of Death Score (PODS). The injuries to the upper extremities are often disregarded as they are usually not limb or life-threatening and can be treated to return to normalcy or near normalcy by medical treatment and physiotherapy. The medical costs associated with this type of treatment are causing burden on the automotive insurance and likewise on the health insurance in all parts of the world.

2 Bone Structure of the Upper Limb

The bones of the upper extremity include the clavicle, scapula, humerus, radius and ulna, eight carpal bones, five metacarpals and the phalanges within the digits (refer Fig. 1). The humerus is the longest bone in the body of upper structure. Each

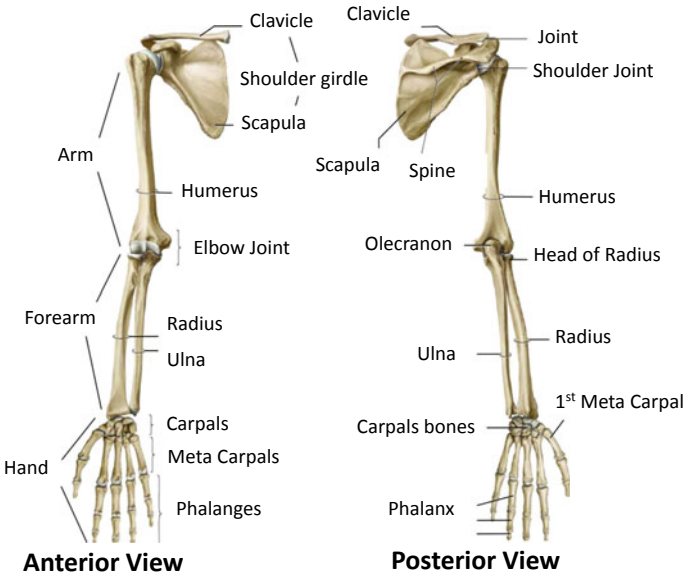

Fig. 1 Bone structure from shoulder to fingers [3]

cylindrical bone consists of the diaphysis or the main shaft, epiphysis, or the expanded ends of the bones and metaphysis which is the transition between the two.

The shoulder joint is the most movable joint of the upper limb and hence is most fragile. The forearm consists of two bones lying parallel to one another—the radius and the ulna. The humerus is joined to the radius and the ulna bone by the elbow joint. The radioulnar joint forms union between the radius and the ulna. The carpal internally is a union of eight bones in two rows. The wrist joint consists of two internal joints and is the one of the most complex joints of the body. The individual fingers have three bones each called as phalanges—distal, middle and proximal. The middle bone in the thumb is not present making it less flexible, but stronger [3].

3 Types of Bone Fractures

The bones lose the continuity under the effect of extreme loading in the form of impact, stress or fatigue, which is above the normal sustaining capacity of the bone. Under any abuse loading, the bones tend to show cracks in the structure which leads to further widening of the cracks and eventually failure leading to discontinuity. The breaking of bone under impact or fatigue loading is called as fracture. The fracture of bone may be of different kinds depending upon the crack in the bone, viz. transverse, spiral, oblique, butterfly, segmental and avulsion fracture as shown in Fig. 2.

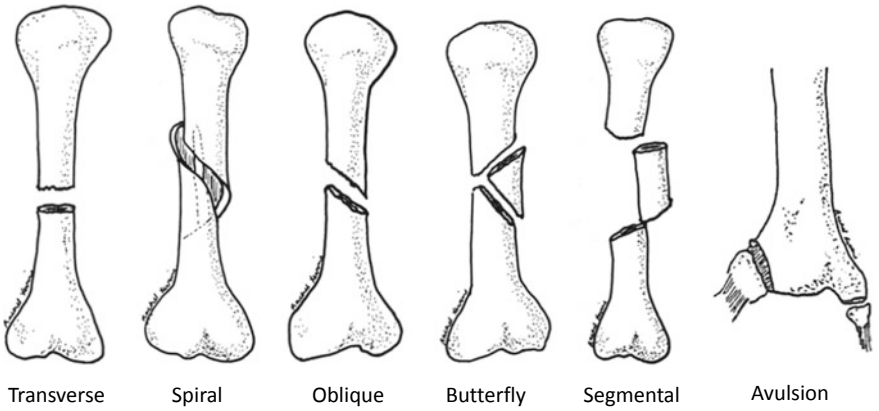

Fig. 2 Types of bone fractures [4]

A fracture is called as non-comminuted, if it is broken in only two pieces and it is called as comminuted if there are more than two fragments of the bone left after the fracture. The fractures of the clavicle occur under very large forces and represent about one-third of all the fractures in the shoulder region. Fractures also occur in the distal humerus bones, the radius and the ulna, which may lead to impairment of the elbow joint. Injuries to radius and the ulna are also equally common and a result of direct blow to the forearm by hitting on the steering wheel or the surrounding trims or window glass. About 14% of the fractures occur in the distal radius region [3]. The scaphoid is the central bone in the palm region and is fractured in about 80% of the injuries to the wrist [3]. The wrist joint injuries are always associated with some form of damage to the radius and/or ulna. The metacarpals and carpal injuries are very common when a person lands on a hard surface with an open hand. The palm is often used to avoid any hard impact on the body and hence fingers/palm is also a common organ to be fractured in the event of automotive crash accident.

4 Bone Fracture Mechanisms

The type of loading which has caused the bone to fracture will be seen in the remains of the bones after the accident. The main ways which can cause a bone to fracture are direct blow, indirect loading, penetration or repetitive loading. Low energy blows cause a single spilt in the bones which may be transverse in nature. High energy direct blows often cause comminuted fractures. Displaced fractures are caused by high energy blows, and non-displaced fractures are caused by relatively low energy blows. Amount of comminution also depends on the inherent strength of the bone. More the strength, less are the chances of a non-comminuted fracture under low

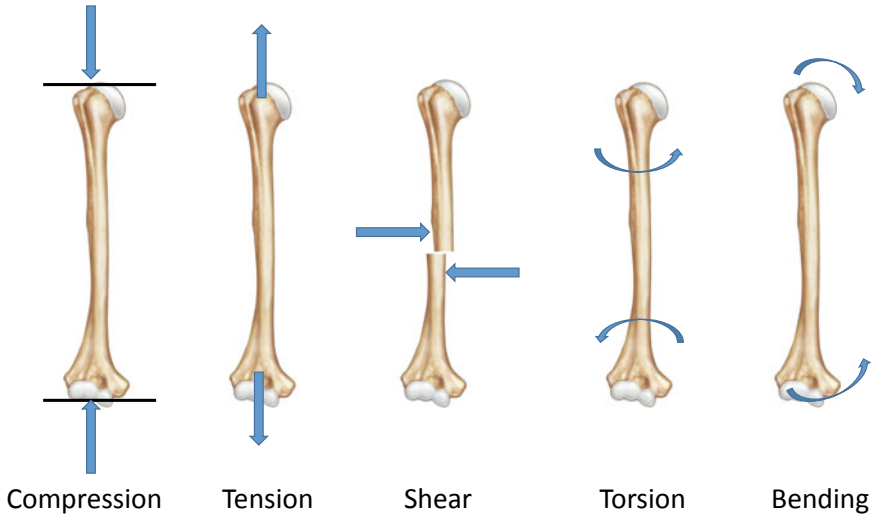

Fig. 3 Bone failure under different loading conditions

Table 1 Range of loading conditions for bone strength

Bone	Long axis compression (kN)	Bending (kN)	Torque (Nm)	Average Max. Moment (kN)
Clavicle	1.89/1.24	0.98/0.60	15/10	30/17
Humerus	4.98/3.61	2.71/1.71	70/55	151/85
Radius	3.28/2.16	1.2/0.67	22/17	48/23
Ulna	4.98/3.61	1.23/0.81	14/11	49/28

Failure/fracture [4]

energy blow [3]. Bones are known to fail under different loading conditions as shown in Fig. 3.

Table 1 shows the approximate strength of each bone in the forearm or the loads/moments to cause fractures in the bones [4].

5 Abbreviated Injury Scale (AIS)

The Abbreviated Injury Scale (AIS) is an anatomy and severity-based index for an injury to any part of the human body. It is devised by the Association for the Advancement of Automotive Medicine (AAAM) which was founded in 1957 and dedicated to limiting injuries from motor vehicle crashes [5, 6]. The AIS is an internationally accepted tool for describing and coding injuries of all types. Topically, the injury is classified and written as a 7-digit number as 12(34) (56).7. (Refer Table 2).

Table 2 Abbreviated Injury Scale digits description [5]

Digit	Indicates	Examples
1	Region of the body	Head/face/neck
2	Type of anatomic structure	Vessels/nerves/organs/skeletal
(34)	Specific anatomic structure	Skin abrasion/burn/amputation
(56)	Level of injury	Fractures, rupture, laceration
.7	AIS (severity score)	Scale from 1 to 6 and 9

Table 3 Abbreviated injury score description—Abbreviated Injury Scale (AIS) post dot digit [5]

Value	Description	Probability of death (%)
1	Minor	0
2	Moderate	1–2
3	Serious	8–10
4	Severe	20–50
5	Critical	50–80
6	Maximum (currently untreatable)	Close to 100
9	Currently unknown	

The AIS score is described as the relative risk of "threat to life" in an average person who sustains the coded injury as his or her only injury. The injuries are classified from AIS1 to AIS6 and AIS9 with AIS6 being the most severe injuries. Injuries are classified based upon the region in which they occur and how severe is the injury with respect to possibility of injury resulting in death of the occupant (refer Table 3). It does not classify injury according to possible outcomes or complications resulting from the injury or the treatment associated with the injury. The injury scale is based upon actual condition of the patient, and post-treatment effects, diagnosis, treatment do not play any role in deciding the code for an injury.

For the purpose of injury measurement and taking a data point, injuries of AIS1 and AIS2 are usually ignored as they may not be very serious and subject to occupant's pain bearing capacity. The injuries which are of severe in nature and which are usually accounted for in research are of AIS2+. Maximum AIS (MAIS2+) is a term used in many of the research literature, which is maximum injury sustained by the occupant amongst all the injuries received to any parts of the body.

6 Injury Severity Score (ISS)

In some cases, AIS alone is not helpful in ascertaining the severity of injuries to human organs. This is particularly true if there are injuries to multiple organs in the body which is true in case of most of the real-life accidents. The Injury Severity

Table 4 ISS calculation example

Region	Injury description	AIS	Square
Head and Neck	Cerebral contusion	3	
Face	No injury	0	
Chest	Broken ribs	3	9
Abdomen	Complex spleen rupture	5	25
Extremity	Fractured tibia	4	16
External	No injury	0	
Injury Severity Score			50

Score (ISS) is helpful in such cases. The ISS is the sum of squares of the highest 3 AIS score to the human organs out of AIS score of all the injury scores. For this purpose, the human body is divided into six regions, viz. i. head and neck ii. face iii. chest iv. abdomen and pelvis, v. extremities and pelvic girdle and vi. external.

ISS is calculated using the formula below (refer Table 4 for example calculation of ISS).

$$\text{ISS} = \text{AIS1}^2 + \text{AIS2}^2 + \text{AIS3}^2 \tag{1}$$

7 PODS—Probability of Death Score

The Probability of Death Score (PODS) is calculated using empirical relationship to ascertain the score. It is also applicable in case of severe injuries to more than one organ in the body

$$\text{PODS} = \frac{e^x}{1 + e^x} \tag{2}$$

Probability of survival score,

$$\text{POSS} = \frac{1}{1 + e^x} \tag{3}$$

$$\text{POSS} = 1 - \text{PODS} \tag{4}$$

where $X = (2.2\ [\text{Highest AIS}] + 0.9\ [\text{Second highest AIS}] - 11.25 + C$
If age is known, then
$X = 2.7\ [\text{Highest AIS}] + 1.0\ [\text{Second highest AIS}] + 0.06\ [\text{age}] - 15.4 + C$
C is a constant found from data, $C = -0.764$ for cars

PODS is always <1.0 and PODS values of closer to 1.0 indicates very severe injury and almost certain death. PODS of 0.96 means is more critical injuries as compared to PODS of 0.85. If anyone of the AIS score is 6.0, then PODS is taken as 1.0.

8 Types of Accidents Causing Injuries in Upper Extremities

The injuries to occupants occur in various types of accidents. Most commonly caused accidents are classified as frontal impact, side impacts, and impacts from large animals, run-off-road, multiple impacts and so on. Rear impact accidents causing any significant injuries to upper extremities are rare. Typically, half of the accidents in which injuries to upper extremities occur are frontal impacts [7]. The remaining half is almost equally divided amongst side impact, multiple impact and run off-road. Frontal impacts are very important from the upper extremities point of view as the occupant is thrown forward due to the vehicle deceleration and backward after impact with the airbag and restraint system. During this occurrence of frontal impact, occupant inadvertently could be using his hands and wrists to protect/restrain himself which could be adding to injuries. It is a natural reflex for the driver and the passenger to support the body with outstretched hands as an avoidance mechanism to an impending obstacle. Another reason for upper extremities injuries in case of frontal impact is airbag firing.

Airbags are known to fire in about 7 out of 10 cases of frontal accidents. The main function of the airbag is to protect the face and head of the occupant from hitting the steering wheel or the front dashboard. Forearms, hand, wrist and fingers are bound to have some impact on the airbag. The impacting of the forearms to dashboard could be another major reason for upper extremities injuries in accidents (refer Figs. 4 and 5). Airbag explosion can push the free arms to go in air and hit the hard surface of side door side trims or the side door glass. In other cases, the airbag explosion itself could be exerting huge loads on the upper limbs to cause fractures in the bones. Here the airbag aggressivity plays a major role. Like inflation of inert gases, airbags also have a deflating or depressurizing characteristic. Slower the deflation, more are chances of causing severe injuries to the arms/wrists and fingers.

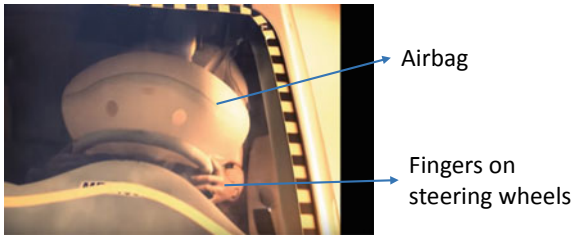

Fig. 4 Hands stuck between airbag and steering wheel

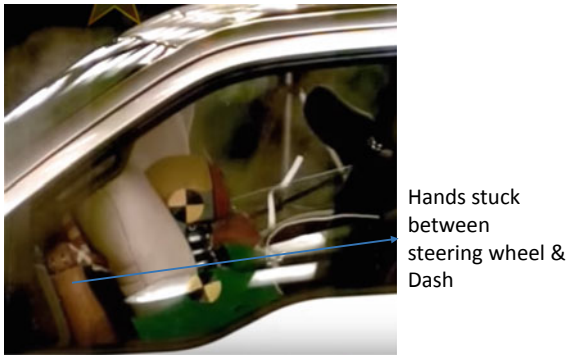

Fig. 5 Hands stuck between airbag and steering wheel

9 Occupant Injuries and Their Occurrences

The injuries in the accidents may be caused by one or more organs at the same time. The injuries to the upper extremities come in the sixth and seventh place in all injuries occurring in the automotive accidents (refer Table 5). In case of the upper extremities, the injured organs in the frontal impacts and side impact are different organs. Typically, the injuries to clavicles, forearms, hands, wrists and forearms are more common in frontal impacts, whereas injuries to the clavicles and shoulder are more common in side impact. It is very certain that the fractures of the clavicle are common to both impacts, and hence, there are organs with the maximum fractures in automotive accidents involving upper extremities (refer Table 5) [8].

In the studies that were conducted, only one bone is fractured in lateral hits which involve the forearm—either the radius or the ulna. It is also seen that the wrist forearm fractures are more common in smaller size occupant irrespective of the gender [1]. Though clavicle fractures are common in frontal and side impacts, the majority of them occur in side impacts as the shoulder is in the direct line of loading in side impact. The unbelted occupants show more upper extremities injuries as compared to the belted injuries, because the unbelted passengers are more likely to be thrown over longer distance and with more velocities towards the hard surfaces of trims and dashboards. Also, arms are more likely to be injured in unbelted occupants as they are often come between the occupant body and the obstacle. The seatbelts in older cars are also the cause of many clavicle fractures as they are very hard, ill-designed due to the absence of pretensioners and force limiters (Table 6).

10 Impairment

In case of injury to an organ of upper extremity, the impairment is calculated as a percentage to the upper extremity as well as a percentage to entire body. Typically, impairment or loss functionality of an upper arm due to the complete fracture to

Table 5 Top 20 fatal injuries in automotive accidents [8]

No	Type of injury sustained	Rate per 100,000 population	Proportion of all traffic injuries
1	Intracranial injury	85.3	24.6
2	Open wound	35.6	10.3
3	Fractured patella, tibia or fibula	26.9	7.8
4	Fractured femur	26.1	7.5
5	Internal injuries	21.9	6.3
6	*Fractured ulna or radius*	*19.2*	*5.5*
7	*Fractured clavicle, scapula or humerus*	*16.7*	*4.8*
8	Fractured facial bones	11.4	3.3
9	Fractured rib or sternum	11.1	3.2
10	Fractured ankle	10.8	3.1
11	Fractured vertebral column	9.4	2.7
12	Fractured pelvis	8.8	2.6
13	Sprains	8.3	2.4
14	Fractured skull	7.9	2.3
15	Fractured foot bones	7.2	2.1
16	Fractured hand bones	6.8	2
17	Spinal cord injury	4.9	1.4
18	Fractured femur	4.3	1.3
19	Intracranial injury	4.3	1.2
20	Other dislocation	3.4	1

Table 6 Percentage of injuries by organ in upper extremities [9]

Organ	Injuries percentage (%)
Fingers	9.8
Hands	16.3
Wrists	19.5
Forearms	14.1
Elbow	6.5
Arm	9.8
Clavicle	24

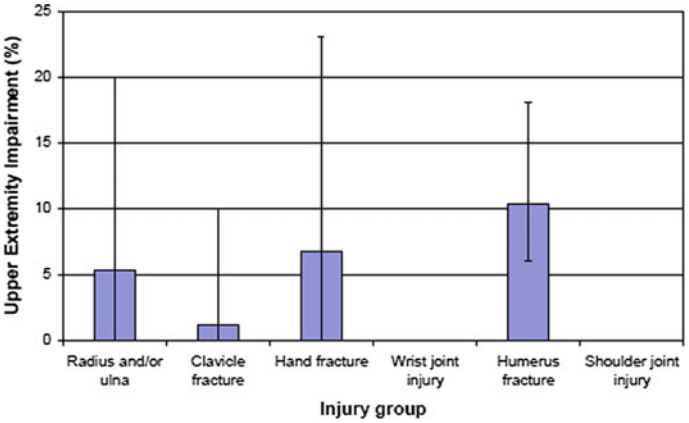

Fig. 6 Typical mean (max. and min.) impairment of upper extremities in frontal impact event [7]

the humerus bone is said to be 100% impairment of upper extremity and a 60% impairment of the whole body. Similarly, a fracture to a single finger at one of the phalanges, leading to its non-functionality is said to be 60% finger impairment and 5% impairment of the upper extremity and 3% impairment of the whole body [7].

The typical fractures and injuries caused in various accidents are categorized by the examples which are as follows. More than half of the fractures of the radius and the ulna were due to the direct impact loading by hitting on the hard surface such as A-Pillar, dashboard and steering wheel. Injuries to the forearm have also been caused due to the airbag firing where the forearm is trapped between the bag and the steering wheel (refer Fig. 6). In such cases, the energy of the airbag deployment could have caused the forearm to fracture. Most of the clavicle fractures in the frontal impact were caused by restraining the forward motion of the body due to seatbelts. The impact on the clavicles can be reduced by fine-tuning the seat belt pretensioners and load limiters. Clavicle and humerus fractures are also common in side impacts due to the direct loading from the door or the B-Pillar post. The side door trim stiffness also plays an important part in the injury to the occupant, particularly to the clavicle/humerus.

11 Recommendation

There is a regulation which is present to access the stiffness of car interiors with respect to head impact [10]. This is the ECE R21 regulations which simulate the head hitting the interior of the car and access the injury to occupant head. Though this regulation is exhaustive in covering all the areas of the vehicle, from the occupant point of view, it uses the spherical impactor which represents the head only. Efforts

should be made to look at the possibility of amending the regulation to involve forms representing other organs, such as shoulders, forearms and hands [7].

12 Summary/Conclusions

The bone structure of the upper extremities was studied with the objective of understanding the impact of injuries in automotive accidents. Effort was made to understand the different loading on the bones which cause injuries or fractures to the bones. The injury mechanism available from some of the literature survey was studied. In particular, emphasis was on how the airbag deployment contributes to the injuries due to hitting of organs on the surrounding hard surfaces of automotive interiors. The classification of the injuries based on the AIS scale helps in standardizing and classifying the injuries based on the severity and hence suitable for comparison in various studies. Also, the ISS and PODS were introduced to understand the severity of injuries in case of injuries to multiple organs at the same time. Out of the bones, the clavicle and humerus fracture seem to be most common and are caused in both frontal and side impact.

This study did not deal with the cost incurred in the treatment and post-treatment measures and loss due to the absence from work. The parameters like the AIS, ISS and PODS can be important in understanding the loss to the society due to the injuries in automotive accidents.

Acknowledgements The authors would like to thanks the BITS, Pilani, K. K. Birla Goa Campus for their support during the preparation of this paper. Kedar Hendre would also like to thank the Management of Tata Technologies, Pune, in providing the support during the preparation of this paper.

References

1. Duma S, Crandall J, Hurwitz R, Pilkey W (1998) Small female upper extremity interaction with a deploying side air bag. In: 42nd STAPP car crash conference, SAE paper 983148
2. Yoganandan P, Eppinger R (1998) Response and tolerance of the human forearm to impact loading. In: Proceedings of the 42nd Stapp car crash conference, SAE 983149
3. Thieme S, Wingren M (2009) Understanding fracture mechanisms of the upper extremities in car accidents. Halmstad University School of Business and Engineering
4. Melvin N (1993) Accidental injury. Springer, New York
5. Association of advancement of Automotive Medicine homepage. http://www.aaam.org. Last accessed 2019/3/1
6. Association of advancement of automotive medicine, AIS 2005: Update 2008 clarification (2008)
7. Hynd D, Carroll J, Cuerden R (2019) Upper extremity injury study: recommendations for injury prevention priorities. TRL Limited, UK
8. World report on road traffic injury prevention, World Health Organization (2004). ISBN 92 4 156260 9

9. Wraighte J, Wallace P, Angus W (2014) Upper extremity injuries in road traffic accidents. The transport research laboratory, UK, Paper number 07-0239
10. Uniform provisions concerning the approval of vehicles with regard to their interior fittings, ECE R21, ECE R-21. The United Nations Economic Commission for Europe. www.unece.org

Comparative Dynamic Performance of Configurations of Hole-entry Journal Bearings under Turbulent Regime

Nathi Ram

Abstract The present paper investigates the comparative dynamic performance of hole-entry symmetric and asymmetric hybrid journal bearing configurations under turbulent lubrication. Constantinescu turbulent model is used to account the influence of turbulent flow on bearing performance. Reynolds equation is altered considering turbulent theory of lubrication by Constantinescu. FEM using Galerkin's technique is utilized to determine the solution of altered Reynolds equation. Dynamic performance for various values of Reynolds numbers has been presented for the configurations of hole-entry bearings. It is observed that the effects of turbulent lubrication on dynamic characteristics of bearings are significant.

Keywords Hydrostatic bearing · Turbulent models · Finite element method · Bearing configurations

1 Introduction

The turbulent lubrication in journal bearings has received increasing attention of many researchers. The hole-entry bearing by capillary restrictor was presented by Yoshimoto et al. [1]. FDM was used for determining the solution of Reynolds's equation. Rowe and Koshal [2] discussed the bearing configuration's selection, materials, geometry, and restrictors for gas- and liquid-lubricated bearings and design strategy for hybrid bearings. Constantinescu [3] presented calculations for the journal and thrust bearings subjected to turbulent lubrication using mixing length theory of Prandtl. Later on, Constantinescu and Galetuse [4] developed a method for evaluating frictional torques and forces in case of bearings using mixing length theory. Hashimoto et al. [5] worked on short bearing under turbulent lubrication. Kumar and Mishra [6] reported performance of non-circular worn bearings by turbulent lubrication. Nicodemus and Sharma [7] analyzed four-pocket hybrid bearing under

N. Ram (✉)
Department of Mechanical and Automation Engineering, Indira Gandhi Delhi Technical University for Women, Delhi, India
e-mail: n.r.jaan10@gmail.com

A. K. Parwani and PL. Ramkumar (eds.), *Recent Advances in Mechanical Infrastructure*, Lecture Notes in Intelligent Transportation and Infrastructure,
https://doi.org/10.1007/978-981-32-9971-9_29

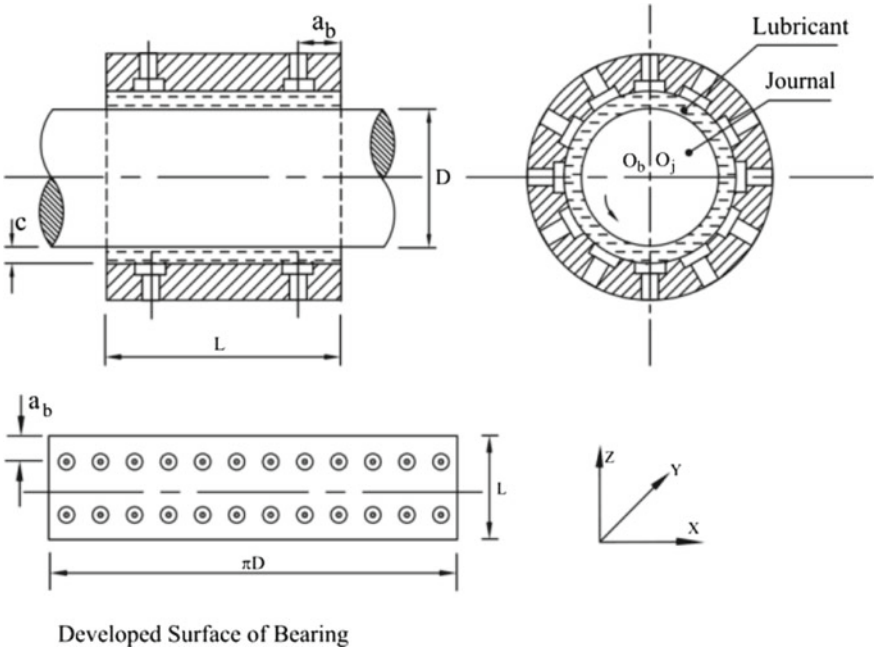

Fig. 1 Symmetric hole-entry bearing configuration

turbulent regime. Soni and Vakharia [8] presented the static analysis of hydrodynamic bearing under turbulent lubrication. Later on, Nathi and Sharma [9, 10] worked on misaligned and aligned hole-entry bearing under turbulent lubrication. Gautam and Ghosh [11] determined the side leakage and dynamic characteristics of seals under turbulent flow. They compared the performance of wavy annular and circular seals and found that the use of seal of wavy shape can enhance the performance of seals. Later on, Nathi [12] reported the results of the symmetric and asymmetric hole-entry journal bearing under turbulent lubrication.

The objective of current study is to determine dynamic characteristics of the hole-entry bearing configurations under turbulent lubrication. These bearing configurations (Figs. 1 and 2) are compensated by constant flow valve restrictors. The Reynolds equation has been solved by FEM and using different values of Reynolds number, the dynamic characteristics have been determined in the present work.

2 Analysis

Reynolds equation for the bearing configurations in laminar and turbulent flow regimes is given by Constantinescu et al. [4], Nicodemus and Sharma [7] as:

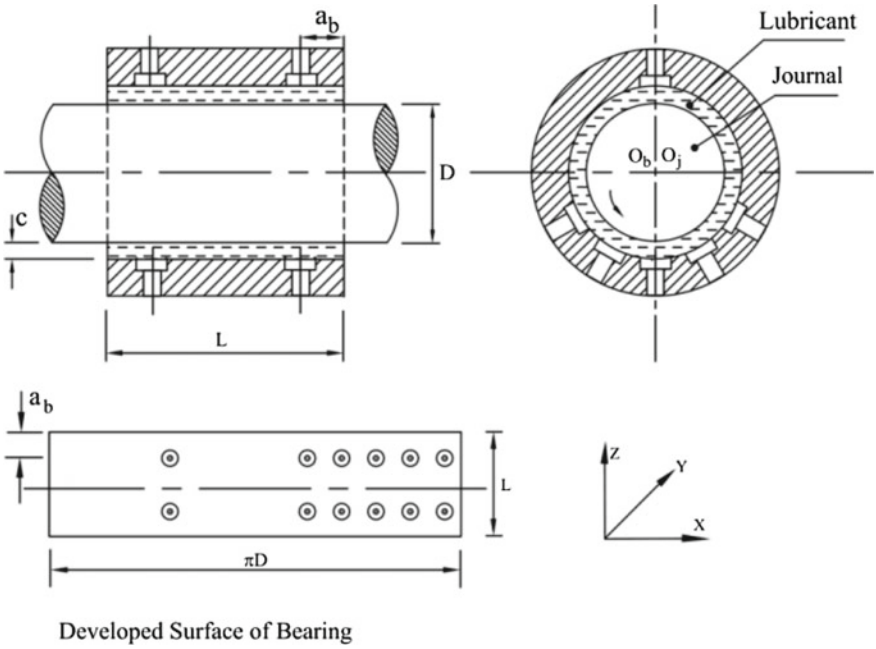

Fig. 2 Asymmetric hole-entry bearing configuration

$$\frac{\partial}{\partial\alpha}\left[\frac{\bar{h}^3}{G_\alpha\bar{\mu}}\frac{\partial\bar{p}}{\partial\alpha}\right]+\frac{\partial}{\partial\beta}\left[\frac{\bar{h}^3}{G_\beta\bar{\mu}}\frac{\partial\bar{p}}{\partial\beta}\right]=\frac{\Omega}{2}\frac{\partial\bar{h}}{\partial\alpha}+\frac{\partial\bar{h}}{\partial\tau} \tag{1}$$

where $\bar{h}$ is given by Eq. (4) and turbulent coefficients G_α and G_β are dependent on local Reynolds number $\left(R_e^*\right)$ and relations derived by Constantinescu et al. [4] are

$$G_\alpha = 12 + 0.026\left(R_e^*\right)^{0.8265} \tag{2}$$

$$G_\beta = 12 + 0.0198\left(R_e^*\right)^{0.741} \tag{3}$$

Fluid-film thickness in case of journal bearing system is described by Sharma et al. [4] as:

$$\bar{h}_0 = 1 - \bar{X}_J\cos\alpha - \bar{Z}_J\sin\alpha \tag{4}$$

The flow of lubricant Q_R by using constant flow valve restrictor is given as:

$$\bar{Q}_\mathrm{R} = \bar{Q}_\mathrm{c} \tag{5}$$

2.1 Finite Element Formulation

The fluid flow is discretized using four-noded quadrilateral isoparametric elements. Applying FE formulation and Galerkin's approach, the following form of Eq. (1) reduces as;

$$\left[\bar{F}\right]^e\{\bar{p}\}^e = \left\{\bar{Q}\right\}^e + \Omega\left\{\overline{R_{\mathrm{H}}}\right\}^e + \dot{\overline{X}}_j\left\{\bar{R}_{xj}\right\}^e + \dot{\overline{Z}}_j\left\{\bar{R}_{zj}\right\}^e \tag{6}$$

where

$$\bar{F}^e_{ij} = \int_{A^e}\int \frac{\bar{h}^3}{\bar{\mu}}\left[\frac{1}{G_\alpha}\frac{\partial N_i}{\partial\alpha}\frac{\partial N_j}{\partial\alpha} + \frac{1}{G_\beta}\frac{\partial N_i}{\partial\beta}\frac{\partial N_j}{\partial\beta}\right]\mathrm{d}\alpha\ \mathrm{d}\beta$$

$$\bar{Q}^e_j = \int_{\tau^e} \frac{\bar{h}^3}{\bar{\mu}}\left[\frac{1}{G_\alpha}\frac{\partial\bar{p}}{\partial\alpha} + \frac{1}{G_\beta}\frac{\partial\bar{p}}{\partial\beta}\right]N_i\mathrm{d}\tau - \frac{\Omega}{2}\int\bar{h}N_i\mathrm{d}\tau$$

$$\bar{R}^e_{\mathrm{H}j} = \int_{A^e}\int\frac{\bar{h}}{2}\frac{\partial N_i}{\partial\alpha}\mathrm{d}\alpha\ \mathrm{d}\beta$$

$$\bar{R}^e_{xij} = \int_{A^e}\int N_i\cos\alpha\ \mathrm{d}\alpha\ \mathrm{d}\beta$$

$$\bar{R}^e_{Zij} = \int_{A^e}\int N_i\ \sin\alpha\ \mathrm{d}\alpha\ \mathrm{d}\beta$$

2.2 Conditions Applied for Boundary

The conditions applied for boundary used in the present work are:

(i) The pressures on nodes and nodes on hole boundary are equal.
(ii) The flow on nodes is zero at all interior node apart from the nodes appearing on hole and exterior boundaries.

3 Solution Procedure

The analysis of compensated bearing configurations needs the concurrent solution of modified Reynolds Eq. (6) jointly with Eq. (5) and boundary conditions. This requires an iterative technique to obtain the matched solutions. Additional iterations are also required for the establishment of equilibrium position of center of journal for particular vertical load. When journal center equilibrium is achieved then dynamic performance of bearing configurations is computed.

4 Results and Discussion

A computer program to analyze the performance of hole-entry bearing configurations under turbulent lubrication have been made. The achieved results in this work have been verified with available results of hydrodynamic journal bearing under turbulent lubrication (Kumar and Mishra [6]) as revealed in Fig. 3 and the results have been found in order. The dynamic characteristics such as coefficients of stiffness and damping of fluid film and parameter of threshold seed have been evaluated for the parameters on the basis of literature are given in Table 1.

Figure 4a, b shows the variation in stiffness coefficients ($\bar{S}_{11}$, $\bar{S}_{22}$). The stiffness coefficients are more for symmetric configuration than asymmetric configuration of bearing at constant value of $\bar{W}_o$ for the bearing operates under laminar and turbulent regimes. For a symmetric configuration of bearing due to effect of turbulence for the higher value of R_e, the values of $\bar{S}_{11}$ and $\bar{S}_{22}$ get increased significantly at constant load than symmetric bearing operates under laminar regime, whereas for asymmetric configuration of bearing, the values of $\bar{S}_{11}$ and $\bar{S}_{22}$ are found to be order of 39.16% and 149.66% for same value of $R_e = 20000$ at $\bar{W}_o = 1.5$ than symmetric bearing under laminar regime at $\bar{W}_o = 1.5$.

Figure 5a, b depicts the variation for the values of coefficients of stiffness ($\bar{S}_{11}$, $\bar{S}_{22}$) for symmetric/asymmetric configurations of bearing with $\bar{C}_{s2}$. The increasing trend has been noticed for stiffness $\bar{S}_{11}$ and $\bar{S}_{22}$ for bearing configurations for values of $\bar{C}_{s2} = 0.05 - 0.25$ when bearing operates under laminar and turbulent regime. It

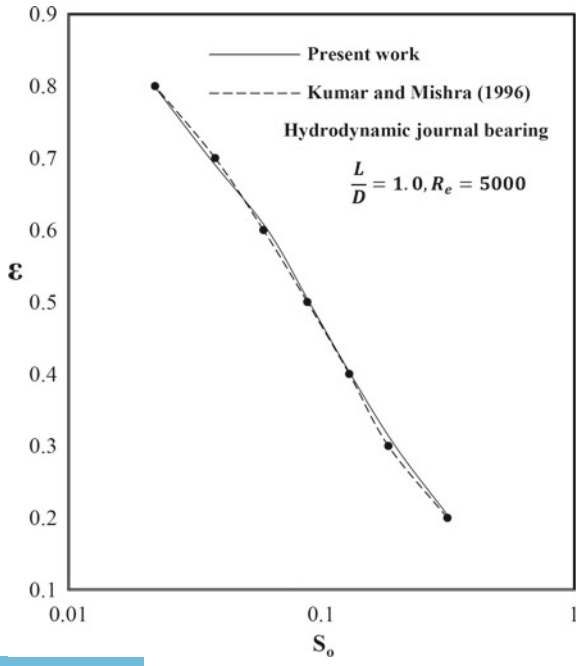

Fig. 3 Variation of eccentricity with Sommerfeld number

Table 1 Parameters of bearing

S. No.	Parameters	Values
1	Bearing aspect ratio (λ)	1.0
2	Land width ratio ($\bar{a}_b$)	0.25
3	Concentric design pressure ratio (β^*)	0.5
4	No. of rows of holes	2
5	No. of holes per row (Symmetric configuration)	12
6	No. of holes per row (Asymmetric configuration)	6
7	Reynolds number (R_e)	0, 5000, 10000, 20000
8	External load ($\bar{W}_o$)	0.25–1.25
9	Restrictor design parameter ($\bar{C}_{s2}$)	0.05–0.25

has been observed that the coefficients ($\bar{S}_{11}$, $\bar{S}_{22}$) are found to be higher for constant $\bar{C}_{s2}$ value for case of symmetric configuration than that of asymmetric configuration of bearing under turbulent regime. The percentage of increase in the coefficients $\bar{S}_{11}$ and $\bar{S}_{22}$ is found to be order of 321.97% and 319.99% for the value of R_e = 20000, respectively, for symmetric configuration as compared to symmetric bearing operates in laminar regime at $\bar{C}_{s2} = 0.25$, whereas for asymmetric configuration, the percentage of increase in $\bar{S}_{11}$ and $\bar{S}_{22}$ values is 20.19% and 167.65%, respectively, for the same value of R_e for constant $\bar{C}_{s2}$ value than symmetric bearing operates in laminar regime.

Figure 6a, b shows the coefficients of damping ($\bar{C}_{11}$, $\bar{C}_{22}$) values for bearing configurations against $\bar{W}_o$. The coefficients $\bar{C}_{11}$ and $\bar{C}_{22}$ are slightly higher for asymmetric configuration as compared to symmetric configuration of bearing at constant load $\bar{W}_o$ when the bearing is operating at higher values of R_e. It may be observed that the coefficients $\bar{C}_{11}$ and $\bar{C}_{22}$ increase, as the value of R_e increases for both symmetric/asymmetric configurations of bearing at constant value of $\bar{W}_o$. The values of direct fluid-film damping coefficients ($\bar{C}_{11}$, $\bar{C}_{22}$) against restrictor design parameter are shown in Fig. 7a, b. It may be noted that the coefficients $\bar{C}_{11}$ and $\bar{C}_{22}$ are higher for asymmetric configuration in comparison with symmetric configuration at constant value of $\bar{C}_{s2}$ for bearing operates under laminar as well as turbulent regimes.

For the Reynolds number R_e = 20000, an increase for value of $\bar{C}_{11}$ and $\bar{C}_{22}$ is 324.52% and 323.07%, respectively, for symmetric bearing than symmetric bearing under laminar regime at $\bar{C}_{s2} = 0.25$. In case of asymmetric configuration, an enhancement for $\bar{C}_{11}$ and $\bar{C}_{22}$ is 393.55% and 384.02% for the same value of R_e and $\bar{C}_{s2}$ than symmetric bearing under laminar regime (Fig. 7a, b).

Figure 8a shows threshold speed $\bar{\omega}_{\text{th}}$ reduces by increasing the value of $\bar{W}_{\text{o}}$ for both the configurations of bearing when these are operated in laminar and turbulent regimes. The threshold speed $\bar{\omega}_{\text{th}}$ is more for symmetric bearing than asymmetric bearing for constant external load. The decrease in $\bar{\omega}_{\text{th}}$ value is 57.30% for load range $\bar{W}_{\text{o}} = 0.25-1.5$ for symmetric bearing under laminar regime. Though, for Reynolds number of R_e = 20000, this loss in threshold speed gets increased by

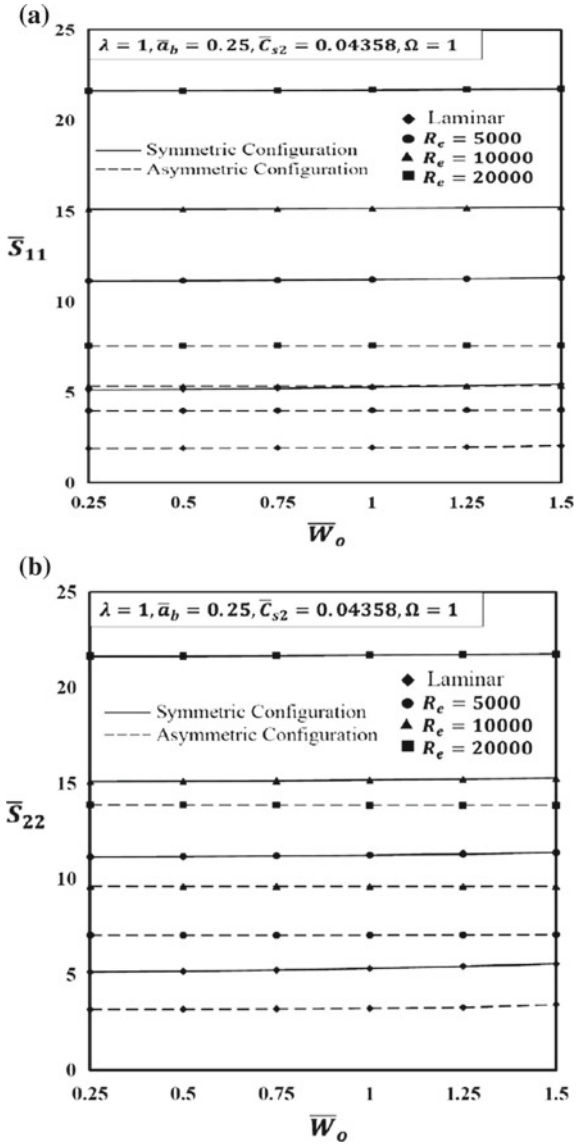

Fig. 4 Variation of **a** $\bar{S}_{11}$, with $\bar{W}_o$ and **b** $\bar{S}_{22}$ with $\bar{W}_o$

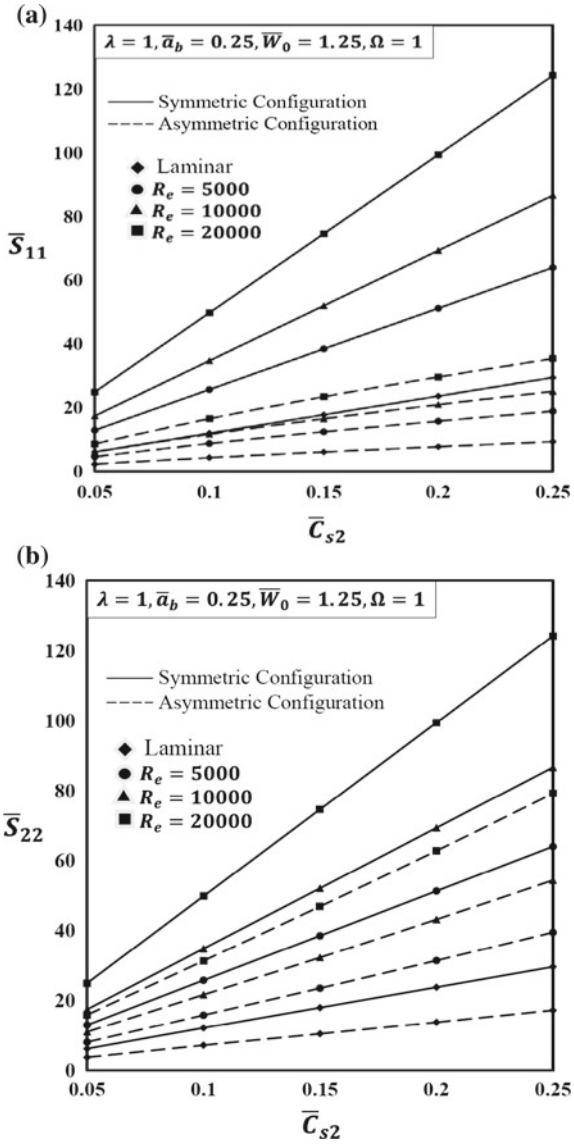

Fig. 5 Variation of **a** $\bar{S}_{11}$, with $\bar{C}_{s2}$ and **b** $\bar{S}_{22}$ with $\bar{C}_{s2}$

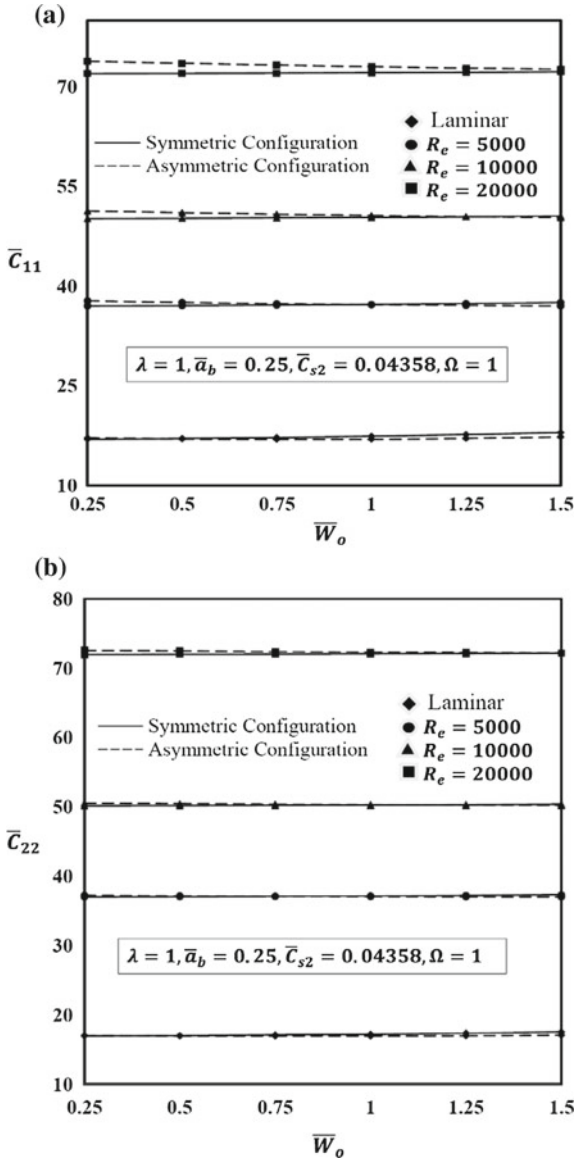

Fig. 6 Variation of **a** $\bar{C}_{11}$, with $\bar{W}_o$ **b** $\bar{C}_{22}$, with $\bar{W}_o$

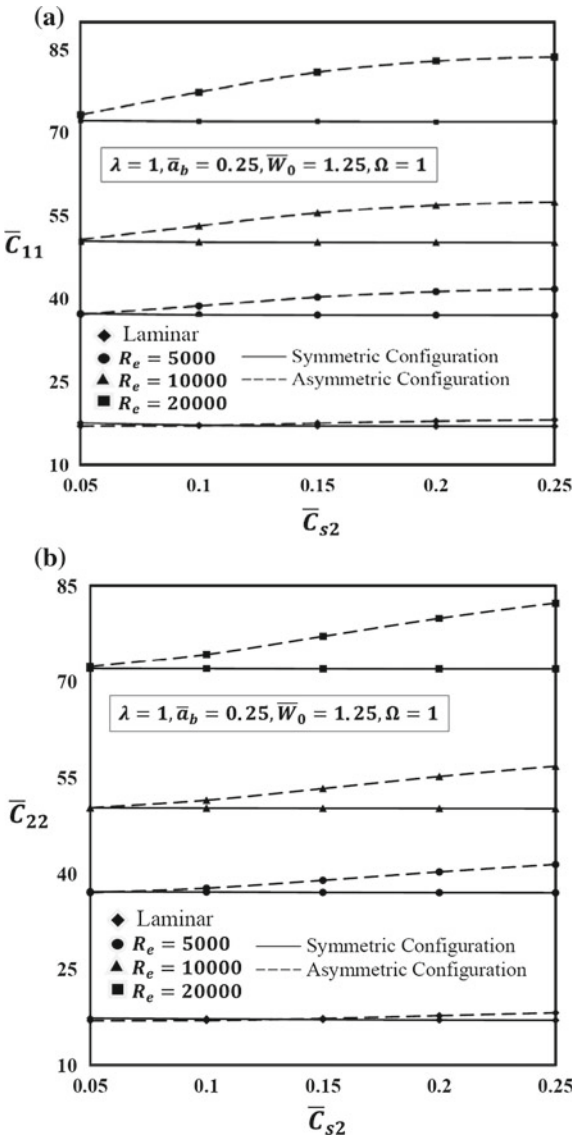

Fig. 7 Variation of **a** $\bar{C}_{11}$, with $\bar{C}_{s2}$ **b** $\bar{C}_{22}$ with $\bar{C}_{s2}$

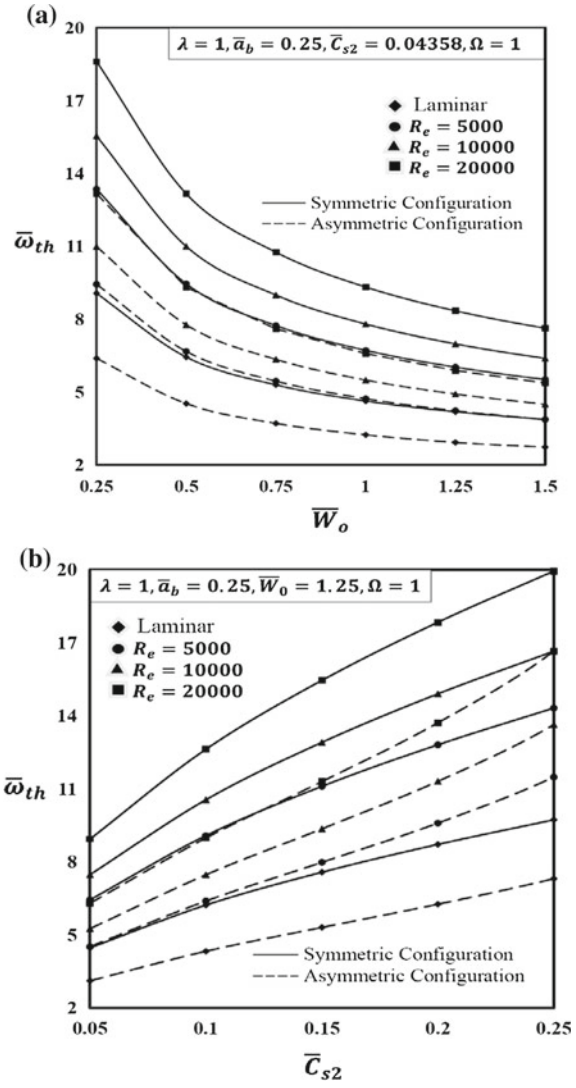

Fig. 8 Variation of **a** $\bar{\omega}_{th}$ with $\bar{W}_o$ and **b** $\bar{\omega}_{th}$ with $\bar{C}_{s2}$

97.02% for $\bar{W}_o = 1.5$ as compared to symmetric bearing in laminar regime, whereas in case of asymmetric bearing, the value of $\bar{\omega}_{th}$ gets compensated by 38.72% for same value of R_e and $\bar{W}_o$ than symmetric bearing under laminar regime. From Fig. 8b, the increasing trend is noticed $\bar{\omega}_{th}$ value for symmetric and asymmetric bearings under laminar/turbulent regime. Further, the threshold speed $\bar{\omega}_{th}$ increases by 117.75% for the $\bar{C}_{s2} = 0.05 - 0.25$ values for symmetric bearing under laminar regime. However, an increase in threshold speed for the values of $R_e = 5000$, 10000, and

20000 is 47.16%, 71.20%, and 105.02%, respectively, for symmetric bearing at $\bar{C}_{s2} = 0.25$ than similar bearing in laminar regime. In case of asymmetric bearing, an enhancement in threshold speed for same Reynolds number values is 18.01%, 40.18%, and 71.25%, respectively, at $\bar{C}_{s2} = 0.25$ than symmetric bearing operates under laminar regime.

5 Conclusions

The conclusions drawn from simulated results of dynamic characteristics of hole-entry bearings for hybrid operation are:

1. The stiffness coefficients are higher for symmetric configuration than asymmetric configuration of hole-entry bearing at constant load and restrictor design parameter ($\bar{C}_{s2}$), when operating under turbulent lubrication.
2. For higher value of Reynolds number, the coefficients of damping are more for asymmetric configuration of bearing for constant restrictor design parameter ($\bar{C}_{s2}$) under turbulent regime.
3. The threshold speed ($\bar{\omega}_{\text{th}}$) for $R_e = 10000$ is found to be order of 71.20% for symmetric configuration, whereas for asymmetric configuration, the value of $\bar{\omega}_{\text{th}}$ for the value of $R_e = 10000$ is found to be order of 40.18% at $\bar{C}_{s2} = 0.25$ than symmetric bearing under laminar regime.

References

1. Yoshimoto S, Rowe WB, Ives D (1998) A theoretical investigation of the effect of inlet pocket size on the performance of hole-entry journal bearing employing capillary restrictors. Wear 127:307–318
2. Rowe WB, Koshal D (1998) A new basis for the optimization of hybrid journal bearing. Wear 64:115–131
3. Constantinescu VN (1962) Analysis of bearing operated in the turbulent regime. Trans ASME, J Basic Engng 84(1):139–151
4. Constantinescu VN, Galetuse S (1965) On the determination of friction forces in turbulent lubrication,". ASLE Trans 8:367–380
5. Hashimoto H, Wada S, Ito J-I (1985) An application of short bearing theory to dynamic characteristic problems of turbulent journal bearings. J Trib Trans ASME 109:307–314
6. Kumar A, Mishra SS (1996) Steady state analysis of non-circular worn journal bearings in nonlaminar lubrication regimes. Tribol Int 29:493–498
7. Nicodemus R, Rajasekhar E, Sharma SC (2010) A study of worn hybrid journal bearing system with different recess shapes under the turbulent regime. ASME J Tribol 132:1–12
8. Soni S, Vakharia DP (2015) Static analysis of finite hydrodynamic journal bearing in turbulent regime with non-newtonian lubricant. Tribology Online 10(4):246–261
9. Ram N, Sharma SC (2013) A study of misaligned hole-entry worn journal bearing operating in turbulent regime. Ind Lubr Tribol 65(2):108–118
10. Ram N, Sharma SC (2014) Influence of wear on the performance hole-entry hybrid misaligned journal bearing in turbulent regime. Ind Lubr Tribol 66(4):509–519

11. Gautam SS, Ghosh MK (2010) Dynamic and static characteristics of wavy annular seals in turbulent flow. Tribology Online 5(1):7–8
12. Ram N (2016) Performance of non-recessed hole-entry hybrid journal bearing operating under turbulent regime. Jurnal Tribologi 8:12–26

Kinematic Analysis of Modified Theo Jansen Mechanism-Based Robot Made of ABS

Keval Bhavsar, Pranav Darji, Dharmik Gohel, Jitendra Modi and Umang Parmar

Abstract This paper shows the kinematic analysis of an intellectual model of a surveillance robot. The objective is to do surveillance on any terrain especially in muddy areas or dessert. This robot is having eight legs which are controlled by two motors. The mechanism used to make these legs is MODIFIED THEO JANSEN MECHANISM, which is an animal walking pattern. For surveillance, a rotating camera is used which works on its own module. Arduino is used for controlling the robot, and that Arduino takes power from battery. This is the first Spider robot which will be made by Acrylonitrile butadiene styrene (ABS) material.

Keywords Modified Theo Jansen mechanism · Walking pattern · Surveillance robot · ABS material · Kinematic analysis

1 Introduction

India is having a huge land border, and to do observation, army require numerous observers or a surveillance robot, till now surveillance robots like four-wheel robot and UAVs are used for observation. The use of the four-wheel robot in observation is valid for most of the terrains except those which are less grippy. The use of UAVs is workable for the surveillance in all terrain, but the problem is that if the enemy's

K. Bhavsar (✉) · P. Darji · D. Gohel · J. Modi · U. Parmar
Aditya Silver Oak Institute of Technology, Ahmedabad, Gujarat, India
e-mail: kevalbhavsar42@gmail.com

P. Darji
e-mail: pdarji576@gmail.com

D. Gohel
e-mail: dharmikgohel67@gmail.com

J. Modi
e-mail: jmodi655@gmail.com

U. Parmar
e-mail: umangparmar.me@socet.edu.in

A. K. Parwani and PL. Ramkumar (eds.), *Recent Advances in Mechanical Infrastructure*, Lecture Notes in Intelligent Transportation and Infrastructure,
https://doi.org/10.1007/978-981-32-9971-9_30

forces see our UAV then most likely they will try to catch it. So, the forces need to essentially stroll in those areas to do an inspection. The spider which is shown in this paper is designed to do observation mostly in any region whether the terrain is even or not. And we can hide the robot by just putting a cover on it. Only two motors are required to run this robot which reduces the vibration problem. The mechanism used to make these legs is MODIFIED THEO JANSEN MECHANISM, which is an animal walking pattern. The kinematic study of the spider is done with the purpose of finding the performance of the spider by creating graphs for numerous parameters. And for the study of those parameters, we have used two software "SOLIDWORKS 2017" and "ANSYS R18".

2 Literature Review

Conventional Theo Jansen Mechanism uses eleven binary links; Sculptor Theo Jansen has designed a planar mechanism that can run in a plane advancing motion [1, 2].

Ying Qu et al. present the expansion of a theoretical model of a self-governing self-driven in-line observation robot, called Smart Spider. The key purpose is to use the robot for oil and gas tube examination [3]. Somak Sengupta et al. present a study of Applications of Jansen's Mechanism in Robot in which the belief relies on the rapid advancement of technologies like metal cutting and 3D printing which will enable developers to easily prototype their conceptual models and also go for mass production if the prototype seems a promising one [4]. Bhavik J. Parekh et al. present to autonomous pitch marking robot using Theo Jansen mechanism. The goal is set up to minimize the input energy and maximize the output. Its also says that if you want to increase the accuracy then you can increase the number of legs [5]. Weiwei Liu et al. present a research on the knowledge acquirement of rapid design for mechanical products which states that during the development of mechanical products rapid design, the key issues that worry a designer are obtaining the design information and extracting the design guidelines. In order to solve the problem of design knowledge complex range, the modular method of product unstructured data division is presented. This method completes the product data reduction and improves the efficiency and accuracy of the design rules extraction [6]. Florina Moldovan et al. present the results of kinematical learning, established upon a ten-bar linkage designed in CAD in order to study the opportunity of using this new type of mechanism for making a walking robot. It also demonstrates the advantages of using CAD simulation tools for examining the path defined by the endpoint of the foot through walking [7]. Servet Soyguder et al. present a research on design and prototype of a six-legged walking insect robot working on cockroach leg mechanism. They used only two motors to reduce weight [8].

2.1 Research Gap

After studying many kinds of literature on Theo Jansen mechanism, we found that very few robots are made of ABS material. This research sets a theoretical basis for forthcoming research into Theo Jansen mechanism. Till now, this mechanism is used only in carriage robots and mobile robots. We are using the updated mechanism for the observation. This is the first Spider robot with Modified Theo Jansen Mechanism which will be made by Acrylonitrile butadiene styrene (ABS) material.

3 Design and Analysis

Modified Theo Jansen Mechanism (shown in Fig. 1) is having six links out of which two are ternary links and four are binary links. The robot is having eight legs (shown in Fig. 2).

When we generated the path in SOLIDWORKS 2017 (shown in Fig. 3) for this mechanism made from ABS (Acrylonitrile butadiene styrene) as shown below is quite smooth. So on the basis of these results, someone can predict that robot will have greater flexibility.

In displacement analysis, displacement graph for Acrylonitrile butadiene styrene (shown in Fig. 4) material robots is shown below and the graph shows that the number of peaks obtained 1.2 per second and the peak is at 76 mm.

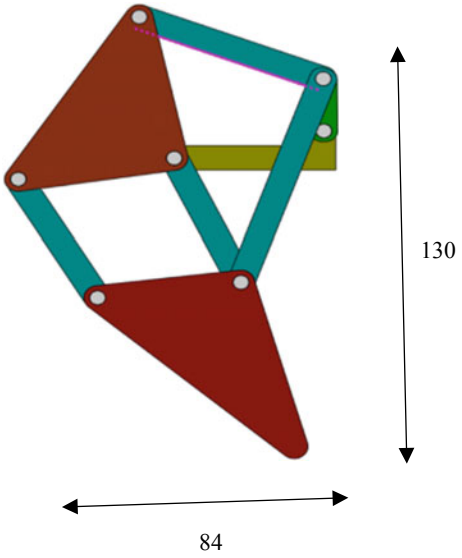

Fig. 1 Modified Theo Jansen mechanism

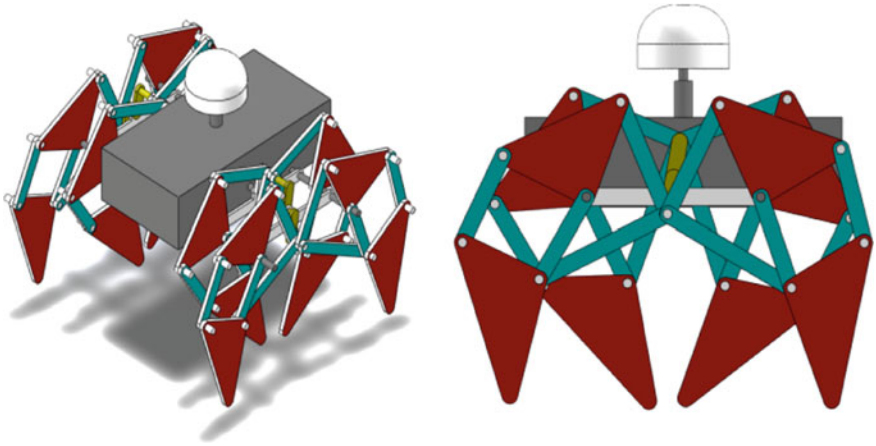

Fig. 2 Isometric view and side view of the robot

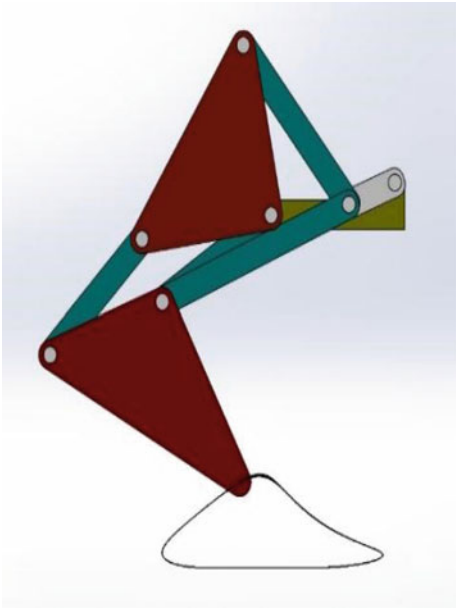

Fig. 3 Modified Theo Jansen path

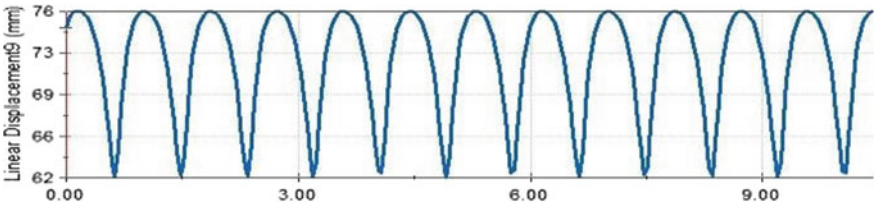

Fig. 4 Modified Theo Jansen displacement analysis

In linear velocity analysis (shown in Fig. 5), velocity for a robot made with ABS material is shown below and resulting graphs show 1.1 peaks per second and the peak is at 384 mm/s.

In acceleration analysis (shown in Fig. 6), acceleration graphs for Acrylonitrile butadiene styrene material robot are shown below and results which are obtained in the graph show 1.2 peaks per second and the peak is at 6163 mm/s^2.

In torque analysis, graph of motor torque for Acrylonitrile butadiene styrene (ABS) (shown in Fig. 7) material robot is shown below, and we found that maximum torque required to run each leg of this robot is 1.1 Newton-mm.

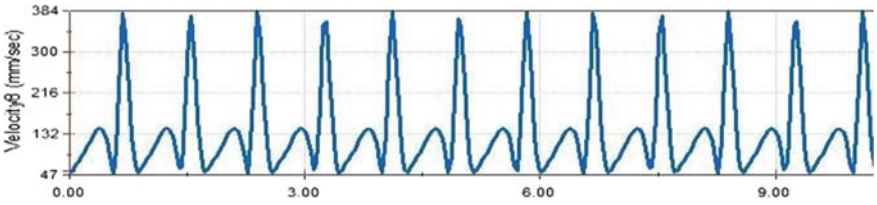

Fig. 5 Modified Theo Jansen velocity analysis

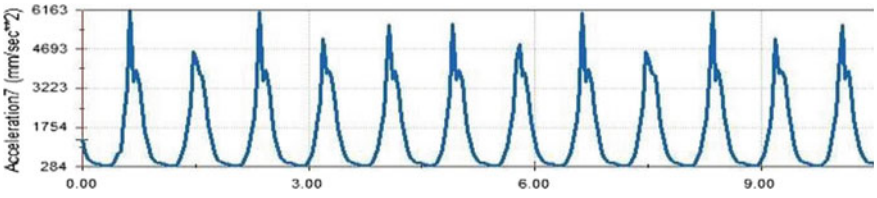

Fig. 6 Modified Theo Jansen acceleration analysis

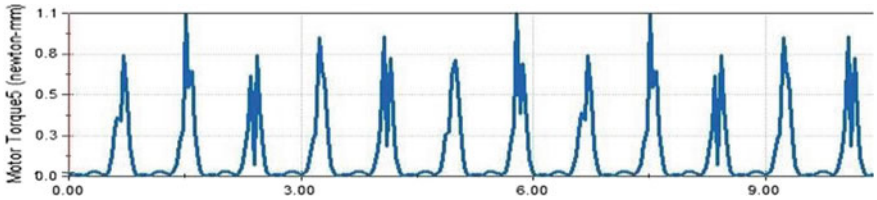

Fig. 7 Modified Theo Jansen torque analysis

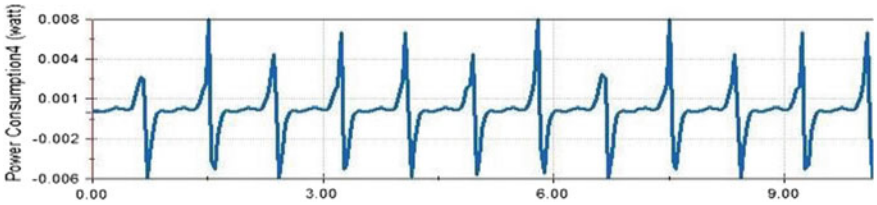

Fig. 8 Modified Theo Jansen power consumption analysis

In power consumption analysis, graph of power consumption for Acrylonitrile butadiene styrene (shown in Fig. 8) material robots is shown below and maximum power required per leg for Acrylonitrile butadiene styrene (ABS) robot is 0.008 W.

When we had done static structural analysis in ANSYS R18.0, we came to know that all the results show that robot which we have designed is safe as per all aspects.

Results of total deformation (Fig. 9) show that the total maximum deformation which will occur in robot under maximum applicable load is nearly 8–9% of the total thickness of any of the part, and it can be neglected.

Results of directional deformation (Fig. 10) show that the total maximum directional deformation that will occur under maximum applicable load is within the allowable range and hence can be neglected.

Results of equivalent elastic strain (Fig. 11) show that during analysis maximum elastic strain induced in robot under maximum applicable load is very less and hence it can be considered as negligible as per design point of view.

Results of equivalent stress (Fig. 12) show that total maximum stress induced in robot under maximum applicable load is nearly 11 MPa which is less than that of allowable strength of the material which we have used. So we can consider that a robot is safe.

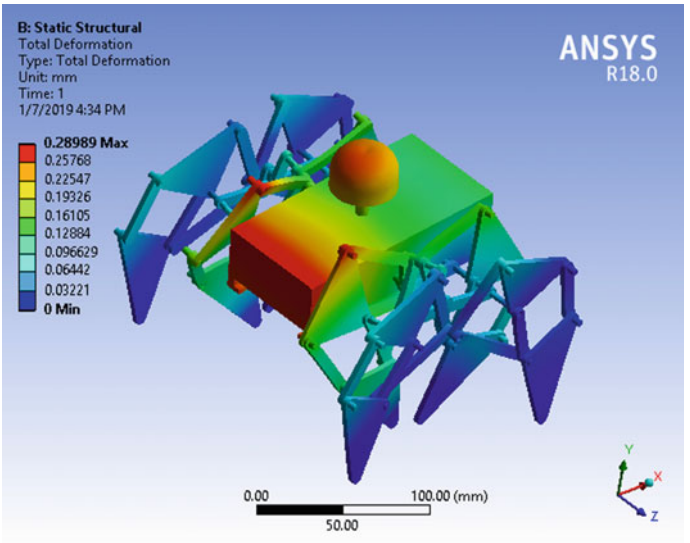

Fig. 9 Results for total deformation

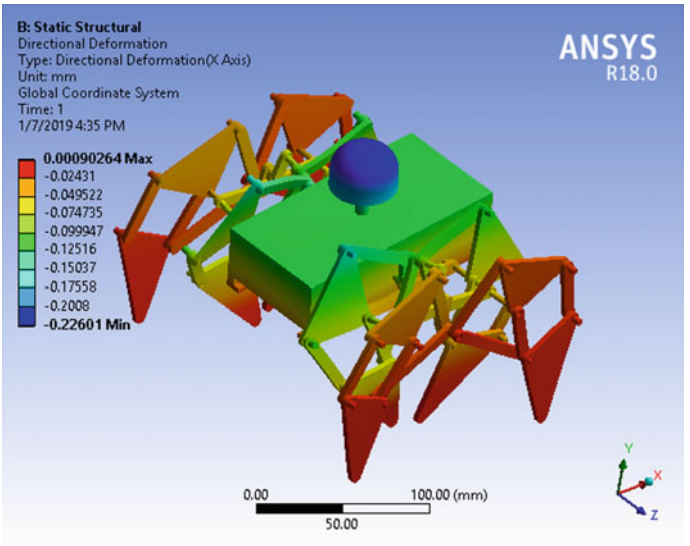

Fig. 10 Results for directional deformation

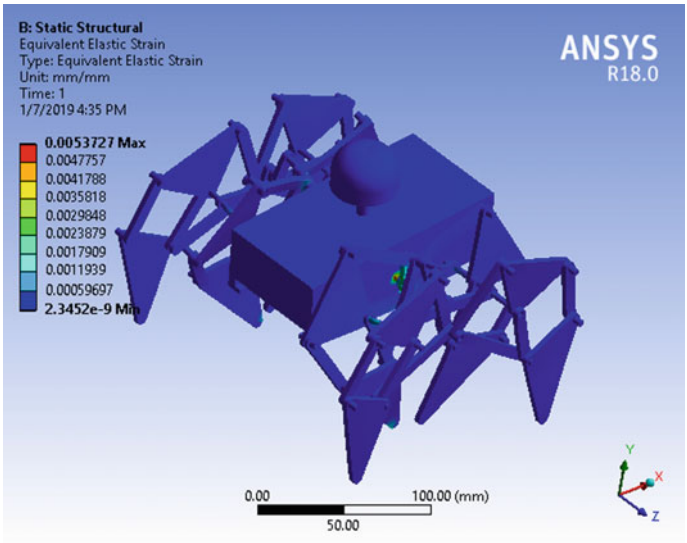

Fig. 11 Results for equivalent elastic strain

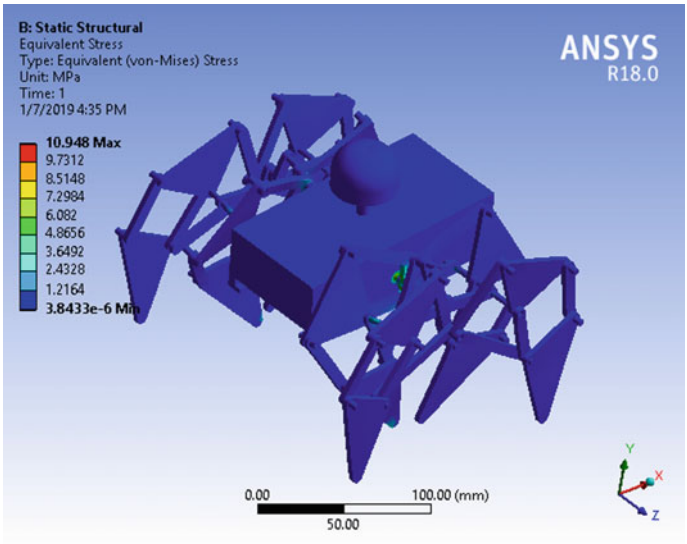

Fig. 12 Results for equivalent stress

4 Conclusion

Using Modified Theo Jansen Mechanism which is having six links (two are ternary and four are binary) in the making of the robotic leg and on the basis of results shown in graphs in DESIGN AND ANALYSIS SECTION says that amount of torque required for each leg of a robot made from ABS is 1.1 Newton-mm, and maximum power consumption per leg is 0.008 W. Also, the conclusion coming from the static structural analysis of robot says that the robot is able to withstand against static loading conditions. And results show that it is statically stable up to 20 N.

References

1. Komoda K (2011) A study of availability and extensibility of Theo Jansen mechanism toward. In: The 21st annual conference of the Japanese neural network society (21st)
2. Patnaik S (2015) Analysis of Theo Jansen mechanism (Strandbeest) and its comparative advantages over wheel based mine escavation system. IOSR J Eng 5(7):43–52
3. Qu Y (2018) Smart-spider: Autonomous self-driven in-line robot for versatile pipeline inspection. IFAC PapersOnLine 51(8):251–256
4. Sengupta S (2017) Study of applications of Jansen's mechanism in robot. Int J Adv Res Innov 5(3):354–357
5. Parekh BJ (2014) Design and analysis of Theo Jansen's mechanism based ports ground (pitch) marking robot. In: Annual IEEE India conference
6. Liu W (2014) Research on the knowledge acquirement of rapid design for. IERI Procedia 7:96–101
7. Moldovan F (2012) A new type of walking robot based upon Jansen mechanism. Adv Mater Res 463–464:997–1001
8. Soyguder S (2007) Design and prototype of a six-legged walking insect robot. Ind Robot: Int J 34(5):412–422

Author Index

A. K. Parwani and PL. Ramkumar (eds.), *Recent Advances in Mechanical Infrastructure*, Lecture Notes in Intelligent Transportation and Infrastructure,
https://doi.org/10.1007/978-981-32-9971-9